

**NUMERICAL INVESTIGATION OF TRANSITION AND TURBULENCE IN PLANAR
AND AXISYMMETRIC EXPANSIONS**

by

Nima Moallemi

B.Sc. in Mechanical Engineering, Shahid Bahonar University of Kerman, 2006

M.Sc. in Mechanical Engineering, Iran University of Science and Technology, 2009

M.A.Sc. in Mechanical Engineering, The University of British Columbia, 2014

A THESIS SUBMITTED IN PARTIAL FULFILLMENT OF
THE REQUIREMENTS FOR THE DEGREE OF

DOCTOR OF PHILOSOPHY

in

THE COLLEGE OF GRADUATE STUDIES

(Mechanical Engineering)

THE UNIVERSITY OF BRITISH COLUMBIA

(Okanagan)

November 2018

© Nima Moallemi, 2018

The following individuals certify that they have read, and recommend to the College of Graduate Studies for acceptance, a thesis/dissertation entitled:

NUMERICAL INVESTIGATION OF TRANSITION AND TURBULENCE IN
PLANAR AND AXISYMMETRIC EXPANSIONS

submitted by Nima Moallemi in partial fulfillment of the requirements of

the degree of Doctor of Philosophy .

Dr. Joshua Brinkerhoff, School of Engineering

Supervisor

Dr. Sunny Li, School of Engineering

Supervisory Committee Member

Dr. Bernard Laval, Department of Civil Engineering, UBC

Supervisory Committee Member

Dr. Steven Rogak, Department of Mechanical Engineering, UBC

University Examiner

Dr. Antonino Ferrante, College of Engineering, University of Washington

External Examiner

Abstract

This thesis documents a series of complementary numerical investigations aimed at understanding the flow instability, transition, and laminarization process through planar and axisymmetric expansions. Direct numerical simulation (DNS) is used to accurately resolve the spatial and temporal scales of the simulated flows.

The first investigation addresses the mechanisms for the initial onset of flow instability in planar expansions at low Reynolds numbers. Various expansion ratios are studied using two-dimensional direct numerical simulations at flow Reynolds numbers up to 5000 and expansion ratios in the range of 1.33 to 4.00. Correlations are developed for the non-dimensional reattachment length and the maximum velocity magnitude in the reverse-flow region in terms of Reynolds numbers and expansion ratios. Bifurcation phenomena resulting in the loss of flow symmetry downstream of the sudden expansion is observed and critical Reynolds numbers for the onset of bifurcation for various expansion ratios are identified. The growth and decay mechanisms of the localized turbulence are analyzed through the transport budgets of instantaneous vorticity.

The effect of transverse jets on the bifurcation and instability of the flow in planar expansions is examined. Transverse injections cause increased levels of mixing and fluctuations downstream of the flow by generating localized disturbances through the activation of inviscid instability modes in the transverse flow.

Finally, the dynamics of turbulent flow in a gradual axisymmetric expansion is investigated. Turbulent inflow is generated in a precursor simulation of a periodic pipe with an annular rib roughness. Validation is accomplished in terms of published mean velocity profile, velocity defect, and fluctuation amplitudes as well as near-wall power spectra. Turbulence from the precursor study is passed to the gradual expansion to examine the downstream growth and

decay of turbulence. This process is described in terms of the evolution of the Reynolds stress tensor in the turbulent and laminarizing regions, morphometrically in terms of the evolution of coherent vortical structures, and mechanistically through analysis of the budgets of the vorticity transport equation.

Lay Summary

Sudden change of pipe diameter can cause different flow structures and appears in many industrial applications. This research focuses on a various type of sudden expansions which can be used in different applications including water treatment plant. The level of mixing and unsteadiness in the flow is improved by adding transverse jets into the flow.

The primary goal of this study is to establish a better understanding of the flow hydrodynamics through the expansion. Different types of water flow scenarios are examined in a virtual environment through series of numerical simulations. The outcomes of this research provide a tool to estimate the flow behavior in sudden and gradual expansions depending on the operating conditions.

Preface

This research was performed under the supervision of Dr. Joshua Brinkerhoff. The research were conducted in UBC Okanagan CFD Laboratory at the School of Engineering, University of British Columbia (UBC). Ethics approval from the UBC Research Ethics Board was not required for this research study.

The list of publications related to this thesis is presented below. While earning my PhD, I was able to publish two journal papers, based on Chapter 4 and Chapter 6 of this study. Appendix A is submitted to the International Journal of Multiphase Flow.

- **Moallemi, N.** and Brinkerhoff, JR, (2016) Numerical analysis of laminar and transitional flow in a planar sudden expansion, *Computers & Fluids*, 140: 209-221. The idea of this research was formed by Dr. Brinkerhoff and I. I performed all the simulations and analysis. In addition, I prepared manuscript, which was further edited by Dr. Brinkerhoff.
- **Moallemi, N.** and Brinkerhoff, JR., (2018) An Instability and Localised Turbulence Associated with an Axisymmetric Sudden Expansion, *International Journal of Heat and Fluid Flow*, 72:161-173. The idea of this research was formed by Dr. Brinkerhoff and I. I performed all the simulations and analysis. In addition, I prepared manuscript, which was further edited by Dr. Brinkerhoff.
- **Moallemi, N.** and Brinkerhoff, JR., (2018) Simulation of Dilute Particle-Laden Laminar Flow Through a Sudden Expansion via the Multiphase Particle-in-Cell Method, *International Journal of Multiphase Flow* (Submitted). The idea of this research was formed by Dr. Brinkerhoff and I. I performed all the simulations and

analysis. In addition, I prepared manuscript, which was further edited by Dr. Brinkerhoff.

The body of the thesis contains Chapters 1–3, which comprise the general introduction of the thesis, a literature review, and a summary of the numerical approach. The bulk of the research in this thesis is contained in Chapters 4-7, in which the above-listed articles are reproduced. Chapter 8 summarizes the contributions of the research, presents the conclusions and how they connect to the objectives of the thesis, and provides recommendations for future research.

Table of Contents

Abstract.....	iii
Lay Summary.....	v
Preface.....	vi
Table of Contents.....	viii
List of Tables.....	xiii
List of Figures	xiv
Acknowledgments.....	xxiv
Dedication	xxv
Chapter 1: Introduction	1
1.1 Motivation	1
1.2 Thesis objectives	3
1.3 Approach	3
1.4 Outline of Thesis	4
Chapter 2: Literature Review	5
2.1 Shear-layer reattachment.....	7
2.2 Onset of flow bifurcation	8
2.3 Instability and growth of localised turbulence	10
2.4 Gradual expansion.....	11
2.5 Transverse jets in sudden expansions.....	13
2.5.1 Generation of turbulent inflow in simulations.....	14
Chapter 3: Methodology.....	17

3.1	Computational platform	17
3.2	Governing equations	18
3.3	Boundary conditions	19
3.3.1	Turbulent inflow generator.....	20
3.4	Solution Method.....	23
3.5	Parallel Processing	24
Chapter 4: Laminar and Transitional Flow in a Planar Sudden Expansion		25
4.1	Numerical approach	26
4.1.1	Computational domain	26
4.1.2	Test cases.....	27
4.1.3	Spatial grids	28
4.1.4	Mesh independence	31
4.2	Shear layer reattachment length	32
4.3	Reversed-flow velocity magnitude.....	36
4.4	Development of flow bifurcation	40
4.4.1	Critical Reynolds number for bifurcation.....	41
4.4.2	Bifurcation onset and growth	44
4.5	Bifurcation instability and transition to turbulence.....	49
Chapter 5: Laminar and Transitional Flow in a Sudden Expansion with Transverse Injections.....		51
5.1	Flow configuration and test cases	52
5.2	Numerical approach	53
5.2.1	Domain and boundary conditions.....	53

5.2.2	Spatial grid.....	54
5.3	Mean flow development.....	59
5.4	The effect of transverse jets on bifurcation.....	65
5.5	The interaction between the transverse jet and the main flow	68
Chapter 6: Instability and Localised Turbulence Associated with an Axisymmetric Sudden Expansion.....		75
6.1	Computational domain	75
6.1.1	Mesh resolution	76
6.2	Comparison of two- and three-dimensional simulations	80
6.3	The shear layer reattachment length.....	82
6.4	Disturbance growth and transition to turbulence	83
6.5	Visualization of transition and localized turbulence	89
Chapter 7: Turbulent Flow through Axisymmetric Gradual and Sudden Expansion		95
7.1	Production of Fully-Developed Turbulent Flow.....	95
7.1.1	Numerical Approach.....	95
7.1.2	Comparison of turbulence statistics.....	99
7.1.3	Vorticity transport.....	107
7.2	Turbulent flow in a circular pipe with a sudden expansion	110
7.3	Turbulent flow in a circular pipe with a gradual expansion.....	114
7.3.1	Results and discussion	116
Chapter 8: Summary, Conclusions, and Future Work		125
8.1	Summary and concluding remarks	125
8.1.1	Laminar and transitional flow in a planar sudden expansion	125

8.1.2	Planar sudden expansion with transverse jets.....	126
8.1.3	Localised turbulence associated with flow through an axisymmetric expansion...	127
8.1.4	Turbulent flow in a pipe with a rib-roughened wall.....	129
8.1.5	Statistics of turbulent flow in a circular pipe with a gradual expansion.....	130
8.2	Recommendations for Future Work.....	131
8.2.1	Instability and localised turbulence associated with an axisymmetric sudden expansion with transverse jets	131
8.2.2	Particle-laden laminar flow through a fluidized bed reactor (FBR) with sudden expansion and transverse jets	132
8.2.3	Laminarization of the turbulent flow at various expansion configurations.....	132
Bibliography		134
Appendix A: Particle-Laden Laminar Flow through a Sudden Expansion.....		153
A.1	Particle-laden flow in sudden expansions	153
A.1.1	Numerical methods for solid/fluid multiphase flows	155
A.2	Numerical approach	157
A.2.1	Computational domain and boundary conditions	157
A.2.2	Spatial grid.....	158
A.2.3	Test cases	161
A.2.4	Solution Method	162
A.2.5	MP-PIC method.....	162
A.3	Validation of the computational approach	166
A.4	Symmetric flow structure	168
A.5	Effect of solid phase on bifurcation onset.....	173

A.6 Transport of suspended particles 181

List of Tables

Table 2-1: Studies of shear-layer reattachment in sudden expansion flows	6
Table 2-2: Studies on bifurcation.....	9
Table 3-1: Description of the computational platforms used in the present research.....	24
Table 4-1: Test cases range for various expansion ratios	28
Table 4-2: Characteristics of computational grids used.....	29
Table 4-3: Critical Reynolds number for the onset of bifurcation in laminar flows in planar sudden expansions.....	42
Table 5-1: Test cases range for various expansion ratios	53
Table 5-2: Characteristics of computational grids used for various sudden expansions	55
Table 5-3: The grids used for the grid-independence study at $Er = 2.0$, $r = 20$, and $Re = 1000$..	57
Table 6-1: Characteristics of the computational grids.	78
Table 7-1: Characteristics of computational grids used.....	112
Table 7-2: Characteristics of computational grids used.....	115
Table A-1: Characteristics of computational grids used.....	159
Table A-2: Test cases range for various expansion ratios	161

List of Figures

Figure 2-1: Schematic of major features of flow through a sudden expansion	5
Figure 2-2: Zoomed view of mean velocity contour in a sudden expansion with $Re = 200$ and $Er = 2.0$ a) Instantaneous velocity contour of particles b) Age of particles.....	12
Figure 3-1: Diagram illustrating a schematic of geometry and the mapping technique: a) schematic of the computational domain (not to scale); (b) data from an interior mapping plane within the simulation is mapped backwards to the inlet boundary; (c) data at the mapped plane continues its development for the rest of the domain.....	21
Figure 3-2: Visualization of the turbulent pipe flow over constant θ plane using instantaneous velocity magnitude contours for various inflow condition in pipe flow a) periodic streamwise boundary condition b) turbulent inlet boundary condition form the OpenFOAM® library c) mapping technique with ribbed Turbulator. Red represents higher values of u and blue represents values of u near zero.....	22
Figure 4-1: Schematic of the computational domain	26
Figure 4-2: Distribution of the spatial grid spacing in the (a) streamwise direction at $y = D/2$ and (b) wall-normal direction at $x/h=10$ for the $Er = 2.00$ case. The dashed line indicates the location of the sudden expansion.....	30
Figure 4-3: Dependence of reattachment lengths to the grid size for different Reynolds number and expansion ratio	31
Figure 4-4: Streamline distribution in sudden expansion with expansion ratio of 4.00 and $Re=100$ for different gird resolution a) $NC = 17,500$, b) $NC = 43,000$, c) $NC = 110,080$, d) $NC = 172,000$	32

Figure 4-5: Comparison of non-dimensional reattachment length (L_r/h) at various Reynolds numbers for $Er = 2.00$ with literature.....	33
Figure 4-6: Reynolds number distribution of the reattachment length for various expansion ratios. Symbols denote numerical results and lines denote Eq. (5.2)	34
Figure 4-7: Primary reattachment length at upper and lower walls for various expansion ratios	35
Figure 4-8: Secondary separation point at various Reynolds numbers for various expansion ratios	36
Figure 4-9: Comparison of the velocity profile for $Re_{max} = 200$ and 300 for $Er = 200$ at different streamwise stations	37
Figure 4-10: Maximum reverse velocity distribution at various Reynolds numbers and expansion ratios and approximate values of $Ur, max/Umax$	38
Figure 4-11: Reynolds number distribution of the maximum reverses velocity for various expansion ratios. Symbols denote numerical results and lines denote Eq. (4.3)	39
Figure 4-12: Streamline pattern near the expansion (zoomed view) (a) Symmetric reattachment for $Re_{max} = 200$ and $Er = 2.00$. (b) Asymmetric reattachment for $Re_{max} = 500$ and $Er = 2.00$	41
Figure 4-13: Correlation equation prediction for Critical Reynolds number for the onset of bifurcation in laminar flows in planar sudden expansions: a) in comparison with computed data for various Expansion ratios, b) in comparison with published investigations for high expansion ratio $2.00 < Er < 10.00$	44
Figure 4-14: Maximum velocity variation of velocity profile at the reattachment point for $Er = 2.00$	45

Figure 4-15: Measured root mean square velocity fluctuation at various positons before onset of flow bifurcation at $Er = 2.00$	47
Figure 4-16: Temporal evaluation of the flow velocity disturbance contour after semi steady state condition at $Re_{max} = 1200$ and $Er = 2.00$	48
Figure 4-17: Velocity contour for flow in sudden expansion with $Er = 4.00$ at various Reynolds numbers: a) Instantaneous velocity b) Mean velocity	50
Figure 5-1: Schematic of major features of flow through a planar sudden expansion with cross injections	51
Figure 5-2: Schematic of the computational domain	54
Figure 5-3: Distribution of the spatial grid spacing in the (a) streamwise direction at centerline of inlet channel and (b) wall-normal direction at centerline of cross injection jets for the $Er = 2.0$ case. The dashed line indicates (a) the location of the sudden expansion and (b) centerline of centerline of inlet channel	56
Figure 5-4: Pressure coefficient (C_p) distributions at various mesh resolutions at $Re = 1000$, $r = 20$ and $Er = 2.0$	58
Figure 5-5: Zoomed view of non-dimensional velocity contour at Reynolds numbers of 2000 and $Er = 2.0$ for the case with cross flow ($r = 1.25$): a) Instantaneous velocity contour b) Mean velocity contour	60
Figure 5-6: Zoomed view of streamline distribution in sudden expansion with at Reynolds numbers of 1000 and $Er = 2.0$ for the case with cross flow ($r = 10$) a) instantaneous streamlines, b) time-averaged streamlines	61

Figure 5-7: Visualization of the laminarization process by instantaneous velocity contour at Reynolds numbers of 600 and $Er = 2.0$ for the case with transverse jets at velocity ratio of 5 62

Figure 5-8: Measured root mean square velocity fluctuation at various positions downstream of transverse jets at $Re = 600$ and $Er = 2.0$ for the case with velocity ratio of 5 63

Figure 5-9: a) Reynolds number distribution of non-dimensional reattachment length (L_r/D). b) Dependence of reattachment length to velocity ratio (r) 64

Figure 5-10: Reynolds number distribution of the reattachment length for various expansion ratios at $r = 20$ 65

Figure 5-11: Zoomed view of non-dimensional velocity contour and streamlines illustrating the bifurcated flow downstream of the planar sudden expansion with $Re = 500$ and $Er = 4.0$ 66

Figure 5-12: Pressure coefficient distributions at various velocity ratios (r) at $Re = 2000$ and $Er = 2.0$ 68

Figure 5-13: Zoomed view of non-dimensional vorticity contour near near-field flow of the transverse jet at Reynolds numbers of 2000 and $Er = 2.0$ for cross flow with velocity ratio of $r = 3.75$: (a) instantaneous non-dimensional vorticity (b) Time-averaged non-dimensional vorticity 70

Figure 5-14: Zoomed view of time-averaged non-dimensional velocity magnitude contour in the near-field wake of the transverse jet for Reynolds numbers of 800 and velocity ratio of $r = 20$ at various expansion ratios 71

Figure 5-15: Zoomed view of time averaged streamlines of the planar sudden expansion with transverse jet at various injection angles for $Re = 1000$ with $Er = 2.0$ and $r = 20$ at $z/h = 15$	73
Figure 5-16: The root-mean-square of Streamwise and vertical velocity fluctuations at various injection angles at $Re = 1000$ with $Er = 2.0$ and $r = 20$	74
Figure 6-1: Schematic of the computational domain	76
Figure 6-2: a) Schematic of the block structure that is used for the simulations. Only 10 out of 70 blocks are shown, b) the spatial grid spacing in radial and tangential directions after the expansion step. For easier visual clarity, the coarsest grid spacing is plotted ...	78
Figure 6-3: Dependence of reattachment lengths to the grid size for $Re = 2000$	79
Figure 6-4: Time-averaged contours of velocity magnitude at $Re = 800$ for the (a) 2D and (b) 3D cases	80
Figure 6-5: Comparison of 2D and 3D results for non-dimensional reattachment length (L_r/h) versus various Reynolds numbers.....	82
Figure 6-6: Comparison of non-dimensional reattachment length (L_r/h) at various Reynolds numbers with previous studies.....	83
Figure 6-7: Root-mean-square streamwise velocity fluctuations along the centerline for flows with various Reynolds numbers.....	84
Figure 6-8: Time-averaged radial velocity profiles at $z/D = 20$ and $Re = 1700-2500$. (a) Axial velocity profile. (b)-(d) Root-mean-square velocity fluctuations in the (b) axial, (c) radial, and (d) tangential directions	87

Figure 6-9: Zoomed view contours for flow in an axisymmetric sudden expansion with $Re = 2500$. a) the mean velocity, b) the instantaneous velocity, c) the turbulence kinetic energy, d) the instantaneous vorticity, e) the time-averaged vorticity.....	88
Figure 6-10: Comparison of the turbulence kinetic energy distributions at different positions at $Re = 2500$	89
Figure 6-11: Non-dimensional instantaneous vorticity magnitude contours at various positions for $Re = 2500$	90
Figure 6-12: Vortical structures observed in the flow through sudden expansion. Iso-surfaces are of $Q(d/U_0)^2 = 10$ and the colouring is according to r/d	92
Figure 6-13: Contour levels of the budgets of instantaneous vorticity transport equation between $z/h = 32$ and 46 : (a) ω_r -stretching, (b) ω_θ -stretching, (c) ω_z -stretching, (d) ω_r -tilting, (e) ω_θ -tilting, (f) ω_z -tilting. Contours are normalized by $(U_0/d)^2$ and multiplied by the sign of the associated vorticity component	94
Figure 7-1: Schematic of the computational domain and boundary conditions. The domain is symmetric about the z -axis.....	97
Figure 7-2: a) Cross-sectional slice of the grid, with every second grid node shown, b) radial distribution of the spatial grid spacing.....	97
Figure 7-3: Variation of the the time-averaged velocity profile at different axial locations downstream of the circular rib	100
Figure 7-4: Comparison of axial the time-averaged velocity normalized by the centerline velocity U_c as function of the distance from the centerline with published DNS and experimental values	101

Figure 7-5: Comparison of the the time-averaged velocity profile at $z/d = 9$ with published DNS and experimental values.....	101
Figure 7-6: Companion DNS results of time-averaged velocity defect $ur = 0 - u/u\tau$ as a function of $(1 - r/R)$	103
Figure 7-7: Axial turbulence intensity $urms' +$ as a function of $(1 - r) +$ in the near-wall region	103
Figure 7-8: Root-mean-square of streamwise velocity fluctuation normalized by the local time-averaged velocity $(urms' +/u +)$ as a function of $(1 - r) +$	104
Figure 7-9: Comparison of Reynolds stress profiles at different axial locations downstream of the circular rib.....	105
Figure 7-10: The power spectrum of the streamwise velocity fluctuations at $y+\approx 12$	105
Figure 7-11: The power spectrum of the streamwise velocity fluctuations at $y+\approx 30$	106
Figure 7-12: Vortical structures observed in the flow through ribbed turbulator. Iso-surfaces are of $Q(U02/d2) = 200$ and are colored according to the magnitude of the vorticity production rate.	108
Figure 7-13: Contour levels of the magnitude of instantaneous vorticity transport equation budgets near circular rib: (a) $D\omega/Dt$, (b) ω -stretching, (c) ω -tilting. Contours are normalized by $(U0/d)2$. Arrows show the locations for average reattachment length	109
Figure 7-14: Contour levels of the budgets of instantaneous vorticity transport equation near circular rib: (a) ω_z -stretching, (b) ω_z -tilting, (c) $D\omega_z/Dt$, (d) ω_r -stretching, (e) ω_r -tilting, (f) $D\omega_r/Dt$, (g) ω_θ -stretching, (h) ω_θ -tilting, (i) $D\omega_\theta/Dt$. Contours are normalized by $(U0/d)2$	111

Figure 7-15: Streamwise velocity profile and velocity fluctuation distribution for various mesh resolution.....	113
Figure 7-16: Schematic of the computational domain.....	114
Figure 7-17: Contours in a axial slice near the gradual expansion; a) instantaneous velocity magnitude, b) mean velocity magnitude, c) turbulence kinetic energy, d) instantaneous vorticity magnitude. (Zoomed view).....	118
Figure 7-18: Streamwise distribution of turbulence kinetic energy along the pipe centerline ($r = 0$)	119
Figure 7-19: Radial profiles of the root-mean-square velocity fluctuations at various axial locations	120
Figure 7-20: Contour levels of the budgets of instantaneous vorticity transport terms: a) vorticity growth rate, b) vorticity convection term, c) vorticity production term, d) vorticity diffusion rate	121
Figure 7-21: Contours illustrating the magnitude of the instantaneous vorticity production rate from Eqn. (8.1): (a) overall production rate, (b) stretching mechanism, (c) tilting mechanism. Contours are normalized by $(U_{max} / d)^2$	122
Figure 7-22: Contours of the budgets of instantaneous vorticity (a) production (b) diffusion rate terms. Axial locations are (from left to right) $z/h = 2, 6, 10, 14$	124
Figure 7-23: Instantaneous vortical structures visualized by iso-surfaces of the second invariant of the velocity gradient tensor, $Qd/U_0 = 4.7$ (Zoomed view).....	124
Figure A-1: Schematic of the computational domain	158

Figure A-2: Distribution of the spatial grid spacing in the (a) streamwise direction at $y = D/2$ and (b) wall-normal direction at $x/h = 20$ for the $Er = 4.0$ case. The dashed line indicates the location of the sudden expansion 160

Figure A-3: Comparison of non-dimensional reattachment length (L_r/h) for single-phase flow in a planar sudden expansion at $Er = 2.0$. Subscripts 1 and 2 denote the upper and lower walls, respectively 167

Figure A-4: Comparison of random packing density in packed bed. Modified from Shang and Liu [159] 168

Figure A-5: Contours of velocity magnitude in the water phase at $Re_{max} = 200$ and $Er = 2.0$: (a) mean or instantaneous velocity contour at $\phi_s = 0$; (b) mean velocity contour for $\phi_s = 0.01\%$; (c) instantaneous velocity contour for $\phi_s = 0.01\%$; (d) mean velocity contour for $\phi_s = 0.02\%$; (e) instantaneous velocity contour for $\phi_s = 0.02\%$ 169

Figure A-6: Time-mean streamline pattern near the sudden expansion for $Re_{max} = 200$, $Er = 2.0$ and $\phi_s = 0, 0.01\%$, and 0.02% 170

Figure A-7: Comparison of the time-mean velocity profile for $Re_{max} = 200$ and $Er = 2.0$ for various solid phase volume fraction and streamwise locations 172

Figure A-8: Average shear layer reattachment length for larger recirculation region for various Reynolds numbers at $Er = 2.0$. Dashed and solid lines represents $\phi_{in} = 0$ and $\phi_{in} = 0.016\%$, respectively 173

Figure A-9: Temporal evolution of the single phase flow structure at $Re_{max} = 400$ and $Er = 2.0$ 174

Figure A-10: Average shear layer reattachment lengths for various Reynolds numbers 175

Figure A-11: Contours of velocity magnitude of the water phase for $Re_{max}=1000$ and $Er = 2.0$: (a) mean or instantaneous velocity contour for $\phi_s = 0$; (b) mean velocity contour for $\phi_s = 0.002\%$; c) instantaneous velocity contour for $\phi_s = 0.002\%$ 176

Figure A-12: Time-mean streamline pattern in a sudden expansion for various Reynolds number with volumetric particle injection rate of $\phi_{in} = 0.016\%$ at $Er = 3.0$ 177

Figure A-13: Average shear layer reattachment lengths at (a) $Re_{max} = 400$ and (b) $Re_{max} = 1000$ for $Er = 2.0$. The particle diameter is fixed at $d_p/d = 0.001$. Subscripts 1 and 2 denote upper and lower walls, respectively..... 179

Figure A-14: Average shear layer reattachment lengths at (a) $Re_{max} = 400$ and (b) $Re_{max} = 1000$ for $Er = 2.0$. The solid phase fraction is fixed at $\phi_s = 0.0016\%$. Subscripts 1 and 2 denote upper and lower walls, respectively..... 180

Figure A-15: Time-mean streamline pattern near the expansion for different particle sizes with $Re_{max} = 400$ and $Er = 2.0$ 181

Figure A-16: Zoomed view for instantaneous velocity contour of particles in a sudden expansion with constant volumetric injection rate of particles $\phi_s = 0.0016$: a) $Re_{max} = 400$ and $Er = 3.0$, b) $Re_{max} = 800$ and $Er = 3.0$ 182

Figure A-17: Zoomed view for age of remained particles in a sudden expansion with constant injection volumetric rate of $\phi_s = 0.0016$: a) $Re_{max} = 400$ and $Er = 3.0$, a) $Re_{max} = 800$ and $Er = 3.0$ 183

Acknowledgements

Firstly I would like to thank my supervisor Dr. Brinkerhoff for all of his help and support. His advice and valuable guidance have been invaluable in the completion of my thesis, and without his assistance, this project would have not been possible. I gratefully acknowledge the contributions of my research supervisor Dr. Sergio Hoyas during my visiting period at Spain whose valuable guidance helped me advance my research quality. I would also like to thank my advisory committee members Dr. Li and Dr. Laval for their encouraging words, feedback and advice on thesis, and time and attention during busy semesters.

This work was aided by the support of many people. I would also like to thank my friends for their continued support and assistance. I gratefully acknowledge my research group members specially, Saeed Rahbarimanesh, Evan Flanagan, Amitvikram Dutta, Mohammad Haji Mohammadi, Guoyu Zhang, Dylan Baxter, Luca Chiabò and Behzad Mohajer. These fellow students became friends as we studied and researched together.

Most of all, I am a debtor to my family who have continuously supported me throughout my years of education, morally, emotionally, and financially. I thank my parents, my mother- and father-in-law, and my sisters for their encouragement and love. I am deeply grateful to my sisters, Negin, Nooshin, Nasim, Sophia, and Fatemeh and my brother Navid for being supportive and caring family. I am always proud of you. And most of all, I owe my deepest gratitude to my wife, Sadaf. Dear, I cannot begin to express how thankful I am for all your love and support, and for all you have sacrificed to help me through this thesis.

Dedication

To my family who supported me each step of the way.

Chapter 1: Introduction

1.1 Motivation

The flow through a sudden expansion occurs in many practical applications including combustors [1], heat exchangers [2], electronic cooling [3], pipe networks [4], and many more [5,6]. The fluid dynamics within this geometry contains flow separation, recirculation, transition to turbulence, and turbulent reattachment, which makes it interesting both in terms of its practical importance to engineers and its fundamental interest due to the varied physical processes occurring in the flow.

The heat-transfer coefficient and pressure drop through a sudden expansion are strongly affected by the length of a reversed-flow region that forms immediately downstream of the expansion due to the high momentum exchange that occurs in that region [7]. This momentum exchange improves mixing of the flow, and so applications requiring mixing of the flow may benefit from the addition of a sudden expansion to promote passive mixing. Therefore, many experimental and numerical investigations have been conducted of the flow in a sudden expansion with the aim of controlling the length of the recirculation region downstream of the expansion and enhancing the mixing in the vicinity of the expansion [8].

Although momentum exchange due to sudden expansion improves mixing in a flow, the level of mixing may not always be sufficient for industrial applications especially at lower Reynolds numbers. Adding transverse jets after the sudden expansion can provide superior mixing in comparison to the case without transverse jets due to the transient formation of vortices and instabilities in the main flow by the jets.

An example of sudden expansions in an industrial application occurs in treating municipal wastewater. Municipal wastewater treatment systems are currently being challenged by the growing size of cities and the aging infrastructure of treatment facilities. In wastewater treatment systems, supernatant of anaerobic digesters has high concentrations of phosphate and ammonium [9]. If magnesium exists, formation of struvite, composed of magnesium ammonium phosphate, can create a major dilemma in wastewater centrifuges, pumps, and piping systems [10]. The UBC Struvite Crystallizer developed by the University of British Columbia (UBC) Phosphorus Recovery Group attempts to remove struvite from wastewater streams through crystallization in a fluidized bed reactor (FBR) [11]. Forrest et al. [12] employed a sequence of sudden expansions in a FBR to enhance the mixing of reagents in a reactor designed for removing crystalline phosphorus from wastewater streams. This FBR is able to efficiently recover around 80% of the soluble phosphate from waste streams [13]. The recovered struvite can then be sold for other uses including agricultural fertilizer, thereby transforming what was heretofore a nuisance into a revenue stream for municipalities.

Sudden geometrical expansions between the different zones of the FBR promote turbulence and therefore cause more frequent particle collisions so that struvite crystals nucleate and grow as the fluid flows upward through four zones of different diameters [14]. High turbulence levels resulting from mixing promotes the rapid nucleation of struvite and efficient phosphorus recovery. As the pipe diameter increases in each stage, the Reynolds number reduces and the level of turbulence decreases. In order to optimize the design of the FBR and to predict its performance for a range of flow rates and reactor sizes, the mixing process inside the FBR needs to be thoroughly understood. Therefore, a fundamental study is required to improve the current understanding of the fluid mechanics in sudden expansion geometries in order to tailor the FBR for maximum

nucleation and growth of struvite crystals. Therefore, a fundamental study is needed to identify how the hydrodynamics, vortex dynamics, and sudden-expansion geometry interact to produce elevated turbulence levels.

1.2 Thesis objectives

The ultimate goal of this study is to improve the present understanding of how flow mixing in an expansion occurs. To reach this goal, three specific objectives are defined for the present thesis:

- 1- Characterize the effect of expansion geometry (expansion ratio and gradual vs. sudden expansion) and flow conditions (Reynolds number) on the mechanisms affecting flow mixing in laminar, transitional, and fully-turbulent flow regimes.
- 2- Characterize the physical mechanisms that lead to the growth and decay of localized turbulence in sudden and gradual expansions (i) structurally in terms of the evolution of coherent vortical structures and (ii) mechanistically through analysis of the budgets of the vorticity transport equation.
- 3- Identify the laminarization of low Reynolds turbulent flow in sudden and gradual expansion (i) structurally in terms of the evolution of coherent vortical structures and (ii) mechanistically through analysis of the budgets of the vorticity transport equation.

1.3 Approach

Flow through planar and axisymmetric expansions encompass a very wide range of hydrodynamic phenomena, including flow separation, growth of various types of shear-layer instabilities, transition to turbulence, growth of turbulent fluctuations, and laminarization of turbulence, to be detailed in Section 2. An accurate investigation flow mixing in sudden and

gradual expansions thus hinges on accurately resolving the effect of various flow and geometrical parameters on these complex phenomena. It is costly to make different experimental setups for the various scenarios that need to be investigated. Moreover, fine temporal and spatial resolution required for detailed analysis of the turbulent flow and the need for spatial and temporal synchronization of the flow field generally restrict the experimental measurements that can be obtained. To overcome these limitations, computational fluid dynamics (CFD) is the methodological approach that will be used to achieve the desired objectives of the present research. A series of CFD simulations will be performed by solving the hydrodynamic equations of motion directly on a highly refined temporal and spatial grid without any turbulence modelling assumptions. This technique is referred to as direct numerical simulation (DNS).

1.4 Outline of Thesis

This chapter presented the motivation and objectives of the current research and outlined the approach that is used to fulfill these objectives. Chapter 2 reviews the literature relevant to flow through sudden expansion and cross injection. Chapter 3 describes the computational approach, which includes a discussion of the governing equations, geometry, boundary conditions, and the method for solving the discretized system of equations. In Chapters 4-7 the thesis objectives enumerated in Section 1.2 are addressed by presenting results that are validated with available numerical and experimental data. Finally, the contributions of the present research are summarized in Chapter 8 along with conclusions and recommendations for future investigation.

Chapter 2: Literature Review

Figure 2-1 shows the characteristics of the flow through a sudden expansion. These characteristics include shear layer reattachment, flow recirculation and reversal, and an inviscid injection jet in the core region. The flow past the sudden expansion creates a free shear layer. Recirculation of the near-wall fluid immediately downstream of the step due to the local pressure field results in the growth of reversed-flow boundary layers adjacent to the wall [15]. The recirculation region is characterized by the reattachment length L_r (which is the point with zero wall-normal velocity gradient at the wall) and the position of the vortex center L_{vc} (which is the point of the maximal vorticity). Increasing Reynolds number causes appearance of secondary recirculation region downstream of primary one. The flow gradually recovers a fully-developed profile in the redeveloping region such that after a certain length (the developing length), it becomes a fully-developed laminar or turbulent flow depending on local Reynolds number downstream of the expansion.

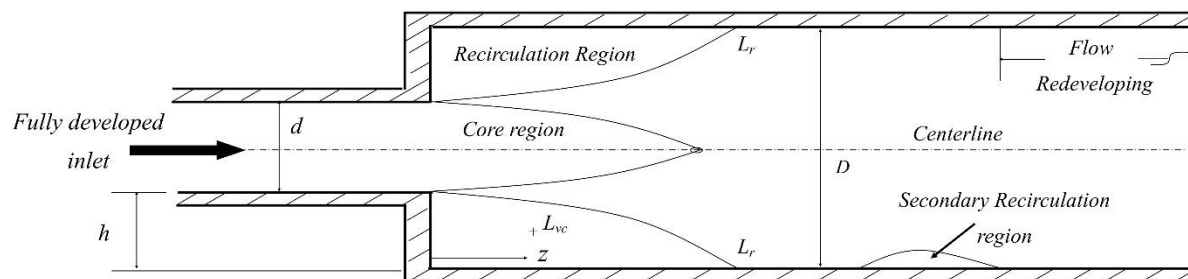


Figure 2-1: Schematic of major features of flow through a sudden expansion

Macagno and Hung [16], Feuerstein et al. [17], and Hammad et al. [18] have conducted experimental studies for laminar flow through axisymmetric sudden expansion while Back and

Roschke [19], Pak et al. [20] and Furuichi et al. [21] have studied the shear layer reattachment length and the reversed-flow region for a wide range of Reynolds numbers covering laminar, transitional, and turbulent regimes. On the other hand, numerical modeling of shear layer reattachment of the laminar flow in a sudden expansion has been discussed by Macagno and Hung [16], Fletcher et al. [22], and Scott et al. [23]. As the Reynolds number increases in sudden-expansion flows, numerous studies have observed bifurcation phenomena through axisymmetric sudden expansion flows with an abrupt loss of symmetry in which the flow bifurcates and reattachment occurs at different locations on the upper and lower channel walls. The growth of unsteady perturbations through onset of bifurcation have been investigated by Cantwell et al. [24], Mullin et al. [25], Sanmiguel-Rojas et al. [26]. Tsai et al. [27] and Khodaparast et al. [28] studied pressure-driven flow in sudden expansion microfluidic channels.

Table 2-1: Studies of shear-layer reattachment in sudden expansion flows

Reference	Er	Inlet flow condition	Re range	Type	Geometry
Macagno & Hung [16]	2.0	Fully developed	1- 400	Experiment	Axisymmetric
Back & Roschke [19]	2.6	Uniform	40- 8400	Experiment	Axisymmetric
Iribarne et al. [29]	2.0	Uniform	180- 2710	Experiment	Axisymmetric
Feuerstein et al. [17]	3.4	Fully developed	444- 1510	Experiment	Axisymmetric
Scott et al. [11]	1.5-4.0	Fully developed	100-400	Numerical	Axisymmetric/ Planar
Latornell & Pollard [8]	2.0	Fully developed & uniform	10-3000	Experiment	Axisymmetric
Pak et al. [20]	2.0-2.6	Uniform	60-80,000	Experiment	Axisymmetric
Badekas & Knight [30]	1.5-6.0	Fully developed	100-400	Numerical	Axisymmetric
Hammad et al. [18]	2.0	Fully developed	40-422	Experiment	Axisymmetric
Furuichi et al. [21]	1.8	Fully developed	500-15,000	Experiment	Axisymmetric
Dağtekin & Ünsal [31]	1.5-10.0	Fully developed	100-1000	Numerical	Axisymmetric/ Planar

2.1 Shear-layer reattachment

Table 2-1 lists the numerous experimental and computational studies that have been conducted of sudden expansions in planar and axisymmetric configurations. The primary parameters affecting sudden expansions are the flow Reynolds number (Re) based on the inlet channel height and maximum inlet velocity and the ratio of the outlet to the inlet channel height, termed the expansion ratio (Er). Several studies [18,32] have found that the streamwise length of the reversed-flow region, termed the reattachment length and denoted by L_r , increases linearly with Reynolds number up to approximately $Re = 250$, which corresponds to a laminar flow regime, and then grows exponentially in the range $400 < Re < 1000$ as unsteady fluctuations develop within the separated shear layers that occur downstream of the sudden expansion. The maximum reattachment length occurs at about $Re=1000$, for which transition to turbulence is completed at the reattachment location [15]. An abrupt decrease in the reattachment length is observed for $1000 < Re < 8000$ as the turbulent region moves upstream towards the step. Finally, a gradual increase in reattachment length is observed for $Re > 10,000$ as transition to turbulence occurs upstream of the expansion. Latornell and Pollard [8] note that the reattachment lengths are also sensitive to the shape of the velocity profile at the inlet to the channel; larger reattachment lengths occur for fully-developed inlet profiles compared to spatially-uniform profiles for the same flow Reynolds number. The effect of the inlet velocity profile on reattachment length is especially pronounced in the transitional Reynolds number range.

In addition to Reynolds number, expansion ratio also has a strong impact on the flow development downstream of a sudden expansion [23,30,31]. These studies show that the reattachment length tends to increase with expansion ratio for a given Reynolds number, with transition to turbulence occurring at successively lower Reynolds numbers as Er increases.

Dağtekin and Ünsal [31] provided a set of semi-empirical correlations for the reattachment length as a function of Reynolds number and expansion ratio for $Er = 1.5-6.0$ and $Re < 500$.

2.2 Onset of flow bifurcation

As the Reynolds number increases in sudden-expansion flows, numerous studies have observed an abrupt loss of symmetry in which the flow bifurcates and reattachment occurs at different locations on the upper and lower channel walls. Early experimental studies by Durst et al. [33], Cherdron et al. [34], and Ouwa et al. [35] have shown that asymmetry of the upper and lower reattachment lengths occurs after a critical Reynolds number is reached. Drikakis [36] and others demonstrated that the value of the critical Reynolds number decreases with increasing expansion ratio. Papadopoulos and Otugen [37] and Battaglia and Papadopoulos [38] showed that bifurcation is a two-dimensional instability and in 3D cases the channel aspect ratio can be incorporated into an effective expansion ratio. A summary of the critical Reynolds numbers for the initial onset of symmetry-breaking bifurcation obtained by different researchers are presented in Table 2-2.

The onset of bifurcation has been described in literature as instability of the symmetric base flow that amplifies disturbances that are initially present within the flow [36]. Mullin et al. [25] used high resolution magnetic resonance imaging techniques to identify the velocity disturbances that precede the onset of bifurcation in an axisymmetric sudden expansion. Their findings determined the critical Reynolds number for the onset of bifurcation to be $Re_d = 1139 \pm 10$ (based on the inlet pipe diameter and average inlet velocity), for an expansion ratio

Table 2-2: Studies on bifurcation

Reference	Er	$Re_{cr,b}$
Alleborn et al. [39]	2.0	218
	3.0	80
	5.0	42.5
Battaglia et al. [40]	1.5	446
	2.0	215
	3.0	81
	4.0	54
Drikakis [36]	2.0	216
	3.0	80
	4.0	53
Durst et al. [41]	2.0	125-200
Fearn et al. [42]	3.0	80.9
Hawa & Rusak [43]	3.0	80.7
Kadja & Touzopoulos [44]	2.0	200
Kudela [45]	3.0	84-187
Luo [46]	3.0	92.4
Manica & De Bortoli [47]	3.0	80-100
Shapira et al. [48]	2.0	215
	3.0	82.6
Schreck and Schäfer [49]	3.0	81
Neofytou & Drikakis [50]	2.0	285
Battaglia & Papadopoulos [38]	1.6	340-345
	2.0	217

of $Er = 2$. Later, Sanmiguel-Rojas et al. [26] used global mode analysis to identify the unsteadiness characteristics of flow through an axisymmetric sudden expansion and tried to explain it with linear stability theory, reporting that linear instability of the axisymmetric state appears for $Re_d > 3273$, which is much higher than the critical Reynolds number measured by Mullin et al. [25]. Sanmiguel-Rojas et al. [26] suggest that this discrepancy between the measured and theoretical critical Reynolds number is due to the flow's sensitivity to the disturbance levels in the incoming flow upstream of the expansion. The incoming disturbances are amplified by the

sudden expansion in which the larger expansion ratios tend to intensify bifurcation at the expansion step and also accelerate transition to turbulence [24]. The non-linearity in the noise amplification and transition process results in the current lack of theoretical approaches for predicting the critical Reynolds number over a range of expansion ratios.

2.3 Instability and growth of localised turbulence

The available literature shows an earlier occurrence of transition to turbulence in experiments as compared to numerical simulations. This is attributed to sensitivity to various types of imperfections that appear in experiments [51]. The effect of these imperfections has been modelled in recent studies by the addition of arbitrary perturbations which generate small disturbances. Duguet [52], Sanmiguel-Rojas and Mullin [53], and Selvam et al. [54] have conducted numerical simulations by adding tilt perturbation to trigger transition to turbulence. However, these perturbations cause discontinuity at the inlet and also onset of bifurcation [51]. Miranda-Barea et al. [55] have conducted an experimental study for sudden expansion ratio of 8 with a rotational inlet pipe to generate swirl perturbation. Recently, Selvam et al. [51] used a small localized vortex perturbation at the inlet, without wall rotation and observed a less abrupt transition to turbulence than observed for the tilt perturbation case.

The results from all of the above studies claim that transition in sudden expansions initiates near the centerline of the flow downstream of the expansion. Initially, the turbulence that is created following transition is damped within a few pipe diameters owing to the lower Reynolds number in the pipe after the expansion. The emphasis of all of these studies was the generation of transition and instability in the sudden-expansion flow. There is a shortage of comprehensive numerical investigations focused on the behavior of the shear layer growth, vorticity transport, and evolution of coherent flow structures in straight pipes with a sudden expansion for transitional and turbulent

flow regimes. In the present thesis, an in-depth analysis of the growth mechanisms of disturbances leading to transition to turbulence after the expansion step will address this shortcoming in the available literature. The goal is to identify the mechanisms for the generation and decay of the localized turbulence in the transitional regime, and the sustained growth of turbulence and recovery to a turbulent pipe flow in the fully-turbulent regime.

Although numerous of numerical and experimental studies have been conducted on sudden expansion, few studies have offered the details on transitional and lower-Reynolds number turbulence flow. Sudden expansion causes laminarization of low Reynolds number turbulent flow after the expansion step which requires more investigation.

2.4 Gradual expansion

Figure 2-2 illustrates the age of injected particles into sudden expansion. As shown, older particles are observed in the recirculation zone. These particles are randomly trapped in the recirculation regions and recirculating with low velocity magnitude compared to the mean flow. This accumulation of low-speed particles in the corners of the sudden expansion may pose problems in real-world applications. For instance, chemical reactions in the UBC Struvite Crystallizer from Chapter 1 form struvite crystals. Clogging by struvite is a common problem at wastewater treatment plants [56]. The high age and the low velocity of the trapped particles in the sudden expansion may promote merging and clogging of struvite in the recirculation regions. Therefore, replacing sudden expansions with gradual ones may shrink the resulting recirculation regions and lead to a reduction of the amount of trapped particles, and thus better mixing of the fluid and solid phases.

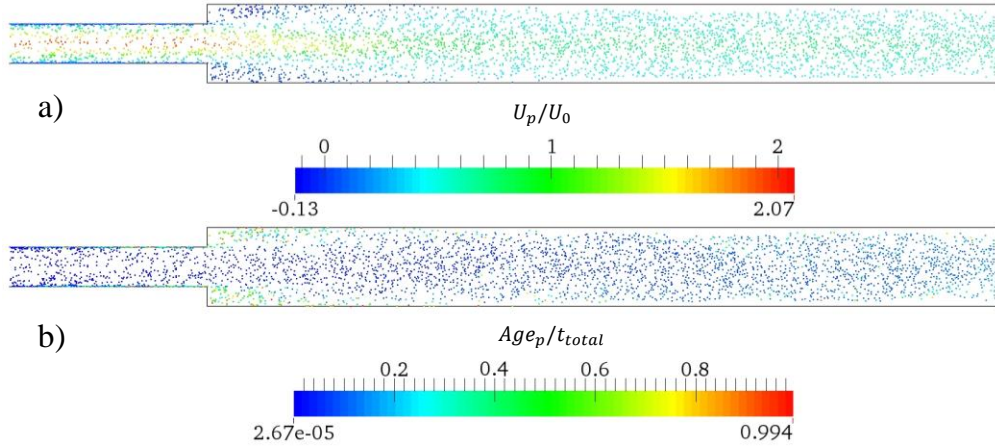


Figure 2-2: Zoomed view of mean velocity contour in a sudden expansion with $Re = 200$ and $Er = 2.0$ a) Instantaneous velocity contour of particles b) Age of remained particles

In comparison to sudden expansions, there are a limited number of studies on the flow through a gradual expansion section. Peixinho and Besnard [57] performed experimental analysis and observed occurrence of transition, localized turbulence, and relaminarization of the flow in slowly diverging pipes. Recently, Selvam et al. [54] performed direct numerical simulation for purely laminar flow in a gradual expansion between two pipes with a constant finite-amplitude perturbation applied to replicate experimental imperfections. The increasing pipe diameter due to the diverging section leads to considerable reduction in the flow Reynolds number and in some cases relaminarization of the flow downstream of expansion. Just like in sudden expansions, the mechanisms by which the flow transitions and then relaminarizes to form a discrete region of localized turbulence is poorly understood. In order to identify the impact of the gradual expansion on the statistics and evolution of coherent structures in the turbulent pipe flow and the laminarization process, further investigation is required.

2.5 Transverse jets in sudden expansions

The flow of a jet injected transversely into a cross flow exists extensively in nature such as pollutant plumes [58] and thermal discharges into rivers [59]. Moreover, it is a common phenomenon in a wide range of industrial applications, particularly in thermal-fluid systems that require high amount of energy release and also efficient and high rate of mixing [60,61], such as cooling of turbine blades [62], fuel-air mixing in turbine combustors [63], and scramjet engines [64]. The interaction of the cross flow with the main flow and generation of vortices in the main flow cause a high degree of near-field mixing [65]. Consequently, understanding the flow structure and mixing characteristic of the jet in cross flow (JICF) is of great interest [58]. Numerous experimental and numerical studies focus on the interaction between the main flow and the transverse jet, finding that the interaction generates a complex pattern of unsteady vortical structures in the flow. Fric and Roshko [66] categorized vortical structures into four different groups: (1) shear-layer vortices; (2) a counter-rotating vortex pair (CVP); (3) a horseshoe vortex; and (4) wake vortices. Different flow field conditions affect the generation and relative strength of these highly complex set of vortical structures. The horseshoe vortices that are formed around the jet column for a wide range of flow conditions become unsteady at jet Reynolds numbers roughly above 2500 for measured velocity ratios of 2 and 4 [67]. Transient wake vortices are shed downstream of the jet orifice as roughly-vertical, tornado-like vortices that span from the jet trajectory to the wall [65]. The strength and coherency of these wake vortices depend on velocity ratio [66,68]. Although these vortical systems increase the mixing efficiency of the flow field, the main mixing rate is due to the formation and evolution of counter-rotating vortex pair (CVP) which is the dominant vortical structure of the transverse jet [69]. The ring-like shear layer vortices consist of the ring vortices that form on the upstream or windward side of the jet boundary.

Karagozian [69], Getsinger et al. [70] and Mahesh [71] provide comprehensive detailed reviews on structural and stability characteristics of transverse jet.

Due to strong degree of cross-stream mixing that cross-injection can achieve, it has been proposed as a control method for improving the mixing efficiency of sudden-expansion flows and avoiding bifurcation in the flow. The mutual interaction of the sudden expansion and transverse jets yields a complex flow field that has not been thoroughly investigated. While there are plenty of comprehensive studies for flow through a sudden expansion without transverse jet injection, the number of numerical and experimental studies that have investigated the effect of wall injection on sudden expansion flows are few. El-Askary et al. [72] conducted numerical and experimental studies on the wall pressure distribution in a sudden expansion with and without cross flow to demonstrate the effect of transverse jet injection on the main flow, but did not adequately address the impact of transverse jets on the flow instabilities identified in earlier studies (e.g. [26]) or how cross-injection affects the level of mixing in the flow. Considering the importance of mixing in the UBC Struvite Crystallizer in Chapter 1, this thesis aims to conduct a comprehensive parametric study of transverse jets in sudden expansions to identify the mixing characteristics and unsteadiness in comparison with the case without transverse jets.

2.5.1 Generation of turbulent inflow in simulations

Incompressible turbulent flow through a smooth pipe is an important phenomenon in fluids engineering which occurs in diverse situations. Numerous studies have been conducted to identify the details of turbulent pipe flows [73–76]. With the rapid development of computational devices and techniques, large-eddy simulation (LES) and direct numerical simulations (DNS) are playing an important role in the advancement of turbulence research [77,78]. Prescribing inflow and initial

conditions for the turbulence that satisfy prescribed spatial and temporal correlations, statistical characteristics, and energy content is vital for obtaining accurate LES and DNS results [79,80]. Several techniques have been developed for turbulent inflow generation, which can be categorized into synthesised turbulence methods and precursor simulation methods.

Synthesis of inlet boundary conditions into particular constraints is a commonly-used method for generating turbulent inflow conditions [80]. The synthetic turbulence is an approximation that is constructed by imposing random perturbations to a deterministic coherent flow condition [81]. Introducing white-noise random components to the inlet velocity is the simplest level of this approach. It is able to generate some of the required characteristics of turbulent flow such as the mean velocity profile but poorly captures velocity fluctuation profiles and Reynolds stress components [82]. The advantage of this method is the simplicity with which specific parameters of the turbulence, such as length scales or turbulent energy levels, can be imposed and modified if conditions change. Tabor and Baba-Ahmadi [79] examined various inflow boundary conditions for generation of fully developed turbulent flow using OpenFOAM®. Their comparative discussion on the response of synthetic inlets and precursor simulation methods concluded that synthetic inflow-generation methods are inherently inaccurate because the imposed random perturbations do not develop towards a fully-developed turbulence condition with proper statistical properties. Therefore, more advanced methods are being investigated involving spatial and/or temporal correlations that yield more realistic fluctuations.

On the other hand, precursor simulation methods can accurately capture the coherent structures associated with turbulent flows [83,84] These methods perform some form of explicit simulation of turbulence and the obtained results are then used to generate a library of turbulent data that is introduced in a temporally-accurate manner at the inlet to the main computational

domain. The precursor simulation methods suffer from increased computational cost and also may not be applicable for cases with complex geometries [83]. The cost of precursor simulations can be reduced via a periodic recycling or remapping technique that imposes a periodic condition within a limited sub-domain of the precursor simulation. Tabor and Baba-Ahmadi [79] suggested that the combination of an internal mapping method with auxiliary feedback control techniques associated with synthetic turbulent inflow generation can optimally drive the flow towards a specified turbulent state.

The accuracy of turbulence statistics in precursor simulations is partially determined by how well the laminar-to-turbulent transition process is captured. In pipe flows with sufficiently high Reynolds numbers, laminar-to-turbulent transition typically occurs in the form of localized turbulent “slugs” [85,86] that are initiated by disturbances in the entrance region of a pipe flow and grow in their spatial extent as they travel downstream. The turbulence becomes fully developed by the sequential merging of slugs downstream of the pipe inlet [87]. Resolution of this transition process in a precursor simulation requires long computational domains in the streamwise direction to account for the growth and merging of the turbulent slugs, and the resulting computational cost makes this approach unfeasible. To reduce the associated cost, surface roughness elements can be used to trigger earlier transition to a turbulent state [88,89]. Experiments by Nishi et al. [85] triggered transition in pipe flows by ring obstacles, showing dependence of the critical Reynolds number on the ring height. Vijiapurapu and Cui [90] investigated the effects of rib roughness on the development of turbulent flow in a pipe using various turbulence models. Recently, Kang and Yang [91] performed large eddy simulation (LES) in circular ribbed pipe flow and identified the characteristics of turbulent pipe flow for various rib configurations and sizes.

Chapter 3: Methodology

This chapter documents the methodological approach used in the current study. Section 3.1 describes an overview of the computing platforms employed in the series of numerical simulations. Section 3.2 shows an overview of the computational domain setup and spatial grids used in the simulations. The boundary conditions used for the simulations are presented in Section 3.3. Sections 3.4 describes a solution methods used for computing. Sections 3.5 represents parallel processing used for partition and run on Compute Canada facilities.

3.1 Computational platform

Direct numerical simulation (DNS) is an appropriate method for simulation of transitional and turbulent flows because it can capture all detail of a flow including the spatial and temporal scales without making modelling assumptions for the sub-grid turbulence. DNS requires solutions to the time-dependent mass and momentum conservation equations. In the current study, the Mach number is sufficiently small for the flow to be considered an incompressible fluid (much smaller than 0.3).

OpenFOAM® version 2.3.0, an open source computational fluid dynamics software package, is used to conduct the present DNS studies for incompressible flows through sudden and gradual expansions [92,93]. The time-varying incompressible Navier–Stokes equations are discretized using a general finite-volume method with fully collocated storage [92,94].

The suitability of OpenFOAM in comparison with other software for DNS of incompressible transitional and turbulent flows was investigated by Van Haren [95] for turbulent channel and pipe flows, finding good agreement in terms of RMS of the fluctuations even for complex geometries. Vigolo et al. [96] validated OpenFOAM for DNS flows in T-junctions in the

laminar–turbulent transitional regime with various computational grids and numerical settings, finding the solver can achieve excellent agreement with experimental data for instantaneous and time-averaged pressure and velocity distributions. Further validation of OpenFOAM was conducted by Habchi and Antar [97] by performing DNS of electromagnetically-forced turbulence, again finding very good agreement with the experimental data for velocity contour and streamlines obtained by Iatridis et al. [98]. Based on these findings, OpenFOAM is selected for the present study. With respect to the specific application to sudden expansion flows, Sanmiguel-Rojas and Mullin [53] performed numerical simulations of a circular pipe flow with expansion using OpenFOAM imposing a parabolic velocity profile together with various finite-amplitude perturbations. Their results are in good agreement with experimental data for the square-root growth of asymmetry at various Reynolds numbers.

3.2 Governing equations

Direct numerical simulation is a suitable approach for studying transitional and turbulent flows because it is able capture all the spatial and temporal scales of a flow without making turbulence modelling assumptions for the sub-grid turbulence. To perform the computation, DNS requires solutions to the time-dependent mass and momentum conservation equations; the energy conservation equation is also required in the case of compressible flows. In the present research, the Mach number is sufficiently small for the flow to be considered incompressible ($M < 0.3$). The Navier–Stokes equations for incompressible viscous flows take the form

$$\nabla \cdot \mathbf{u} = 0 \tag{3.1}$$

representing the conservation of mass and

$$\frac{\partial \mathbf{u}}{\partial t} + (\mathbf{u} \cdot \nabla) \mathbf{u} = -\frac{\nabla p}{\rho} + \nu \nabla^2 \mathbf{u} \quad (3.2)$$

representing the conservation of momentum equations. These equations are discretized using a general finite-volume method by the *pisoFoam* solver of the OpenFOAM-2.3.0. The integral forms of the compressible mass and momentum conservation equations can be expressed using index notation as:

$$\frac{\partial}{\partial t} \int_{\mathcal{V}} \rho d\mathcal{V} + \int_S \rho u_j dn_j = 0 \quad (3.3)$$

$$\frac{\partial}{\partial t} \int_{\mathcal{V}} \rho u_j d\mathcal{V} + \int_S \rho u_i u_j dn_j = - \int_S p dn_j + \int_S \mu \left(\frac{\partial u_i}{\partial x_j} + \frac{\partial u_j}{\partial x_i} \right) dn_j \quad (3.4)$$

where the S and \mathcal{V} indicate integration over a surface and volume, respectively, and n_j is the outward-pointing normal surface vector associated with each surface. The full detail of the integral forms of the mass and momentum conservation equations for finite-volume method and discretization approach are presented in [99].

3.3 Boundary conditions

A steady, parabolic inflow boundary is imposed at the inlet boundary for laminar and transitional cases. Turbulent inflow condition is generated for pipe flow via a streamwise-mapping technique and ribbed turbulator as explained in Section 3.3.1. All walls are represented by no-slip boundaries. Also, a zero-gauge static pressure and a zero streamwise velocity gradient are imposed at the outlet boundary. The outlet boundary is placed far from the expansion to minimize outlet boundary effects on the region of interest. Insensitivity of the results to the location of the outflow boundary was examined for all different geometries by repeating the DNS with varying domain lengths with the conclusion that the effect is negligible.

3.3.1 Turbulent inflow generator

A special inlet boundary condition that uses an internal mapping-type boundary condition efficiently generates turbulent inflow information. The internal mapping method uses the data from a cutting plane well downstream of the inlet boundary condition and forces the flow to convert into a fully-developed profile upstream of a subdomain. To keep the desired through-flow mass flux, the average volumetric mass flux of the remapped flow should be checked and corrected [100]. The location of the mapping plane must be a reasonable distance downstream of the inlet boundary to provide a sufficient streamwise distance for the flow to develop [101]. Moreover, it should be far enough from the outlet boundary to prevent corruption of the mapped plane by the upstream effects of the outlet boundary. As shown in Figure 3-1, a small annular ribbed turbulator is added to the inlet pipe to trigger transition and accelerate the development of turbulent flow conditions in the DNS. In this study, the mapping plane is located at $7.5d$ (out of a total inlet pipe length of $10d$). The turbulator has a fixed blockage ratio based on the rib height and pipe diameter of $BR = 0.06$. The pitch ratio (PR) of 5 refers to the ratio of the rib's streamwise length to the rib's radial height. Figure 3-1a shows a schematic and provides additional details of the computational domain.

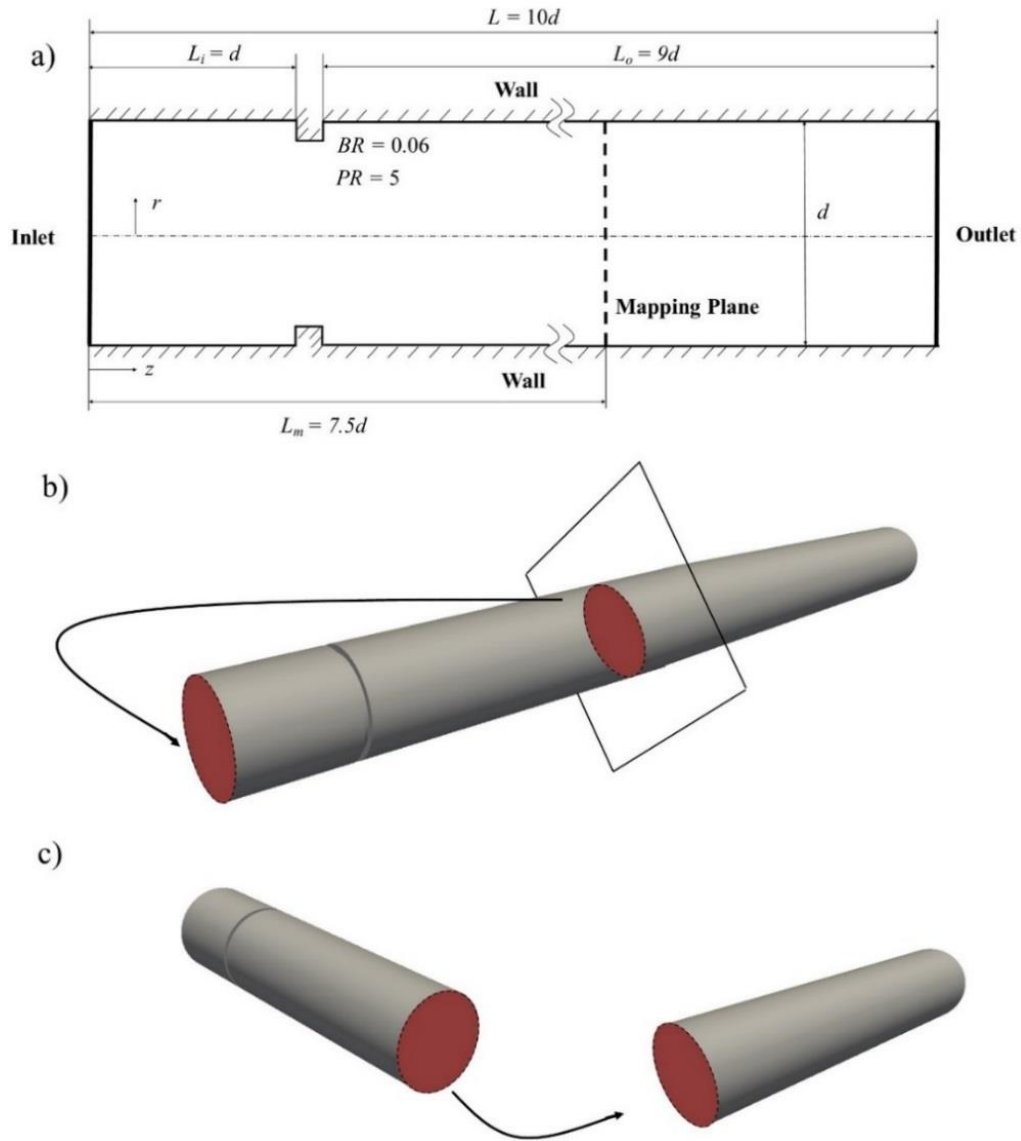


Figure 3-1: Diagram illustrating a schematic of geometry and the mapping technique: a) schematic of the computational domain (not to scale); (b) data from an interior mapping plane within the simulation is mapped backwards to the inlet boundary; (c) data at the mapped plane continues its development for the rest of the domain

Various methods have been used to generate turbulent inflow conditions in published literature. Periodic streamwise boundary conditions are a popular method for turbulent flow simulation research by providing a long enough developing flow region in the streamwise direction

which makes computed turbulent flow characteristics comparable with experimental data. Chin et al. [102] and Wu and Moin [78] performed DNS using periodic streamwise boundary condition which are in excellent agreement with experimental measurements by Eggels et al. [103] and Ng et al. [104]. However, Figure 3-2a shows that the initial uniform velocity profile will be merely converted into a parabolic velocity profile if the periodic streamwise boundary condition is used in the present study without adding disturbances to the flow. The inclusion of such disturbances is possible in OpenFOAM® using a library that imposes random irregular disturbances, but the imposed disturbance is different from actual turbulence and it also disappears at low Reynolds numbers (see Figure 3-2b). The obtained results with longer axial domain size indicates that these types of random disturbances also have the tendency to be damped into a parabolic velocity profile. Figure 3-2c shows the results based on the mapping technique and an annular ribbed turbulator. It should be mentioned that the simulation using the mapping boundary without a ribbed turbulator produced similar contours to the periodic streamwise boundary condition.

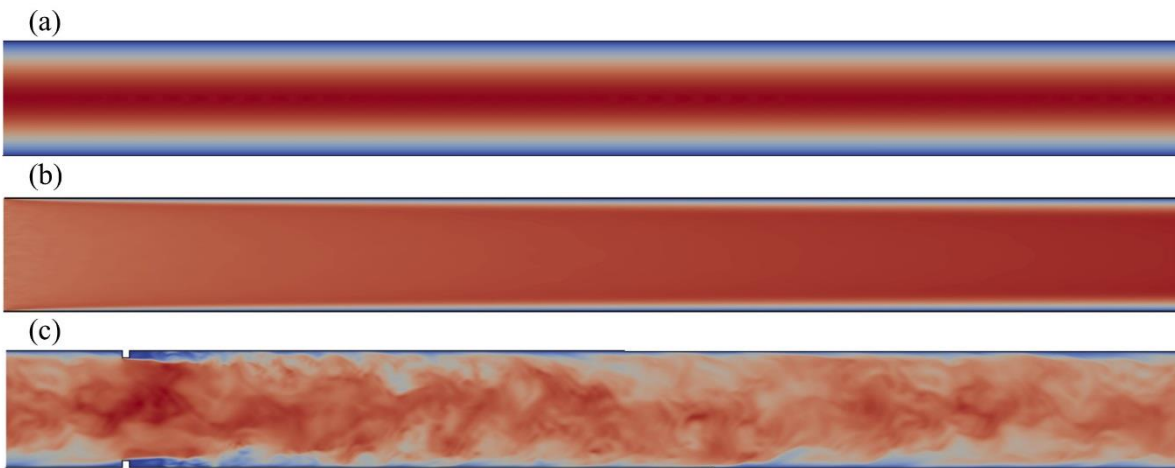


Figure 3-2: Visualization of the turbulent pipe flow over constant θ plane using instantaneous velocity magnitude contours for various inflow condition in pipe flow a) periodic streamwise boundary condition b) turbulent inlet boundary condition form the OpenFOAM® library c) mapping technique with ribbed Turbulator. Red represents higher values of u and blue represents values of u near zero

3.4 Solution Method

OpenFOAM® discretized the governing equations by means of the finite volume method [92,105]. The velocity and pressure coupling was solved with the pressure-implicit splitting operating (PISO) algorithm. Convergence at each timestep was achieved when the root-mean-square residuals of the pressure and momentum equations fell below 5×10^{-8} . Second-order central differencing and second-order Euler backward differencing were used to discretize the spatial and temporal derivatives, respectively. Dimensional form of Navier Stokes equations were solved using OpenFOAM®. Water at 1 atm and 25°C is the working fluid.

The time-step size in each simulation varied according to the Reynolds number and size of the spatial grid. In order to accommodate start-up effects associated with the imposed initial velocity field, the time-step size is set for each simulation to keep the maximum Courant number less than 0.05 for all cases during the first 1000 iterations [78]. After that the computational time step is increased and the maximum allowed Courant number is set to be less than 0.5 [107], with $\Delta t = 10^{-6}$ s being the smallest timestep used (for $Re = 2000$, $r = 20$ and $Er = 2$) and $\Delta t = 10^{-3}$ s being the largest timestep used (for $Re = 25$, $r = 20$ and $Er = 1.33$).

Each simulated test case was initialized with a zero relative static pressure and an initial velocity equal to the mean velocity at the inflow boundary and were then integrated in time for approximately 10 flow through times (defined as $L_i/U_i + L_o/U_o$, where subscripts i and o denote inlet and outlet pipe, respectively) to reach a statistically-steady state and then approximately 5 flow through times were collected for analysis.

Table 3-1: Description of the computational platforms used in the present research

Cluster Name	Type of Simulation	CPU for each Simulation	Total Number of cases
Orcinus	3D	512	18
Lattice	2D and 3D	36 and 512	109
Jasper	2D	36	144
Parallel	3D	512 and 1024	24
Bugaboo	3D	128 and 256	16
GreX	2D	32	30
Cedar	3D	512	10

3.5 Parallel Processing

The large number of computational nodes required for performing DNS leads to large memory requirements and long simulation periods. This problem is addressed through parallel processing, where the computational domain is divided into smaller subdomains and each subdomain is assigned to a separate processor. In the current research, partitioning is performed using a message-passing interface (MPI) parallelization strategy. Several computational platforms are used in the present research; a brief description of each cluster is presented in Table 3-1. All platforms are Compute Canada facilities. It should be noted that simulations are performed on 36 CPUs for 2D cases and 512 CPUs for most of 3D cases. The average usage of computational resources for this research was 1460 and 1180 CPU-years (approximately 13 and 10 million CPU hours) for 2016 and 2017, respectively.

Chapter 4: Laminar and Transitional Flow in a Planar Sudden

Expansion

This chapter is based on the following published journal paper. This research was performed by Nima Moallemi under the direction of Dr. Joshua Brinkerhoff. The full results for this chapter are published as: Moallemi, N, Brinkerhoff, J.R. Numerical analysis of laminar and transitional flow in a planar sudden expansion, *Computers & Fluids*, 140: 209-221 (2016) (*Published*).

In this chapter, the laminar and transitional flow through a planar sudden expansion with various expansion ratios is studied using two-dimensional direct numerical simulations at flow Reynolds numbers up to $Re_{max} = U_{max}d/\nu = 5000$ and expansion ratios in the range of $Er = 1.33 - 4.00$. Within the present discussion of the simulation results, velocities are normalized by the maximum velocity occurring at the inlet of the computational domain (denoted U_{max}) and spatial scales are normalized by the step height of the sudden expansion (h). Transition to turbulence was noted in some of the simulated test cases, but because the computational domain is two-dimensional and thus unable to accurately resolve the discrete, three-dimensional vorticity fluctuations that accompany the latter stages of transition, the analysis of the simulated results for these cases is limited to the laminar regions of the flow.

Following a brief explanation of the numerical approach of the present study, the discussion of the simulation results are structured as follows: first, shear layer separation and reattachment downstream of the sudden expansion and the development of the recirculation region is described, and predictive correlations are proposed for the reattachment length and the maximum velocity magnitude occurring in the reversed-flow region. Next, the onset of symmetry-breaking bifurcation is investigated and a physical explanation for its cause is explored. Finally, a

correlation for the critical Reynolds number at the onset of bifurcation is proposed for a range of expansion ratios.

4.1 Numerical approach

4.1.1 Computational domain

The computational domain shown in Figure 4-1 consists of two channels with heights of d and D mated together to produce a sudden planar expansion with a step-height of h . The expansion ratio of the sudden expansion is defined as

$$Er = \frac{D}{d} = 1 + \frac{2h}{d} \quad (4-1)$$

The range of expansion ratios of the simulated cases are discussed in Section 4.1.2 The lengths of the computational domain upstream and downstream of the sudden expansion are L_i and $L_o=60h$, respectively.

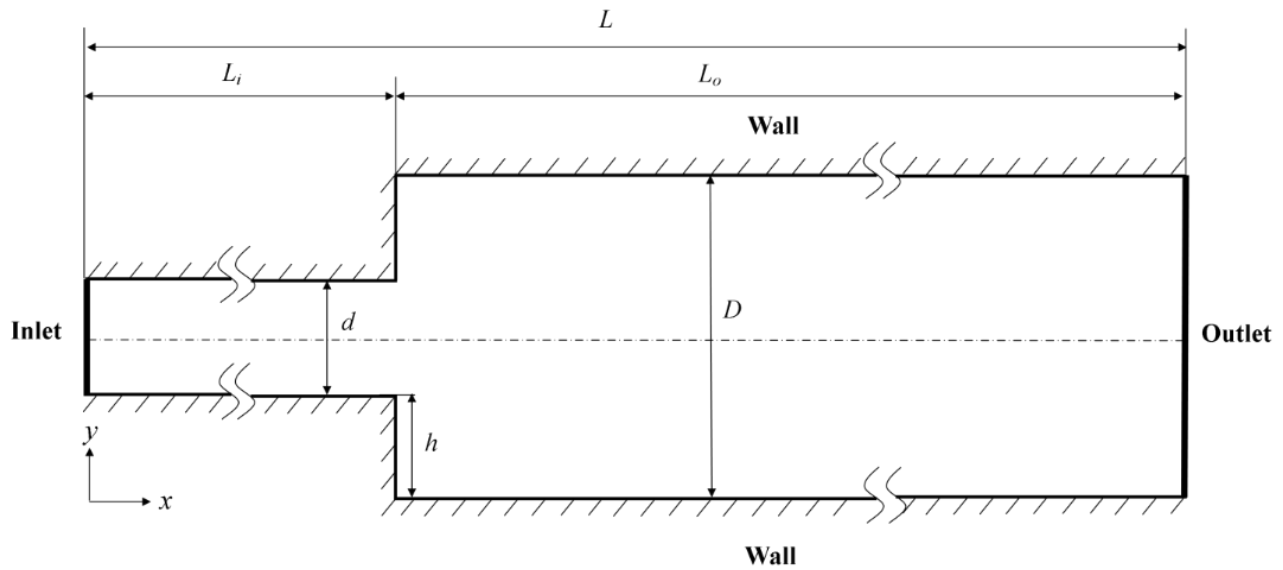


Figure 4-1: Schematic of the computational domain

Insensitivity of the results to the location of the outflow boundary was examined for a case with $Re_{max} = 1000$ and $Er = 2.00$ by repeating the simulation with downstream domain lengths of $L_o=60h$ and $L_o=80h$. Both simulations returned very similar results in terms of the reattachment length and the Reynolds stress profiles occurring at the reattachment location.

4.1.2 Test cases

In the planar sudden expansion study, 144 simulations were performed with Reynolds numbers between $Re_{max} = 25$ and 5000 based on maximum inlet velocity at expansion ratios of $Er=1.33, 1.43, 1.67, 1.82, 2.00, 2.60, 3.20,$ and 4.00. The range of test cases for each expansion ratio is presented in Table 4-1. For the cases with high Reynolds numbers and particularly at high expansion ratios, transition to turbulence was observed in the domain which cannot be accurately captured in the present two-dimensional study. The range of Reynolds number for $Er=1.43, 1.67, 1.82$ is wide enough to identify the critical Reynolds number for the onset of bifurcation. The upper and lower limit of the Reynolds number range for other expansion ratios are such that a wide range of flow behaviors prior to and after bifurcation are obtained. At very high expansion ratios (e.g. $Er > 4.00$), the effect of wall shear stress and its recirculation region on the flow become less significant and its behavior is similar to a jet released into a quiescent region. On the other hand, at very low expansion ratios (e.g. $Er < 1.33$), the recirculation regions become very small and the flow behaves similar to a developed channel with a localized roughness element in the wall.

Table 4-1: Test cases range for various expansion ratios

Er	Re_{max} range	Number of cases
1.33	25-5000	21
1.43	1000-3000	15
1.67	600-1200	12
1.82	600-1000	14
2.00	25-3000	24
2.60	25-1000	23
3.20	25-600	15
4.00	25-2000	20

4.1.3 Spatial grids

A structured, non-uniform, orthogonal finite-volume grid was mapped to the computational domain. The numbers of grid cells in the regions upstream and downstream of the expansion are given in Table 4-2 for each value of the simulated expansion ratios. The cells are non-uniformly spaced in the streamwise (x) and cross-stream (y) directions in order to place a higher number of cells near the sudden expansion region and no-slip walls, respectively, where the flow will experience large spatial gradients. In these 2D simulations, the domain is one cell thick in the spanwise direction and the governing equations in the z direction are not solved. A grid-refinement study was performed at $Er = 2.00$ and 4.00 by varying the total number of cells between 10,750 and 172,000; the results of the grid independency analysis are presented in Section (4.1.4). Using the reattachment length as a metric, it was confirmed that about 110,000 cells is sufficient to guarantee grid independence for all Reynolds numbers and expansion ratios considered in this paper, and thus the grids described in Table 4-2 are conservatively refined. The streamwise and cross-stream grid spacing distribution for the $Er=2.00$ case is shown in Figure 4-2 which shows the degree of grid refinement near the step (in the streamwise direction) and near the no-slip walls

of the domain (in the cross-stream direction). As shown in Figure 4-2(a), the grids become coarse at the inlet and outlet, where the streamwise grid spacing in these regions is about twice that of the grid near the sudden expansion; its location in Figure 4-2(a) is indicated by a dashed line. A similar grid spacing distribution is used for the other expansion ratio cases.

Table 4-2: Characteristics of computational grids used

<i>Er</i>	$(N_x, N_y)_i$ Upstream of step	$(N_x, N_y)_o$ Downstream of step	Total cells
1.33	(100, 200)	(600, 200)	132,000
1.67	(100, 90)	(600, 210)	135,000
2.00	(100, 80)	(600, 240)	152,000
2.60	(100, 62)	(600, 262)	163,400
3.20	(100, 54)	(600, 274)	169,800
4.00	(100, 40)	(600, 280)	172,000

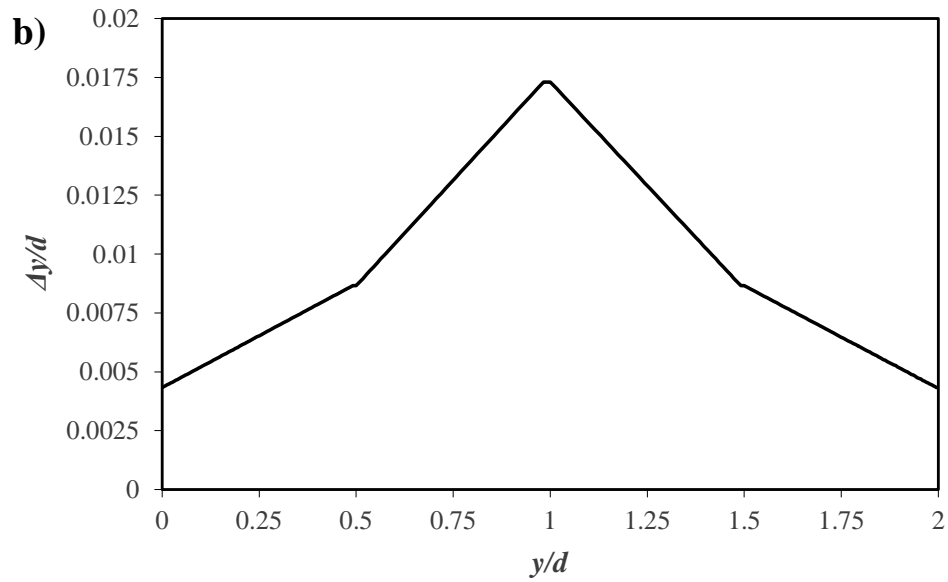
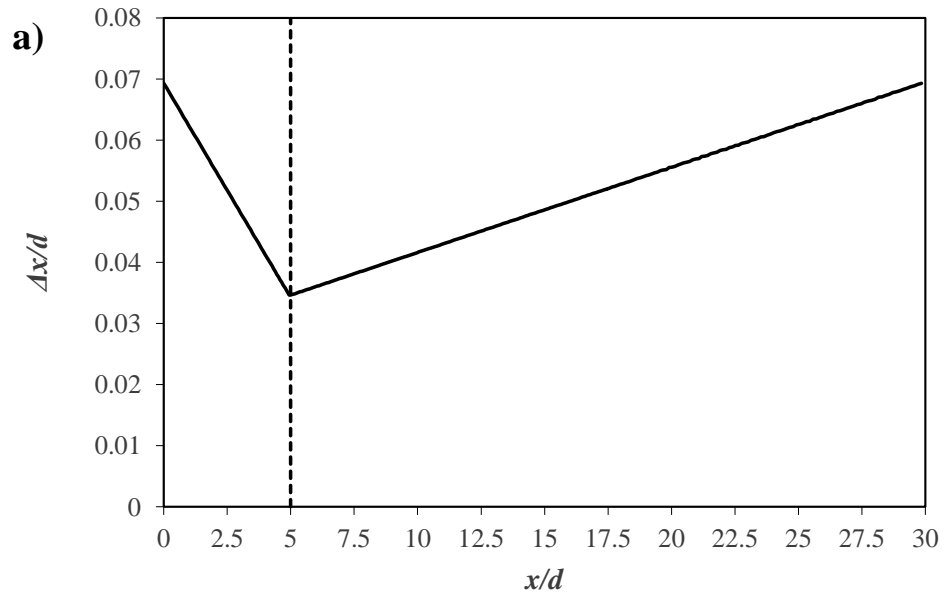


Figure 4-2: Distribution of the spatial grid spacing in the (a) streamwise direction at $y = D/2$ and (b) wall-normal direction at $x/h=10$ for the $Er = 2.00$ case. The dashed line indicates the location of the sudden expansion

4.1.4 Mesh independence

In order to ensure grid independence, Figure 4-3 plots the normalized reattachment length (L_r/h) is compared for four different mesh refinements. The discrepancy between computed lengths has reduced by increasing the grid resolution and the variation of the predictions is very small for high grid resolutions, after the mesh amount 97,280 cells for $Er = 2.00$ or 110,080 for $Er = 4.00$. The results also indicate that intermediate Reynolds numbers are more sensitive to the grid size in comparison with low and high Reynolds numbers for both expansion ratios ($Er = 2.00$ and $Er = 4.00$). Streamlines are presented for different grid resolution at $Er = 4.00$ and $Re = 100$. Comparison between results from Figure 4-3(a) and Figure 4-3(b) reveals that the coarsest mesh (Figure 4-4a) is not able to predict bifurcation accurately and the flow asymmetry is inaccurate. Although, the bifurcation phenomena are semi-developed in Figure 4-4 (b), the streamlines still show slight deviations, particularly in the size of secondary recirculation region. The streamlines show quite similar results in Figure 4-4 (c) and (d). Therefore, in current study, the numerical simulations are performed using the cell count presented in Figure 4-4 (d).

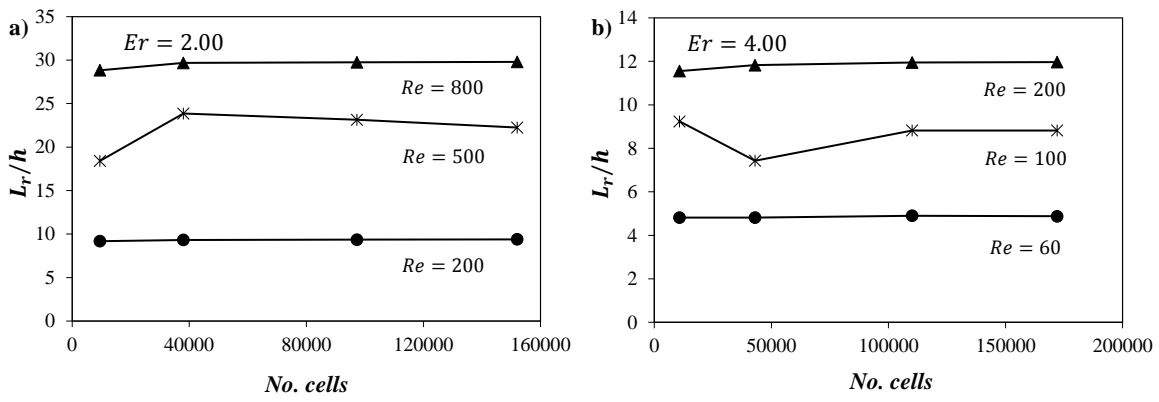


Figure 4-3: Dependence of reattachment lengths to the grid size for different Reynolds number and expansion ratio

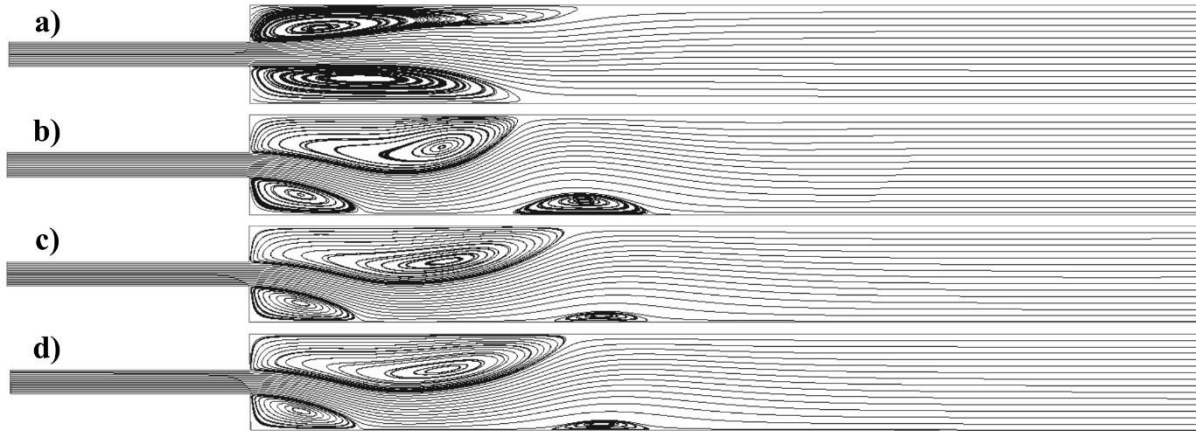


Figure 4-4: Streamline distribution in sudden expansion with expansion ratio of 4.00 and $Re=100$ for different grid resolution a) $NC = 17,500$, b) $NC = 43,000$, c) $NC = 110,080$, d) $NC = 172,000$

4.2 Shear layer reattachment length

Figure 4-5 compares the computed reattachment lengths as a function of the Reynolds number for $Er = 2.00$ with published numerical and experimental results. The present simulation results are in good agreement with published investigations for $Re_{max} \leq 218$. For $Re_{max} > 218$, bifurcation begins; the formation of bifurcation is discussed in Section 4.4. The excellent agreement for lower Reynolds numbers suggests that the 2D simulations are capable of capturing laminar reattachment of the flow downstream of the sudden expansion. Although not shown, similar agreement is obtained between the present results and Back and Roschke [19] at $Er = 2.60$. The linear trend for reattachment length in the laminar flow regime is anticipated as the average shear stress remains approximately constant at any fixed axial distance downstream of the sudden expansion, implying that viscous diffusion is the main source for the development of the recirculation region in the vertical direction. As a result, as the Reynolds number increases within the laminar regime, the higher velocity implies a longer streamwise distance is needed for the separated flow to reattach to the wall [18].

Figure 4-6 plots the normalized reattachment length as a function of Reynolds number for expansion ratios of $Er = 1.33-4.00$. The maximum Reynolds number plotted in Figure 4-6 for each expansion ratio value corresponds to the critical Reynolds number value at which bifurcation is observed in the simulations, to be discussed in Section 4.4. As shown in Figure 4-6, the reattachment length increases linearly with respect to max Reynolds number for each expansion ratio. The reattachment length also increases with increasing expansion ratio at a fixed max Reynolds number, although the critical Reynolds number for the onset of bifurcation is reduced. The following correlation for the normalized reattachment length is fitted to the computed results in Figure 4-6:

$$\frac{L_r}{h} = 0.353 - 0.243Re_{max} - 0.049Er - 0.075Re_{max}Er + 0.309Re_{max}\sqrt{Er} \quad (4.2)$$

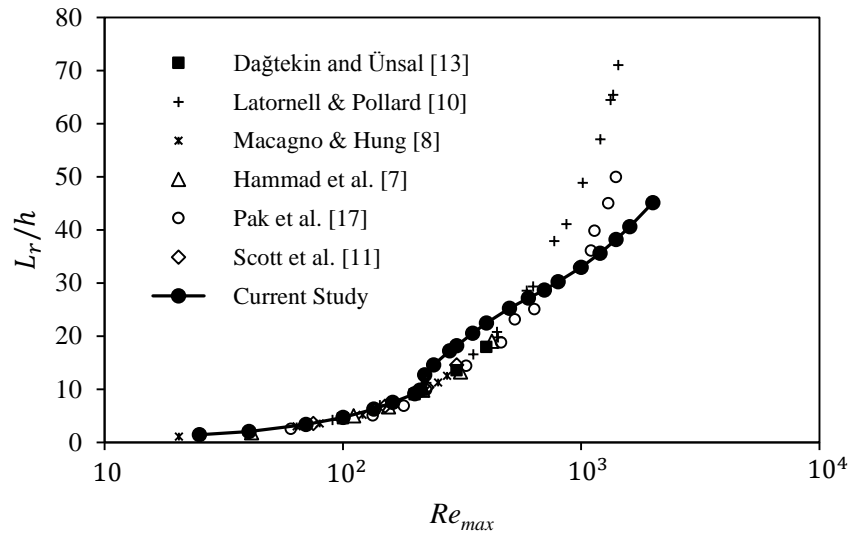


Figure 4-5: Comparison of non-dimensional reattachment length (L_r/h) at various Reynolds numbers for $Er = 2.00$ with literature

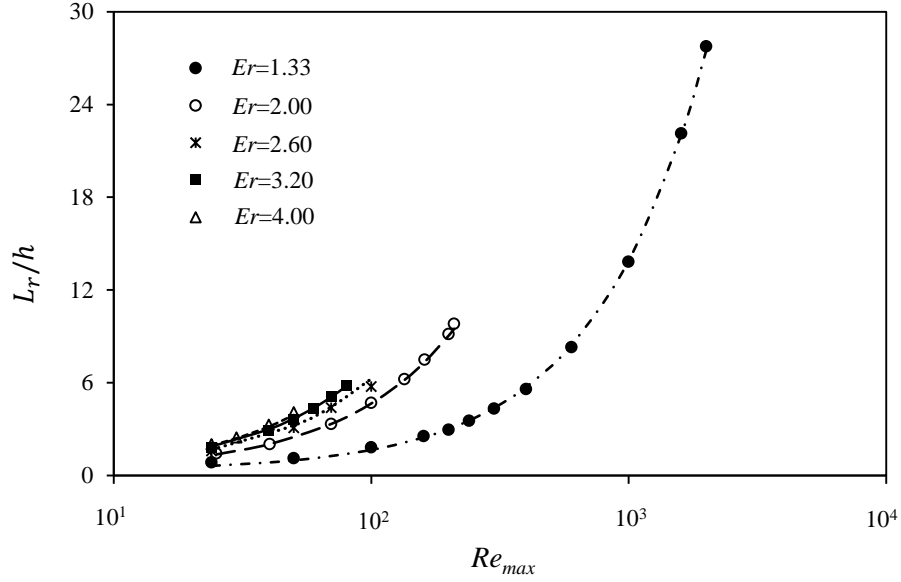


Figure 4-6: Reynolds number distribution of the reattachment length for various expansion ratios. Symbols denote numerical results and lines denote Eq. (5.2)

From Figure 4-6, it is clear that Eq. (4.2) achieves excellent agreement with the computed results; the norm of the residual is $R^2 > 0.99$. The correlation is validated for expansion ratios in the range $1.33 < Er < 4.00$ and maximum Reynolds numbers in the range $24 < Re_{max} < Re_{c,b}$, where $Re_{c,b}$ is the critical Reynolds number for the onset of bifurcation.

The primary reattachment lengths and their variation after bifurcation is summarized in Figure 4-7 for various expansion ratios. As is clear, before bifurcation, upper and lower walls have equal reattachment lengths ($L_{r1} = L_{r2}$), i.e. the flow is symmetric. For $Re_{max} > Re_{c,b}$, branching occurs in Figure 4-7 and one of the recirculation zones shrinks while the zone on the opposite wall continues to grow. The tendency for the longer recirculation zone to occur on the upper or lower wall of the computational domain was noted to be random. As the Reynolds number increases, the computed reattachment lengths on both walls increase, although the growth rate of L_{r2} is much lower than L_{r1} . The maximum Reynolds number plotted in Figure 4-7 for each expansion ratio

value corresponds to the point where time-dependent flow is observed in the simulations. Above this Reynolds number, transition to turbulence is initiated in the shear layer and the present 2D simulations are not an accurate method to predict the flow behavior. The shear layer reattachment lengths variation with Reynolds number is in excellent agreement with the data obtained by Kadja et al [108].

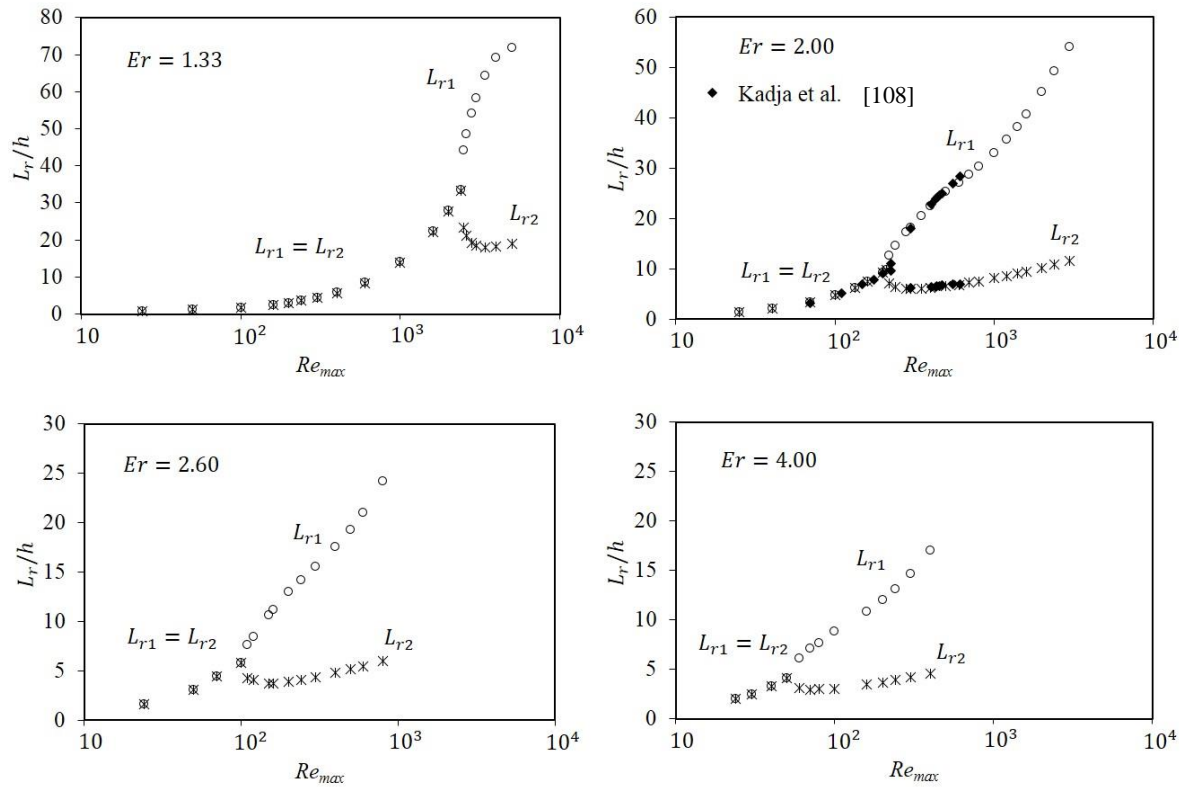


Figure 4-7: Primary reattachment length at upper and lower walls for various expansion ratios

In most of the bifurcated cases, a secondary recirculation zone develops downstream of the primary recirculation zone on the wall experiencing the shorter primary reattachment length. Indeed, as discussed in Section 4.5, as the Reynolds number increases past the critical Reynolds number for the onset of bifurcation, the number of recirculation regions increases. The streamwise

separation location of the secondary recirculation zone (denoted L_s) is presented in Figure 4-8 along with published data, achieving very good agreement within the range of the published data.

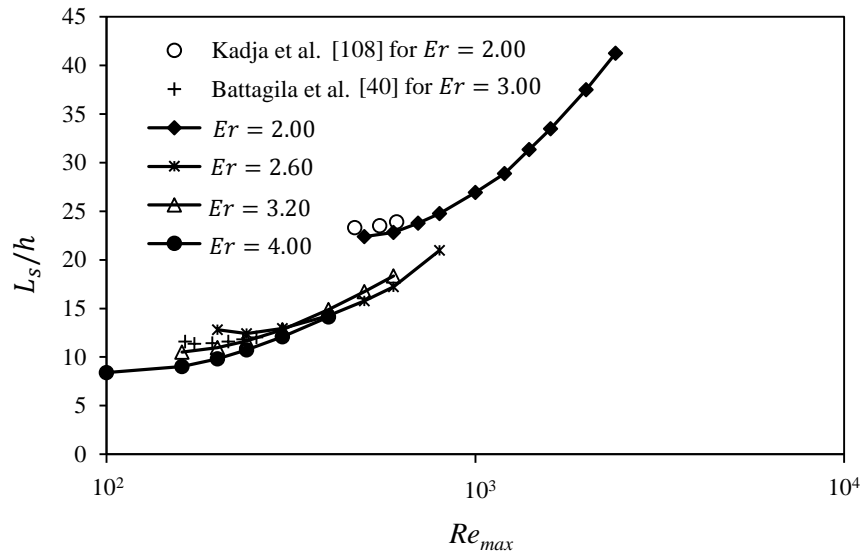


Figure 4-8: Secondary separation point at various Reynolds numbers for various expansion ratios

4.3 Reversed-flow velocity magnitude

Mass and momentum conservation at the sudden expansion dictates that the sudden increase in the flow area is accompanied by a decrease in the average velocity and a corresponding increase in static pressure, yielding an adverse streamwise pressure gradient in the vicinity of the sudden expansion. The flow recirculation discussed in Section 4.2 occurs in the low-momentum fluid near the wall in response to the local adverse pressure gradient. When a sudden expansion is used as means to passively enhance mixing, the velocity magnitude in the reversed-flow region provides a convenient estimate of the level of shear created in the flow due to the expansion and is thus a simple way of approximating the mixing effectiveness of the flow. Figure 4-9 shows the velocity profile from the $Re_{max} = 200$ and 300 and $Er = 2.00$ cases.

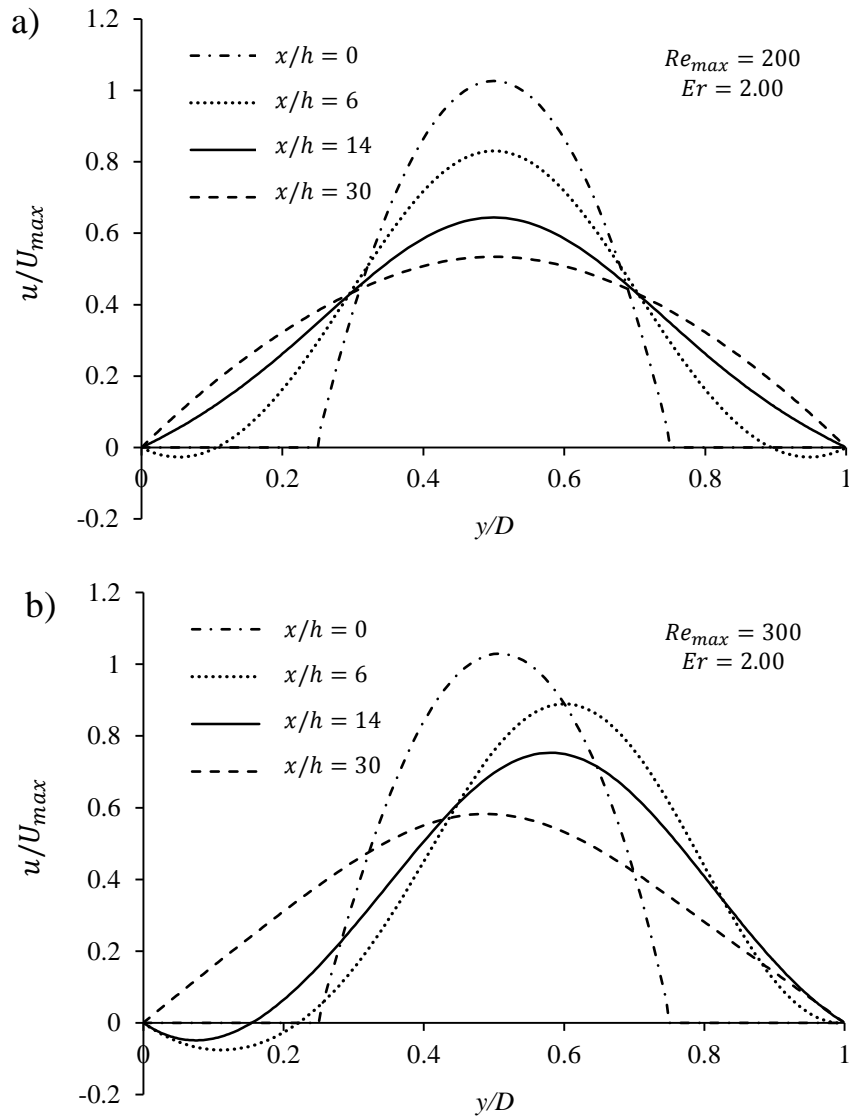


Figure 4-9: Comparison of the velocity profile for $Re_{max} = 200$ and 300 for $Er = 200$ at different streamwise stations

The results illustrate that the flow at $Re_{max} = 200$ remains symmetric at this Reynolds number. The parabolic laminar velocity profile upstream of the expansion is altered downstream and a reversed-flow velocity profile develops in the near-wall regions on both sides. As the flow travels farther downstream of the expansion, the magnitude of the reverse velocity initially increases in response to the adverse pressure gradient and then decreases as viscous diffusion

mixes the centerline flow until the reversed flow disappears at the point of shear layer reattachment. Figure 4-9 shows that at $Re_{max} = 300$, bifurcation occurs and flow reversal occurs only on one side. At higher Reynolds numbers, similar magnitudes of reversed velocity are noted in the secondary recirculation regions. Figure 4-9 also shows that downstream of flow reattachment (which occurs at $x/h = 9.05$ for $Re_{max} = 200$ and $x/h = 5.96$ and 18.16 for the upper and lower walls at $Re_{max} = 300$) a parabolic velocity profile is recovered before the flow reaches the end of the computational domain.

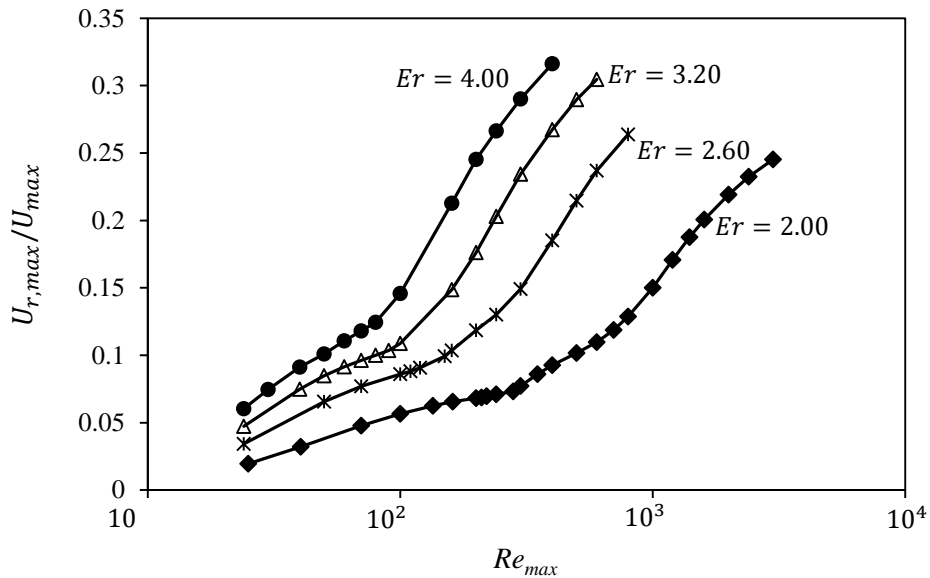


Figure 4-10: Maximum reverse velocity distribution at various Reynolds numbers and expansion ratios and approximate values of $U_{r,max}/U_{max}$

Figure 4-10 plots the maximum velocity magnitude of the reversed flow ($U_{r,max}$) normalized by the maximum inlet velocity (U_{max}) for $Er = 2.00-4.00$. For a fixed value of Er , an increase in the Reynolds number yields an increase in the maximum reverse velocity due to stronger corner recirculation regions. However, the dependence of the maximum reverse velocity on Reynolds number becomes weaker at higher Reynolds numbers, eventually reaching an

asymptotic value within the laminar regime. In contrast, the expansion ratio has a very dominant effect on the maximum velocity in the reversed-flow region, exhibiting a stronger influence on reversed velocity magnitude (and, by extension, mixing effectiveness) than Reynolds number, at least within the laminar regime. A correlation for predicting the maximum magnitude of the reversed velocity is given below:

$$\frac{U_{r,max}}{U_{max}} = -0.068Er - 0.267 \log(Re_{max}) + 0.037Er \log(Re_{max}) + 251 \log(Er Re_{max}) \quad (4.3)$$

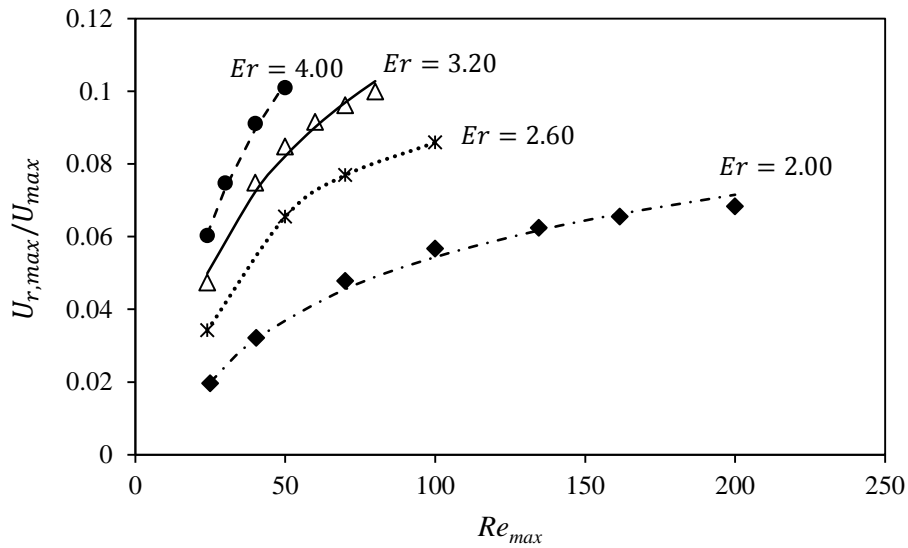


Figure 4-11: Reynolds number distribution of the maximum reverses velocity for various expansion ratios. Symbols denote numerical results and lines denote Eq. (4.3)

which is obtained by regression of the data in Figure 4-10. Equation (4.3) is valid in the range of $25 \leq Re_{max} \leq Re_{cr,b}$ and $2.00 \leq Er \leq 4.00$, where $Re_{cr,b}$ is the critical Reynolds number for symmetry breaking bifurcation described in Section 4.4. A comparison between the computed values of $U_{r,max}/U_{max}$ and those obtained by Eqn. 4.2 is illustrated in Figure 4-11, which shows that the correlation can predict computed values of $U_{r,max}/U_{max}$ with better than 3% accuracy at

intermediate Reynolds numbers and 5–6% accuracy at low and high Reynolds numbers for investigated range of expansion ratio.

4.4 Development of flow bifurcation

As shown in Figure 4-7, bifurcation is observed in the present results for all the expansion ratios under investigation. To provide a qualitative illustration of bifurcation, Figure 4-12 plots the streamline patterns for $Re_{max} = 200$ and 500 at an expansion ratio of $Er = 2.00$. For the lower Reynolds number, the streamline pattern is symmetric and the reattachment length is equal on the upper and lower channel walls. For the higher Reynolds number, however, bifurcation results in the recirculation region shrinking on one wall and lengthening on the other, and a secondary recirculation region develops on the side with the smaller primary region. This progression from symmetric to asymmetric flow is likely the result of the amplification of small disturbances in the flow [26]. According to this hypothesis, the small disturbances in the flow will increase as the Reynolds number increases until the disturbance amplitude reaches a critical threshold for the onset of symmetry-breaking bifurcation. While there are numerous studies that investigate the effect of Reynolds number and expansion ratio on bifurcation (e.g. see Table 2-2), literature has not provided any predictive correlations for the critical Reynolds number for the onset of bifurcation or any insight on what type of disturbance results in bifurcation. These two questions are addressed in the present section.

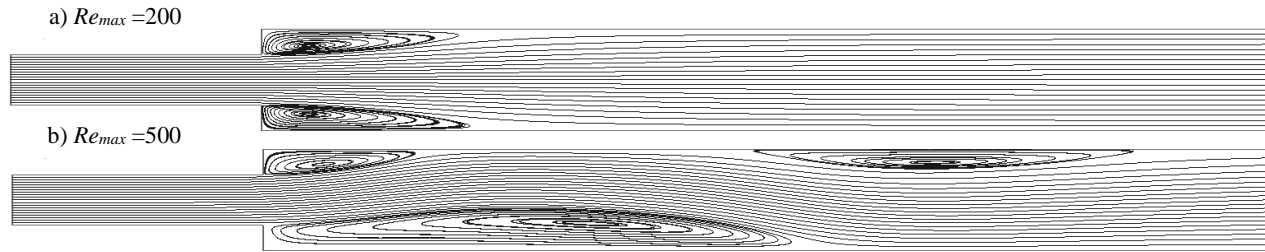


Figure 4-12: Streamline pattern near the expansion (zoomed view) (a) Symmetric reattachment for $Re_{max} = 200$ and $Er = 2.00$. (b) Asymmetric reattachment for $Re_{max} = 500$ and $Er = 2.00$

4.4.1 Critical Reynolds number for bifurcation

The critical Reynolds number for the onset of bifurcation ($Re_{c,b}$) is defined as the minimum Reynolds number that bifurcation appears and is tabulated in Table 4-3 for the expansion ratios studied. The critical Reynolds number for symmetry-breaking bifurcation is estimated for different expansion ratios. As shown in Table 4-3, the flow becomes asymmetric at lower Reynolds number by increasing the expansion ratio and the computations indicate an inverse relationship between critical Reynolds number ($Re_{c,b}$) and expansion ratio (Er). Very small disturbances that exist in the incoming laminar flow may be amplified at the sudden expansion, as the step behaves as a noise amplifier with a gain proportional to the step height [24].

The critical Reynolds numbers shown in Table 4-3 were obtained through an iterative, trial-and-error approach. For each expansion ratio, the flow was simulated at a Reynolds number much lower than $Re_{c,b}$ until it reached a steady state, and then the Reynolds number was incrementally increased and the simulation was repeated. The uncertainty in Table 4-3 is based on the number of cases there were performed and the Reynolds number increment between each case. As the expansion ratio decreases, bifurcation initiates at higher Reynolds numbers and capturing the exact critical Reynolds number requires more cases to be run and as a result higher computational cost.

The total number of simulations required to produce Table 4-3 was 144. The computational cost of each case varied almost inversely with the expansion ratio; at smaller expansion ratios, the critical Reynolds number became larger and the onset of bifurcation required a much longer time to occur, requiring much longer simulation times. For example, for the same Reynolds number, bifurcation in the $Er = 2.00$ case occurred almost four flow-through times after the symmetric flow field reached a quasi-steady state, whereas close to one flow-through time was required for the $Er = 4.00$ case. As most of the previous studies on the onset of bifurcation were for expansion ratios between 2 and 3, the present study with smaller expansion ratios extends the existing dataset in support of developing predictive correlations.

Table 4-3: Critical Reynolds number for the onset of bifurcation in laminar flows in planar sudden expansions

Expansion ratio (Er)	$Re_{c,b}$
1.33	2460±20
1.43	1270±20
1.67	475±10
1.82	340±10
2.00	218±1
2.60	105±5
3.20	80±5
4.00	55±5

Other studies of flows with bifurcations note that the temporal discretization method and initial conditions of the simulation can affect the onset of bifurcation phenomena by affecting the magnitude and amplification rate of disturbances via non-linearities introduced by the temporal discretization method (e.g. Drikakis [36], Panaras et al. [109]). To ensure that the critical Reynolds number values for bifurcation onset presented in Table 4-3 are independent of the temporal discretization method, the simulations for the critical Reynolds number at $Er = 2.00$ were repeated

with identical initial conditions but using the steady-state SIMPLE method of Patankar [110] for pressure-velocity coupling. In these cases, the steady solution is obtained upon convergence of the discrete equations without consideration to temporal derivatives. The critical Reynolds number was calculated by incrementally adjusting the Reynolds number in the same fashion as in the transient simulations, and an identical value of $Re_c = 218$ was found. In addition, to ensure that the values in Table 4-3 are independent of the initial conditions, the transient simulations at $Er = 2.00$ (which were initialized with uniform velocity equal to the mean inlet velocity) were repeated using the symmetric field present before bifurcation onset as the initial condition. This method also found an identical value of $Re_c = 218$ for the critical Reynolds number. Together, these results suggest that the critical Reynolds numbers in Table 4-3 are independent of the temporal discretization procedure and initial conditions of the simulations.

A correlation function for the critical Reynolds number at the onset of bifurcation is proposed in Eqn. (4.4) based on the data presented in Table 4-3:

$$Re_{c,b} = \exp\left(\frac{4.63}{\ln^{0.42}(Er)}\right) \quad (4.4)$$

This correlation and the data from Table 4-3 on which it is developed are shown in Figure 4-13(a). The correlation equation achieves very good agreement with numerical measurements for all expansion ratios ($1.33 < Er < 4.00$) with a least-squares regression coefficient of $R^2=0.99$. This correlation provides a simple method for approximating the critical Reynolds number for a wide range of expansion ratios. Figure 4-13(b) compares Eqn. (5.4) with values from published investigations for high expansion ratios ($2.00 < Er < 10.00$). Again, the proposed correlation achieves excellent agreement with published data; the only outlier is the $Er = 7.00$ case computed by Battaglia et al. [38] which also does not match the other published values.

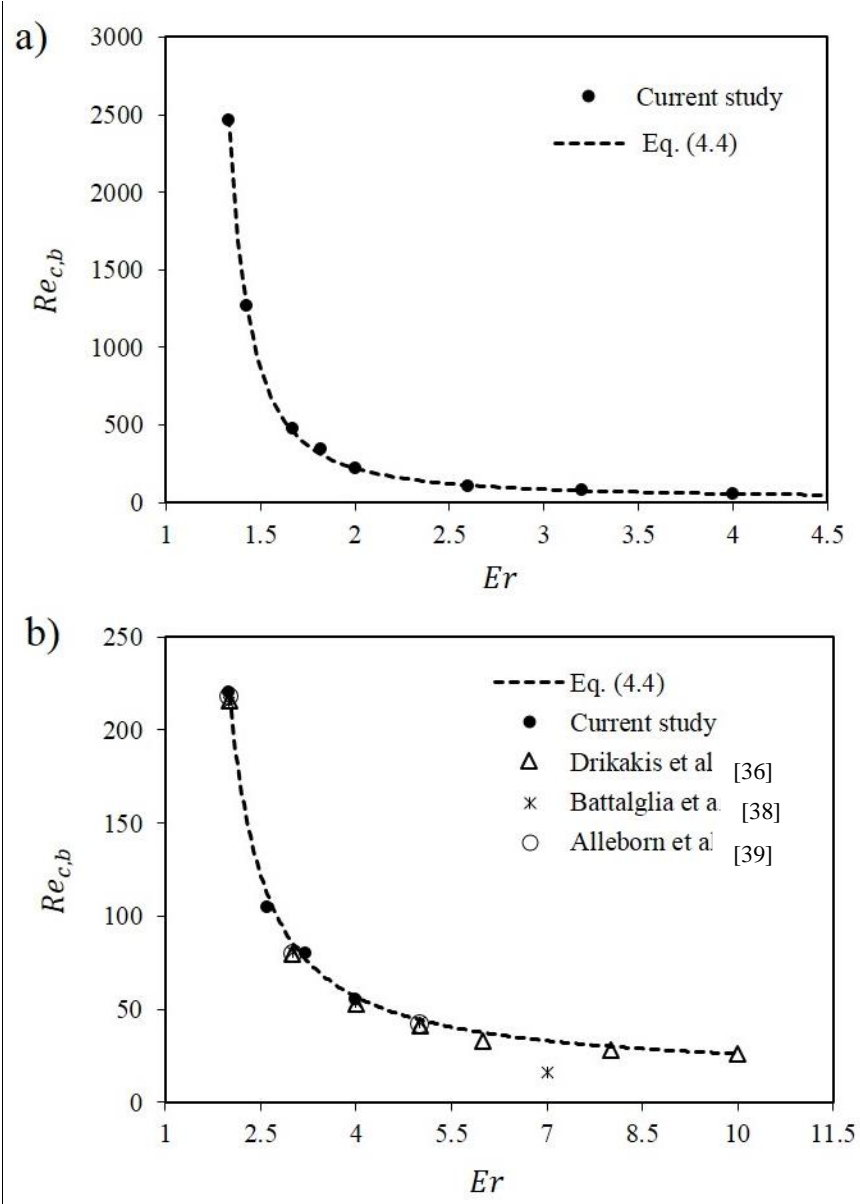


Figure 4-13: Correlation equation prediction for Critical Reynolds number for the onset of bifurcation in laminar flows in planar sudden expansions: a) in comparison with computed data for various Expansion ratios, b) in comparison with published investigations for high expansion ratio $2.00 < Er < 10.00$

4.4.2 Bifurcation onset and growth

In this section, the onset of flow bifurcation is analyzed by observing the evolution of the simulated cases at Reynolds numbers above the critical Reynolds numbers given in Table 4-3. For

each case, the flow initially reaches a symmetric condition, which we refer to as the “semi-steady state”. The temporal evolution of the flow from the semi-steady state to the fully bifurcated condition is illustrated in Figure 4-14 by plotting the maximum streamwise velocity that occurs at the streamwise location of flow reattachment in the symmetric condition. The velocity in Figure 4-14 is normalized by the centerline velocity that occurs at the reattachment location in the semi-steady condition, denoted U_{SSS} . As such, a unity value in Figure 4-14 corresponds to the semi-steady condition and deviations from unity indicate the onset of asymmetry in the velocity distribution at that streamwise location. Figure 4-14 shows that the time spent in the semi-steady state prior to the onset of bifurcation, which we refer to as the “bifurcation initiation time”, depends on how close the flow Reynolds number is to the critical Reynolds number for bifurcation; large Reynolds number cases have short bifurcation initiation time, while those closer to $Re_{c,b}$ have much longer times.

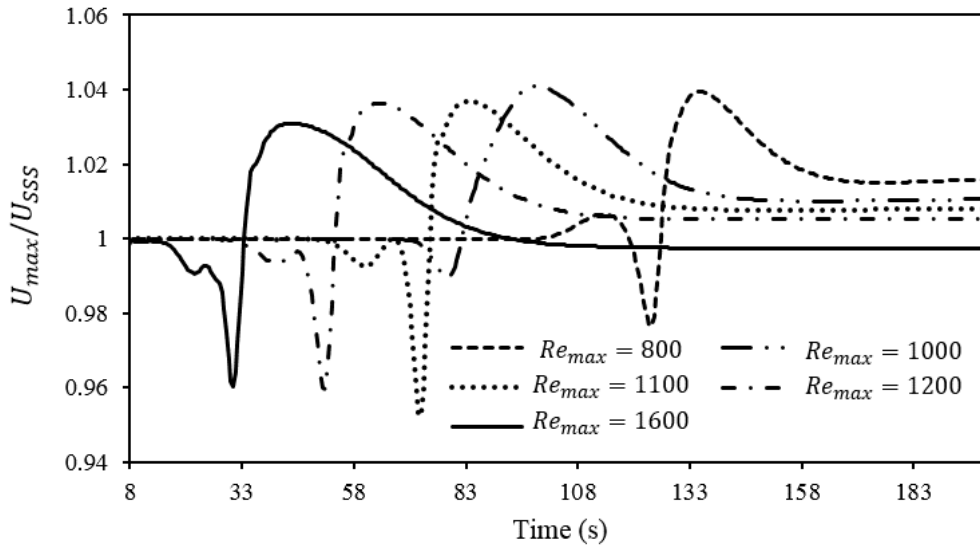


Figure 4-14: Maximum velocity variation of velocity profile at the reattachment point for $Er = 2.00$

The dependence of bifurcation initiation time on the flow Reynolds number may be due to differences in the initial disturbance levels, or it may be due to higher amplification rates of disturbances within the flow leading to bifurcation, or both. A distinct trend is seen in Figure 4-15 for the $Re = 800$ case compared to the higher Reynolds number cases; the velocity initially increases before decreasing, then peaks and finally settles on a steady asymmetric condition. At $Re = 600$ (not shown), the initial increase is even more pronounced, but has largely disappeared by $Re = 1000$. This distinct trend suggests that bifurcation initiates differently at high Reynolds numbers compared to those closer to the critical Reynolds number. To investigate this, the magnitude of the velocity disturbances within the flow prior to the onset of flow bifurcation needs to be analyzed. This is shown in Figure 4-15 by plotting the root-mean-square (RMS) of the streamwise velocity at various streamwise locations downstream of the sudden expansion. The RMS profiles are computed from the semi-steady flow before bifurcation initiated. Profiles for the flow upstream of the sudden expansion are not plotted because the amplitudes there are very small, on the order of the convergence criteria for the governing equations. Figure 4-15 shows that for $Re = 800$ the velocity disturbance amplitude is largest near the step, and gradually decreases with streamwise distance. In contrast, at $Re = 1000$ and 1200 , the disturbance amplitude is largest near $x/h = 30$ and 40 , respectively, which is near the reattachment location for these Reynolds numbers. This indicates that at Reynolds numbers close to $Re_{c,b}$, the largest disturbances occur near the sudden expansion, and as the Reynolds number increases, the location of the largest disturbance moves downstream. Moreover, Figure 4-15 shows that for $Re = 800-1200$, the RMS fluctuation profiles are symmetric about the centerline of the domain, implying that the fluctuations develop during the bifurcation initiation time when the flow is still symmetric. However, the $Re = 1600$ case shows a significant departure from this trend. At that Reynolds number, the disturbance

amplitude has increased by an order of magnitude, the largest amplitude occurs near the end of the domain at $x/h = 58$ (note that the outflow boundary is at $x/h = 60$), and the fluctuation profile is asymmetric. This suggests that the disturbance triggering bifurcation does not develop during the bifurcation initiation time, but is generated earlier during the initial period of the simulation when the flow field is adjusting to the outlet boundary and initial conditions. Because the Reynolds number was large enough, this initial disturbance was sufficiently strong to trigger bifurcation near the outflow boundary, and the disturbance wave then travelled upstream of the sudden expansion.

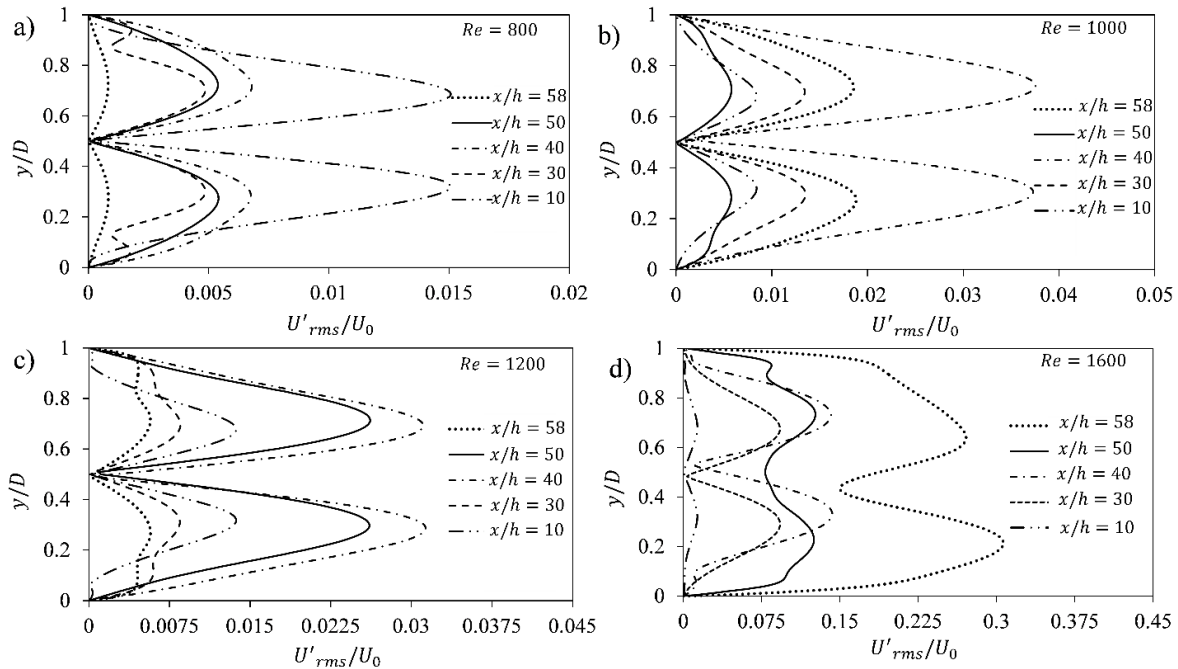


Figure 4-15: Measured root mean square velocity fluctuation at various positions before onset of flow bifurcation at $Er = 2.00$.

The spatio-temporal evolution of the velocity disturbances is shown in Figure 4-16 by plotting contours of the streamwise velocity fluctuation at several instances in time between the onset of bifurcation and the time when the bifurcated flow reaches a steady, asymmetric profile. The velocity fluctuation is obtained by subtracting the local value of the velocity in the steady-

state condition (u_{ss}) from the instantaneous velocity (u). Dimensionless time is defined as $t' = tU_{max}/D$, where $t = 0$ is defined as the onset of bifurcation and D denotes the channel height downstream of the expansion. The arrows pointing towards and away from the walls represent the locations of flow reattachment and separation, respectively. As presented, the flow alters from a stable symmetric pattern into an asymmetric pattern due to small perturbations that seem to be triggered near the semi-steady state reattachment location. The initial disturbance then grows and moves upstream and downstream of the flow.

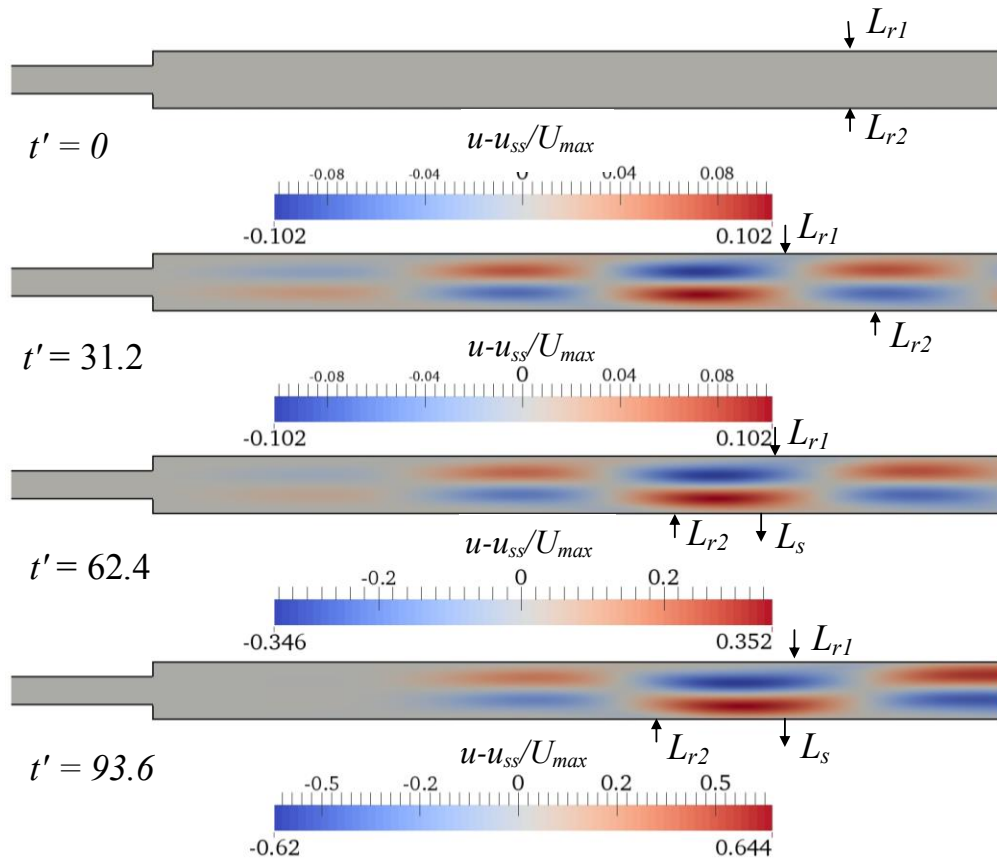


Figure 4-16: Temporal evaluation of the flow velocity disturbance contour after semi steady state condition at $Re_{max} = 1200$ and $Er = 2.00$

4.5 Bifurcation instability and transition to turbulence

The role of the bifurcation phenomenon in the lead-up to transition of the sudden-expansion flow from a steady laminar state to an unsteady turbulent state is illustrated in Figure 4-17 by plotting the instantaneous and mean velocity contours and flow streamlines for the $Er = 4.0$ case at several Reynolds numbers between $Re_{max} = 50$ and 2000. The fluctuating flow at the highest Reynolds numbers is considered “unsteady” rather than turbulent because the two-dimensional nature of the simulations inhibits accurate resolution of turbulent vortical structures. At $Re_{max} = 50$, the flow is symmetric with equal reattachment lengths on the upper and lower walls. At $Re_{max} = 100$, two unequal recirculation zones occur. With further increase in the Reynolds number to $Re_{max} = 500$, secondary recirculation zones occur on the same side as the smaller primary recirculation zone. Tertiary separation zones form downstream of the secondary recirculation region and even smaller-scale recirculation zones begin to form within the longer primary recirculation region. The cascading development of successively smaller-scale, steady 2D recirculatory regions are a precursor to the complete break-down of the flow to unsteadiness. This is evidenced by noting that at $Re_{max} = 1000$, the onset of unsteady fluctuations occurs near the end of the longer primary recirculation region, precisely where the smaller-scale recirculation zones were located. This suggests that the break-down into unsteady fluctuations originates in the successive formation of smaller-scale recirculation zones. This observation is consistent with break-down via an inviscid mode; considering that small-scale recirculation zones imply that the local velocity profile is highly inflectional, the flow will be unstable to rapidly-growing inviscid instability modes that amplify due to the high strain rate and trigger break-down to unsteady flow. Further increases in the Reynolds number brings the onset of unsteady fluctuations upstream so that by $Re_{max} = 2000$, the unsteadiness occurs immediately downstream of the sudden expansion.

The fluctuations enhance mixing within the flow so that the time-mean velocity contours at $Re_{max} = 2000$ appear symmetric. Thus, while bifurcation facilitates the onset of unsteadiness within the sudden-expansion flow, it disappears once the flow moves into the transitional regime.

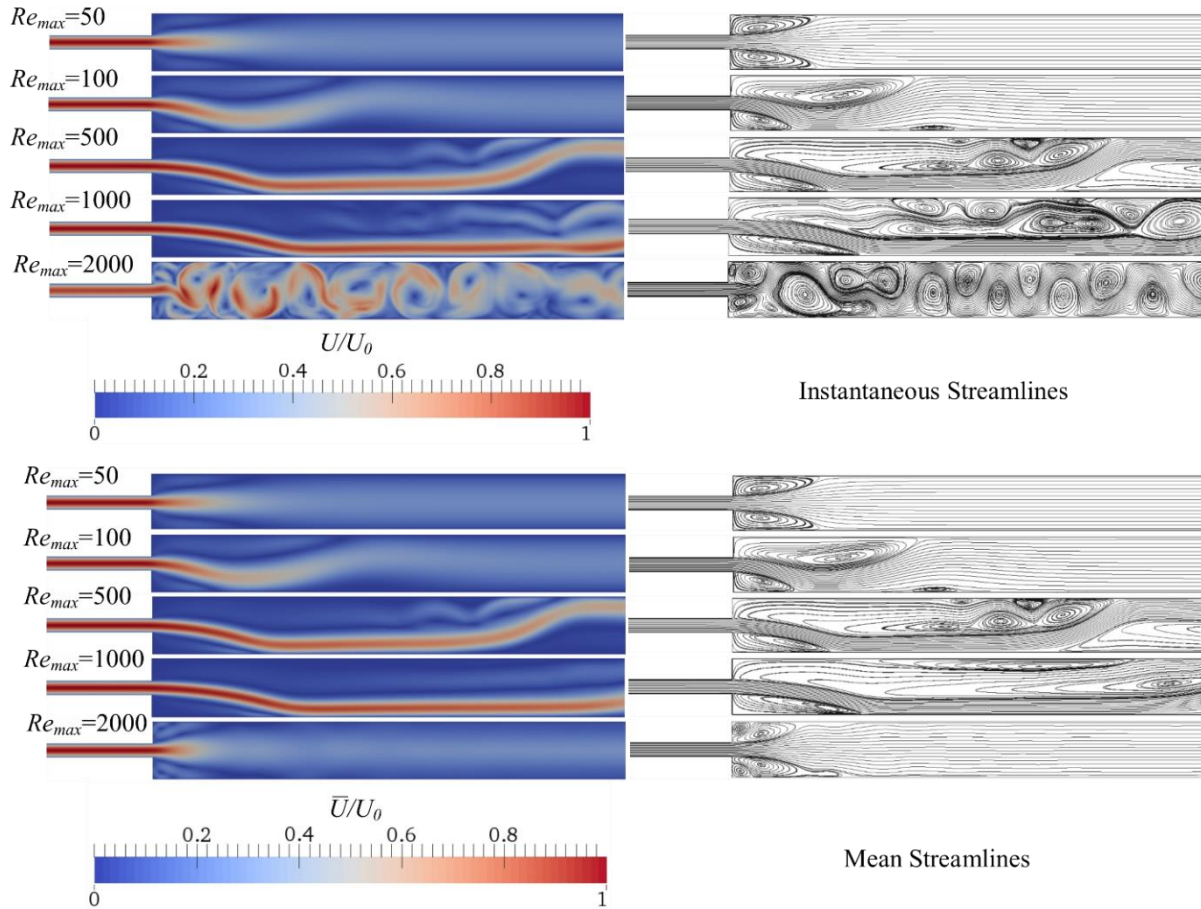


Figure 4-17: Velocity contour for flow in sudden expansion with $Er = 4.00$ at various Reynolds numbers: a) Instantaneous velocity b) Mean velocity

Existence of solid particles affects the reattachment length and momentum transfer in the recirculation region. Also, the symmetric flow structure downstream of the sudden expansion and onset of bifurcation phenomena alter with injection of solid particles. Appendix A provides a supplementary study that analyzes the impact of particles on the sudden expansion.

Chapter 5: Laminar and Transitional Flow in a Sudden Expansion with Transverse Injections

In this chapter, laminar and transitional flow through a planar sudden expansion with transverse jets is studied using two-dimensional direct numerical simulations at various expansion ratios and velocity ratios. Results represent the influence of transverse jet injection on the bifurcation phenomenon downstream of the sudden expansion. The effect of injection angle on transient flow development downstream of the sudden expansion is also studied.

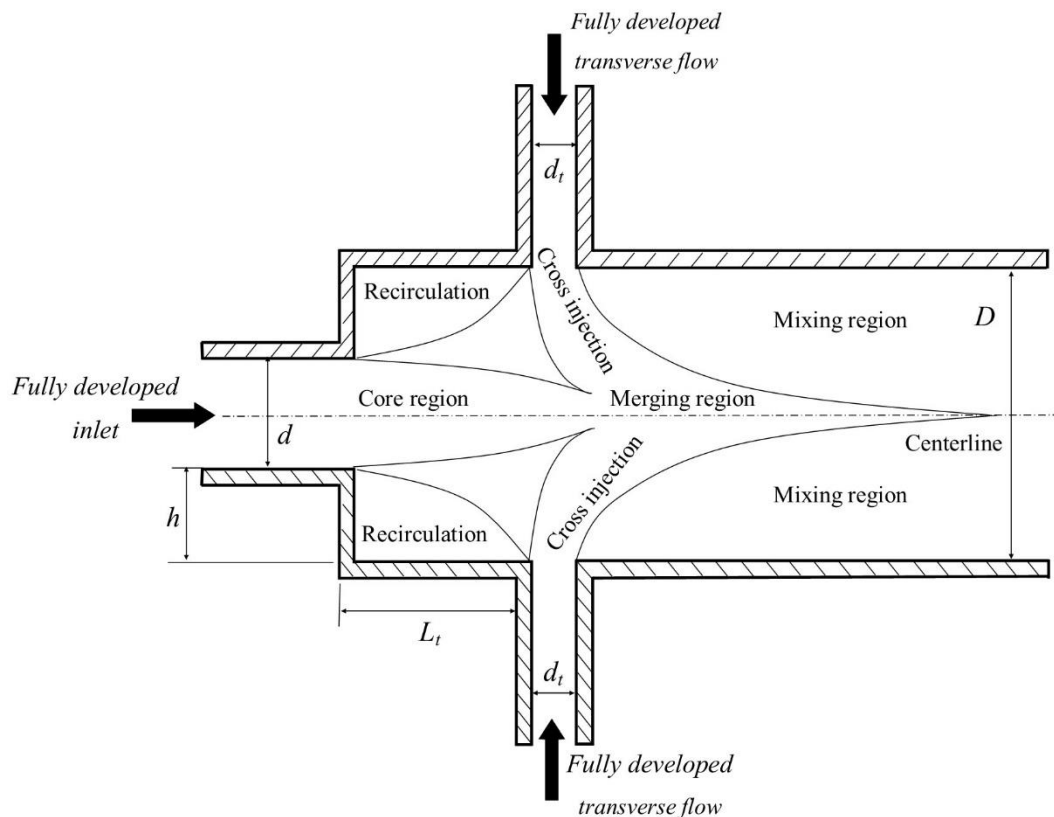


Figure 5-1: Schematic of major features of flow through a planar sudden expansion with cross injections

5.1 Flow configuration and test cases

A series of numerical simulations are performed for flow over a symmetric planar sudden expansion with and without transverse injections. Figure 5-1 shows the schematic view of the flow. The interaction between the injected transverse jet and main flow causes a high level of vorticities and mixing in the flow [65]. This interaction generates different regions in the flow such as core of the main and transverse flows, recirculation, merging, and mixing regions. For a sudden expansion with transverse injections, the flow field depends on the expansion ratio,

$$Er = D/d, \quad (5.1)$$

the jet-to-main-flow velocity ratio,

$$r = U_{t,max}/U_{max} \quad (5.2)$$

the main flow Reynolds number,

$$Re = U_{max}d/v \quad (5.3)$$

and the transverse jet Reynolds number,

$$Re_t = U_{t,max}d_t/v \quad (5.4)$$

where U_{max} and $U_{t,max}$ are the main flow and transverse jet maximum velocities, respectively; d , D , and d_t are the inlet channel, outlet channel, and transverse jet heights, respectively; and v denotes the kinematic viscosity. A velocity ratio greater than unity causes a complex system of vortical structures in the flow field surrounding the transverse jet injection [69]. Simulations are carried out with expansion ratios of 1.5, 2.0, 3.0 and 4.0 at various Reynolds numbers. Also, the effect of the jet-to-main-flow velocity ratio (r) and transverse jet injection angle (α) is examined for $Er = 2.0$. The range of test cases for each expansion ratio is presented in Table 5-1.

Table 5-1: Test cases range for various expansion ratios

<i>Er</i>	<i>Re range</i>	<i>Velocity ratio (r)</i>	<i>Injection angle (α) for upper/lower jet</i>	<i>No. cases</i>
1.5	400-1000	20	90°/90°	8
2.0	400-2000	5-40	60°/60°, 90°/90°, 60°/120°, 120°/120°	32
3.0	400-1000	10-20	90°/90°	8
4.0	400-1000	10-20	90°/90°	8

5.2 Numerical approach

5.2.1 Domain and boundary conditions

The computational domain used in the current simulations consists of two channels connected by a sudden expansion, shown schematically in Figure 5-2. Transverse jets are injected after the sudden expansion from two symmetric channels along the upper and lower walls. A fully developed parabolic inflow boundary is used as an inlet condition for the main and jet flow boundaries. The no-slip condition is applied on all walls and a zero streamwise velocity gradient and a zero gauge static pressure are imposed at the outlet boundary. The step-height, $h = (D-d)/2$, is used as the characteristic length scale in this study. The inlet length of the computational domain is $L_i = 10h$. Three outlet domain lengths are considered to study the laminarization of the flow with $L_o = 60h$, $120h$, and $300h$. The transverse jet injection location is chosen based on the primary recirculation length of the case without cross flow. As illustrated in chapter 4, the bifurcation phenomenon causes different reattachment lengths on the upper and lower walls. The shorter reattachment length varies between $5.9h$ and $10.7h$, while the longer reattachment length grows continuously for the bifurcated laminar cases. Therefore, the jet location is chosen as $L_t = 5h$ in order to interrupt the bifurcation phenomena and trigger maximal unsteadiness in the domain.

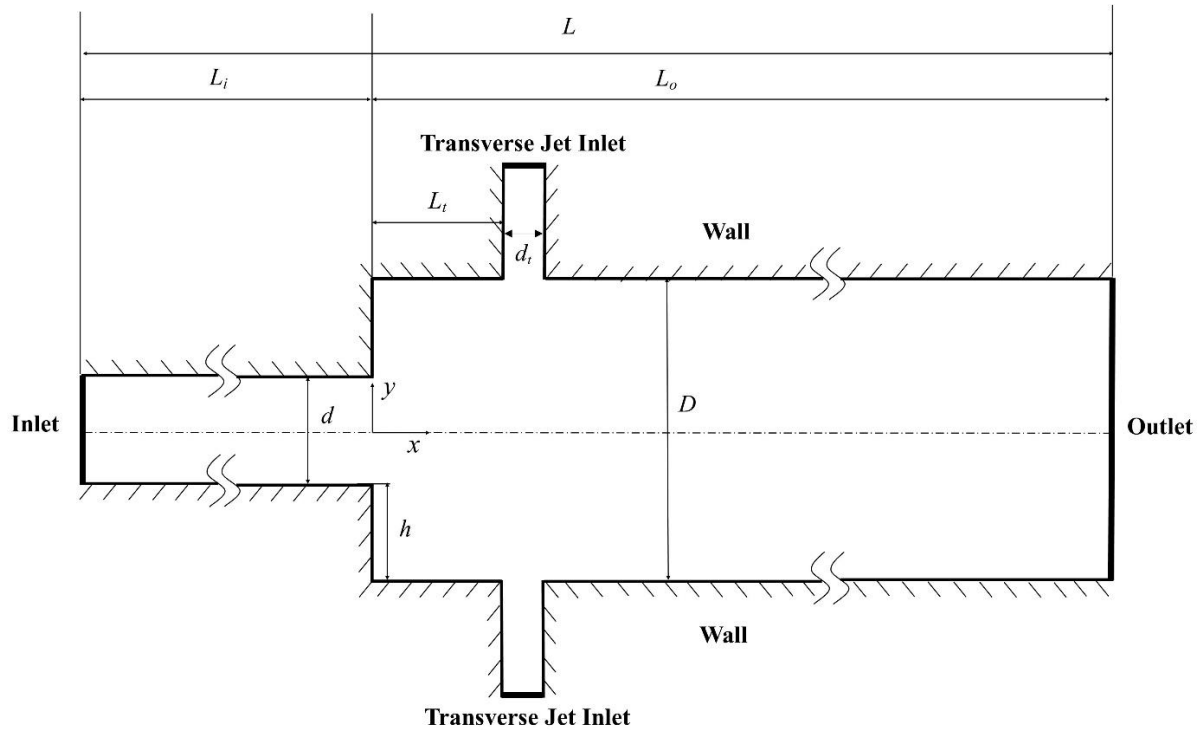


Figure 5-2: Schematic of the computational domain

5.2.2 Spatial grid

A structured, non-uniform, orthogonal finite-volume grid was mapped to the computational domain. The number of grid cells in the regions upstream and downstream of the expansion are shown in Table 5-2 for each value of the simulated expansion ratios. N_x and N_y refer to the number of cells in the streamwise and vertical directions, respectively. Figure 5-3 illustrates the streamwise and cross-stream grid spacing distribution for the $Er = 2.0$ case. The cells are non-uniformly spaced in both directions in order to have higher resolution near the sudden expansion region, no-slip walls, and the regions with high shear stress where the flow will experience larger spatial gradients. As shown in Figure 5-3(a), the grid resolution increases as the flow reaches the step of the sudden expansion. The grid cells are uniformly spaced in the streamwise direction from the step to the end of cross injection jets. The dashed line in Figure 5-3(a) indicates the location of the sudden expansion step. The coarsest grid occurs near the domain outlet where the streamwise grid size is

four times larger than the grid size near the sudden expansion centerline of channels. Figure 5-3(b) shows the grid spacing in the vertical direction at the centerline of transverse jets; the dashed line indicates the centerline of inlet channel. As shown, the grids become coarse at the centerline of inlet channel, where the vertical grid size in these regions is about twice that along the no-slip walls at the transverse jet injection point. Similar grid size distributions are used for the other expansion ratio cases.

In order to check the accuracy of the numerical results, a grid sensitivity study is performed using five grid resolutions at $Er = 2.0$ for Reynolds numbers of 1000 and $r = 20$. The detailed information of the grids used for grid-independence analysis is illustrated in Table 5-3.

Table 5-2: Characteristics of computational grids used for various sudden expansions

<i>Er</i>	$(N_x, N_y)_i$	$(N_x, N_y)_o$	$(N_x, N_y)_t$	<i>Total</i>
	<i>Upstream of</i>	<i>Downstream of</i>	<i>Upstream of</i>	<i>cells</i>
	<i>step</i>	<i>step</i>	<i>cross flows</i>	
1.5	150 , 60	820 , 120	20 , 60	109,800
2.0	150 , 60	820 , 180	20 , 60	159,000
3.0	150 , 60	820 , 300	20 , 60	452,400
4.0	150 , 60	820 , 420	20 , 60	628,800

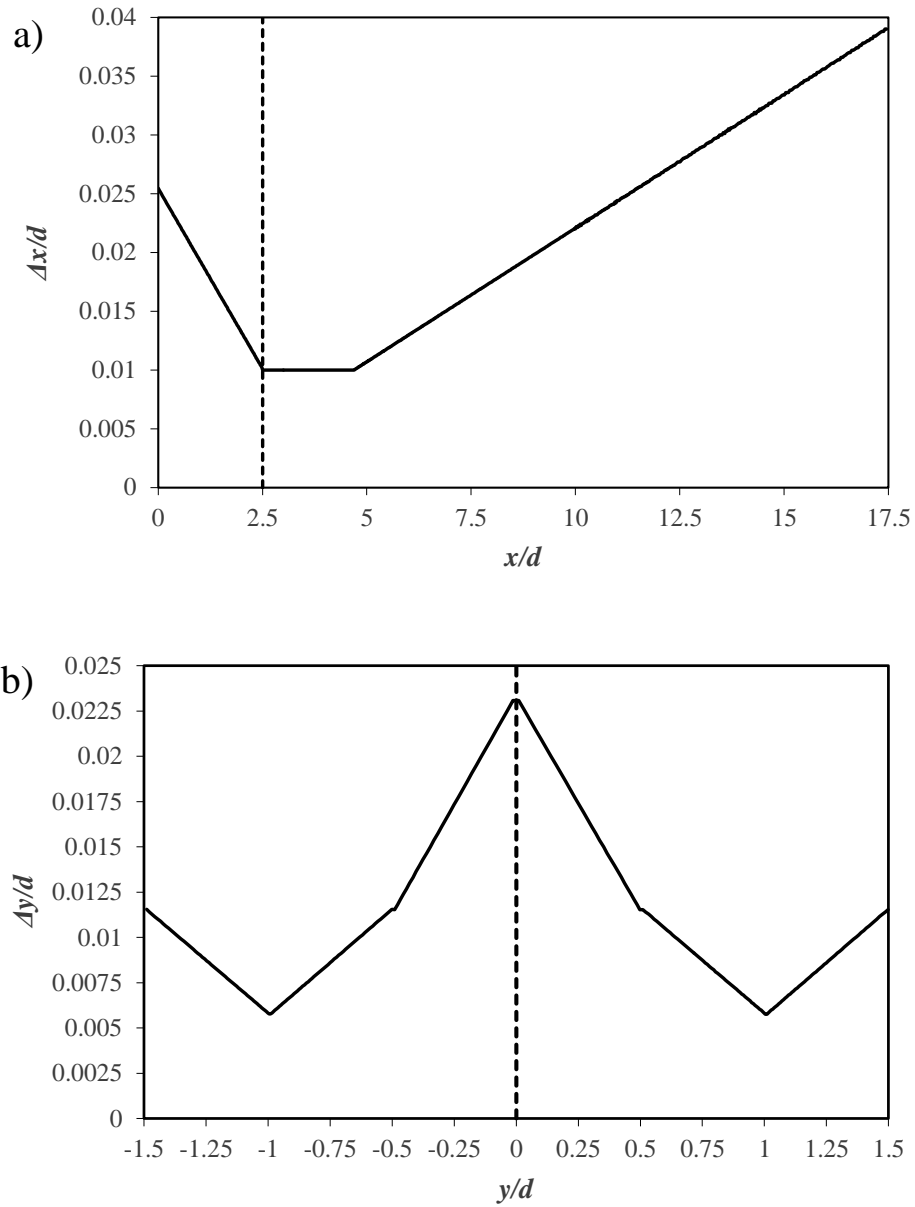


Figure 5-3: Distribution of the spatial grid spacing in the (a) streamwise direction at centerline of inlet channel and (b) wall-normal direction at centerline of cross injection jets for the $Er = 2.0$ case. The dashed line indicates (a) the location of the sudden expansion and (b) centerline of centerline of inlet channel

Table 5-3: The grids used for the grid-independence study at $Er = 2.0$, $r = 20$, and $Re = 1000$

<i>Grid</i>	$(N_x, N_y)_i$	$(N_x, N_y)_o$	$(N_x, N_y)_t$	<i>Total</i>
<i>Level</i>	<i>Upstream of</i>	<i>Downstream</i>	<i>Upstream of</i>	<i>cells</i>
	<i>step</i>	<i>of step</i>	<i>cross flows</i>	
M0	75, 30	410, 90	10, 30	39,750
M1	75, 40	410, 120	10, 40	53,000
M2	120, 60	646, 180	16, 60	127,200
M3	150, 60	820, 180	20, 60	159,000
M4	240, 80	1084, 240	24, 80	254,400

Figure 5-4 compares the wall pressure coefficient for the five mesh refinements. Analysis using the wall pressure coefficient and the normalized root mean square of velocity fluctuation distributions confirmed that about 159,000 cells are sufficient to guarantee grid independence for all Reynolds numbers considered in this chapter. Although, the results indicate that grids M0 and M1 are significantly different, increasing mesh refinement yields similar results for grids M2, M3, and M4. Sensitivity to mesh resolution is highest in the corner of the sudden expansion where the primary recirculation exists and immediately downstream of the transverse jet injection around $x/h \approx 5$. Therefore, although grid M2 seems to obtain adequate results, the numerical simulations are conservatively performed using refinement M3.

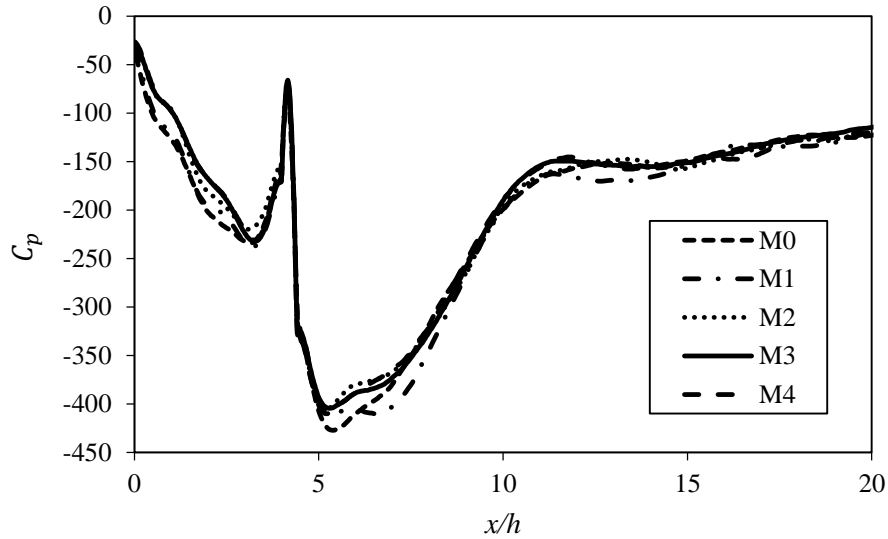


Figure 5-4: Pressure coefficient (C_p) distributions at various mesh resolutions at $Re = 1000$, $r = 20$ and $Er = 2.0$

5.2.2.1 Solution methodology

OpenFOAM® discretizes the governing equations by means of the finite volume method [111]. Second-order central differencing and implicit second-order Euler backward differencing are used to discretize the spatial and temporal derivatives, respectively. The time-step size in each simulation varies depending on the Reynolds number and grid size. The Courant number is kept below 0.5 [78,107], with $\Delta t = 10^{-6}$ s being the smallest time-step size used for $Re = 2000$ and $r = 20$, and $\Delta t = 5 \times 10^{-4}$ s being the largest timestep used for $Re = 200$ and $r = 5$. The working fluid is water at 1 atm and 25°C. Zero relative static pressure and an initial velocity equal to the mean velocity at the inflow boundary were used as initial boundary conditions. Each simulated test case was run for approximately 10 flow through times (defined as $L_i/U_i + L_o/U_o$, where subscripts i and o denote inlet and outlet pipe, respectively) to reach a statistically steady state and then approximately 10 more flow through times to collect the results for analysis. The velocity and

pressure coupling was solved with the PISO algorithm. Each simulation was performed in a parallel-processing environment on 32 and 64 CPUs using domain decomposition and a message-passing interface (MPI) parallelization strategy.

5.3 Mean flow development

Within the present discussion of the simulation results, velocities are normalized by the maximum velocity occurring at the inlet of the computational domain (denoted U_{max}) and spatial scales are normalized by the step height of the sudden expansion (h). The location of the transverse jet is placed such that it is within the recirculating region immediately downstream of the sudden expansion. This placement allows the injected flow to destabilize the recirculation zone to promote mixing and reattachment. Figure 5-5 plots the instantaneous and time-mean velocity magnitude and illustrates a strong initial interaction between the injected flow and the main flow that results in the formation of unsteady fluctuations immediately downstream of the injection. Although the fluctuations subside after about 10 diameters of the transverse jets, a periodic oscillatory pattern is set up in the downstream main flow that persists for much longer.

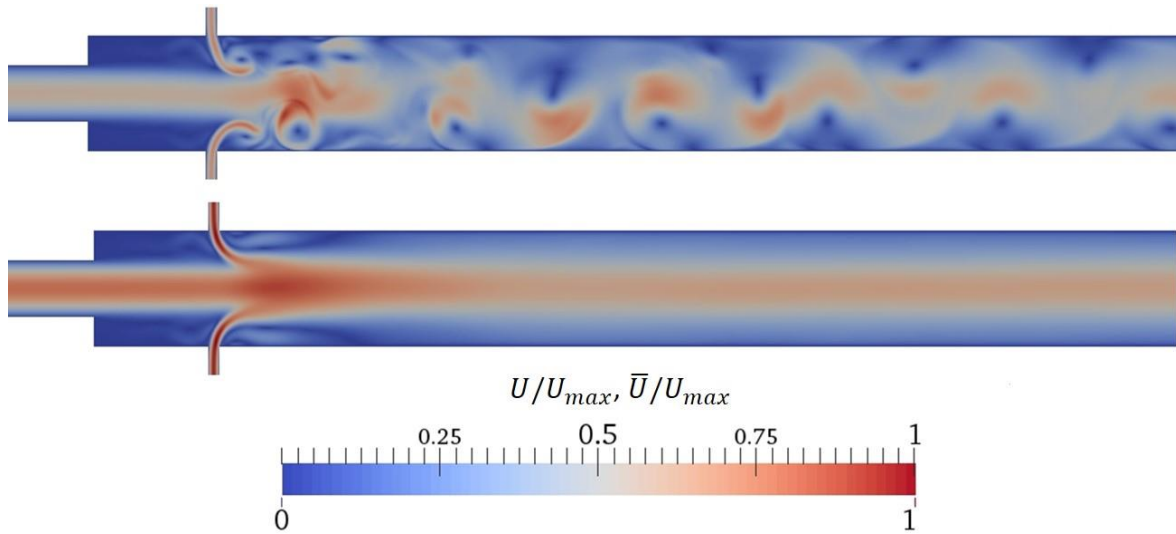


Figure 5-5: Zoomed view of non-dimensional velocity contour at Reynolds numbers of 2000 and $Er = 2.0$ for the case with cross flow ($r = 1.25$): a) Instantaneous velocity contour b) Mean velocity contour

Figure 5-6 represents the instantaneous and mean flow streamlines for the $Er = 2.0$ case at Reynolds numbers of 2000 and velocity ratio of 10. As predicted, the interaction of the main flow and the transverse jets triggers unsteadiness in the form of localized eddies and recirculations in the near-wall region surrounding the jet. Some of these disturbances are convected by the flow and generate an asymmetry wave that corresponds to the long-lived oscillations observed in Figure 5-5. The frequency of the asymmetry depends on the jet-to-main-flow velocity ratio and their Reynolds numbers. The mean flow streamlines show more or less symmetric patterns with two equal circulation regions downstream of the transverse jets. Two small circulation regions are also observed inside the primary recirculation regions. Existence of these regions in the shadow of the transverse jets provides enough support to surmise that the transverse jets act like a rigid curved obstacle in the flow and forces the main flow to move into a narrow region close to the centerline.

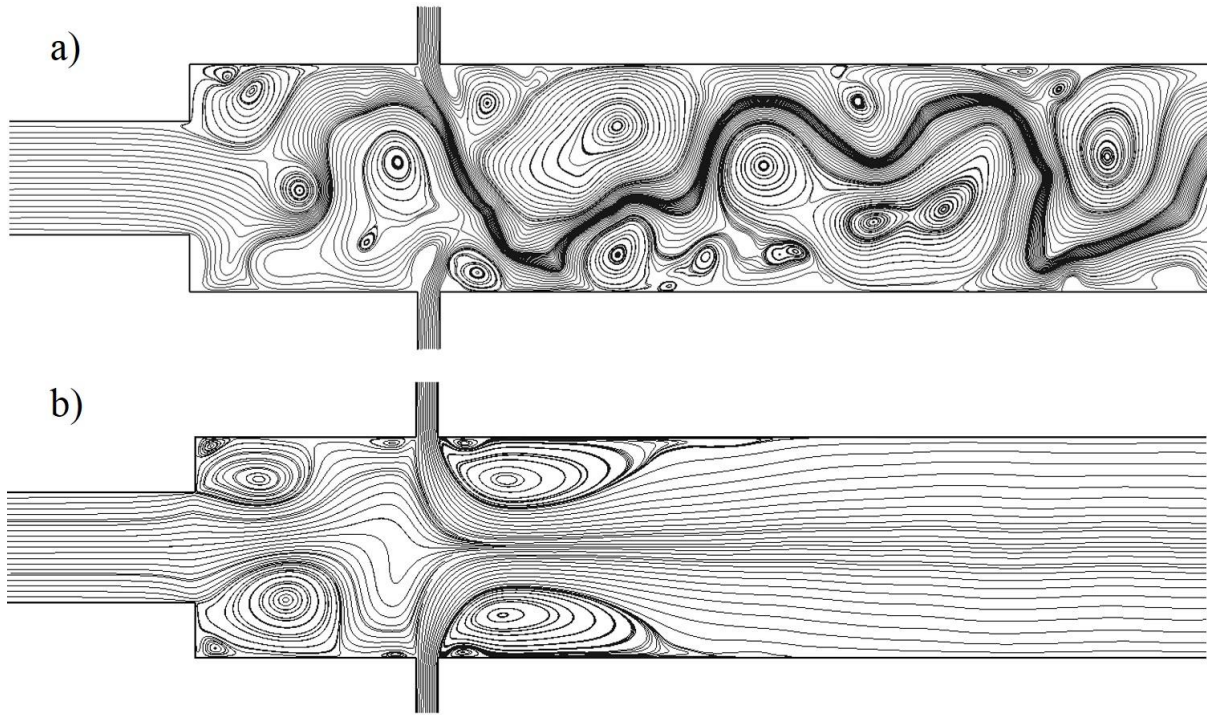


Figure 5-6: Zoomed view of streamline distribution in sudden expansion with at Reynolds numbers of 1000 and $Er = 2.0$ for the case with cross flow ($r = 10$) a) instantaneous streamlines, b) time-averaged streamlines

In order to visualize development of the flow downstream of the transverse jets, a simulation case is carried out for Reynolds numbers of 600 at $Er = 2.0$ and $r = 5$ with a very long outlet length downstream of the transverse jets ($300h$). Figure 5-7 shows that the interaction causes roll-up of the transverse flows into semi-coherent, rotational structures near the interface of the core and transverse flows. As these structures convect downstream, their coherence and amplitude decreases due to the reduced Reynolds number past the expansion. Dissipation of these rotational flow structures corresponds with the decreasing fluctuations in the laminarizing zone.

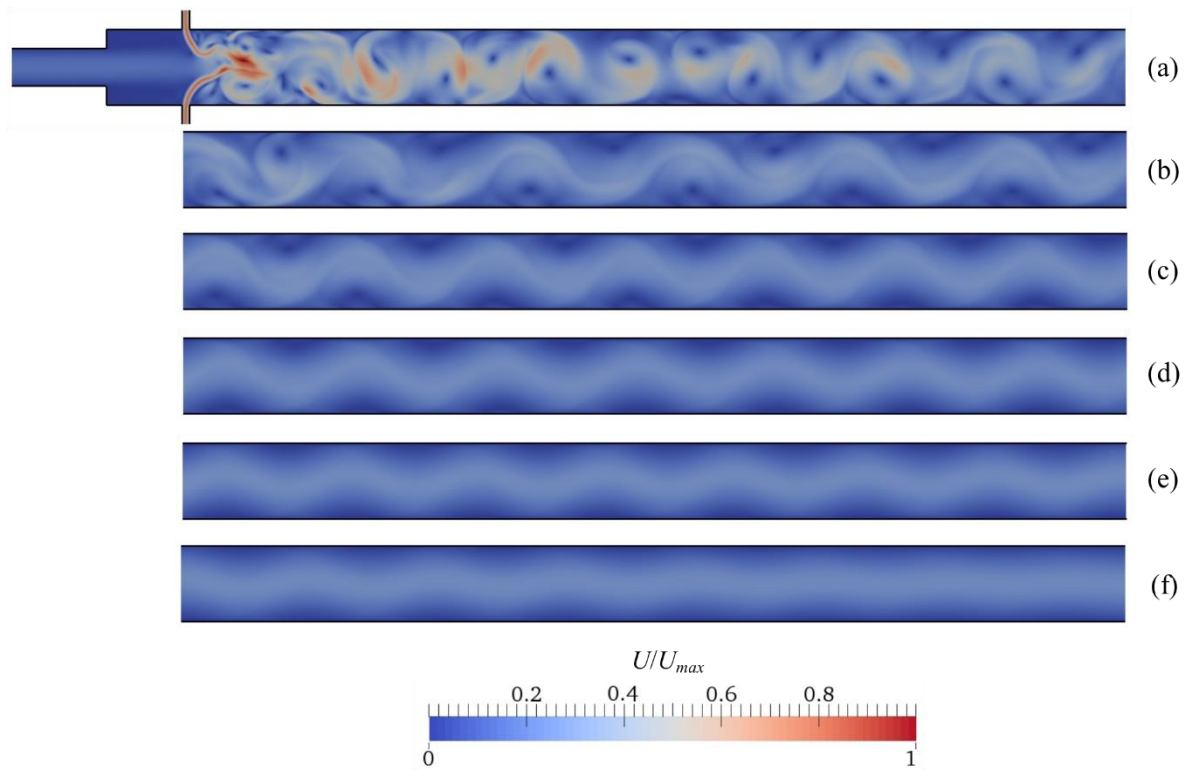


Figure 5-7: Visualization of the laminarization process by instantaneous velocity contour at Reynolds numbers of 600 and $Er = 2.0$ for the case with transverse jets at velocity ratio of 5

Figure 5-8 plots the root-mean-square (RMS) of the axial and vertical velocity fluctuation components at various streamwise stations downstream of the transverse jets. Profiles show the velocity fluctuation amplitude is largest near the transverse jets, and gradually decreases with streamwise distance. This indicates the relaminarization of the flow and damping of the large disturbance moving downstream. Moreover, Figure 5-8 shows RMS fluctuation profiles are symmetric about the centerline of the domain, implying that the average flow is still symmetric at this velocity ratio. The largest amplitude occurs upstream at $x/h = 20$ while computed fluctuation profiles at $x/h = 250$ have decreased by almost an order of magnitude.

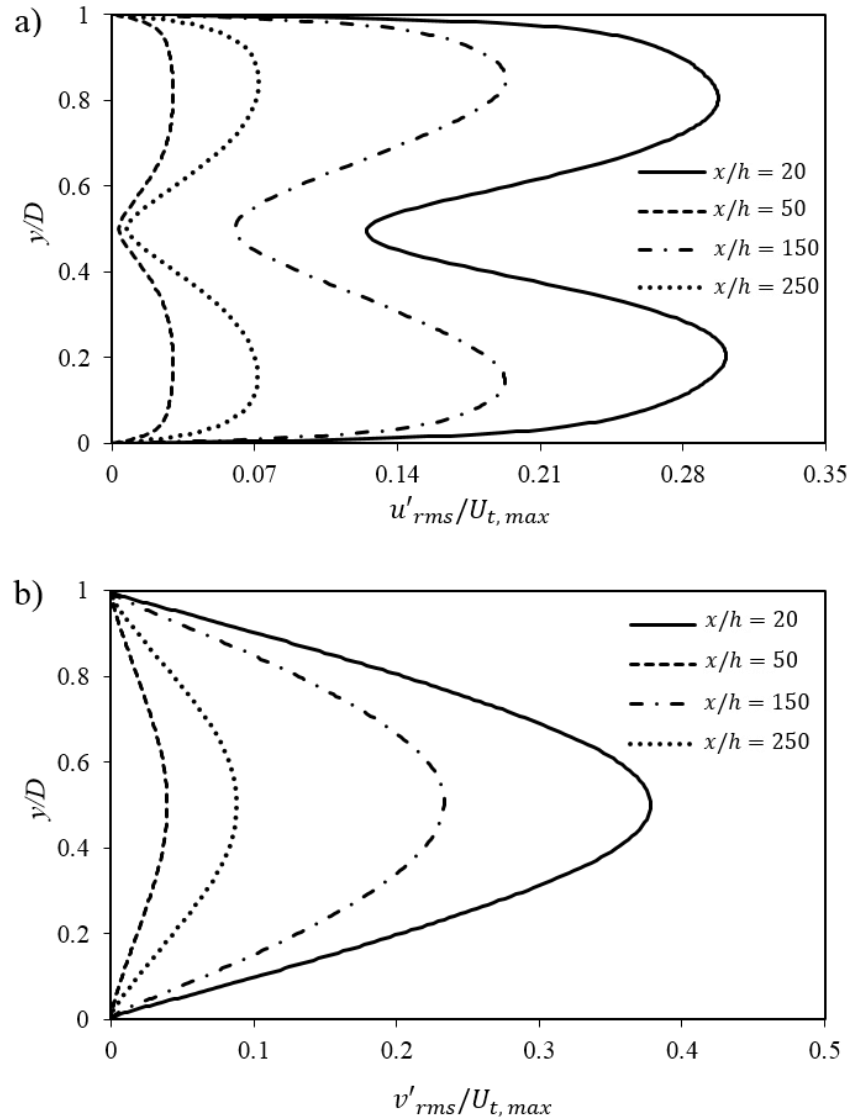


Figure 5-8: Measured root mean square velocity fluctuation at various positions downstream of transverse jets at $Re = 600$ and $Er = 2.0$ for the case with velocity ratio of 5

The length of primary reattachment regions after the injection of transverse jets is a function of main and transverse jet Reynolds numbers, expansion ratio, and velocity ratio. Figure 5-9(a) shows the computed reattachment lengths as a function of the Reynolds number for $Er = 2.0$ and $r = 20$. The reattachment length decreases with increasing Reynolds number. As

anticipated, development of unsteadiness and fluctuations due to transitional flow with increasing Reynolds number causes a sharp decrease in the reattachment length until it reaches a minimum value. The reattachment length remains approximately constant with small fluctuations for Reynolds numbers larger than 1200.

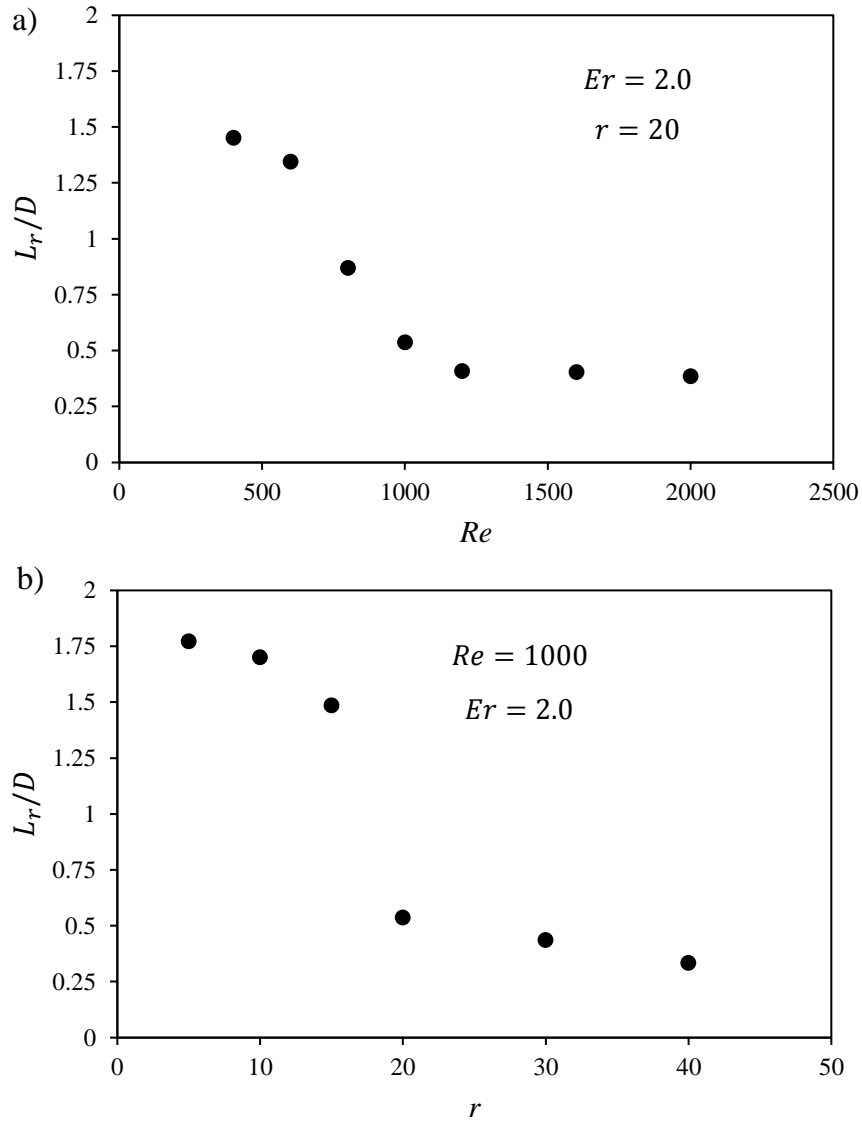


Figure 5-9: a) Reynolds number distribution of non-dimensional reattachment length (L_r/D). b) Dependence of reattachment length to velocity ratio (r)

Figure 5-10 plots the normalized reattachment length as a function of Reynolds number for expansion ratios of $Er = 1.5-4.0$. As seen previously in Chapter 4, the reattachment length decreases with increasing Reynolds number for each expansion ratio. The reattachment length also decreases with increasing expansion ratio at a fixed Reynolds number, although the rate of its reduction is reduced after $Er = 2.0$ and becomes negligible by $Er = 4.0$. It therefore seems that for a fixed jet velocity ratio, larger expansion ratios assist the transverse jets in reattaching the separated flow downstream of the expansion, possibly decreasing the mutual interaction of the transverse jets with each other at the centerline of the channel.

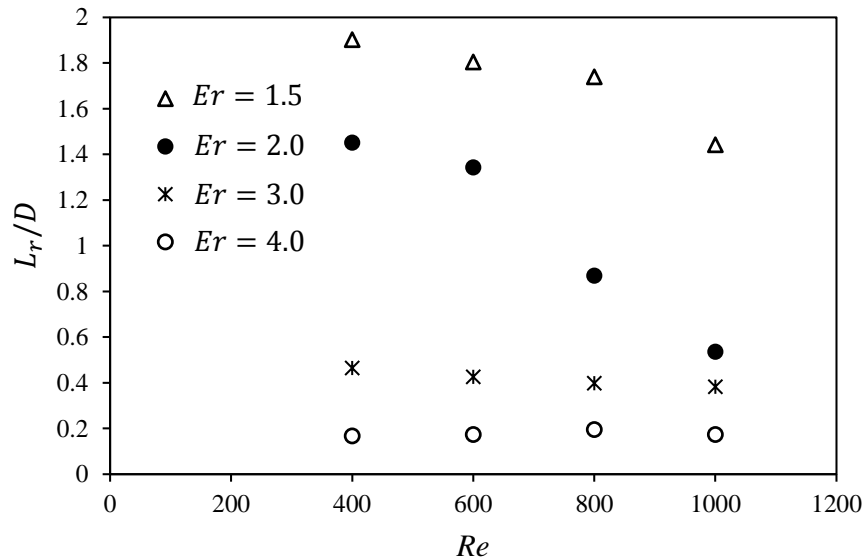


Figure 5-10: Reynolds number distribution of the reattachment length for various expansion ratios at $r = 20$

5.4 The effect of transverse jets on bifurcation

The phenomenon of transverse jet injection has been discussed in several research studies [69] but its effect on decay of bifurcation after a sudden expansion is an interesting phenomenon which needs more investigation. At low Reynolds numbers and with no transverse jets, the main

flow remains symmetric downstream of the sudden expansion with equal recirculation regions on both the upper and lower walls of the channel. As the Reynolds number exceeds a critical value, the disturbances in the flow become larger and an asymmetric structure appears and grows in the flow, termed bifurcation. During bifurcation, the recirculation region on one wall shrinks while the one on the opposite wall grows. Injection of transverse jets causes growth of unsteadiness and the decay of bifurcation in the time-averaged flow. To illustrate this, Figure 5-11 plots the velocity field associated with bifurcation at $Re = 500$ and $Er = 4.0$ with $r = 0$. For the case with no cross-injection, the degree of asymmetry downstream of the sudden expansion increases with increasing Reynolds number but the flow retains its steady, laminar structure. Although secondary and tertiary separation zones and even smaller-scale recirculation zones begin to form near the end of the long primary recirculation region, eliminating the bifurcation requires a cascading development of small-scale disturbances near the expansion. Adding the transverse jets, as shown in the streamlines of Figure 5-6(b), can provide the necessary unsteadiness for decay of the bifurcation.

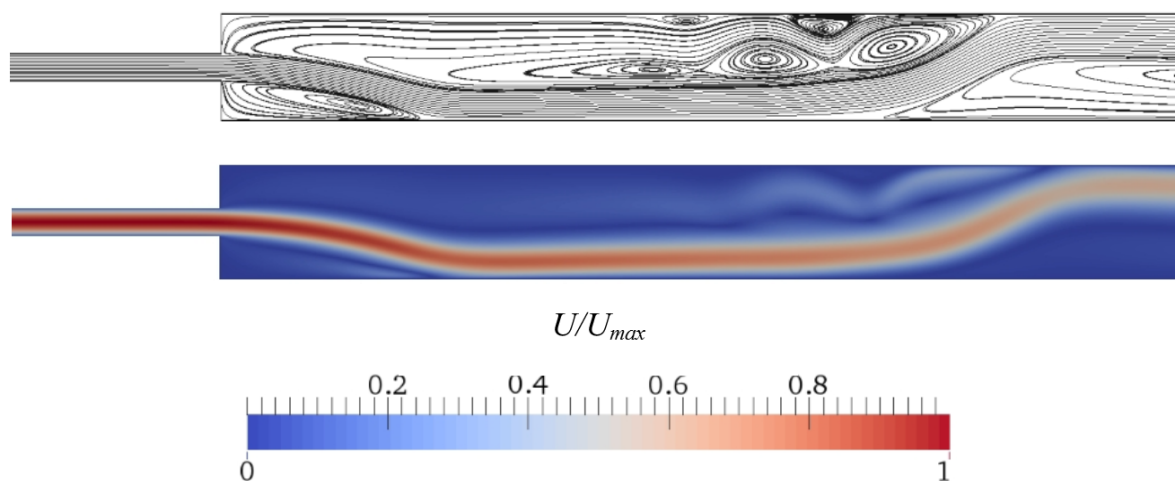


Figure 5-11: Zoomed view of non-dimensional velocity contour and streamlines illustrating the bifurcated flow downstream of the planar sudden expansion with $Re = 500$ and $Er = 4.0$

The effectiveness of transverse jets on bifurcation decay can also be determined by computing wall skin friction and pressure coefficient distributions for various velocity ratios. The pressure coefficient distribution, C_p is defined as

$$C_p = \frac{\bar{p}_w - \bar{p}_{in}}{\frac{1}{2}\rho U_{max}^2} \quad (5.5)$$

where \bar{p}_{in} is the upstream centerline mean pressure at the inlet boundary corresponding to the maximum inlet velocity U_{max} and \bar{p}_w is time averaged pressure on the wall. As shown in Figure 5-12a, for the case without transverse jets (e.g. $r = 0$), the Reynolds number is higher than the critical Reynolds number for symmetry-breaking bifurcation (as per Chapter 4). Hence, asymmetric flow occurs and the lower and upper walls demonstrate different values for the pressure coefficients. As shown in Figure 5-12, the pressure reduces lower than the inlet value due to the sudden expansion and a negative value appears for pressure coefficient at $x = 0$. This value increases as it reaches the center of the primary recirculation regions on both walls. During bifurcation, one circulation region grows and its reverse velocity magnitude becomes smaller while the other circulation region shrinks with increasing of reverse velocity magnitude in its recirculation zone. Therefore, the wall pressure on upper and lower walls are different due to unequal recirculation regions. The wall with a smaller primary recirculation region has lower wall pressure than the one with a larger recirculation region. For the case with transverse injection jets (e.g. $r > 0$), a pressure drop occurs downstream of the transverse jet injections with similar a trend on both walls. The discrepancy between pressure coefficient profiles on upper and lower walls decreases as the jet-to-main-flow velocity ratio is increased. As shown in Figure 5-12, wall pressure coefficient distributions have similar trends on both walls at $r = 3.75$. The wall pressure coefficients on the upper and lower wall also remain the same for higher ratios. Further

downstream of the transverse jet, the pressure initially increases; it reaches a maximum value, and then gradually reduces toward the outlet. The oscillation and inconsistency in pressure distribution occur due to the formation of secondary recirculation regions. The effect of this behavior and its amplitude become more visible with increasing of the jet-to-main-flow velocity ratio.

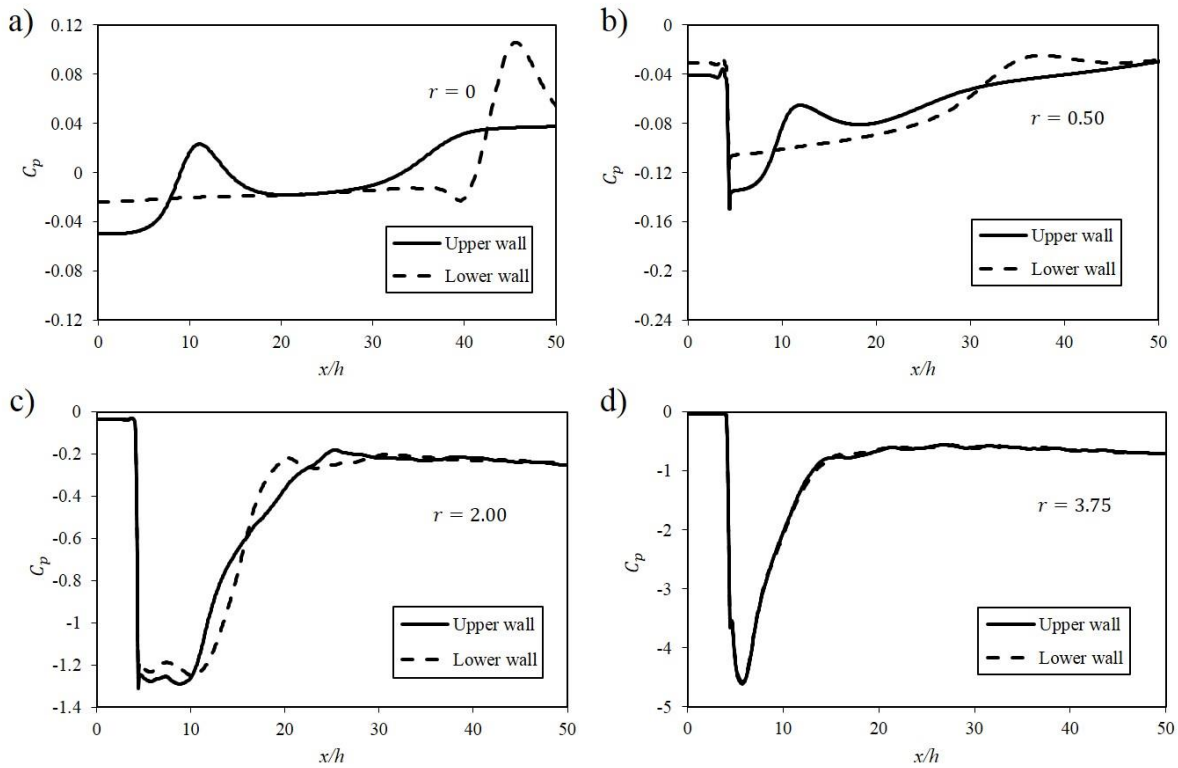


Figure 5-12: Pressure coefficient distributions at various velocity ratios (r) at $Re = 2000$ and $Er = 2.0$

5.5 The interaction between the transverse jet and the main flow

One of the common features of a transverse jet is horizontal shear-layer vortices along the upwind side of the jet. Figure 5-13 plots the instantaneous and time-averaged vorticity of the transverse jet near its injection location. The vorticity magnitude is nondimensionalized by d/U_{max} . The mixing of jet fluid with the main flow is visible in the instantaneous vorticity contours. The interface between the transverse jet and main flow becomes wavy and instability grows due to

formation of shear layer vortices along the upwind edge of the jet and continues throughout the lifetime of the jet. These type of shear-layer vortices are due to an inviscid Kelvin–Helmholtz-like instability of the jet shear layer [67,112–114]. Roll-up of both shear layers appear from the jets at the cross injection which is also observable in Figure 5-13a through instantaneous contours of vorticity magnitude. The streamwise grouping of transverse vorticity causes roll-up of the separated shear layer. Downwind of the jet, the magnitude of time-averaged vorticity decreases in the downwind shear layer as the parallel movement of the entrained fluid reduces the level of shear. Other vortical structures observed farther downwind of the jet are likely associated with unsteady recirculating flow patterns generated by the transient separation and flow reversal in the jet wake. These structures tend to increase the overall disturbance level downstream of the jet and assist in eliminating the bifurcated flow pattern.

The jet trajectory is clear from time-averaged vorticity field in Figure 5-13b. Karagozian [69] suggested improvement of mixing with higher trajectory (or jet penetration) in the main flow. Although increasing the expansion ratio generates unsteadiness at the expansion step, it causes high reduction of main flow velocity after the step. Moreover, at higher expansion ratios, transverse jets have a longer distance to develop and interact with the main flow before reaching the centerline of the main flow. Figure 5-14 shows the velocity magnitudes at different expansion ratios. The upper limit of each figure represents the centerline of the domain. At $Er = 1.5$, the transverse jet reaches the center with a higher velocity compared to $Er = 4.0$. Shorter development length causes greater interaction between main flow and transverse jet and bending of jet trajectory in direction of the flow. On the other hand, Figure 5-14d demonstrates that high expansion ratio creates a more vertical trajectory of the transverse jet and a diminished jet velocity at the centerline.

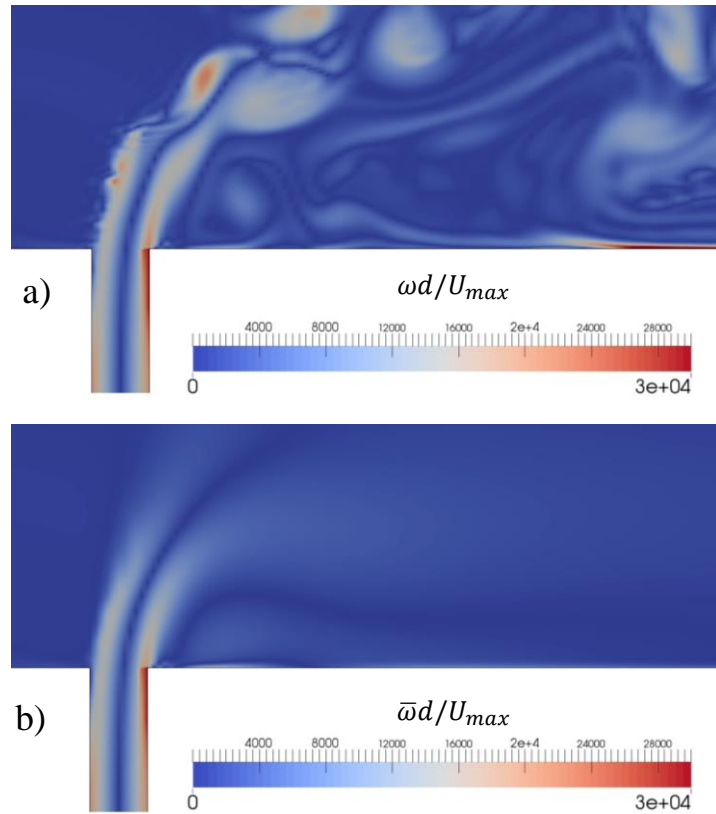


Figure 5-13: Zoomed view of non-dimensional vorticity contour near near-field flow of the transverse jet at Reynolds numbers of 2000 and $Er = 2.0$ for cross flow with velocity ratio of $r = 3.75$: (a) instantaneous non-dimensional vorticity (b) Time-averaged non-dimensional vorticity

The effectiveness of the interaction between the main flow and the transverse jets in generating mixing after the expansion also depends on the jet injection angles. Figure 5-15 represents time averaged streamlines at similar condition but at various transverse jet injection angles. As shown, increasing injection angles causes growth of primary recirculation zones downstream of the transverse jet and consequently, a smaller central core region results in a higher velocity. Figure 5-15(c) shows that the intended reverse velocity due to larger injection angle might lead the flow into a symmetry state upstream of the transverse jets and decay of symmetry breaking bifurcation.

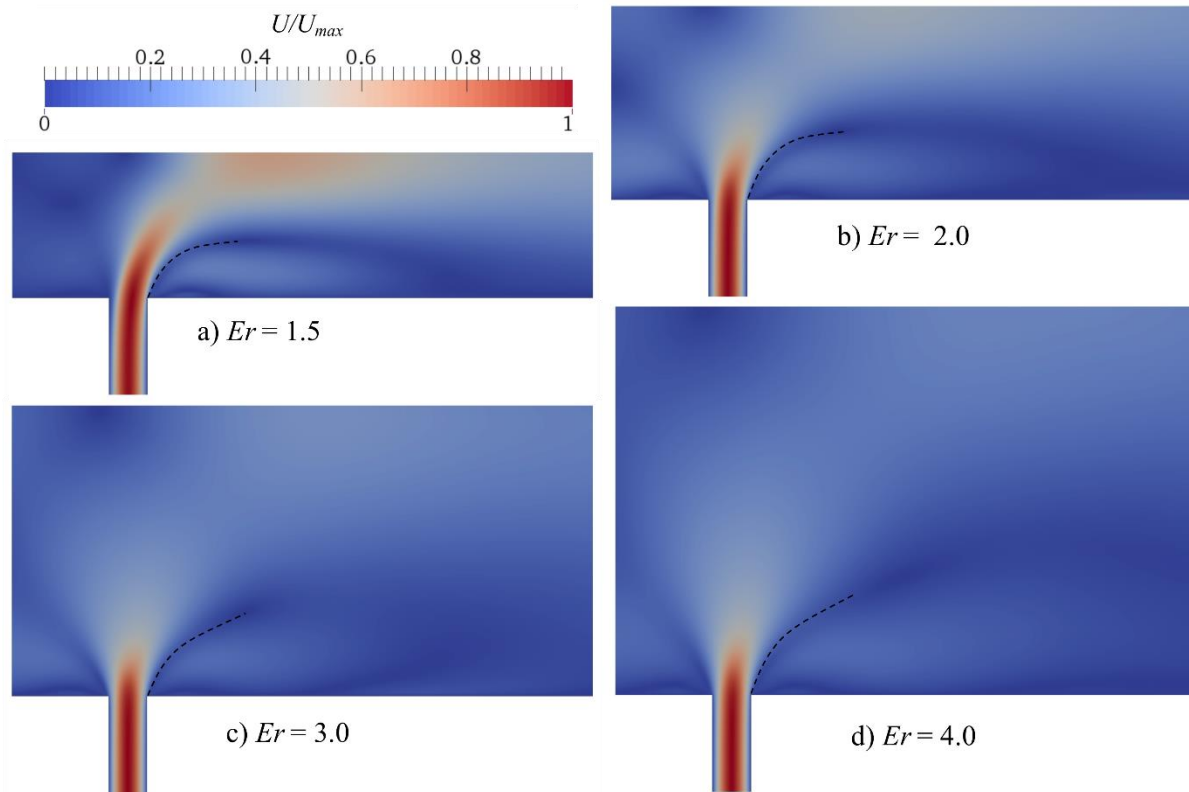


Figure 5-14: Zoomed view of time-averaged non-dimensional velocity magnitude contour in the near-field wake of the transverse jet for Reynolds numbers of 800 and velocity ratio of $r = 20$ at various expansions ratios

The effect of unequal injection angles is also determined in Figure 5-15(d) with $\alpha_1 = 60^\circ$ and $\alpha_2 = 120^\circ$. The unequal injection angles not only cause bifurcated behavior downstream of the injections but also create a central circulation region upstream of the injections which creates a source of central swirl upstream and minimizes number of individual circulation regions upstream of transverse jet injections.

The spatial distribution of the turbulent fluctuations is illustrated in Figure 5-16 through root-mean-square (rms) profiles of the axial and vertical velocity components for various injection angles. The fluctuations are measured at $z/h = 15$, which corresponds to a location downstream of the expansion where there is no sign of bifurcation in the flow. The profile for axial fluctuations

shows two peaks that correspond to the trajectories of the injected transverse jets. It is also notable that the highest level of axial and vertical fluctuations appears for the completely vertical transverse jets, for which the transverse jets also achieve maximum penetration into the main flow. The level of velocity fluctuation for the case with $\alpha_1 = 90^\circ$ and $\alpha_2 = 90^\circ$ is approximately 30% larger than the case with $\alpha_1 = 60^\circ$ and $\alpha_2 = 60^\circ$.

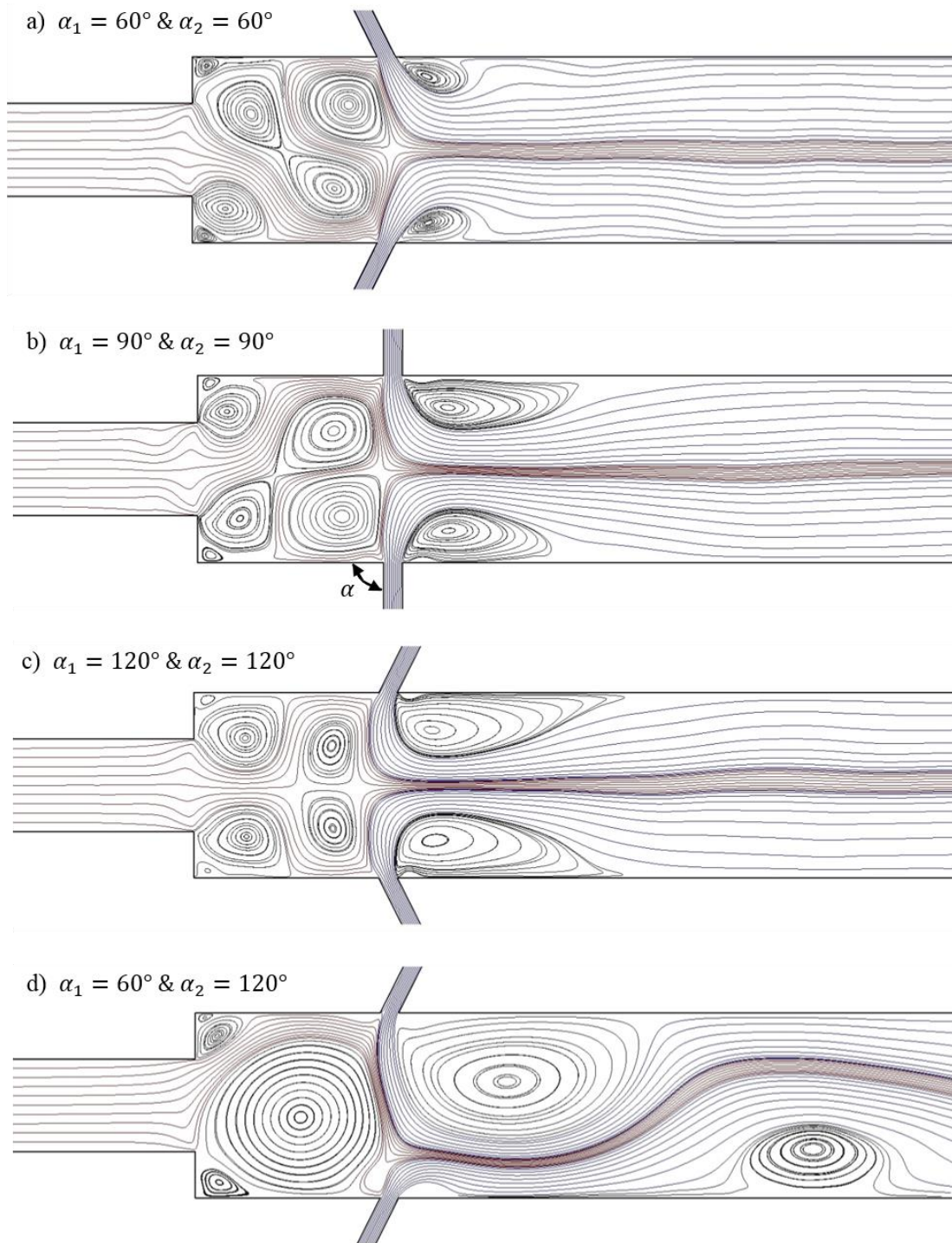


Figure 5-15: Zoomed view of time averaged streamlines of the planar sudden expansion with transverse jet at various injection angles for $Re = 1000$ with $Er = 2.0$ and $r = 20$ at $z/h = 15$

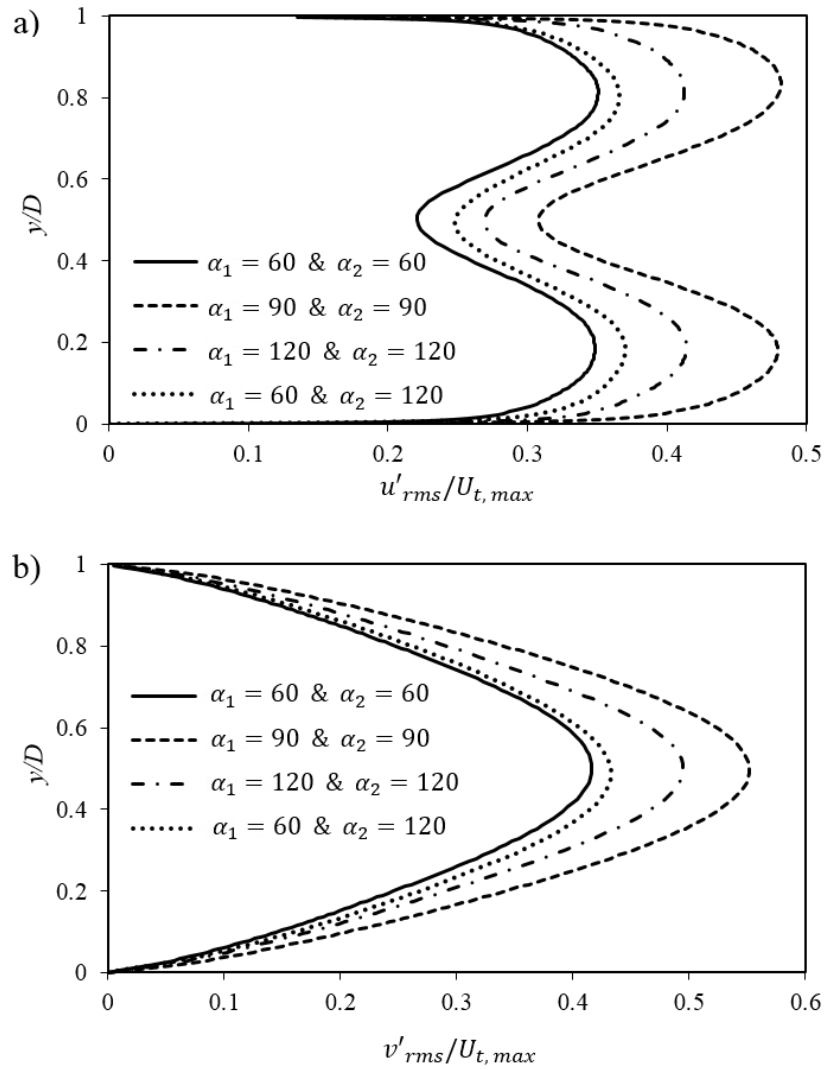


Figure 5-16: The root-mean-square of Streamwise and vertical velocity fluctuations at various injection angles at $Re = 1000$ with $Er = 2.0$ and $r = 20$

Chapter 6: Instability and Localised Turbulence Associated with an Axisymmetric Sudden Expansion

This chapter is based on the following accepted journal paper. This research was performed by Nima Moallemi under the direction of Dr. Joshua Brinkerhoff. The full results for this chapter are published as: Moallemi, N, Brinkerhoff, J.R., Instability and Localized Turbulence Associated with Flow through an Axisymmetric Sudden Expansion, *International Journal of Heat and Fluid Flow*, 72: 161-173 (2018) (*Published*).

This chapter begins by detailing the computational setup and simulated test cases that are used for this analysis. The results begin with comparing the two and three-dimensional simulations to show the weakness of two-dimensional cases due to onset of bifurcation at Reynolds numbers higher than critical. The objective of this chapter is to identify the shear layer reattachment length, time-averaged statistics of flow in the vicinity of the localized turbulence region and also the development and decay of localized turbulence.

6.1 Computational domain

For axisymmetric laminar and transitional cases, simulations are performed for Reynolds numbers between 15 and 2500 based on the mean bulk velocity and inlet pipe diameter. The total number of simulations is 28. The computational domain, shown in Figure 6-1, consists of two pipes with diameter of d and D mated together to produce an axisymmetric sudden expansion with a step-height of h and the expansion ratio of $D/d=2$. The lengths of the computational domain upstream and downstream of the expansion are $L_i=5h$ and $L_o=100h$, respectively. Insensitivity of the results to the streamwise length of the computational domain is confirmed by repeating the DNS with domain lengths of $90h$, $100h$, and $120h$, with the conclusion that the effect is negligible.

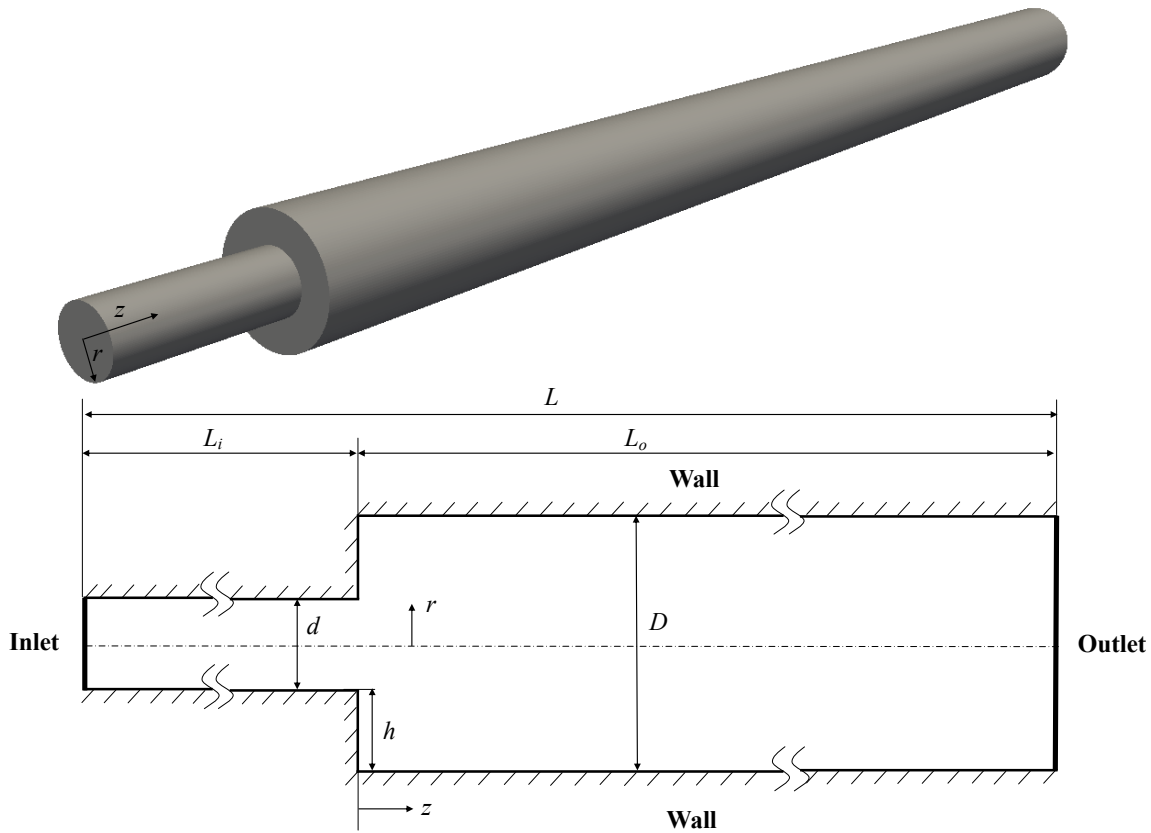


Figure 6-1: Schematic of the computational domain

6.1.1 Mesh resolution

A structured, non-uniform, orthogonal finite-volume grid was mapped to the computational domain. A grid independency analysis was performed at $Re=2500$ in order to find a sufficient spatial resolution for all simulations. Five different block-structured grids were used in this study in order to confirm the independence of the computational results from grid size. The number of grid cells varied from 1,538,816 to 16,398,336. The multi-block structure of the structured grid, shown in Figure 6-2, consists of 70 blocks. The detailed information about grid cells in the regions

upstream and downstream of the expansion step is shown in Table 6-1 for each of the simulated cases; N_r , N_θ , and N_z refers to number of cells in the radial, tangential, and axial directions, respectively. The cells are uniformly spaced in the tangential (θ) direction and non-uniformly spaced in the axial (z) and radial (r) directions in order to place a higher number of cells near the sudden expansion, no-slip walls, and regions with high shear stress where the flow will experience larger spatial gradients.

The mesh near the inlet of the domain was refined in order to capture the smaller-scale structural interactions that will be present in the cases with turbulent inflow (presented in Chapter 7). The central blocks have a fairly uniform grid spacing, with an increasing degree of grid refinement after the central block. The finest radial grid resolution appears at $r/d=0.5$, which corresponds to the no-slip region near the wall. This region contains high shear stress and velocity gradients. The radial grid spacing increases after the wall near the smaller pipe, with the coarsest cells appearing at the center of the expansion near to the centerline of the recirculation zone. The grid spacing of the near-wall region of the larger pipe at $r/d=1$ is similar to that of the near-wall grid spacing of the smaller pipe at $r/d=0.5$. The sudden expansion has the highest grid resolution in the streamwise direction, with the grid becoming coarser in both the upstream and downstream direction. The coarsest streamwise grid spacing is located at the outlet boundary condition, where the cell length is about 18 times that of the grid near the step of the sudden expansion. The maximum aspect ratio of each grid is kept below 75.

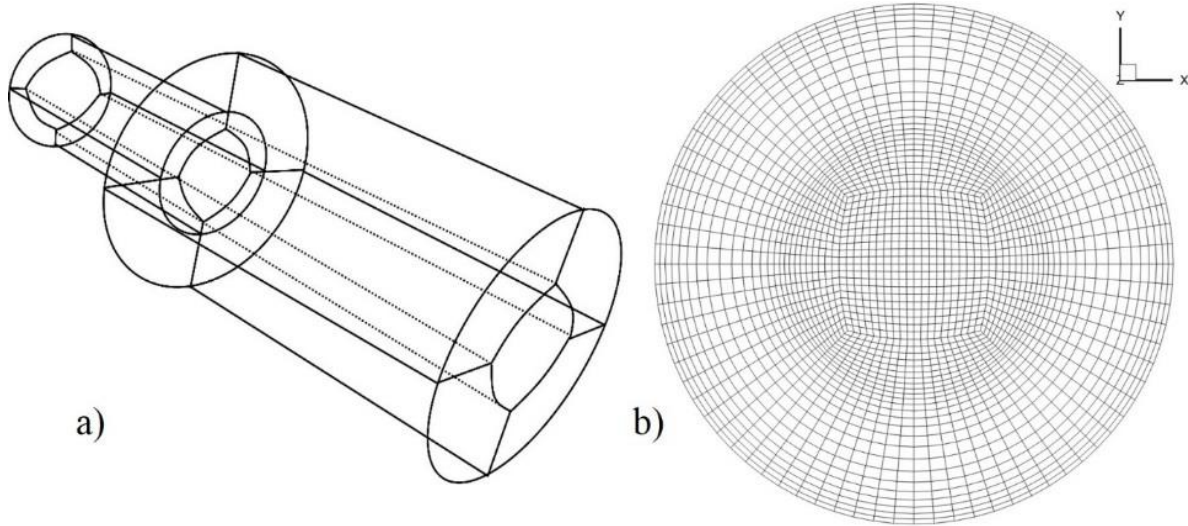


Figure 6-2: a) Schematic of the block structure that is used for the simulations. Only 10 out of 70 blocks are shown, b) the spatial grid spacing in radial and tangential directions after the expansion step. For easier visual clarity, the coarsest grid spacing is plotted

Table 6-1: Characteristics of the computational grids.

<i>Grid Level</i>	<i>Er</i>	$(N_r, N_\theta, N_z)_i$ <i>Upstream of</i> <i>step</i>	$(N_r, N_\theta, N_z)_o$ <i>Downstream of</i> <i>step</i>	<i>Total cells</i>
G0	2.00	(45, 96, 30)	(81, 96, 247)	1,538,816
G1	2.00	(76, 160, 50)	(108, 160, 292)	3,027,200
G2	2.00	(90, 192, 60)	(162, 192, 494)	6,924,672
G3	2.00	(90, 192, 80)	(162, 192, 658)	9,224,064
G4	2.00	(120, 256, 80)	(216, 256, 658)	16,398,336

Mesh independency is studied using the normalized reattachment length (L_r/h) for the five different mesh refinements. Figure 6-3 shows the normalized reattachment length (L_r/h) for the five different grid refinement levels. The results indicate that about 9 million cells are sufficient

enough to guarantee grid independence for all Reynolds numbers considered. Therefore, in the current study, the numerical simulations are performed using grid G3.

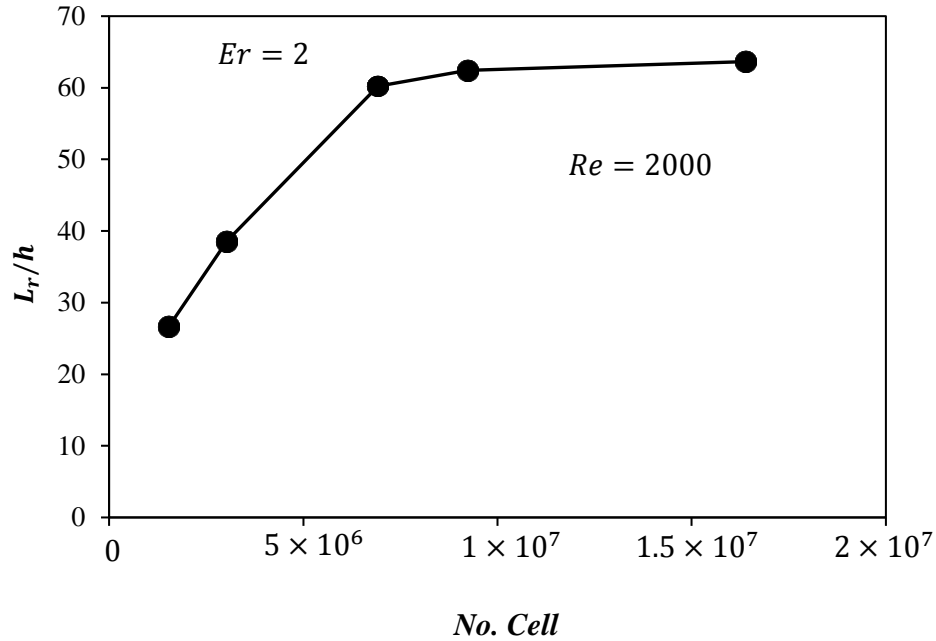


Figure 6-3: Dependence of reattachment lengths to the grid size for $Re = 2000$

The analysis of the results begins by comparing the development of the recirculation region in two- versus three-dimensional cases to highlight deficiencies associated with two-dimensional simulations due to the presence of flow bifurcation at certain Reynolds numbers. The shear layer reattachment length and time-averaged flow statistics are then discussed, especially near the localized turbulence region, followed by an evaluation of the development and decay of localized turbulence. In the last section, the effect of artificial forced disturbances on the flow reattachment length is investigated.

6.2 Comparison of two- and three-dimensional simulations

The occurrence of the sudden expansion causes an abrupt adverse streamwise pressure gradient downstream of the expansion and serves to amplify small fluctuations that develop upstream of the expansion [115]. Different flow patterns are observed depending upon the value of the Reynolds number and result in differing characteristics of the recirculation region downstream of the expansion and a corresponding variation in the downstream length required for the flow to reattach. Interpretation of the simulated flow in the axisymmetric sudden expansion is assisted by comparing the 3D results to simulations of a 2D sudden expansion. Figure 6-4 plots the time-averaged velocity magnitude of the 2D and 3D cases. Bifurcation phenomena occurs in the 2D simulation and causes asymmetric flow, as documented by numerous prior studies [36,116]. Bifurcation is attributed to the amplification of small-scale flow disturbances localized at the time-averaged reattachment location of the symmetric condition. As the disturbances amplify, bifurcation progresses as one recirculation zone shrinks and becomes shorter while the other grows.

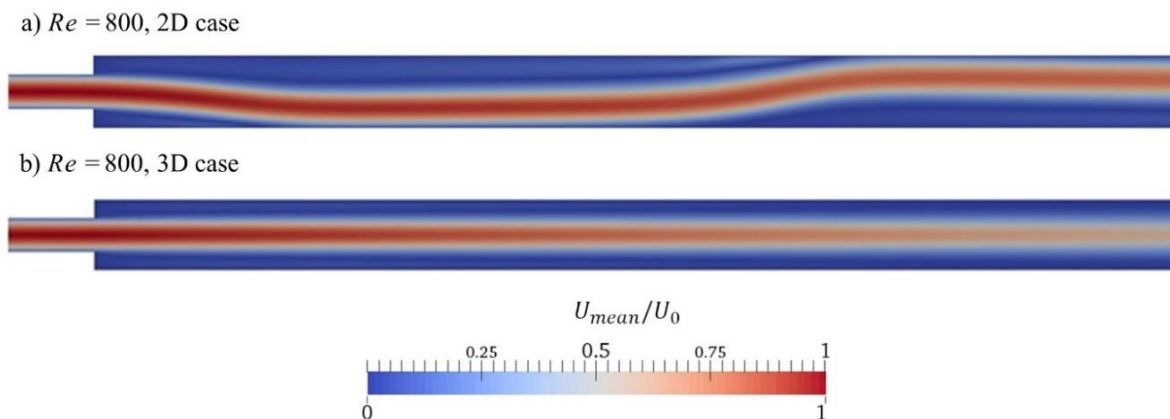


Figure 6-4: Time-averaged contours of velocity magnitude at $Re = 800$ for the (a) 2D and (b) 3D cases

Figure 6-4 illustrates that bifurcation does not occur in the 3D case at the same Reynolds number. This is also illustrated in Figure 6-5 by plotting the reattachment length versus Reynolds number for the 2D and 3D cases. Agreement occurs for Reynolds numbers less than the critical Reynolds number for bifurcation onset. Symmetry-breaking bifurcation initiates around $Re = 218$ for the 2D case. This is close to the predicted critical Reynolds number of 216 by Drikakis [36]. On the other hand, the 3D flow remains axisymmetric up to the maximum simulated Reynolds number of 2500. The absence of bifurcation in the 3D case agrees with published literature, which indicates that the critical Reynolds number for bifurcation onset in axisymmetric geometries is much higher than for 2D flows. For instance, Sanmiguel-Rojas et al. [26] numerically estimated the critical Reynolds number for bifurcation onset as $Re_{c,b} \simeq 3273$ using global instability analysis. In contrast, experiments by Mullin et al. [25] observed a relatively abrupt bifurcation at $Re_{c,b} \simeq 1139$. Flow disturbances are a possible cause of this discrepancy between numerical and experimental results; Cantwell et al. [24] note that sudden expansions behave like a noise amplifier and can trigger the bifurcation process, as the flow is extremely sensitive to incoming perturbations that are inevitably present in any experiment. To approximate these disturbances in a numerical simulation, Sanmiguel-Rojas and Mullin [53] introduced finite-amplitude perturbations and obtained bifurcation at around $Re_{c,b} \sim 1500$, depending upon the amplitude of the applied perturbation. As no external perturbations are imposed in the present study, the 3D flow remains axisymmetric.

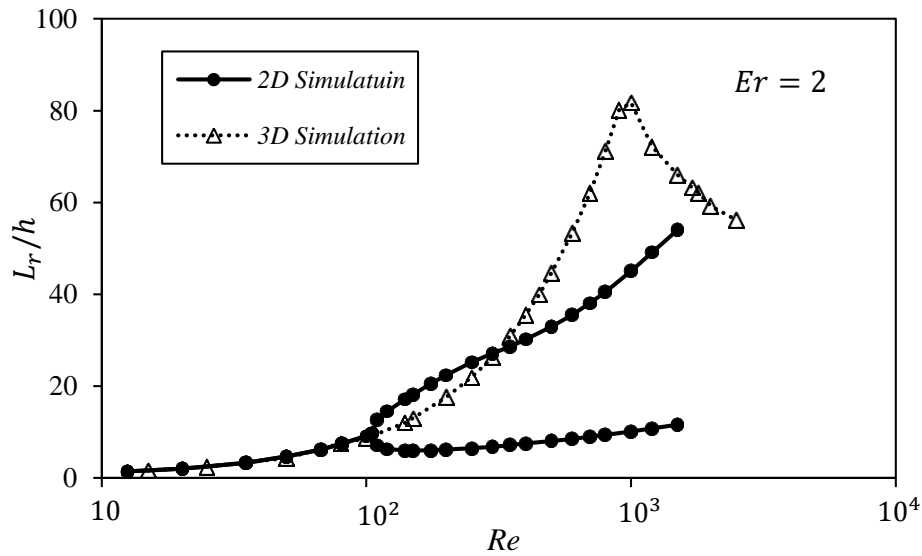


Figure 6-5: Comparison of 2D and 3D results for non-dimensional reattachment length (L_r/h) versus various Reynolds numbers

6.3 The shear layer reattachment length

The non-dimensional reattachment length at various Reynolds numbers is presented in Figure 6-6 in comparison with previous studies [8,18,20,23,31,32]. The results show good agreement with literature for low Reynolds numbers. As the Reynolds number increases, the results obtained by Pak et al. [20] and Latornell and Pollard [8] deviate from each other. As the transitional regime starts, the flow downstream of the sudden expansion becomes unsteady, secondary recirculation zones appear, and the primary reattachment length decreases. The present numerical results achieve good agreement with the critical Reynolds number identified by Latornell and Pollard [8] for the onset of flow unsteadiness. However, for Reynolds numbers above the critical threshold, the present results yield longer reattachment lengths than Latornell and

Pollard [8]. This is likely due to lower levels of background disturbances in the present numerical simulations relative to the experiments, as discussed in Section 6.4.

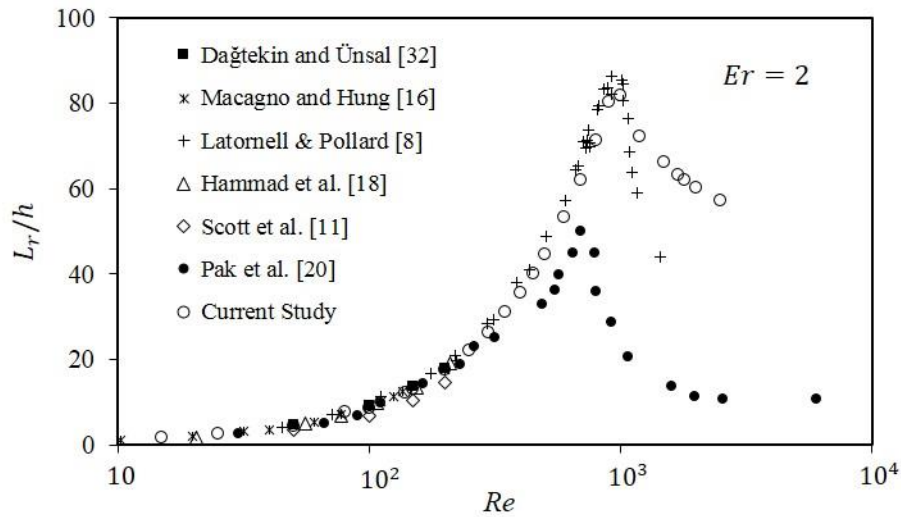


Figure 6-6: Comparison of non-dimensional reattachment length (L_r/h) at various Reynolds numbers with previous studies

6.4 Disturbance growth and transition to turbulence

To illustrate the growth of flow disturbances downstream of the sudden expansion, Figure 6-7 plots the streamwise distribution of the time averaged and fluctuating velocity amplitudes along the flow centerline in terms of the root-mean-square amplitude at various Reynolds numbers. The centerline velocity is twice of the spatially-averaged streamwise velocity at the inlet, denoted U_0 . As shown, the smooth reduction of centerline velocity due to sudden expansion changes dramatically near the reattachment position where the localized turbulence is observed. Upstream of the sudden expansion ($z/h < 0$), the normalized fluctuation

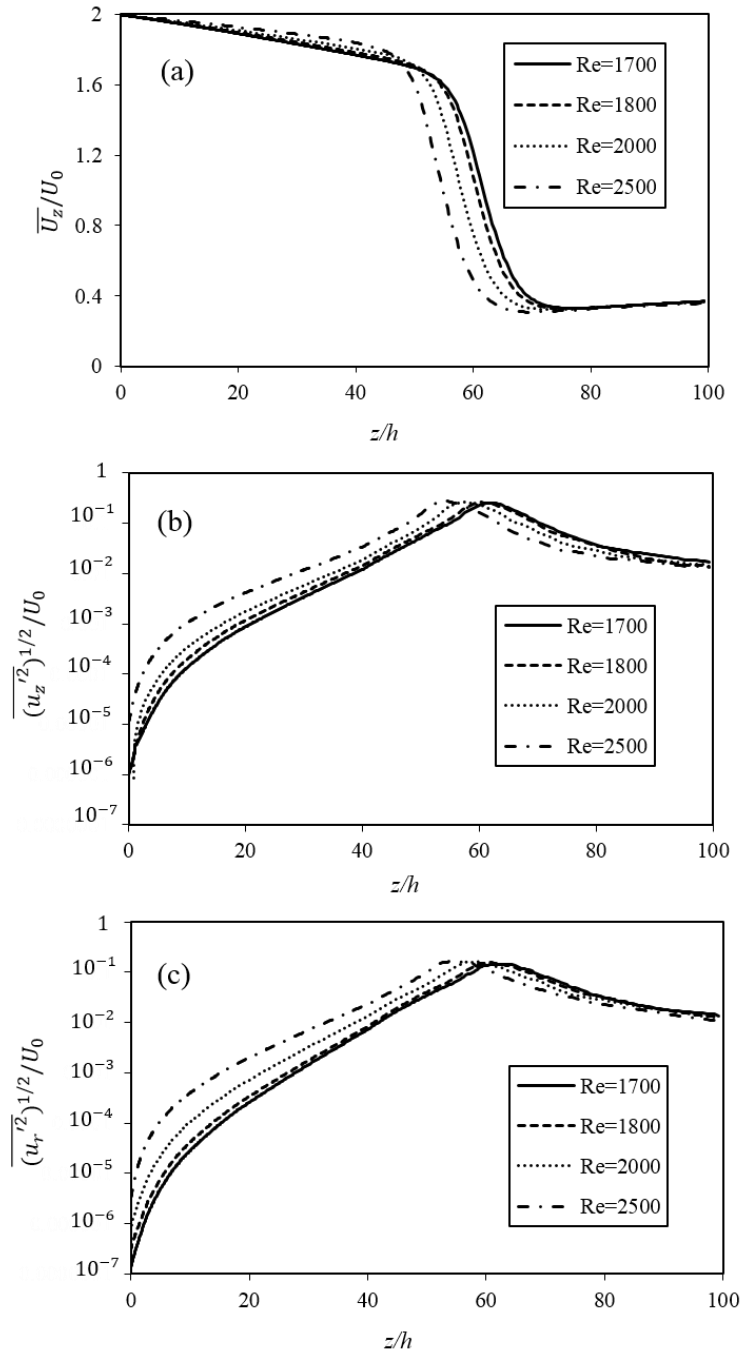


Figure 6-7: Root-mean-square streamwise velocity fluctuations along the centerline for flows with various Reynolds numbers

amplitude is below 10^{-7} , which is close to the convergence criteria of the iterative solver. Downstream of the sudden expansion ($z/h > 0$), the growth of disturbances is exponential with two different slopes. Upstream of about $z/h = 10$, an initial large amplification rate is observed that is proportional to the Reynolds number. Downstream of about $z/h = 20$, a lower amplification rate is observed that appears independent of Reynolds number. Nearly equal disturbance growth rates are present for all cases, although the peak amplitude is slightly higher for the higher Reynolds numbers due to their larger initial amplification rate. The disturbance amplitude peaks slightly upstream of the time-averaged reattachment point; e.g. at $Re = 2500$, the peak occurs at $z/h = 54$, while reattachment occurs at $L_r/h = 56.2$. Moreover, the upstream movement of the peak disturbance location with Reynolds number matches the upstream shift in reattachment point noted in Figure 6-6. This suggests that the localized turbulence promotes reattachment of the separated flow. Downstream of the reattachment location, the velocity fluctuations gradually decay and the flow relaminarizes. The decay rate is similar for all Reynolds numbers, and similar fluctuation amplitudes are present for all cases after relaminarization.

To illustrate the form of the disturbances growing in the laminar region upstream of the transition point, Figure 6-8 plots the radial velocity profiles for various Reynolds numbers at $z/h=20$. This axial location is upstream of the time-averaged reattachment location for all plotted Reynolds numbers and approximately corresponds to the position where the amplification rate becomes insensitive to Reynolds number. The time-averaged axial velocity profile is plotted in Figure 6-8(a), while (b)-(d) show the root-mean-square amplitude of the velocity fluctuations in the three cylindrical coordinates. While the mean axial velocity profile shows negligible variation with Reynolds number, the fluctuation amplitudes are strongly affected, with increasing Reynolds numbers producing stronger fluctuations in the flow, which is consistent with Figure 6-7. The

radial velocity fluctuations reach a peak value at the center of the pipe, while the axial and azimuthal fluctuations peak near $r/d = 0.2$. Additionally axial disturbances achieve a larger amplitude by approximately one order of magnitude compared to the azimuthal and radial components. As will be shown, this radial location coincides with the location of maximum vorticity in the annular shear layer that is formed when the flow separates from the wall downstream of the sudden expansion. Curiously, this radial location also coincides with a slope change in the radial fluctuation profiles, which suggests that radial fluctuations inside the annular shear layer are amplified much more strongly than outside the shear layer. It is in this interior region of the annular shear layer ($r/h \lesssim 0.4$) that coherent structures are observed and appear to play an important role in triggering the break down of the shear layer into turbulence, detailed in Section 6.5.

The spatial distribution of the disturbances shown in Figure 6-8 is illustrated in Figure 6-9 by plotting contours of velocity and vorticity magnitude in a slice that intersects the centerline. Figure 6-9(a)-(b), which plot the instantaneous and time-averaged velocity magnitude field, show that the separated flow past the sudden expansion can be viewed in terms of a core jet flow. The disturbances in Figure 6-8 within the separated shear layer appear in Figure 6-9(a) as oscillations along the periphery of the centerline core jet. These oscillations result in transition of the shear layer to turbulence. Oscillations in the azimuthal shear layer along the periphery of the core jet are also visible in Figure 6-9(d)-(e), which plot the instantaneous and time-averaged vorticity magnitude field. They are caused by a succession of instability modes on the growing vorticity field, beginning with a sequential grouping of azimuthal vorticity in the separated shear layer into coherent vortical structures that have a smaller spatial scale and concentrated vorticity magnitude, described further in Section 6.5. The development of these coherent vortices coincide with the

rapid break-down of the shear layer and transition to turbulence. Figure 6-9(c) plots the fluctuating kinetic energy (TKE) distribution associated with the break down of the shear layer. Consistent with Figure 6-8, the fluctuating kinetic energy is initially localized in the shear layer about the radius with maximum vorticity. As transition proceeds, the region of large fluctuation energy broadens and eventually coalesce at the centerline, producing an energy distribution that is relatively uniform in the radial direction. The fluctuation energy is gradually and fairly uniformly dissipated in the relaminarizing zone.

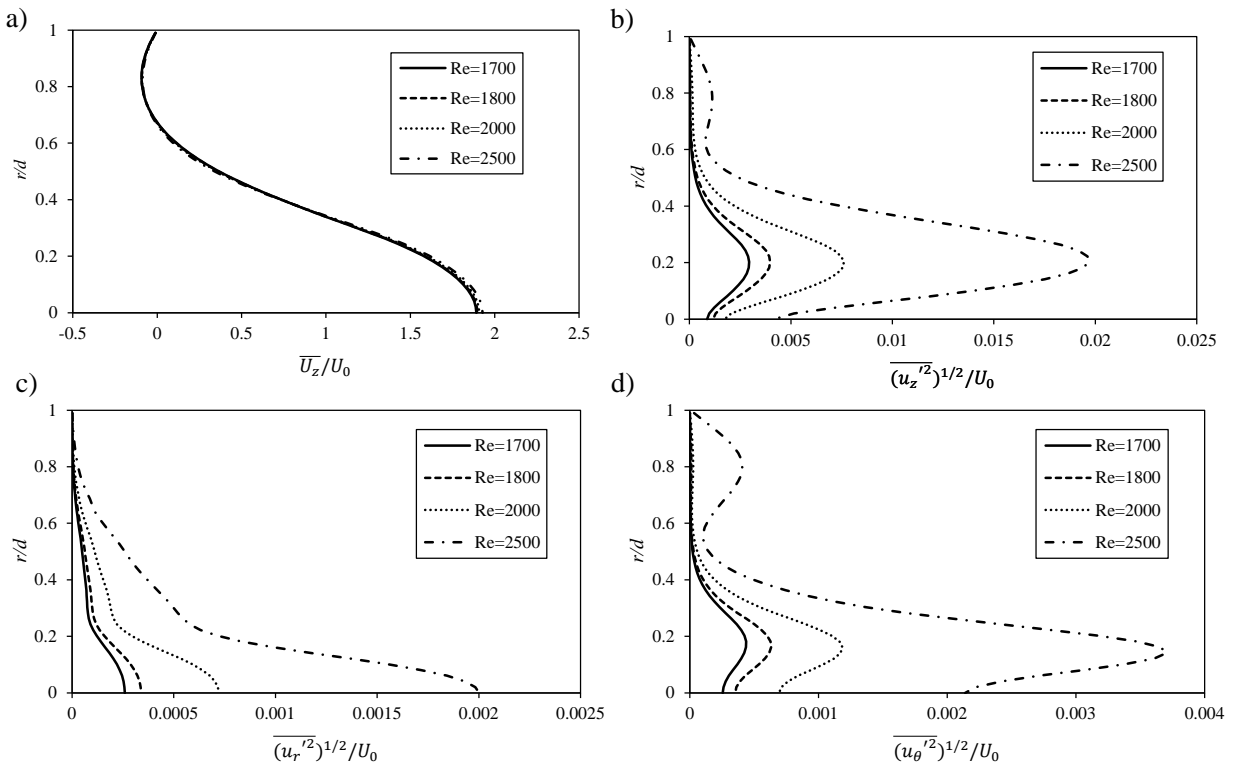


Figure 6-8: Time-averaged radial velocity profiles at $z/D = 20$ and $Re = 1700-2500$. (a) Axial velocity profile. (b)-(d) Root-mean-square velocity fluctuations in the (b) axial, (c) radial, and (d) tangential directions

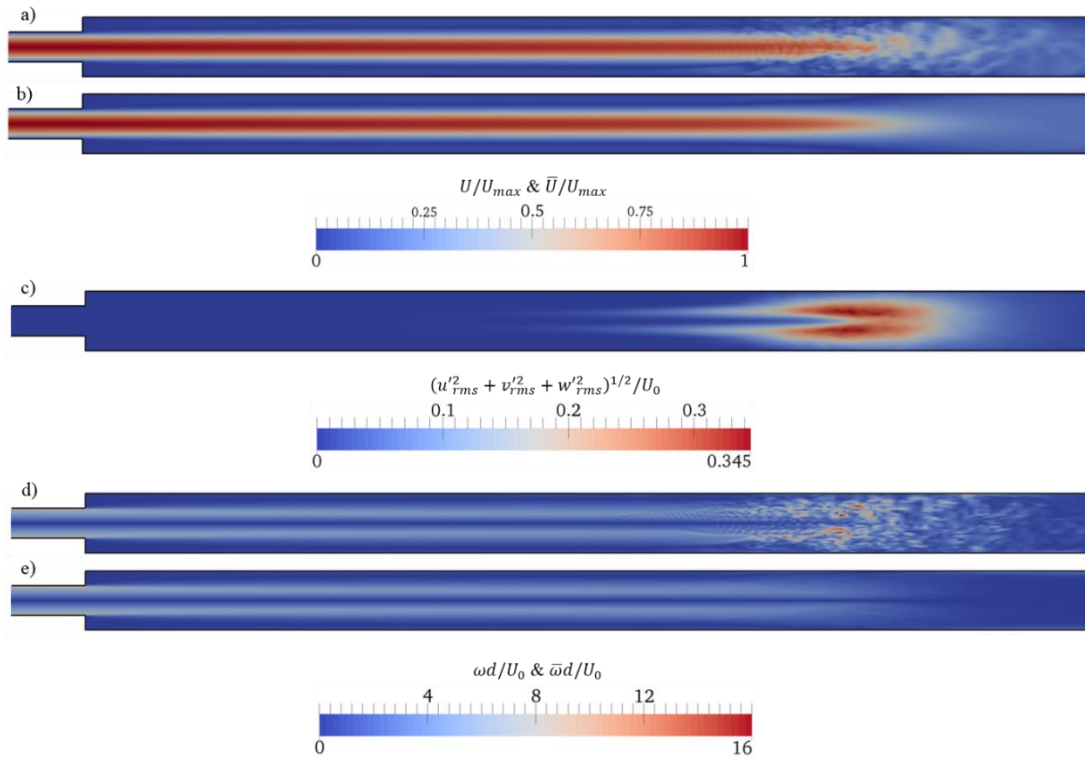


Figure 6-9: Zoomed view contours for flow in an axisymmetric sudden expansion with $Re = 2500$. a) the mean velocity, b) the instantaneous velocity, c) the turbulence kinetic energy, d) the instantaneous vorticity, e) the time-averaged vorticity

In Figure 6-10, radial profiles of the turbulence kinetic energy are plotted at four axial slices ($z/h = 40, 50, 56,$ and 64) for the $Re = 2500$ case. Results show that maximum TKE is localized at about $r/h = 0.3$, in the shear layer at the periphery of the core jet. As the flow develops in the streamwise direction, the TKE increases on the tip of core region where tilting of the structures can also be observed as a natural consequence of high shear layer instability. Just after the reattachment zone, the turbulence level decreases in the region following shear layer reattachment until the flow is completely laminarized.

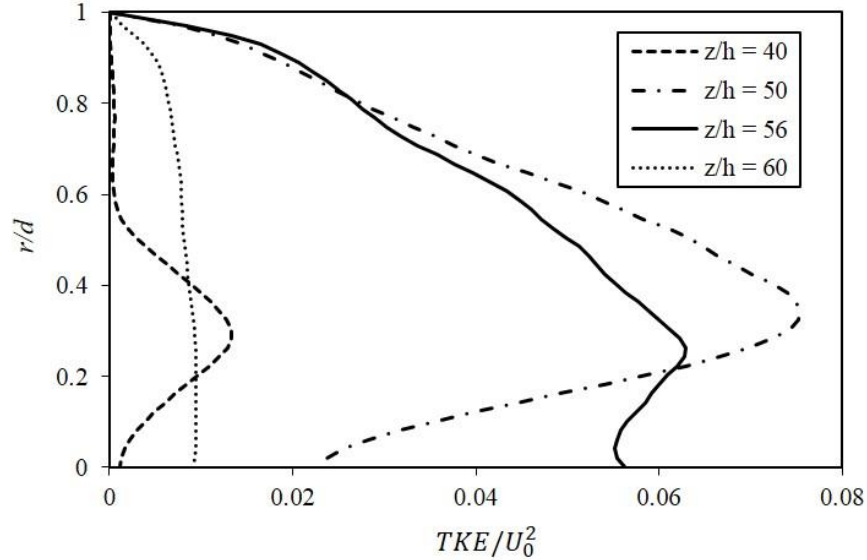


Figure 6-10: Comparison of the turbulence kinetic energy distributions at different positions at $Re = 2500$

6.5 Visualization of transition and localized turbulence

Figure 6-11 shows the non-dimensional vorticity magnitude contours at $Re = 2500$ for different locations near the time-averaged reattachment location ($L_r/h = 56.22$). The non-dimensional vorticity vector is defined as $\Omega_i = \omega_i d/U_0$. The near-wall vorticity magnitude upstream of the expansion is small and spatially diffused compared to the fluctuating vorticity field in the localized turbulence region, with very low vorticity magnitude observed at $z/h = 38$, increasing to very high vorticity magnitudes between $z/h = 46$ and 60 , and then dissipating to very low values by $z/h = 80$. In this series of figures, the maximum amplitude of the fluctuating vorticity appears to occur at about $z/h = 52$ which is slightly upstream of the reattachment point ($L_r/h = 56.22$). The flow structure approaches a fully developed pipe flow in the redeveloping region ($z/h > 56$), where velocity gradients become lower, damping of vortical structures occurs, and vorticity disappears.

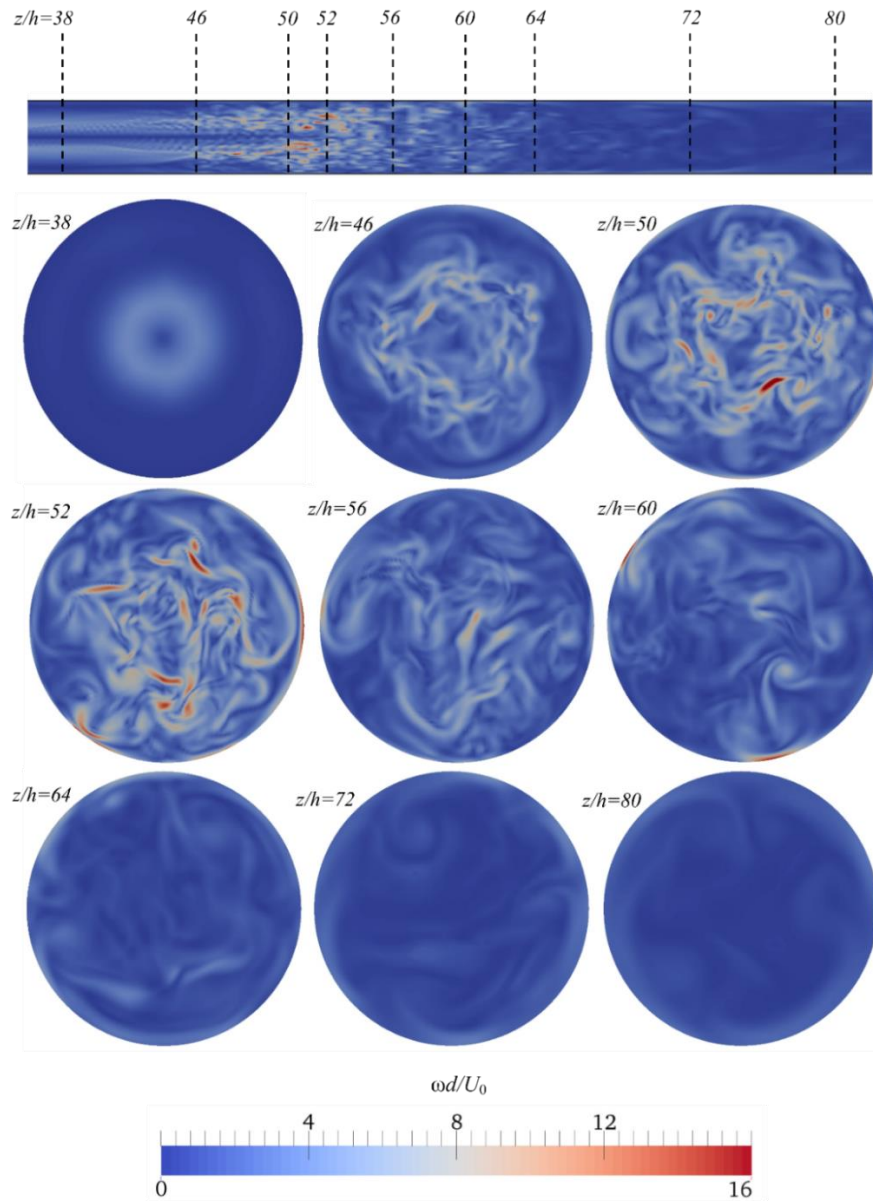


Figure 6-11: Non-dimensional instantaneous vorticity magnitude contours at various positions for $Re = 2500$

Figure 6-12 represents these vortical structures through iso-surface plots of the second-invariant of the velocity gradient tensor (Q) normalized by $(U_0/d)^2$ at a temporal instance that corresponds to Figure 6-11. The iso-surfaces are coloured according to their radial distance from

the centerline to aid in discerning their relative proximity to the pipe wall. The first coherent vortical structures to appear in the flow are streamwise core vortices (SCV) located a small radial distance off of the pipe centerline. Their location near $r/d = 0.1-0.3$ suggests that they are associated with the growing fluctuations in the core region that were discussed in Figure 6-7. Simultaneously, the SCV begins to tilt radially toward the walls. It appears that the radial tilting of the SCV is due to the mutual interaction with the unstable separated shear layer; the azimuthal coherent vortices produced by the inviscid instability of the separated shear layer induce radial strain rates that tilt the SCV. Stretching of the SCV in the axial and radial directions is also visible in Figure 6-12, which together cause the SCV to have the noted oblique orientation. The stretching and tilting appears to accelerate the amplification of disturbances in the shear layer such that the azimuthal vortices shed from the separated shear layer roll-up into smaller-scale, coherent shear-layer vortices (SLV). Figure 6-12 shows that these have the appearance of prograde and retrograde hairpin-like vortices, and are more prominent in the near-wall region. The production of SCV and SLV along with small-scale vortices drives the enlargement of the turbulent region and transition to fully turbulent flow. After this, Figure 6-12 illustrates that the vortical structures become weaker and finally disappear due to relaminarization of the flow. Also, the relaminarization seems to begin with the damping of smaller-scale vortices, and the damping appears to be insensitive to the radial location such that the last coherent structures visible in Figure 6-12 are streamwise vortices at various radial locations.

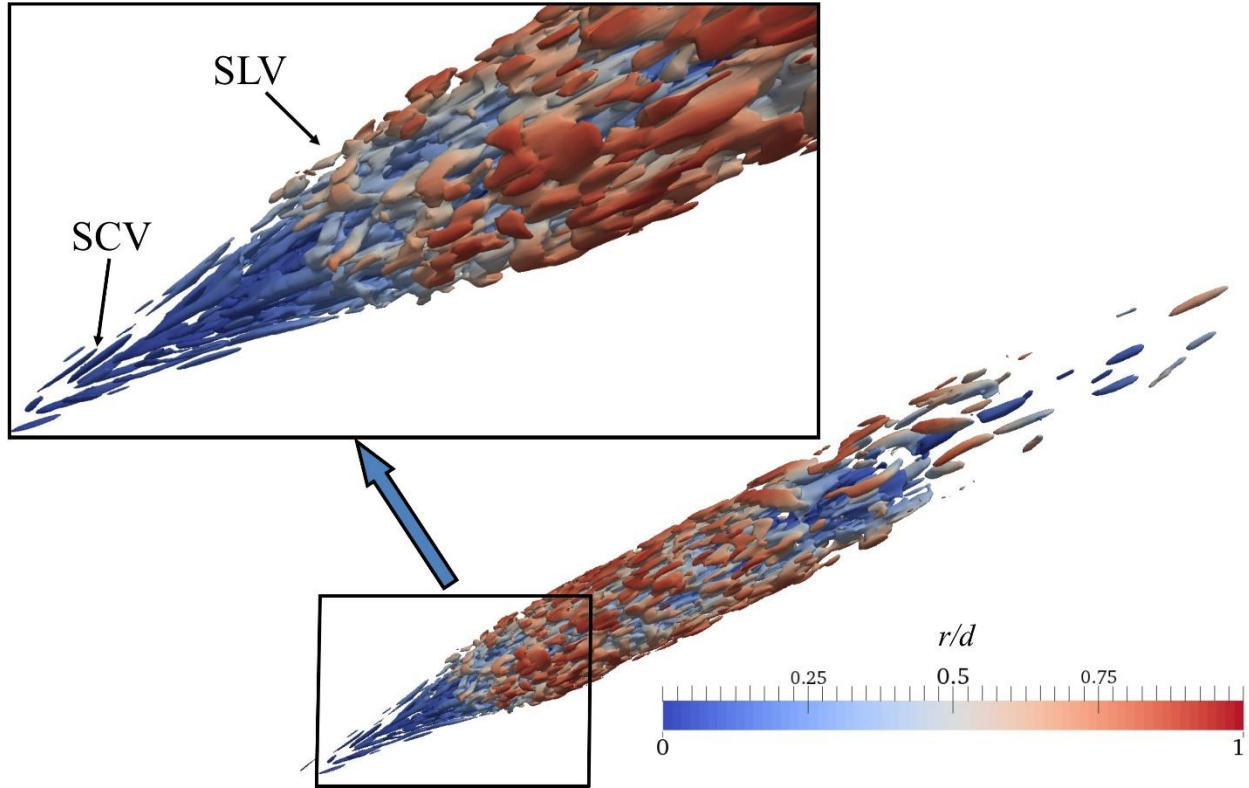


Figure 6-12: Vortical structures observed in the flow through sudden expansion. Iso-surfaces are of $Q(d/U_0)^2 = 10$ and the colouring is according to r/d

A quantitative description of the physical mechanisms contributing to the development of localized turbulence is obtained by examining the vorticity transport equation. The transport equation for instantaneous vorticity in an incompressible fluid is

$$\frac{\partial \vec{\omega}}{\partial t} = -(\vec{u} \cdot \nabla) \vec{\omega} + (\vec{\omega} \cdot \nabla) \vec{u} + \nu \nabla^2 \vec{\omega} . \quad (6.1)$$

The term on the left-hand side of Eq. (6.1) is the unsteady term of $\partial \vec{\omega} / \partial t$ that embodies unsteadiness in the vorticity field [117]. On the right hand side, the first term describes the convective transport of vorticity in the flow, the second term represents the production of vorticity by vortex stretching ($\omega_i \partial u_i / \partial x_i$) and tilting ($\omega_j \partial u_i / \partial x_j, i \neq j$) by the local instantaneous strain rates, and the last term denotes the dissipation rate of vorticity by viscous effects. In the present

work, the vorticity transport equation is analyzed in cylindrical coordinates to illustrate the mechanisms for the growth in vortical fluctuations. The connection between the vorticity growth rates and instability in the flow is obtained by analysing the budgets of Eq. (6.1). Figure 6-13 shows the distribution of the vorticity production due to both vortex stretching (a-c) and tilting (d-f). The budgets are non-dimensionalized by $(U_0/d)^2$. In order to ensure that positive contours in Figure 6-13 imply growth of vorticity and negative contours imply decay of vorticity, the non-dimensional vorticity budgets are multiplied by the sign of the corresponding vorticity component. The resulting contours are plotted in Figure 6-13 at times that correspond to Figure 6-11 and Figure 6-12 for the zoomed view between $z/h = 32$ and 46. It is obvious that the growth of vorticity in the transitional region starts primarily with the radial vorticity component via radial tilting, which is likely the radial tilting of the SCV described above. This is followed by growth of the azimuthal component by azimuthal stretching, which is likely an indication of the SLVs being stretched by the azimuthal strain rates induced by the SCVs.

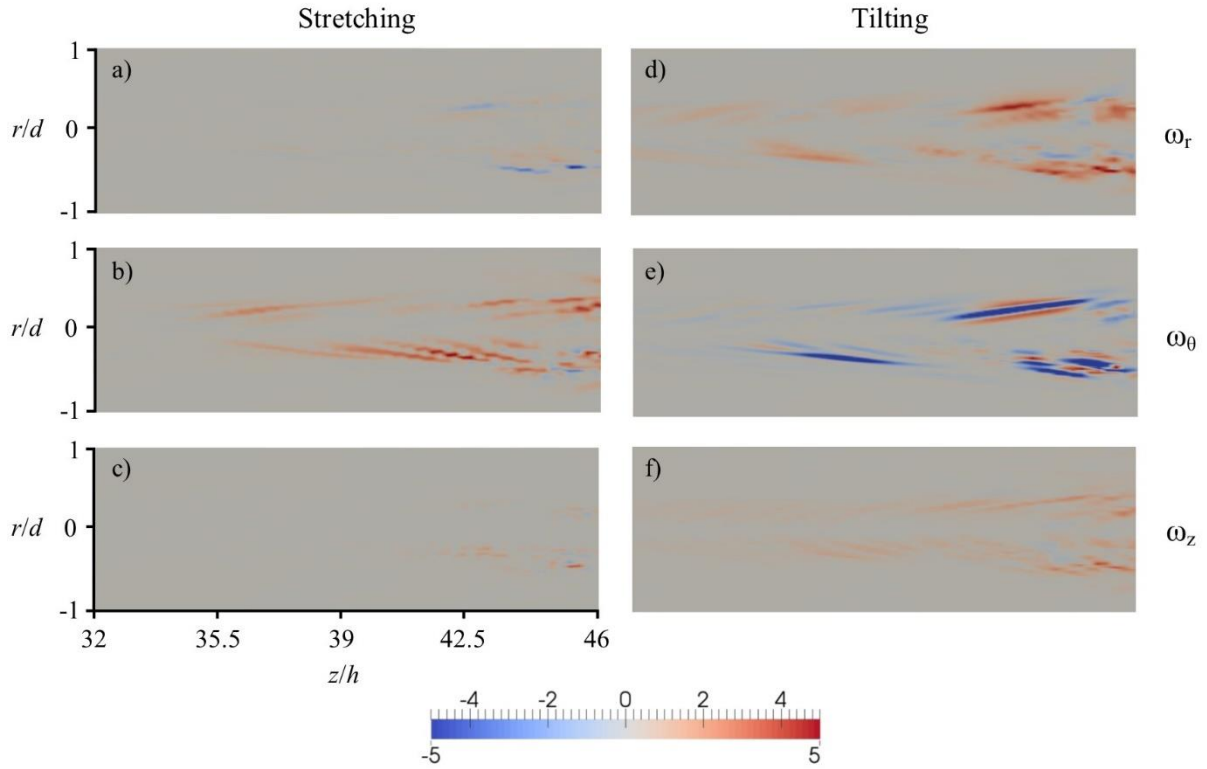


Figure 6-13: Contour levels of the budgets of instantaneous vorticity transport equation between $z/h = 32$ and 46 : (a) ω_r -stretching, (b) ω_θ -stretching, (c) ω_z -stretching, (d) ω_r - tilting, (e) ω_θ - tilting, (f) ω_z - tilting. Contours are normalized by $(U_0/d)^2$ and multiplied by the sign of the associated vorticity component

Chapter 7: Turbulent Flow through Axisymmetric Gradual and Sudden Expansion

In this chapter, the turbulent flow through an axisymmetric gradual and sudden expansion with an expansion ratio of 2 is studied using direct numerical simulations. The main objective of this chapter is to represent the effect of expansion on the flow structure and its laminarization. In the first section, a method is described for generating transient turbulent inflow conditions via a supplementary numerical simulation in an axially-periodic pipe with an annular rib turbulator. This approach is validated by comparing the generated turbulence fields with available numerical and experimental data. In the following sections, the results for turbulent through axisymmetric gradual and sudden expansion are presented.

7.1 Production of Fully-Developed Turbulent Flow

7.1.1 Numerical Approach

7.1.1.1 Computational domain and boundary conditions

Figure 7-1(a) illustrates a schematic of the computational domain. As shown, a rectangular annular rib is added to the inlet pipe to trigger turbulent flow conditions in the DNS. In this study, the mapping plane is located at $7.5d$ (out of a total inlet pipe length of $10d$). The rib has a fixed blockage ratio (BR), defined as the ratio of rib height (h_r) to the pipe diameter, of $BR = 0.06$ and a pitch ratio (PR), defined as the ratio of the rib's streamwise length to height, of $PR = 5.0$. The rib height in wall units is $y^+ = 20$, where inner scaling is based on conditions in the time-averaged

turbulent boundary layer $5d$ axial distance downstream of the annular rib. No-slip conditions are used for all walls. The outflow boundary is set to enforce Neumann conditions in a weak sense for the velocity components in order to minimise the possibility of numerical oscillations and reflections of outgoing waves [53,54]. Inflow conditions are specified by specifying a uniform velocity and employing an internal flow recycling technique that enforces axial periodicity by mapping flow in a time-accurate manner from the mapping plane to the inlet. To maintain the proper flow rate through the domain, the average volumetric flux of the remapped flow is adjusted. This can be specified by two sample steps [100]: first, the velocity of each grid scale at the sampling plane is mapped back to the inlet; second, the corresponding inlet velocity is calculated and scaled to ensure a constant integrated inlet flux is maintained. The location of the mapping plane is placed a sufficient distance downstream of the inlet boundary to provide sufficient development length for the turbulence before it is re-mapped to the inlet [101]. Moreover, it is far enough from the outlet boundary to avoid any upstream influence of outflow boundary effects. The velocity field resulting from the imposed initial condition and periodic recycling yields a Reynolds number based on the pipe diameter and mean inlet velocity of $Re = 5300$, which corresponds to a friction Reynolds number of $Re_\tau = 367$ based on time-averaged conditions $5d$ downstream of the rib.

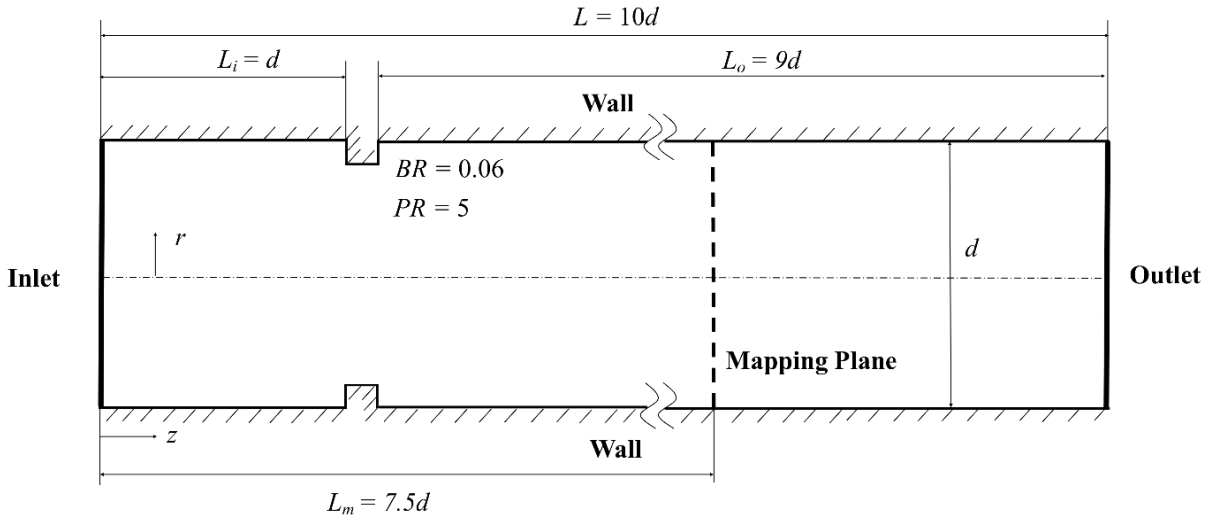


Figure 7-1: Schematic of the computational domain and boundary conditions. The domain is symmetric about the z -axis

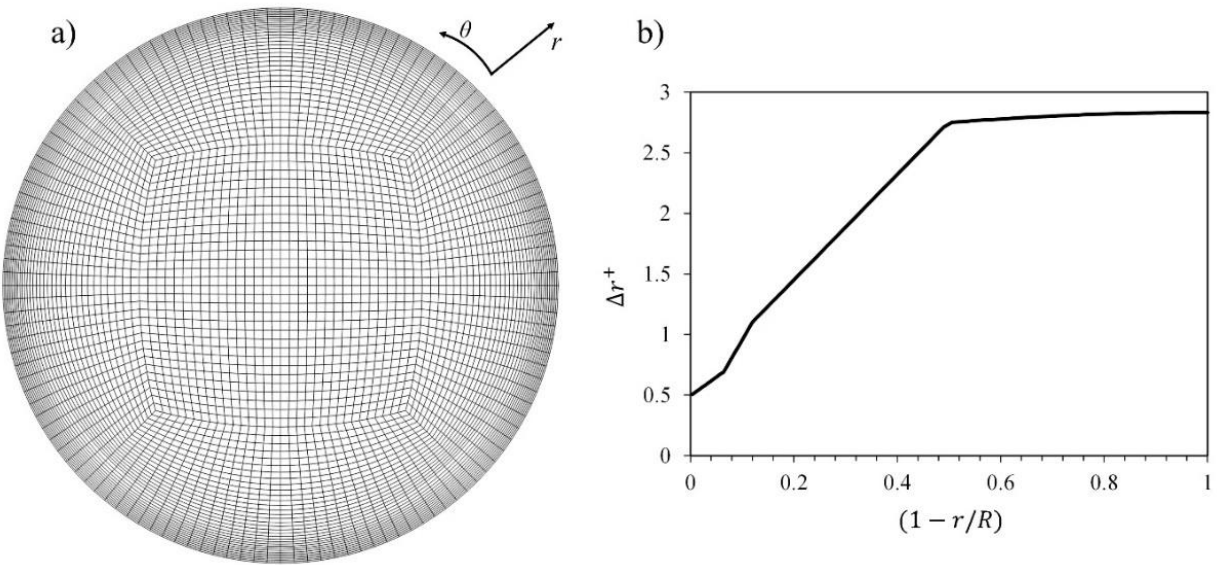


Figure 7-2: a) Cross-sectional slice of the grid, with every second grid node shown, b) radial distribution of the spatial grid spacing

7.1.1.2 Spatial grids

A structured non-uniform grid consisting of orthogonal finite volumes is mapped to the computational domain using a block-structured layout with approximately 17.5 million cells. To ensure the accuracy of the DNS, the spatial grid is refined to the order of the Kolmogorov length scale (η), which for turbulent pipe flow at $Re_d=5300$ is approximately $\eta^+=1.6$ near a no-slip boundary [103]. Figure 7-2 illustrates the resulting grid by plotting an axial slice; for improved visibility, only every second node is plotted in the radial and circumferential directions. The maximum circumferential grid spacing is $(R\Delta\theta)^+ \approx 4.32$ at the wall ($r=R$). The radial grid-spacing distribution is plotted in Figure 2(a), showing that the minimum and maximum wall-normal grid spacing are $\Delta r^+ = 0.5$ at the wall and $\Delta r^+ = 2.9$ at the pipe centerline, respectively. The grid spacing at the wall is approximately 3-4 times smaller than the Kolmogorov length scale at the target Reynolds number. In the axial direction, a uniform grid distribution is used with a constant spacing of $\Delta z^+ = 4.7$, corresponding to approximately three times the Kolmogorov length scale at the present Reynolds number.

7.1.1.3 Solution method

The incompressible Navier-Stokes equations in Cartesian coordinates are discretized based on central differencing and second-order Euler backward differencing for the spatial and temporal derivatives, respectively. Simulations are initialized with a zero relative static pressure and an initial velocity equal to the mean velocity at the inflow boundary. During the first 1000 iterations, the maximum Courant–Friedrichs–Lewy (CFL) number was fixed at 0.05 and the corresponding time step was $\Delta t = 10^{-5}$ s. This small value of CFL improves stability during start-up to transient disturbances that originate in the solution to the pressure Poisson equation owing to mismatch

between the initial velocity and pressure fields [78]. After the first 1000 iterations, the computational time step is increased and the maximum allowed CFL number is less than 0.5 with $\Delta t = 5 \times 10^{-4}$ s. The simulation was partitioned and executed in parallel on 512 processors using a message-passing interface (MPI) parallelization strategy. Approximately 10 flow through times were required for the turbulence to reach a statistically steady state, following which statistical quantities were sampled for an additional 10 flow-through times. To ensure the results are independent of the initial conditions, two different initial conditions were used. The first specified a uniform initial velocity and pressure field and integrated the flow until stationary turbulence statistics were reached. The second was initialized with an instantaneous velocity and pressure field from the first case and integrated for an equivalent flow time. Identical steady-state turbulence statistics were achieved from both cases, suggesting insensitivity to initial conditions.

7.1.2 Comparison of turbulence statistics

The the time-averaged velocity profile normalized by the mean velocity at the inlet is presented in Figure 7-3 at different axial locations. The ribbed turbulator is located at $z/d = 1.0$ downstream of the inlet boundary. As the flow develops downstream of the ribbed turbulator, the centerline velocity reduces in proportion with the growth of axial velocity in the near-wall region. The development region of the turbulent flow continues up to $z/d = 5$, beyond which the mean velocity profile remains unchanged.

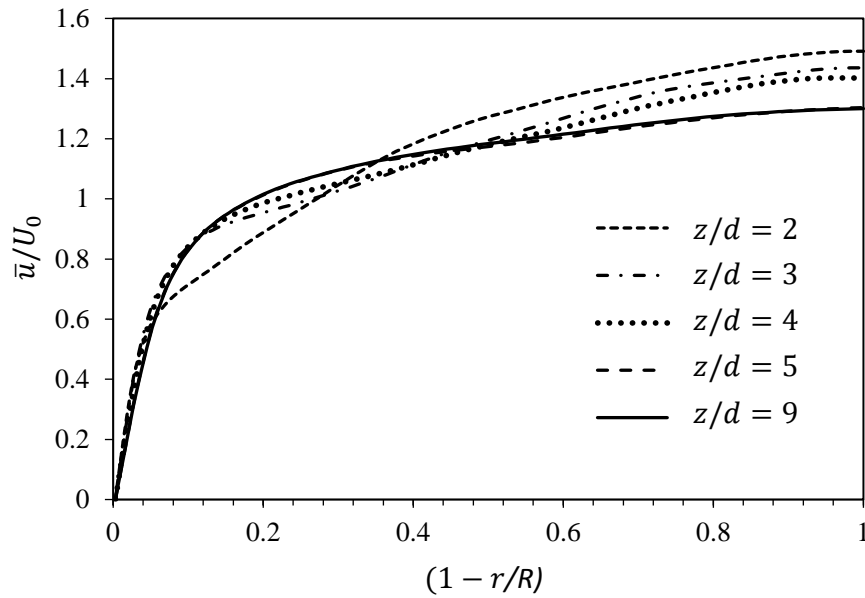


Figure 7-3: Variation of the the time-averaged velocity profile at different axial locations downstream of the circular rib

Figure 7-4 shows the the time-averaged velocity profile normalized by the centerline in comparison with the numerical and experimental results of Eggels et al. [103] at $z/d = 5$. The present study's result is hardly visible because it completely collapses onto the DNS profile from Eggels et al. [103]. Figure 7-5 plots the normalized time-averaged velocity profile according to inner variables at $z/d = 9$ against the published pipe flow DNS results of Wu and Moin [78] and Eggels et al. [103] and LDV experimental measurements of Toonder and Nieuwstadt [118] and Eggels et al. [103], which shows that the computed time-averaged velocity achieves very good agreement with the published results.

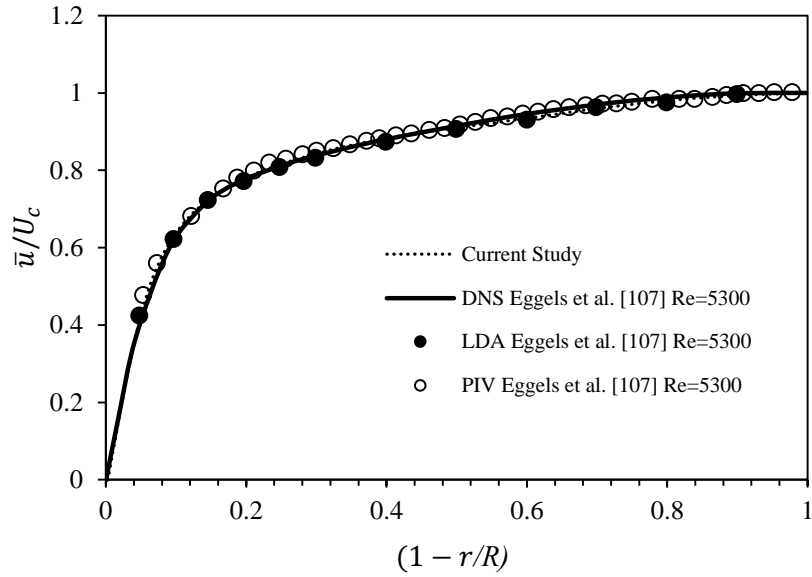


Figure 7-4: Comparison of axial the time-averaged velocity normalized by the centerline velocity U_c as function of the distance from the centerline with published DNS and experimental values

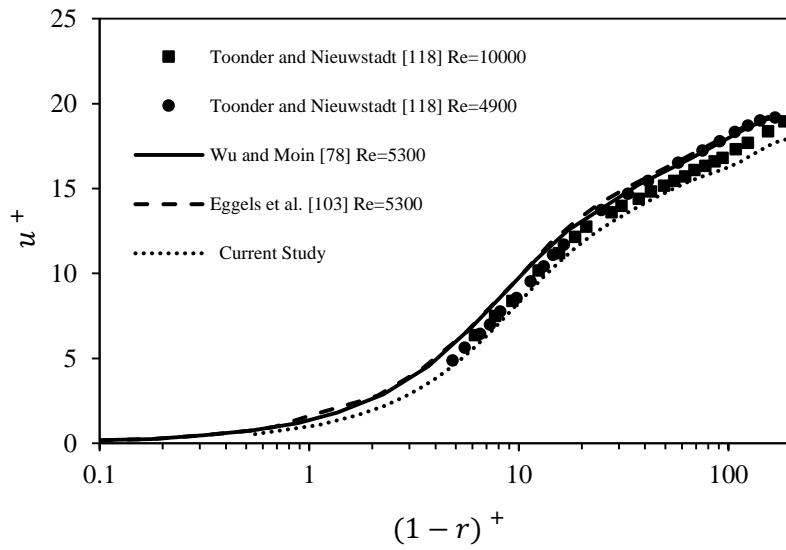


Figure 7-5: Comparison of the the time-averaged velocity profile at $z/d = 9$ with published DNS and experimental values

Figure 7-6 shows universal outer scaling of the normalized time-averaged velocity defect $[\bar{u}(r = 0) - \bar{u}]/u_\tau$ at $z/d = 9$ achieves excellent agreement with DNS results of Wu and Moin [78] at $Re = 5300$ and laser-Doppler measurements (LDA) of Durst et al. [106] at $Re = 7442$. Shear velocity (u_τ) is defined as $u_\tau = \sqrt{\tau_w/\rho}$ where τ_w is shear stress at the boundary. At higher Reynolds numbers, Zagarola and Smits [119] report poor collapse of mean velocity defect profiles for Reynolds numbers of $Re_d = 31,000-35,000$. Wu and Moin [78] claimed that a universal velocity defect law does not hold in the wider range of $5300 < Re_d < 44,000$. Figure 7-7 illustrates turbulence intensities normalized by u_τ in the near-wall region together with the DNS results of Wu and Moin [78] at $Re = 5300$. In addition, the experimental data of Toonder and Nieuwstadt [118] are also plotted in the figure for various Reynolds numbers. The axial turbulence intensity grows sharply in the viscous sublayer and bending appears in the region of $10 < (1 - r)^+ < 14$, forming a knee point. The maximum value of axial turbulence intensity achieves a similar peak as reported by Wu and Moin [78]. The comparison is excellent for $(1 - r)^+ < 90$ but slightly over-predicts the fluctuation amplitudes at radial locations nearer to the centerline. The semi-linearity of axial turbulence intensity in turbulent pipe flow from $(1 - r)^+ = 90$ to the pipe centreline is captured but with a smaller variation in the radial direction compared to Wu and Moin [78]. Further evaluation of the near-wall region is provided in Figure 7-8, which plots u'_{rms}/u^+ in the near wall region. Profiles achieve excellent agreement with experimental data of Toonder and Nieuwstadt [118] and the DNS results of Eggels et al. [103]. These results confirm the effectiveness of the mapping method and annular rib for generating near-wall turbulence conditions.

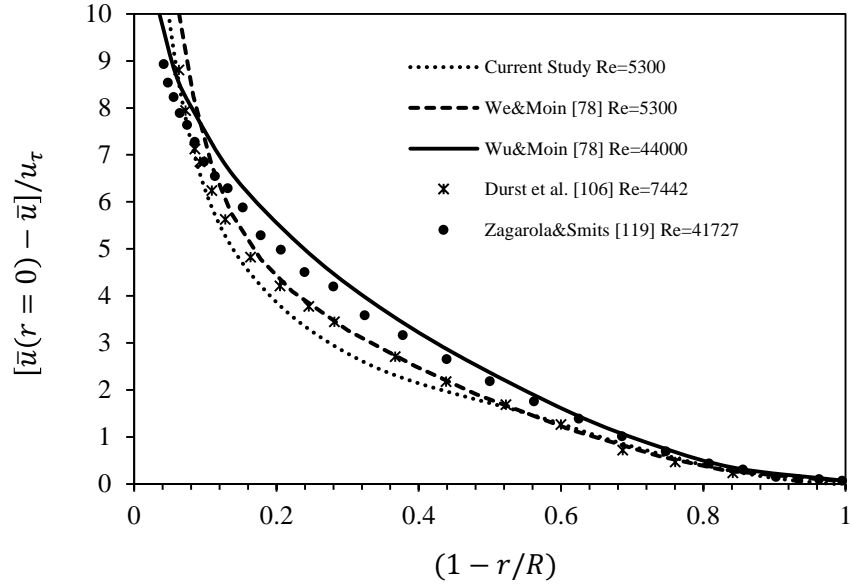


Figure 7-6: Companion DNS results of time-averaged velocity defect $[\bar{u}(r = 0) - \bar{u}]/u_\tau$ as a function of $(1 - r/R)$

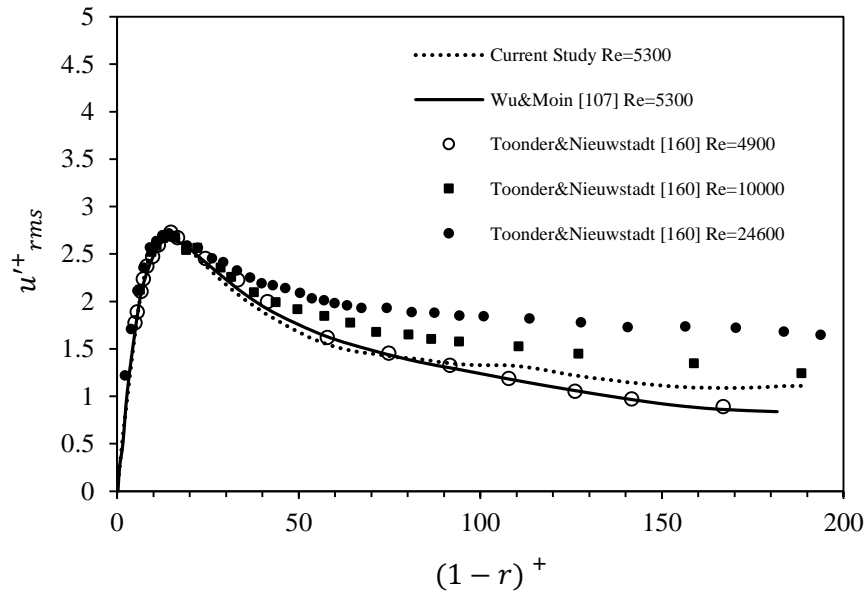


Figure 7-7: Axial turbulence intensity u'^+_{rms} as a function of $(1 - r)^+$ in the near-wall region

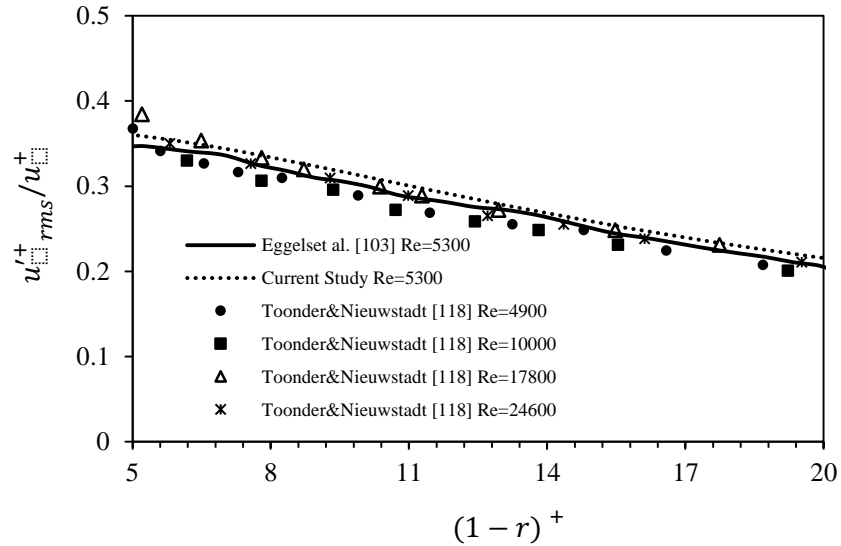


Figure 7-8: Root-mean-square of streamwise velocity fluctuation normalized by the local time-averaged velocity (u'_{rms}/u^+) as a function of $(1-r)^+$

Reynolds shear stress component ($\overline{u'_z u'_r}$) is computed and illustrated in Figure 7-9 at five streamwise locations to show the effect of the circular rib on the fully developed turbulent flow. The circular rib causes recirculation in the flow with primary and secondary recirculation regions. Just after the primary reattachment zone, the near-wall peak appears in the Reynolds shear stress profile with high turbulent intensity magnitude. As the flow develops downstream, the Reynolds shear stress reduces. The development of turbulent flow continues up to $z/d = 7$, beyond which the Reynold shear stress profile remains similar to $z/d = 9$ when the entry length was computed around $z/d = 5$ based on time-averaged velocity distribution.

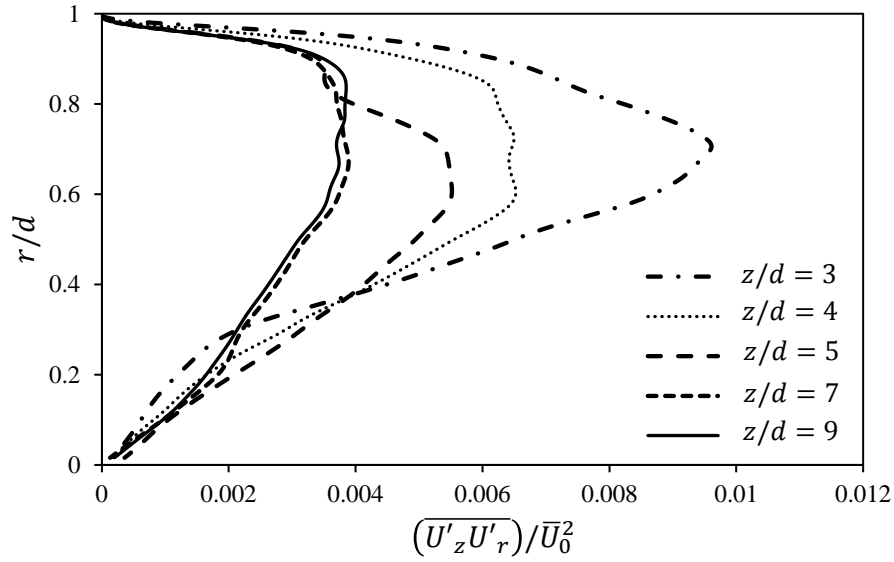


Figure 7-9: Comparison of Reynolds stress profiles at different axial locations downstream of the circular rib

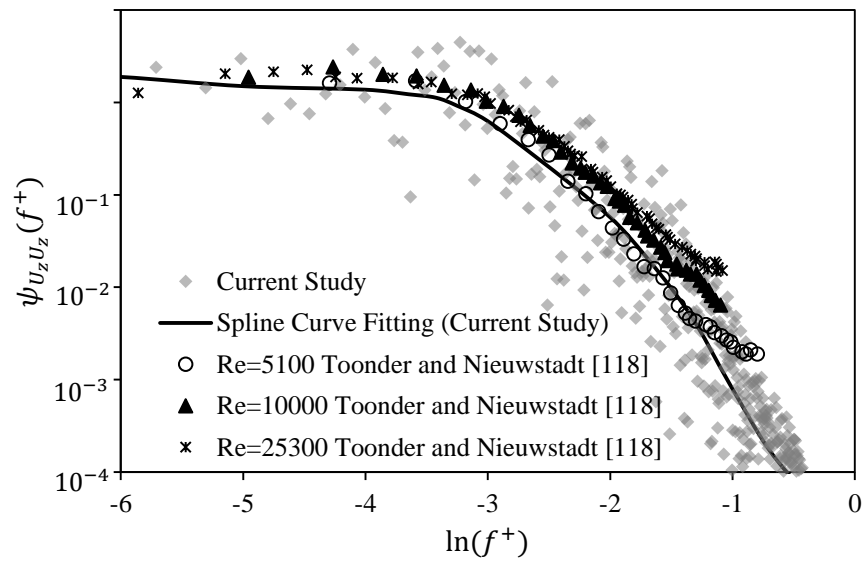


Figure 7-10: The power spectrum of the streamwise velocity fluctuations at $y^+ \approx 12$

The power spectra of the streamwise velocity fluctuations measured at $y^+ \approx 12$ is shown in Figure 7-10. The spectrogram for u , $\psi_{uu}^+ = f/u_\tau^2 \psi_{uu}$ is illustrated as a function of the

logarithm of the dimensionless frequency, $f^+ = f\nu/u_\tau^2$. Here u_τ is shear velocity and ψ_{uu} is the power spectral density of streamwise velocity fluctuations. To assist in identifying trends in the power spectra results, a spline-based least-squares curve is fitted to the spectral data (regression coefficient $R^2 = 0.926$). The increase of the streamwise power spectrum with reduction of frequency is due to collapse of small-scales in the near-wall region while the large-scale contribution is seen to increase. This trend is very consistent with the experimental results for three Reynolds numbers obtained by Toonder and Nieuwstadt [118], again suggestive of the accuracy of the present numerical approach for generating inflow turbulence. It follows from Figure 7-11 that similar behavior as at $y^+ \approx 12$ is observed for the power spectra shown at $y^+ \approx 30$. The streamwise power spectrum is only slightly changed at low frequencies.

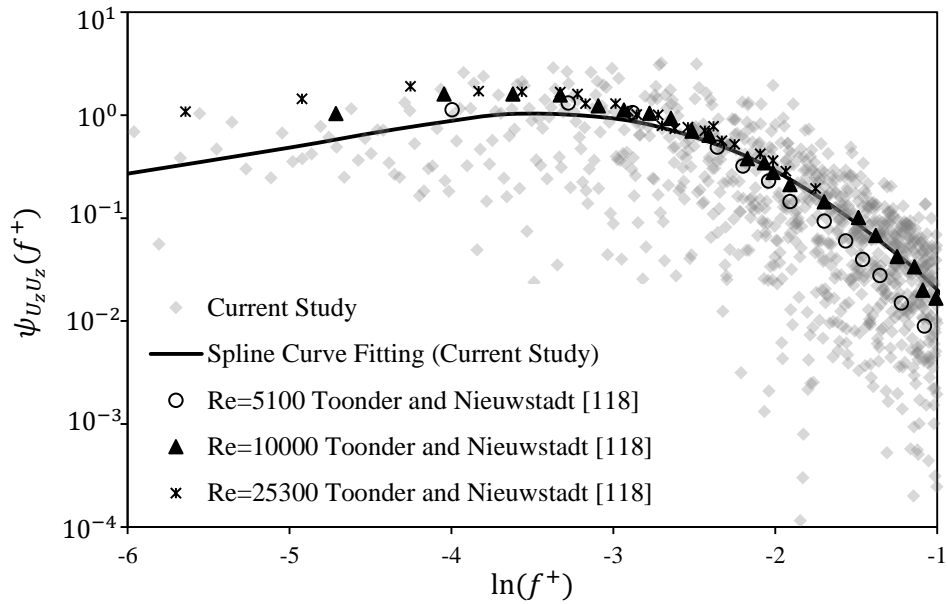


Figure 7-11: The power spectrum of the streamwise velocity fluctuations at $y^+ \approx 30$

7.1.3 Vorticity transport

The physical role of the ribbed turbulator in generating near-wall turbulence is obtained by examining the equation governing the transport of instantaneous vorticity, ω_i :

$$\frac{\partial \omega_i}{\partial t} = -u_j \frac{\partial \omega_i}{\partial x_j} + \omega_j \frac{\partial u_i}{\partial x_j} + \nu \left(\frac{\partial^2 \omega_i}{\partial x_j \partial x_j} \right) \quad (7.1)$$

where u_i denotes the instantaneous velocity vector and Einstein summation is implied over the indexed terms. The terms on the right-hand side of (8.1) respectively represent the convective transport of ω_i , the production of ω_i due to vortex stretching ($i=j$) and tilting ($i \neq j$), and the viscous diffusion of ω_i [120]. Figure 7-12 shows coherent vortical structures developing downstream of the ribbed turbulator by plotting iso-contours of the second invariant of the velocity gradient tensor, Q , defined by Chong et al. [121], colored by the magnitude of the vorticity production term from (8.1). Both quantities are normalized by $(U_0/L)^2$. Large-scale streamwise coherent vortices (SCV) exist near the centerline of the pipe upstream and downstream of the rib. These structures achieve large wavelengths, are primarily streamwise oriented, and are responsible for a significant amount of turbulent fluctuations in the centerline region as they are periodically re-mapped into the inlet boundary. In the near-wall region, high vorticity production coincides with the streamwise-oriented legs of horseshoe-shaped coherent vortices that form downstream of the rib. These horseshoe-shaped structures originate from a circumferentially-contiguous region of vorticity around the rib referred to as the shear layer vortex (SLV). The streamwise reorientation of the circumferential vorticity and its circumferential grouping produces streamwise “fingers”, visible in Figure 7-12, that evolve into horseshoe-shaped vortices as they convect downstream. The contour shading illustrates that the production rate of vorticity is largest at the leading-edge of the circular rib and along the legs of the horseshoe-shaped vortices. The former is likely related

to formation of the SLV, while the latter is due to tilting of the mean circumferential vorticity near the wall. Local strain rates induced by the horseshoe-shaped vortices legs tilt the circumferential near-wall vorticity in the radial and axial directions, contributing to the proliferation of horseshoe-shaped vortices and the production of near-wall turbulent fluctuations.

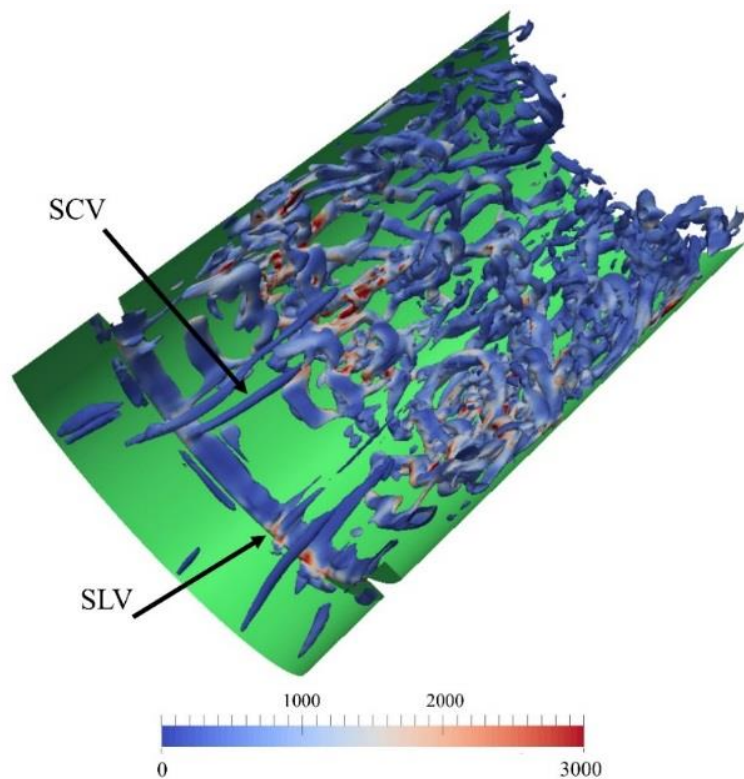


Figure 7-12: Vortical structures observed in the flow through ribbed turbulator. Iso-surfaces are of $Q(U_0^2/d^2) = 200$ and are colored according to the magnitude of the vorticity production rate.

To provide a closer look of the effect of the rib on the growth of vorticity in the flow, Figure 7-13 plots contours of magnitude of the vorticity growth rate (i.e. the norm of the three vorticity growth rate components) in an r - z slice through the centerline of the pipe. The magnitude of the vorticity production term in (8.1) is also plotted in Figure 7-13, broken down

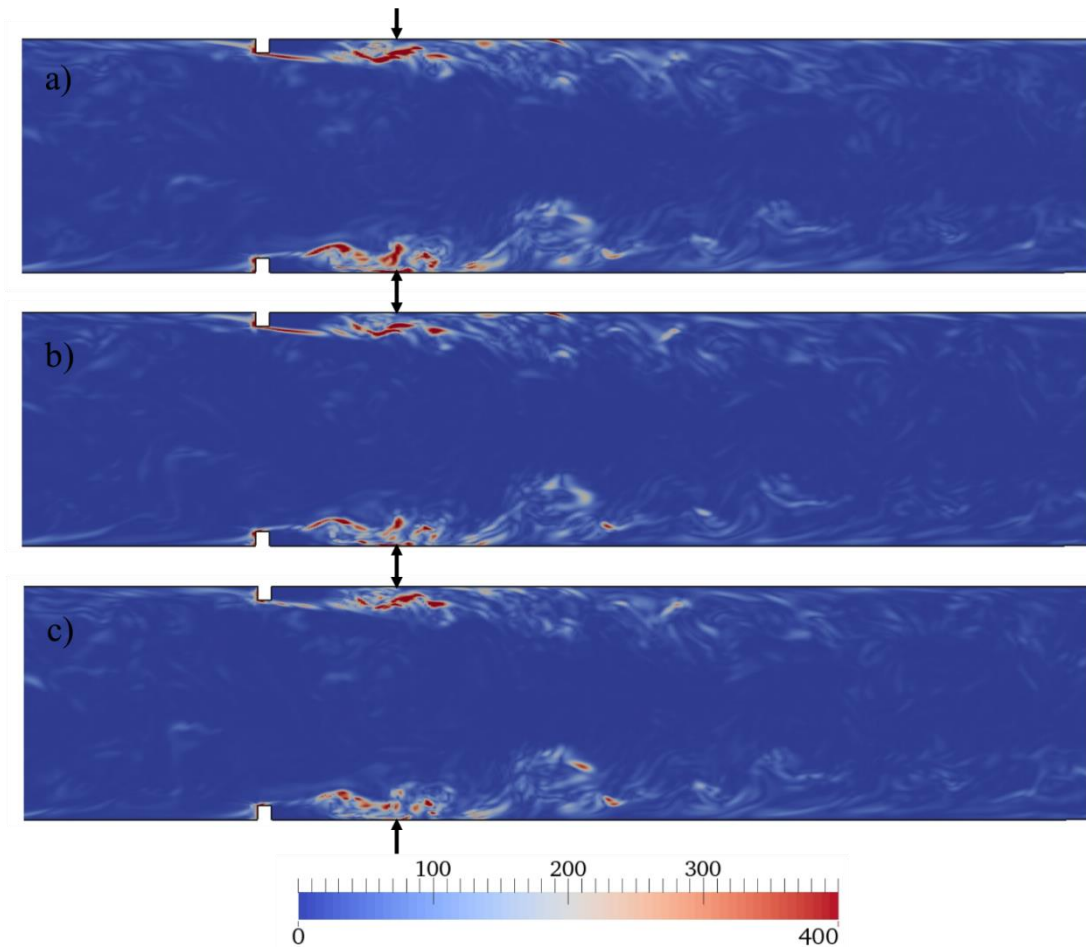


Figure 7-13: Contour levels of the magnitude of instantaneous vorticity transport equation budgets near circular rib: (a) $D\omega/Dt$, (b) ω -stretching, (c) ω -tilting. Contours are normalized by $(U_0/d)^2$. Arrows show the locations for average reattachment length

into the vortex stretching and tilting terms to characterize the difference between the two processes. As expected, the interaction between the inlet-pipe core flow and the separated mixing layer from the circular rib causes a significant growth in the vorticity downstream of the rib. When broken into the stretching and tilting mechanisms, the production budgets indicate that stretching and tilting mechanisms are approximately equivalent in their contributions to the production of vorticity. As shown in Figure 7-13, the production due to stretching is initiated in the back of annular rib while tilting appears downstream of the rib. Tilting and stretching terms represent

similar behavior near the reattachment region. By developing of the turbulent flow far downstream of the reattachment region, the magnitude of vorticity production is reduced and similar production trends become dominant in the near wall region. This shows the appearance of roll-up into three-dimensional vortices and production of smaller scale vortices near the wall due to penetration of the shear layer vortices.

Figure 7-14 plots the distribution of the vector components of the budgets of (7.1) at similar time and location plotted in Figure 7-13. Both tilting and stretching mechanisms work towards maintaining the alignment of turbulence. Although the effect of all components are obvious downstream of the circular rib, the tilting term has a wider influence than stretching in the circular rib region. In addition, there is also high vorticity generation in the reattachment region.

7.2 Turbulent flow in a circular pipe with a sudden expansion

Although numerous of numerical and experimental studies have been conducted on sudden expansion, few experimental studies have offered the details on transitional and lower-Reynolds number turbulence flow. Statistics of turbulent and relaminarization for lower-Reynolds number turbulence flow are required in order to determine the level of instability and mixing in the flow. DNS is performed for turbulent pipe flow with sudden expansion at $Re = 5300$ and $Er = 2$.

A structured, non-uniform grid consisting of orthogonal finite volumes is mapped to the computational domain. To ensure the accuracy of the DNS, the spatial grid is refined to the order of the Kolmogorov length scale (η), which for turbulent pipe flow at $Re = 5300$ is

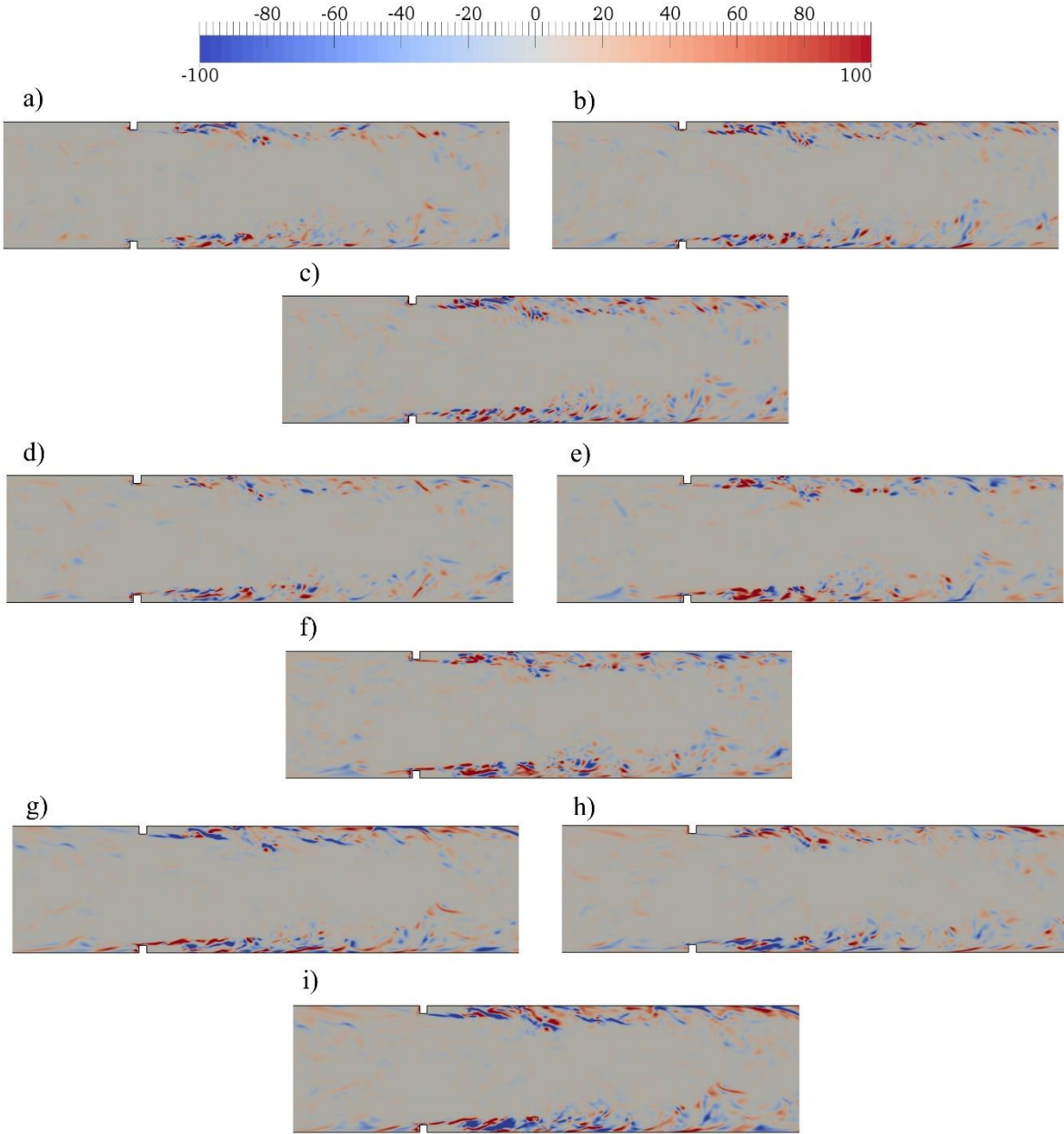


Figure 7-14: Contour levels of the budgets of instantaneous vorticity transport equation near circular rib: (a) ω_z -stretching, (b) ω_z -tilting, (c) $D\omega_z/Dt$, (d) ω_r -stretching, (e) ω_r -tilting, (f) $D\omega_r/Dt$, (g) ω_θ -stretching, (h) ω_θ -tilting, (i) $D\omega_\theta/Dt$. Contours are normalized by $(U_0/d)^2$

estimated to be approximately $\eta^+ \simeq 1.6$ close to a no-slip boundary [103]. The maximum circumferential grid spacing is attained at the wall ($r=R$) with $(R\Delta\theta)^+ \approx 4.32$. The minimum and maximum wall-normal grid spacing before the expansion step are $\Delta r^+ \approx 0.32$ at the outer wall

and $\Delta r^+ \approx 2.83$, at the pipe centerline, respectively. The outer-wall spacing of $\Delta r^+ \approx 0.32$ is approximately 5 times smaller than the Kolmogorov length scale at the target Reynolds number. The wall-normal grid spacing increases into $\Delta r^+ \approx 0.56$ at the outer wall and $\Delta r^+ \approx 4.12$, at the pipe centerline after the expansion step. In the axial direction, a uniform grid distribution is used with the minimum and maximum grid spacing of $\Delta z_{min}^+ \approx 2.89$ (near the step of expansion) and $\Delta z_{max}^+ \approx 29.1$ (near the outlet boundary) where $\Delta z_{min}^+ \approx 2.89$ corresponding to approximately 2 times the Kolmogorov length scale at the present Reynolds number. Due to the abrupt expansion step, the number of grid nodes increases to over 47 million cell which incurs a high computational cost. The length of the inlet and outlet sections are $5d$ and $20d$, respectively. A small imperfection is considered as an annular rib turbulator with fixed blockage ratio (BR) of 0.06 and the pitch ratio of 5. The position of the annular rib turbulator is $1d$ downstream of inlet boundary. The grid convergence study will be performed as shown in Table 7-1 for each of the simulated cases. N_r , N_θ , and N_z refers to number of cells in the radial, circumferential, and streamwise directions, respectively.

Table 7-1: Characteristics of computational grids used

<i>Grid</i>	$(N_r, N_\theta, N_z)_i$	$(N_r, N_\theta, N_z)_o$	
<i>Level</i>	<i>Upstream of expansion</i>	<i>Downstream of expansion</i>	<i>Total cells</i>
S1	(52, 128, 285)	(84, 128, 561)	7,055,616
S2	(78, 192, 380)	(126, 192, 748)	21,166,848
S3	(104, 256, 475)	(168, 256, 935)	47,037,440

Unfortunately, as also shown in Figure 7-15, after a year and half performing simulations for the highest resolution case with 512 processors using a message-passing interface (MPI)

parallelization strategy, major dependence of results to mesh resolution is observed due to unexpected unsteadiness that grows at the expansion step. Even higher grid refinement is apparently required at the expansion step. Therefore, performing a simulation for with a finer grid is desired to achieve grid-independent results in order to characterize the dynamics of fully turbulent flow through a sudden expansion.

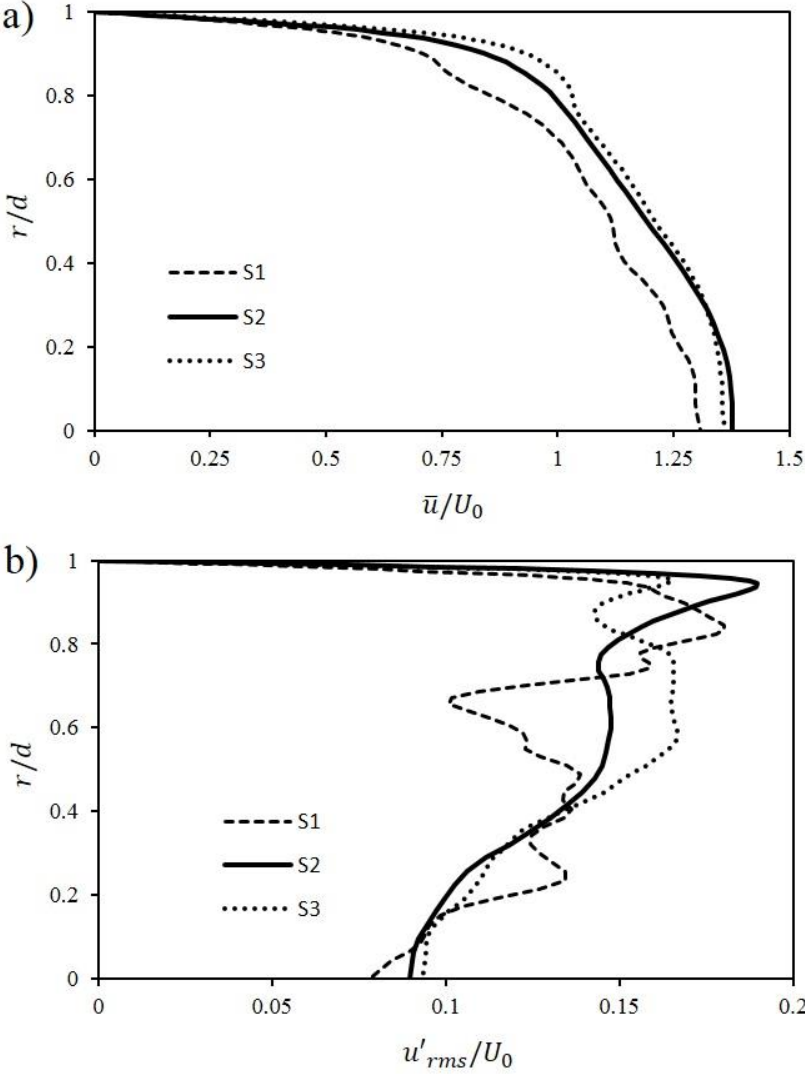


Figure 7-15: Streamwise velocity profile and velocity fluctuation distribution for various mesh resolution

7.3 Turbulent flow in a circular pipe with a gradual expansion

Figure 7-16 illustrates the geometry and computational of the flow through the gradual expansion. As shown, it consists of three main regions: (i) the straight inlet pipe, (ii) the diverging section and (iii) the straight outlet pipe. Simulations are performed for an outlet-to-inlet diameter expansion ratio of $D/d = 2$ and a Reynolds number of 5300 based on the diameter and maximum velocity in the inlet pipe. The streamwise lengths of the domain are $L_i = 10d$, $L_d = 1d$, $L_o = 29d$. The divergence angle is $\alpha = 26.57^\circ$. An annular ribbed turbulator of height $0.06d$ is added to the inlet pipe at $5d$ to trigger turbulent flow conditions in the DNS, and the flow at $7.5d$ is periodically recycled back to the inlet boundary allow fully-developed turbulence to develop in the inlet pipe.

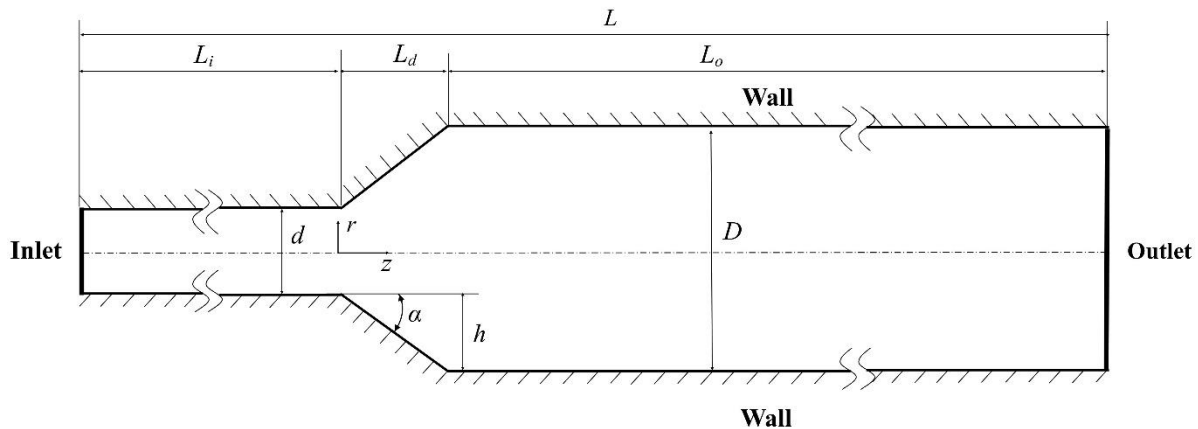


Figure 7-16: Schematic of the computational domain

To keep the desired through-flow mass flux, the average volumetric mass flux of the remapped flow is corrected at each time step [100]. The location of the mapping plane is far enough from the inlet boundary that the developed turbulence contains multiple instances of the largest eddy length scales [101]. As the mapping is conducted over many cycles, it produces fully-developed turbulent flow conditions upstream of the gradual expansion. The resulting turbulence intensity at $2.5d$ upstream of the gradual expansion is approximately $0.055\bar{U}_{max}$. A no-slip

condition is used for radial boundaries, and the outlet boundary condition is zero-gauge static pressure and zero streamwise velocity gradient. Insensitivity of the results to the length of the outlet pipe was examined by repeating the DNS with a domain length of $45d$ with negligible impact on the results.

A structured non-uniform grid consisting of orthogonal finite volumes is mapped to the computational domain illustrated in Figure 7-16. The grid is refined spatially to have at least three cells within the viscous sublayer which are on the order of the Kolmogorov length scale (η). A mesh convergence is studied using four different block-structured grid resolutions with 1.3 million to 30.4 million cells. The detailed information about the grid cells in the inlet, expansion and outlet is illustrated in Table 7-2 for each of the simulated cases; N_r , N_θ , and N_z refers to number of cells in the radial, circumferential, and streamwise directions, respectively.

Table 7-2: Characteristics of computational grids used

<i>Grid</i>	$(N_r, N_\theta, N_z)_i$	$(N_r, N_\theta, N_z)_o$	
<i>Level</i>	<i>Upstream of expansion</i>	<i>Downstream of expansion</i>	<i>Total cells</i>
G1	(33, 84, 195)	(33, 84, 384)	1,323,651
G2	(49, 128, 293)	(49, 128, 576)	4,554,752
G3	(65, 168, 391)	(65, 168, 768)	10,598,364
G4	(98, 256, 488)	(98, 256, 960)	30,358,016

The governing equations are discretized based on central differencing and second-order Euler backward differencing for the spatial and temporal derivatives, respectively. Water at 1 atm and 25°C is the working fluid. The computational time step size in each case varies according to the resolution of the spatial grid. In order to accommodate start-up effects associated with the imposed initial velocity field, the time-step size is set for each simulation to keep the maximum

Courant number less than 0.05 for all cases during the first 1000 iterations [78]. The computational time step is then increased such that the maximum Courant number is less than 0.5. Each simulated test case is initialized with a zero relative static pressure and an initial velocity equal to the mean velocity at the inflow boundary and are then integrated in time for approximately 10 flow through times (defined as $L_i/U_i + L_o/U_o$, where subscripts i and o denote inlet and outlet pipe, respectively) to reach a statistically-steady state, following which approximately four flow through times were collected for analysis. The simulations are partitioned and executed in parallel on 512 processors using a message-passing interface (MPI) parallelization strategy.

7.3.1 Results and discussion

In the present discussion of the results, lengths are normalized by the expansion step height, $h = 0.5d$, and velocities are normalized by the maximum average velocity at the inlet, \bar{U}_{max} . The turbulence in the inlet pipe upstream of the expansion is characterized in chapter 6. The instantaneous and mean velocity field that occurs downstream of the gradual expansion is shown in Figure 7-17(a)-(b). Regions of separated flow exist in the corners near the gradual expansion. As the turbulent core flow in the inlet pipe mixes with the low-momentum flow near the outer wall, transverse momentum transfer causes the centreline velocity to be reduced by approximately half. Figure 7-17(c) shows that this mixing produces an abrupt increase in the local turbulence kinetic energy (k) near the interface of the core and outer-wall flow that spreads outwards towards the centreline and then decreases as the flow laminarizes due to the reduced Reynolds number after the expansion. The associated instantaneous vorticity field in Figure 7-17 (d) shows that an annular turbulent mixing layer is formed at the sudden expansion, and the roll-up instability of this layer assists in the transverse mixing between the core and outer-wall regions. Larger-scale, coherent

vortex structures are initially present in the mixing layer, but gradually lose their coherence as smaller-scale structures are produced more uniformly across the pipe diameter. The streamwise distribution of turbulence kinetic energy along the centreline is plotted in Figure 7-18. The location where the small-scale vortex structures uniformly span across the whole outer pipe diameter corresponds to the point with maximum turbulence kinetic energy. Dissipation of the small-scale structures corresponds with the decreasing turbulence kinetic energy in the laminarizing zone.

The spatial distribution of the turbulent fluctuations is presented in Figure 7-19 through radial profiles of the root-mean-square (rms) of the velocity components at four axial locations. At $z/h = 10$, which corresponds to the maximum turbulence kinetic energy location, the axial fluctuation intensity is approximately 40% larger than the azimuthal and radial components. By $z/h = 22$, which is well into the laminarizing zone, the three components have approximately equal fluctuation intensities, indicating flow disturbances become nearly isotropic during relaminarization. It is also notable that the axial and azimuthal disturbances become nearly spatially homogeneous in the laminarizing zone, while the radial disturbances seem to be damped near the wall.

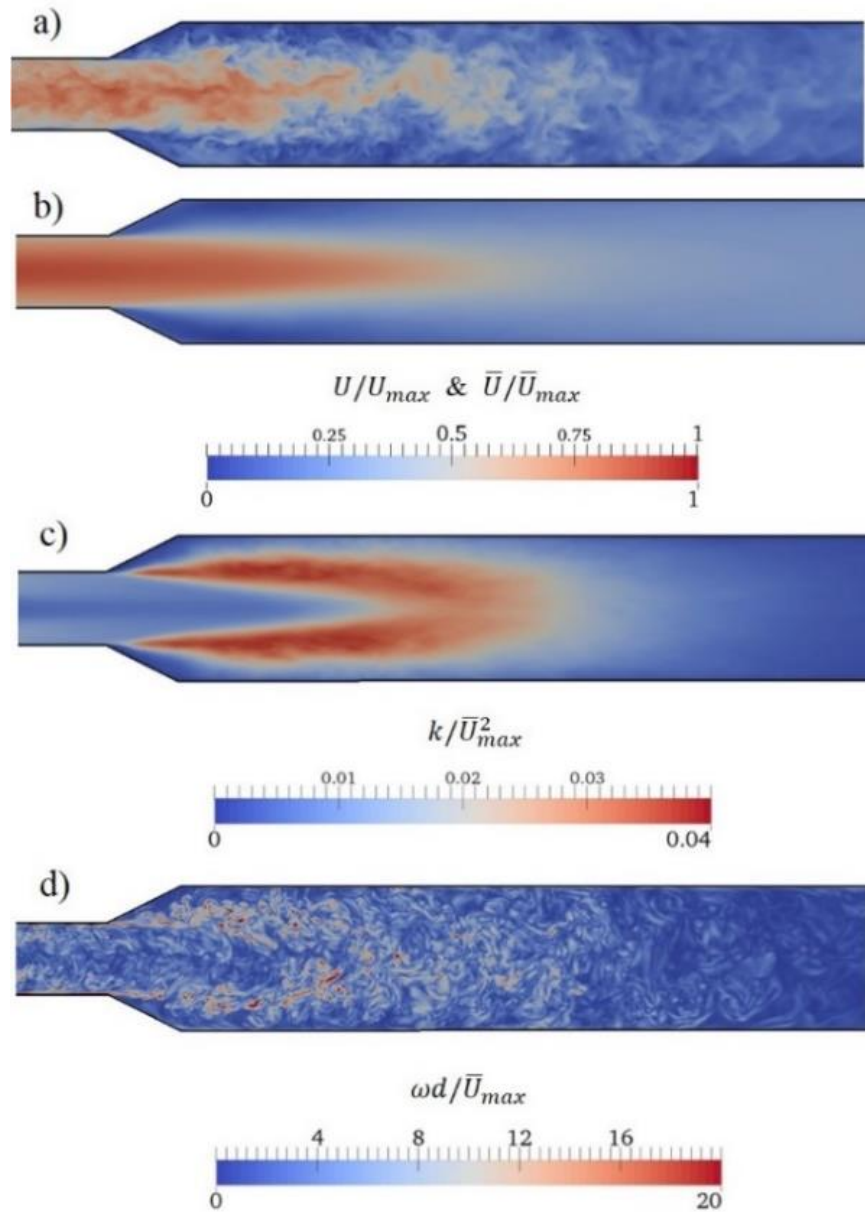


Figure 7-17: Contours in a axial slice near the gradual expansion; a) instantaneous velocity magnitude, b) mean velocity magnitude, c) turbulence kinetic energy, d) instantaneous vorticity magnitude. (Zoomed view)

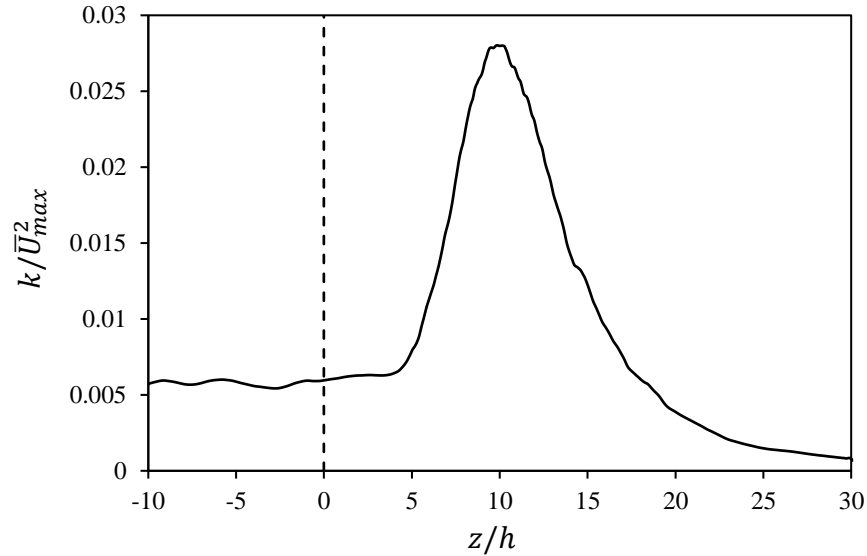


Figure 7-18: Streamwise distribution of turbulence kinetic energy along the pipe centerline ($r = 0$)

The development of the separated mixing layer and the interaction with the turbulent core flow is studied through budgets of the instantaneous vorticity transport equation (7.1). The budgets in an axial slice through the centreline are plotted in Figure 7-20. The vorticity growth rate in Figure 7-20(a) shows that high vorticity growth rate occurs in the turbulent boundary layer of the inlet pipe, which Figure 7-20(b) identifies is mainly attributable to convection of vorticity by the turbulent velocity field. This vorticity is convected into the gradual expansion, where Figure 7-20(c) shows that vorticity production mechanisms are activated and enhance the production of vorticity within and immediately downstream of the sudden expansion. Vorticity production is localized primarily in the region where the inlet-pipe core flow interacts with the separated mixing layer. Viscous diffusion of vorticity is plotted in Figure 7-20(d), which shows that viscous diffusion is largest in the near-wall region in the inlet pipe, where the mean vorticity gradient (i.e. mean shear) is highest. Downstream of the expansion, the mean shear reduces owing

to the reduced Reynolds number. As a result, the viscous diffusion of the vorticity moves away from the wall nearer to the centerline.

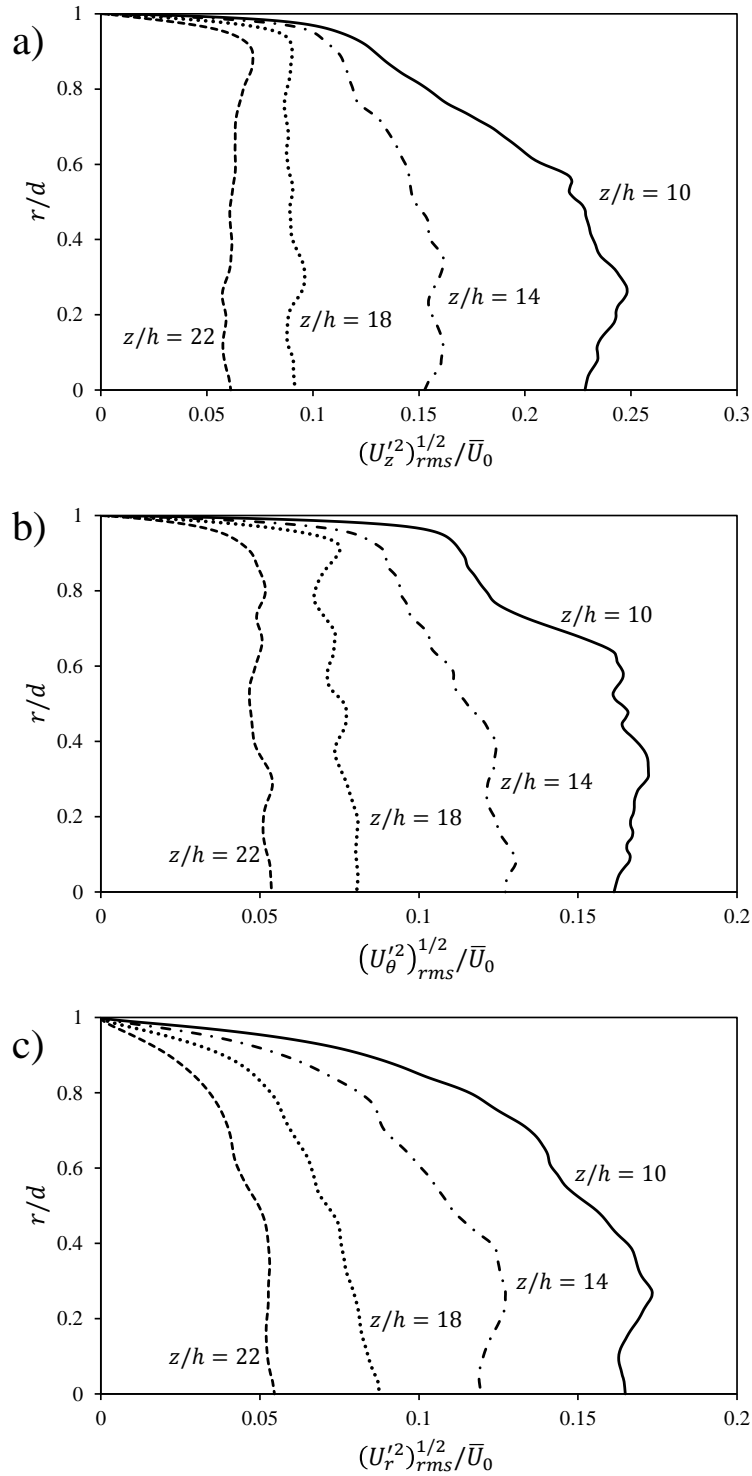


Figure 7-19: Radial profiles of the root-mean-square velocity fluctuations at various axial locations

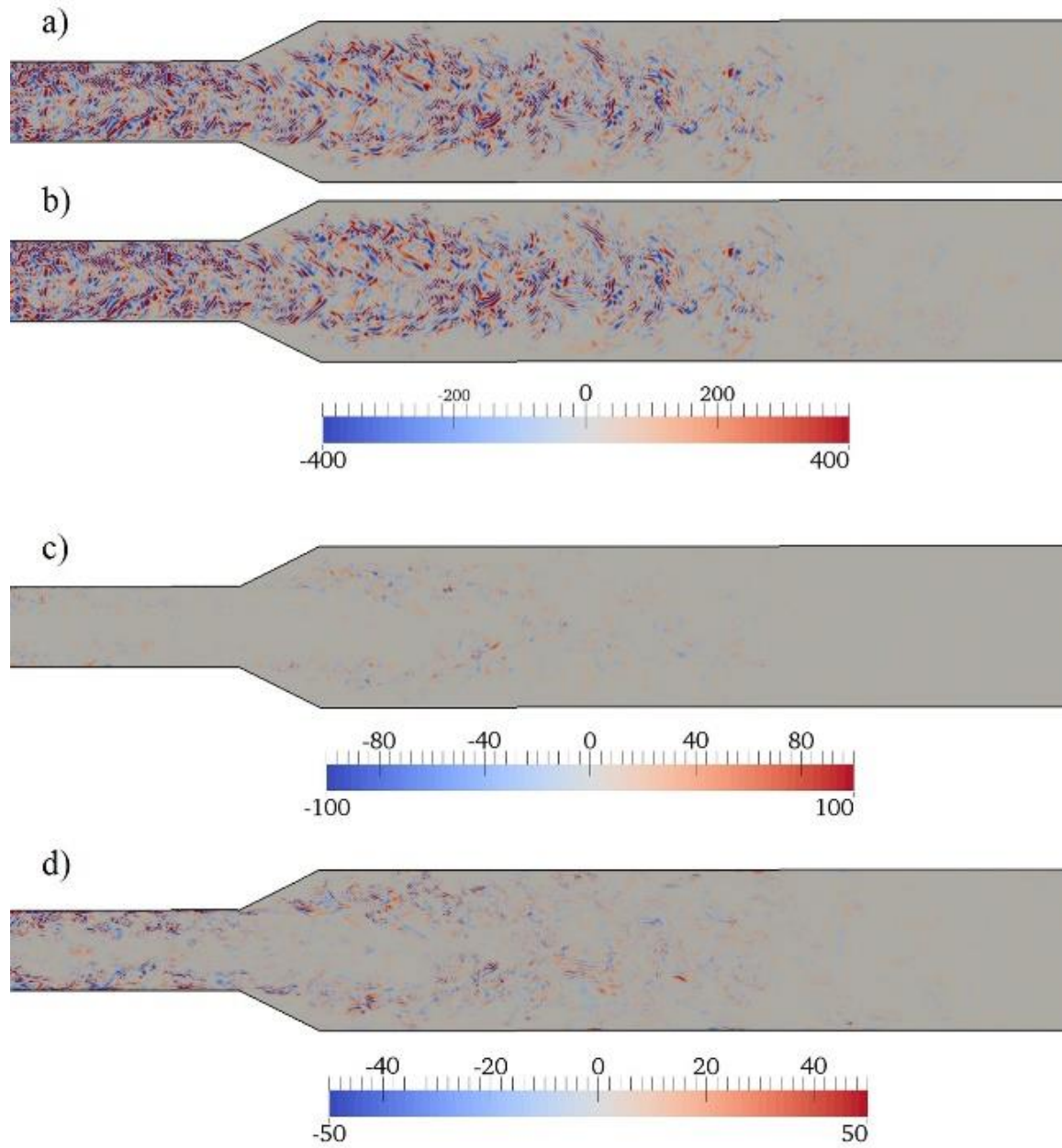


Figure 7-20: Contour levels of the budgets of instantaneous vorticity transport terms: a) vorticity growth rate, b) vorticity convection term, c) vorticity production term, d) vorticity diffusion rate

Figure 7-21 plots the relative magnitude of the vortex stretching and tilting mechanisms of the vorticity production term in Eqn. (7.1). The contours show the magnitude of the relative terms

normalized by $(\bar{U}_{max}/d)^2$. Again, the interaction between the inlet-pipe core flow and the separated mixing layer is noted to significantly increase the overall vorticity production rate, shown in Figure 7-21 (a). When broken into the stretching and tilting mechanisms shown in Figure 7-21 (b) and (c), respectively, the two mechanisms seem to have roughly equivalent contributions to the production of vorticity in the flow.

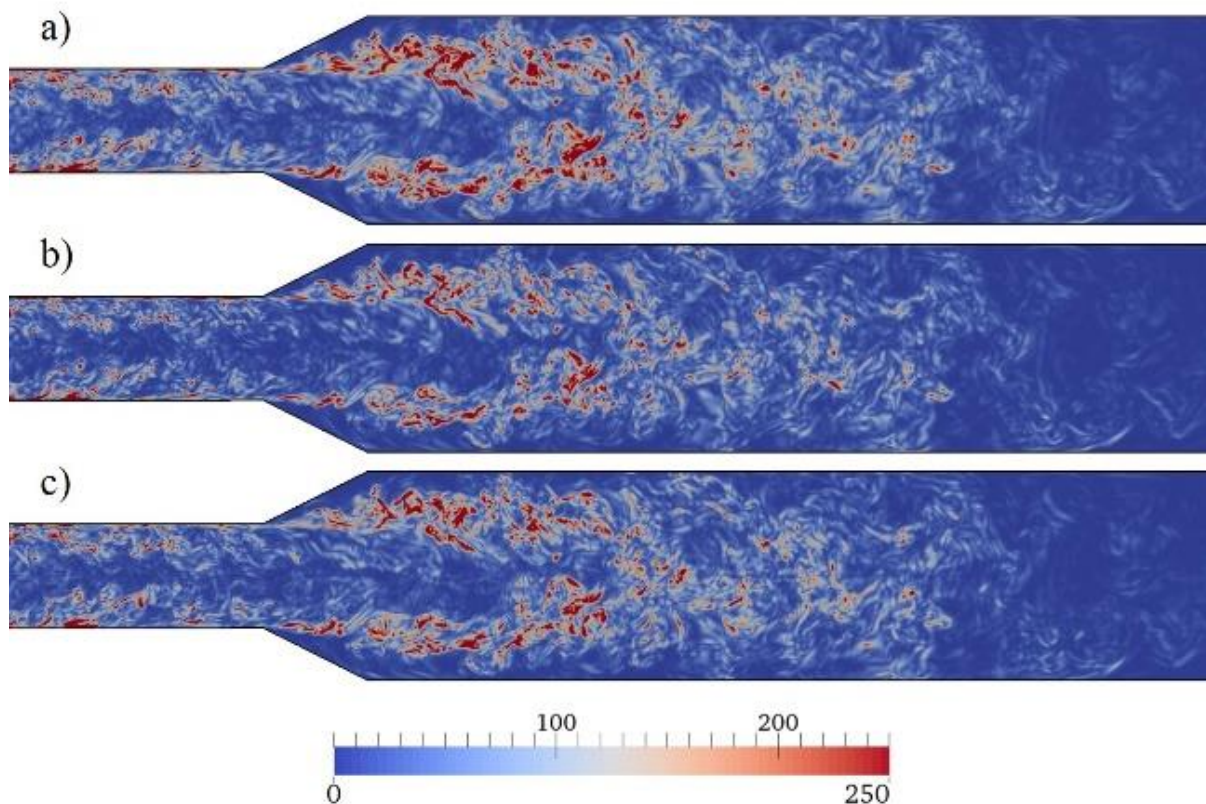


Figure 7-21: Contours illustrating the magnitude of the instantaneous vorticity production rate from Eqn. (8.1): (a) overall production rate, (b) stretching mechanism, (c) tilting mechanism. Contours are normalized by $(\bar{U}_{max}/d)^2$

The spatial evolution of the vorticity production and diffusion budgets are plotted in Figure 7-22 through contours at four axial slices. Vorticity production and diffusion rates are highest near the separated mixing layer. Upstream of $z/h = 2$ (not shown), the production and

dissipation rate contours are relatively contiguous in the azimuthal direction. However, by $z/h = 2$, the budgets are grouped into coherent regions. This indicates that inviscid instability modes have been activated in the mixing layer that produce roll-up into azimuthally-spaced coherent vortical structures. Figure 7-21 also supports such a conclusion; roll-up of the contiguous mixing layer into axially-spaced vertical structures is also visible immediately downstream of the sudden expansion. The azimuthal coherence of vorticity budgets within the mixing layer continues to degrade downstream of $z/h = 2$ as the coherent vortical structures are broken into small-scale structures in the laminarizing zone. The structure of the coherent vortices are visualized in Figure 7-23 by iso-surfaces of the second invariant of the velocity gradient tensor normalized by U_0/d . The appearance of coherent vortical structures depend on the threshold value of iso-surfaces. As observed, the vortical clusters are oriented in both streamwise and spanwise directions, forming prograde and retrograde hairpin vortices. Downstream of the gradual expansion, the vortical clusters are reoriented more in the spanwise direction and gradually disappear due to laminarization of the flow.

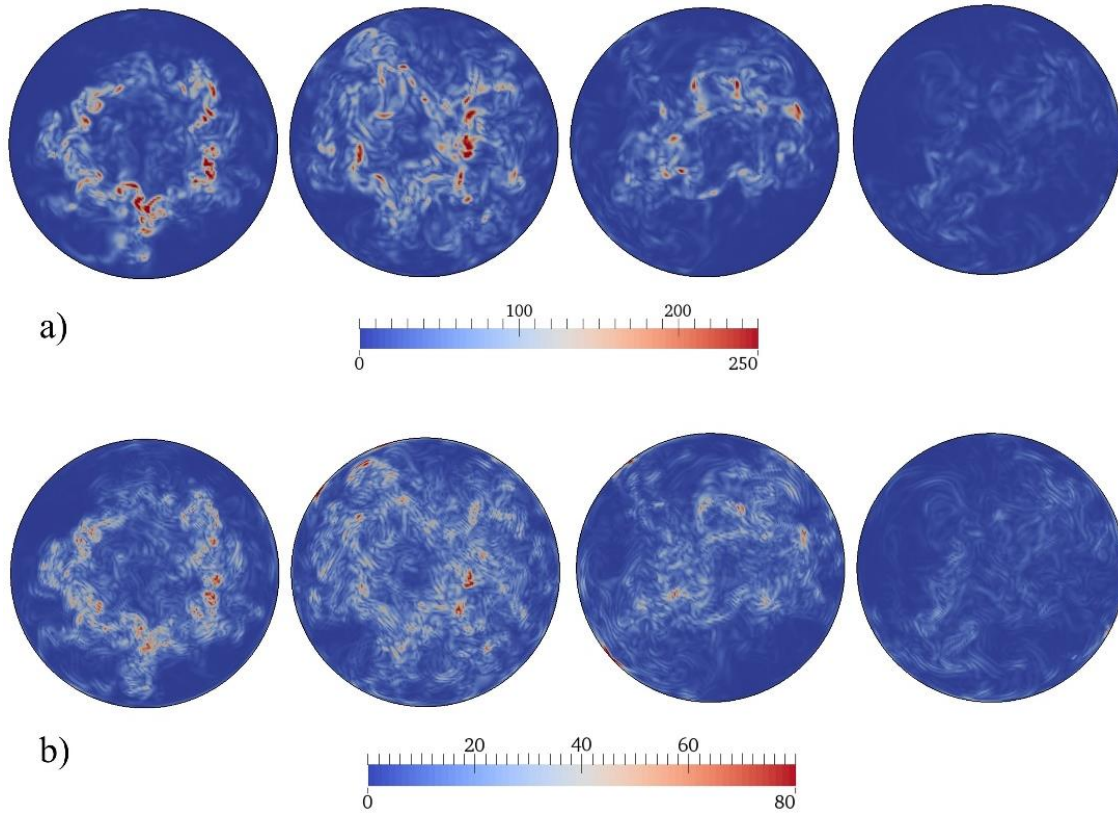


Figure 7-22: Contours of the budgets of instantaneous vorticity (a) production (b) diffusion rate terms. Axial locations are (from left to right) $z/h = 2, 6, 10, 14$



Figure 7-23: Instantaneous vortical structures visualized by iso-surfaces of the second invariant of the velocity gradient tensor, $Qd/U_0 = 4.7$ (Zoomed view)

Chapter 8: Summary, Conclusions, and Future Work

8.1 Summary and concluding remarks

8.1.1 Laminar and transitional flow in a planar sudden expansion

A numerical analysis is performed of the laminar and transitional flow in a planar sudden expansion. The effect of Reynolds number and expansion ratio on the reattachment length, the onset of flow bifurcation, and the maximum velocity magnitude in the reversed-flow region are quantified. Correlations proposed for the non-dimensional shear layer reattachment length (L_r/h) and maximum reverse velocity ($U_{r,max}/U_{max}$) as a function of Reynolds number and expansion ratio are in good agreement with the computed data and available results from the literature. While [13] has proposed a similar set of correlations, the present correlations extend to a lower expansion ratio value (1.33 in the present study versus 1.50 for [13]). Moreover, the correlation coefficients in [13] require tuning depending on the expansion ratio, while the present study provides a general correlation that does not require tuning.

The development of symmetry-breaking flow bifurcation is initially investigated by identifying the critical Reynolds number for the onset of flow bifurcation for a range of expansion ratios. The computations indicate that the value of this critical Reynolds number decreases with increasing expansion ratio. A correlation is proposed for the critical Reynolds number at bifurcation-onset in terms of the expansion ratio. Such a correlation has not appeared in the literature to date. Excellent agreement is achieved between the proposed correlation and published studies for a broad range of expansion ratios; agreement is even achieved with published studies that have higher expansion ratios than the range in the present study. Following this, an analysis

of the bifurcation onset mechanism reveals that the spatial location of velocity disturbances in the flow prior to the onset of bifurcation is influenced by the flow Reynolds number. For Reynolds numbers slightly larger than the critical Reynolds number for bifurcation, the development of bifurcation is initiated by streamwise velocity disturbances that develop near the step. For Reynolds numbers much larger than the critical Reynolds number, velocity disturbances develop near the reattachment location in the quasi-steady symmetric condition that exists prior to bifurcation. As the Reynolds number is increased following bifurcation, a secondary recirculation region develops downstream of the primary recirculation region on the wall with the shorter reattachment length. As the Reynolds number is further increased, a successive generation of smaller-scale, steady recirculation zones are noted to occur. The formation of these successive recirculation zones is a precursor to the break-down of the flow into a disordered, unsteady condition. Break-down is thus attributed to inviscid instability of the inflectional velocity profiles that result from the development of these smaller-scale zones. Investigation of the flow past the onset of unsteadiness is not possible in this study because the simulations are two-dimensional. Notwithstanding that limitation, the present study facilitates the optimization of sudden expansions for mixing enhancement in practical applications and validates the numerical approach for follow-on three-dimensional studies.

8.1.2 Planar sudden expansion with transverse jets

Direct numerical simulation is used to study the flow behavior in a sudden expansion with two symmetric jets ejected transversely into a laminar main flow. After the jet cross injections, a Kelvin–Helmholtz-like instability of the upwind and downwind jet shear layers grows and causes a roll-up of the shear layers, leading to the formation of shear-layer vortices. The flow becomes laminar again due to a decrease of Reynolds number and dissipation of small scale structures.

The effect of Reynolds number and expansion ratio on the reattachment length is identified. The reattachment length decreases with increasing expansion ratio at a fixed Reynolds number. Although the reattachment length decreases with respect to Reynolds number for each expansion ratio, it becomes constant at high Er due to transition to local turbulence. As the flow becomes time dependent by increasing the jet-to-main-flow velocity ratios, bifurcation diminishes and finally disappears. The amount of instability and disturbance in the flow is strongly related to the jet to the main flow velocity ratio.

Although the interaction between the main flow and transverse jets causes mixing, the effectiveness depends on transverse jet injection angles. The results for distribution of the turbulent fluctuations far downstream of the expansion indicate that the highest level of axial and vertical fluctuations appear in the completely vertical transverse jet with $\alpha_1 = 90^\circ$ and $\alpha_2 = 90^\circ$ when the transverse jets have the maximum penetration in the main flow.

8.1.3 Localised turbulence associated with flow through an axisymmetric expansion

Direct numerical simulation (DNS) is used to identify the laminar and transitional characteristics in a flow through an axisymmetric sudden expansion. The 2D and 3D simulation results are compared in order to identify the limitations of two-dimensional simulations. The 2D simulation is seen to be only valid for very low Reynolds number where there is no bifurcation. The measured reattachment length is in excellent agreement with previous experimental observations and numerical predictions up to a maximum where the laminar regime governs. After this peak, the flow becomes unsteady and the reattachment lengths decrease with increasing Reynolds number. By instability development and transition to turbulence, the reattachment

location travels back toward the step. However, the amount of reduction for computed results is less than observed in available experimental data.

For Reynolds numbers higher than critical, the flow structures have been classified into four different flow regions. Fully developed laminar flow imposed in the inlet remained up to the expansion step. After the expansion step and far upstream of the reattachment, flow is steady with no sign of high velocity fluctuations or vorticity. The maximum Reynolds shear stress and fluctuations are observed on the region close to reattachment location. In the redeveloping region, vortical structures become weak and diminish. The flow becomes highly anisotropic slightly before reattachment where high levels of velocity fluctuations exist. It becomes isotropic after shear layer reattachment due to dissipation of vortical fluctuations and viscous diffusion.

Analysing the instantaneous vorticity transport equation reveals that the instability growing from the core region causes growth of vertical structures resulting in shear layer instability and reduction of the reattachment length. Sweep motions produced by the coherent streamwise structures generate strong instantaneous strain rates. The strain rates drive vortex stretching and tilting processes that result in the production of small-scale vortices which grow in the localized turbulence region.

Small imperfections lead to smaller reattachment lengths due to growth of shear layer instability in the flow. It is not easy to obtain a quantitative connection between numerical predictions and experimental data since the source of imperfections in physical systems is unknown and not limited. On the other hand, the structure of shear layer instability and localised turbulence in flow with laminar inlet profile forming time dependent flow and transition to turbulence agrees with experiments.

8.1.4 Turbulent flow in a pipe with a rib-roughened wall

Assigning appropriate representation of turbulence at the inlet boundary is essential for the accuracy of pipe flow DNS. The performance of different turbulent inflow conditions is studied by DNS. Results reveals the ineffectiveness of periodic boundaries with and without artificial disturbances to resolve transitional and turbulent pipe flow at moderately low Reynolds numbers. Instead, a streamwise mapping condition in concert with an annular ribbed turbulator is used to generate the transient inflow condition needed to resolve the growth of turbulence in the pipe flow. Comparison with published numerical and experimental data shows that the flow at least five diameters downstream of the turbulator achieves remarkable quantitative agreement with smooth-walled pipe turbulence at $Re = 5300$. In particular, the mean velocity profile achieves excellent agreement with Wu and Moin [78] for both the inner and outer regions of the boundary layer. Streamwise fluctuation amplitudes in the inner region are well predicted, and the power spectra within the inner region matches the experiments of Toonder and Nieuwstadt [118] at $Re = 5100$. Although the streamwise velocity fluctuation amplitude is slightly over-predicted near the pipe centreline, the present mapping technique with a ribbed turbulator is deemed to be effective for producing turbulent inflow and initial conditions for pipe flow simulations. Budgets of the vorticity transport equation are analyzed to identify how the rib promotes generation of vortical disturbances. Vortex stretching and tilting processes are initiated at the rib, resulting in the growth of horseshoe-shaped vortices at the obstacle. The production of these vortices continuously drives the enlargement of turbulent spots downstream of the rib that maintain fully developed turbulent pipe flow.

8.1.5 Statistics of turbulent flow in a circular pipe with a gradual expansion

Turbulent pipe flow at an inlet Reynolds number of 5600 through a 26.57° gradual expansion with an expansion ratio of 2:1 is investigated using DNS. Turbulence in the inlet pipe with an intensity of 5.5% is developed using a ribbed turbulator and a streamwise-periodic remapping procedure. The simulated turbulence in the inlet pipe is validated against numerical and experimental results for pipe flows at similar Reynolds numbers, achieving excellent agreement in terms of the mean velocity profile, fluctuation amplitudes, and spectral content. A turbulent mixing layer is formed immediately downstream of the gradual expansion as the inlet-pipe core flow separates from the outer wall. Transverse momentum exchange between the high-speed turbulent core and the separated outer-wall flow is facilitated by the instability of the mixing layer via inviscid modes. Analysis of the budgets of the instantaneous vorticity transport equation illustrates that this instability results in the roll-up of the mixing layer into hairpin-shaped coherent vortical structures. The orientation of the hairpin vortices are both prograde (legs pointing upstream) and retrograde (legs pointing downstream). These structures trigger vorticity production and diffusion mechanisms that result in the rapid growth in vorticity inside and immediately downstream of the sudden expansion. As the structures are broken into relatively spatially-uniform, small-scale vortices, the point where the vortex scales are most uniform across the diameter of the pipe corresponds to the location of maximum turbulence kinetic energy and maximum anisotropy of the turbulent fluctuations. Downstream of this location, diffusion of vorticity and turbulence dissipation results in a gradual laminarization of the flow and progression towards more spatially homogeneous and isotropic velocity fluctuations in the laminarized region of the outlet pipe.

8.2 Recommendations for Future Work

8.2.1 Instability and localised turbulence associated with an axisymmetric sudden expansion with transverse jets

The jets ejected transversely into the flow have several industrial applications due to the resulted liquid instability and mixing. Instability and localised turbulence generated by the transverse flow causes high amount of vortical structures and secondary recirculation regions in the flow. As future work, the interaction between a transverse jet and main flow through axisymmetric sudden expansion can be considered. The transverse jets can have many different configurations. They could be ejected by couple of circular jets or a circular slot that intersect with varied angles. Also, the projected jet flow directions on the target plate could be in the opposite direction or the same directions. The effects of transverse to main flow diameter and velocity ratios could be investigated. Each configuration will result in the observations of new, interesting flow fields. As a recommendation for future work, I suggest examining the interaction between the main flow fields and transverse flow formed by circular or slot of vertical or inclined jets with varied configurations. The study can be carried out experimentally and numerically. The author believes that the computed results for planar transverse jets in the present work can be used as a preliminary study to any form of axisymmetric gradual or sudden expansion configuration, only the effect of bifurcation of the flow in planar cases should be considered.

8.2.2 Particle-laden laminar flow through a fluidized bed reactor (FBR) with sudden expansion and transverse jets

The UBC Struvite Crystallizer developed by the University of British Columbia (UBC) Phosphorus Recovery Group attempts to remove struvite from wastewater streams through crystallization in a fluidized bed reactor (FBR) [11]. Forrest et al. [12] employed a sequence of sudden expansions in a FBR to enhance the mixing of reagents in a reactor designed for removing crystalline phosphorus from wastewater streams. In order to optimize the design of the FBR for more efficient recovery at low Reynolds numbers, transverse jets could be added to sequence of sudden expansions for higher local turbulence levels and mixing that promotes the rapid nucleation of struvite. Generally, as observed for the single phase flow, the interaction between main flow and cross flow results in interesting fluid dynamics and high level of turbulent kinetic energy (TKE) after the injections. Thus, one may expect to also observe interesting mixing performances due to the triple interaction of particles, main flow, and cross flow with varied configurations.

8.2.3 Laminarization of the turbulent flow at various expansion configurations

The present work focused on the laminarization of the turbulent flow for only two configurations through sudden and gradual expansions. The influence of expansion ratio and expansion angle between two inlet and outlet pipes are still unclear. Although there is extensive literature available regarding the hydrodynamic mechanisms yielding the production of turbulence kinetic energy at very high Reynolds numbers where turbulent flow exists on both sides of the expansion step, laminarization of the flow downstream of the expansion when flow has turbulent

structure with a low Reynolds number upstream of expansion step has received little attention. More importantly, to the best of the author's knowledge, there is not any study available on the hydrodynamic and thermal performance of the laminarizing flow at various expansion configurations. Moreover, performing simulations for section 8.2 with a finer grid is desired to achieve a grid-independent result in order to characterize the dynamics of fully-turbulent flow through a sudden expansion and compare the obtained results with gradual expansion. Performing these simulations might require computational resources of 1024 CPUs for around 2 years.

Bibliography

- [1] W.A. El-Askary, I.M. Eldesoky, O. Saleh, S.M. El-Behery, A.S. Dawood, Behavior of downward turbulent gas-solid flow through sudden expansion pipe, *Powder Technol.* 291 (2016) 351–365. doi:10.1016/j.powtec.2016.01.002.
- [2] C. Keepaiboon, P. Thiangtham, O. Mahian, A.S. Dalkılıç, S. Wongwises, Pressure drop characteristics of R134a during flow boiling in a single rectangular micro-channel, *Int. Commun. Heat Mass Transf.* 71 (2016) 245–253. doi:10.1016/j.icheatmasstransfer.2015.12.013.
- [3] P.R. Kanna, J. Taler, V. Anbumalar, a. V. Santhosh Kumar, A. Pushparaj, D.S. Christopher, Conjugate Heat Transfer from Sudden Expansion Using Nanofluid, *Numer. Heat Transf. Part A Appl.* 67 (2014) 75–99. doi:10.1080/10407782.2014.915685.
- [4] S.S. Dol, Particle image velocimetry investigation of steady flow over a backward- facing step, *Exp. Fluid Mech.* 114 (2016) 1–7. doi:http://dx.doi.org/10.1051/epjconf/201611402018.
- [5] J.K. Eaton, J.P. Johnston, A review of research on subsonic turbulent flow reattachment, *AIAA J.* 19 (1981) 1093–1100.
- [6] D. Ratha, A. Sarkar, Analysis of flow over backward facing step with transition, *Front. Struct. Civ. Eng.* 9 (2014) 71–81. doi:10.1007/s11709-014-0270-x.
- [7] M. Shusser, A. Ramus, O. Gendelman, Flow in a Curved Pipe With a Sudden Expansion, *J. Fluids Eng.* 138 (2016) 21203.
- [8] D.J. Latornell, a. Pollard, Some observations on the evolution of shear layer instabilities in laminar flow through axisymmetric sudden expansions, *Phys. Fluids.* 29 (1986) 2828–2835. doi:10.1063/1.865481.

- [9] A. Capdevielle, E. Sýkorová, B. Biscans, F. Béline, M.-L. Daumer, Optimization of struvite precipitation in synthetic biologically treated swine wastewater—Determination of the optimal process parameters, *J. Hazard. Mater.* 244 (2013) 357–369.
- [10] J.D. Doyle, S.A. Parsons, Struvite formation, control and recovery, *Water Res.* 36 (2002) 3925–3940.
- [11] M.S. Rahaman, D.S. Mavinic, A. Meikleham, N. Ellis, Modeling phosphorus removal and recovery from anaerobic digester supernatant through struvite crystallization in a fluidized bed reactor, *Water Res.* 51 (2014) 1–10.
- [12] A.L. Forrest, K.P. Fattah, D.S. Mavinic, F.A. Koch, Optimizing struvite production for phosphate recovery in WWTP, *J. Environ. Eng.* 134 (2008) 395–402.
- [13] A. Adnan, D.S. Mavinic, F.A. Koch, Pilot-scale study of phosphorus recovery through struvite crystallization examining the process feasibility, *J. Environ. Eng. Sci.* 2 (2003) 315–324.
- [14] A.G. Capodaglio, P. Hlavínek, M. Raboni, Physico-chemical technologies for nitrogen removal from wastewaters: a review, *Rev. Ambient. Agua.* 10 (2015) 481–498.
- [15] E. Adams, J. Johnston, Effects of the separating shear layer on the reattachment flow structure Part 2: Reattachment length and wall shear stress, *Exp. Fluids.* 6 (1988) 493–499. <http://link.springer.com/article/10.1007/BF00196511> (accessed December 10, 2014).
- [16] E.O. Macagno, T.-K. Hung, Computational and experimental study of a captive annular eddy, *J. Fluid Mech.* 28 (1967) 43–64.
- [17] I.A. Feuerstein, G.K. Pike, G.F. Round, Flow in an abrupt expansion as a model for biological mass transfer experiments, *J. Biomech.* 8 (1975) 41–51.
doi:[http://dx.doi.org/10.1016/0021-9290\(75\)90041-X](http://dx.doi.org/10.1016/0021-9290(75)90041-X).

- [18] K.J. Hammad, M. V. Ötügen, E.B. Arik, A PIV study of the laminar axisymmetric sudden expansion flow, *Exp. Fluids*. 26 (1999) 266–272. doi:10.1007/s003480050288.
- [19] L. Back, E. Roschke, Shear-layer flow regimes and wave instabilities and reattachment lengths downstream of an abrupt circular channel expansion, *J. Appl. Mech.* (1972) 677–681.
<http://appliedmechanics.asmedigitalcollection.asme.org/article.aspx?articleid=1400500>
(accessed December 10, 2014).
- [20] B. Pak, Y.I. Cho, S.U.S. Choi, Separation and reattachment of non-newtonian flows in a sudden expansion pipe fluid, *J. Nonnewton. Fluid Mech.* 37 (1990) 175–199.
- [21] N. Furuichi, Y. Takeda, M. Kumada, Spatial structure of the flow through an axisymmetric sudden expansion, *Exp. Fluids*. 34 (2003) 643–650. doi:10.1007/s00348-003-0612-2.
- [22] D.F. Fletcher, S.J. Maskell, M.A. Patrick, Heat and mass transfer computations for laminar flow in an axisymmetric sudden expansion, *Comput. Fluids*. 13 (1985) 207–221. doi:10.1016/0045-7930(85)90026-X.
- [23] P. Scott, F. Mirza, J. Vlachopoulos, A finite element analysis of laminar flows through planar and axisymmetric abrupt expansions, *Comput. Fluids*. 14 (1986) 423–432.
<http://www.sciencedirect.com/science/article/pii/0045793086900162> (accessed December 10, 2014).
- [24] C.D. Cantwell, D. Barkley, H.M. Blackburn, Transient growth analysis of flow through a sudden expansion in a circular pipe, *Phys. Fluids*. 22 (2010) 034101. doi:10.1063/1.3313931.
- [25] T. Mullin, J.R.T. Seddon, M.D. Mantle, a. J. Sederman, Bifurcation phenomena in the

- flow through a sudden expansion in a circular pipe, *Phys. Fluids*. 21 (2009) 014110.
doi:10.1063/1.3065482.
- [26] E. Sanmiguel-Rojas, C. del Pino, C. Gutiérrez-Montes, Global mode analysis of a pipe flow through a 1:2 axisymmetric sudden expansion, *Phys. Fluids*. 22 (2010) 071702.
doi:10.1063/1.3458889.
- [27] C.-H. Tsai, H.-T. Chen, Y.-N. Wang, C.-H. Lin, L.-M. Fu, Capabilities and limitations of 2-dimensional and 3-dimensional numerical methods in modeling the fluid flow in sudden expansion microchannels, *Microfluid. Nanofluidics*. 3 (2006) 13–18. doi:10.1007/s10404-006-0099-2.
- [28] S. Khodaparast, N. Borhani, J.R. Thome, Sudden expansions in circular microchannels: flow dynamics and pressure drop, *Microfluid. Nanofluidics*. 17 (2014) 561–572.
- [29] A. Iribarne, F. Frantisak, R.L. Hummel, J.W. Smith, An experimental study of instabilities and other flow properties of a laminar pipe jet, *AIChE J.* 18 (1972) 689–698.
- [30] D. Badekas, D. Knight, Eddy correlations for laminar axisymmetric sudden expansion flows, *J. Fluids Eng.* 114 (1992) 119–121.
<http://fluidsengineering.asmedigitalcollection.asme.org/article.aspx?articleid=1427318>
(accessed December 10, 2014).
- [31] İ. Dağtekin, M. Ünsal, Numerical analysis of axisymmetric and planar sudden expansion flows for laminar regime, *Int. J. Numer. Methods Fluids*. 65 (2011) 1133–1144.
doi:10.1002/fld.
- [32] E.O. Macagno, T.-K. Hung, Computational and experimental study of a captive annular eddy, *J. Fluid Mech.* 28 (1967) 43–64. doi:10.1017/S0022112067001892.
- [33] F. Durst, A. Melling, J.H. Whitelaw, Low Reynolds number flow over a plane symmetric

- sudden expansion, *J. Fluid Mech.* 64 (1974) 111–128. doi:10.1017/S0022112074002035.
- [34] W. Cherdron, F. Durst, J.H. Whitelaw, Asymmetric flows and instabilities in symmetric ducts with sudden expansions, *J. Fluid Mech.* 84 (1978) 13–31.
- [35] Y. Ouwa, M. Watanabe, H. Asawo, Flow visualization of a two-dimensional water jet in a rectangular channel, *Jpn. J. Appl. Phys.* 20 (1981) 243–247.
<http://iopscience.iop.org/1347-4065/20/1/243> (accessed December 10, 2014).
- [36] D. Drikakis, Bifurcation phenomena in incompressible sudden expansion flows, *Phys. Fluids.* 9 (1997) 76–87. doi:10.1063/1.869174.
- [37] G. Papadopoulos, V. Otugen, A modified Borda-Carnot relation for the prediction of maximum recovery pressure in planar sudden expansions flows, *Trans. ASME J. Fluids Engrg.* 120 (1998).
- [38] F. Battaglia, G. Papadopoulos, Bifurcation Characteristics of Flows in Rectangular Sudden Expansion Channels, *J. Fluids Eng.* 128 (2006) 671–679. doi:10.1115/1.2201639.
- [39] N. Alleborn, K. Nandakumar, H. Raszillier, F. Durst, Further contributions on the two-dimensional flow in a sudden expansion, *J. Fluid Mech.* 330 (1997) 169–188.
doi:10.1017/S0022112096003382.
- [40] F. Battaglia, S.J. Tavener, A.K. Kulkarni, C.L. Merkle, Bifurcation of low Reynolds number flows in symmetric channels, *AIAA J.* 35 (1997) 99–105.
- [41] F. Durst, J. Pereira, C. Tropea, The plane symmetric sudden-expansion flow at low Reynolds numbers, *J. Fluid Mech.* 248 (1993) 567–581.
http://journals.cambridge.org/abstract_S0022112093000916 (accessed December 10, 2014).
- [42] R.M. Fearn, T. Mullin, K.A. Cliffe, Nonlinear flow phenomena in a symmetric sudden

- expansion, *J. Fluid Mech.* 211 (1990) 595–608.
- [43] T. Hawa, Z. Rusak, The dynamics of a laminar flow in a symmetric channel with a sudden expansion, *J. Fluid Mech.* 436 (2001) 283–320.
- [44] M. Kadja, D. Touzopoulos, Use of a new convection scheme and multigrid acceleration for indepth study of flow bifurcation in channel expansions, *Proceedings, Comput. Asymptot. Methods, BAIL 2004, Int. Conf. Bound. Inter. Layers.* (2004) 1–8.
- [45] H. Kudela, Viscous flow simulation of a two-dimensional channel flow with complex geometry using the grid-particle vortex method, in: *ESAIM Proc.*, EDP Sciences, 1999: pp. 215–224.
- [46] L.-S. Luo, Symmetry breaking of flow in 2D symmetric channels: simulations by lattice-Boltzmann method, *Int. J. Mod. Phys. C.* 8 (1997) 859–867.
- [47] R. Manica, A.L. De Bortoli, Simulation of sudden expansion flows for power-law fluids, *J. Nonnewton. Fluid Mech.* 121 (2004) 35–40.
- [48] M. Shapira, D. Degani, D. Weihs, Stability and existence of multiple solutions for viscous flow in suddenly enlarged channels, *Comput. Fluids.* 18 (1990) 239–258.
- [49] E. Schreck, M. Schäfer, Numerical study of bifurcation in three-dimensional sudden channel expansions, *Comput. Fluids.* 29 (2000) 583–593.
- [50] P. Neofytou, D. Drikakis, Non-Newtonian flow instability in a channel with a sudden expansion, *J. Nonnewton. Fluid Mech.* 111 (2003) 127–150. doi:10.1016/S0377-0257(03)00041-7.
- [51] K. Selvam, J. Peixinho, A.P. Willis, Flow in a Circular Expansion Pipe Flow: Effect of a Vortex Perturbation on Localized Turbulence, *ArXiv Prepr. ArXiv1602.07151.* (2016).
- [52] Y. Duguet, Pipe flow clogged with turbulence, *J. Fluid Mech.* 776 (2015) 1–4.

- doi:10.1017/jfm.2015.285.
- [53] E. Sanmiguel-Rojas, T. Mullin, Finite-amplitude solutions in the flow through a sudden expansion in a circular pipe, *J. Fluid Mech.* 691 (2012) 201–213.
doi:10.1017/jfm.2011.469.
- [54] K. Selvam, J. Peixinho, A.P. Willis, Localised turbulence in a circular pipe flow with gradual expansion, *J. Fluid Mech.* 771 (2015) 1–13. doi:10.1017/jfm.2015.207.
- [55] A. Miranda-Barea, B. Martínez-Arias, L. Parras, M.A. Burgos, C. del Pino, Experimental study of rotating Hagen-Poiseuille flow discharging into a 1: 8 sudden expansion, *Phys. Fluids.* 27 (2015) 34104.
- [56] K.P. Fattah, Pilot scale struvite recovery potential from centrate at Lulu Island Wastewater Treatment Plant, University of British Columbia, 2004.
- [57] J. Peixinho, H. Besnard, Transition to turbulence in slowly divergent pipe flow, *Phys. Fluids.* 25 (2013). doi:10.1063/1.4833436.
- [58] L. Jia, C. Dai, J. Zhang, Z. Shu, On an inclined jet in crossflow at low velocity ratios, 58 (2016) 11–18. doi:10.1016/j.ijheatfluidflow.2015.12.001.
- [59] N. Gui, W. Xu, L. Ge, J. Yan, Effects of Flow Ratio of Transverse Jet on Flow and Heat Transfer : A LBE Study, *Flow, Turbul. Combust.* (2015) 61–77. doi:10.1007/s10494-015-9606-4.
- [60] L. Gevorkyan, T. Shoji, D.R. Getsinger, O.I. Smith, A.R. Karagozian, Transverse jet mixing characteristics, *J. Fluid Mech.* 790 (2016) 237–274. doi:10.1017/jfm.2016.5.
- [61] A.R. Karagozian, The jet in crossflow, *Phys. Fluids.* 26 (2014) 101303.
- [62] L. Thompson, G. Natsui, C. Velez, J. Kapat, S.S. Vasu, Planar Laser-Induced Fluorescence Experiments and Modeling Study of Jets in Crossflow, *J. Fluids Eng.* 138

- (2016) 081201. doi:10.1115/1.4032581.
- [63] F.E. Agbonzikilo, I. Owen, J. Stewart, S.K. Sadasivuni, M. Riley, V. Sanderson, Experimental and Numerical Investigation of Fuel–Air Mixing in a Radial Swirler Slot of a Dry Low Emission Gas Turbine Combustor, *J. Eng. Gas Turbines Power.* 138 (2015) 061502. doi:10.1115/1.4031735.
- [64] W. Huang, M. Li, L. Yan, Mixing augmentation mechanism induced by the pseudo shock wave in transverse gaseous injection flow fields, *Int. J. Hydrogen Energy.* 41 (2016) 10961–10968. doi:10.1016/j.ijhydene.2016.04.078.
- [65] J.R. Brinkerhoff, M.I. Yaras, Direct numerical simulation of a square jet ejected transversely into an accelerating, laminar main flow, *Flow, Turbul. Combust.* 89 (2012) 519–546. doi:10.1007/s10494-012-9406-z.
- [66] T.F. Fric, A. Roshko, Vortical structure in the wake of a transverse jet, *J. Fluid Mech.* 279 (1994) 1–47.
- [67] R.M. Kelso, A.J. Smits, Horseshoe vortex systems resulting from the interaction between a laminar boundary layer and a transverse jet, *Phys. Fluids.* 7 (1995) 153–158.
- [68] S.H. Smith, M.G. Mungal, Mixing, structure and scaling of the jet in crossflow, *J. Fluid Mech.* 357 (1998) 83–122.
- [69] A.R. Karagozian, Transverse jets and their control, *Prog. Energy Combust. Sci.* 36 (2010) 531–553. doi:10.1016/j.peccs.2010.01.001.
- [70] D.R. Getsinger, L. Gevorkyan, O.I. Smith, A.R. Karagozian, Structural and stability characteristics of jets in crossflow, *J. Fluid Mech.* 760 (2014) 342–367.
- [71] K. Mahesh, The Interaction of Jets with Crossflow, *Annu. Rev. Fluid Mech.* 45 (2013) 379–407. doi:10.1146/annurev-fluid-120710-101115.

- [72] W.A. El-Askary, M. El-Mayet, A. Balabel, On the performance of sudden-expansion pipe without/with cross-flow injection: experimental and numerical studies, *Int. J. Numer. Methods Fluids*. 69 (2012) 366–383.
- [73] G. Papadopoulos, A Functional Relationship for Modeling Laminar to Turbulent Flow Transitions, *J. Fluids Eng.* 139 (2017) 91202.
- [74] S. Salehi, M. Raisee, M.J. Cervantes, A. Nourbakhsh, The Effects of Inflow Uncertainties on the Characteristics of Developing Turbulent Flow in Rectangular Pipe and Asymmetric Diffuser, *J. Fluids Eng.* 139 (2017) 41402.
- [75] D.A. Hullender, Alternative Approach for Modeling Transients in Smooth Pipe With Low Turbulent Flow, *J. Fluids Eng.* 138 (2016) 121202.
- [76] T. Mullin, Experimental Studies of Transition to Turbulence in a Pipe, *Annu. Rev. Fluid Mech.* 43 (2011) 1–24. doi:10.1146/annurev-fluid-122109-160652.
- [77] D. Chung, B.J. McKeon, Large-eddy simulation of large-scale structures in long channel flow, *J. Fluid Mech.* 661 (2010) 341–364.
- [78] X. Wu, P. Moin, A direct numerical simulation study on the mean velocity characteristics in turbulent pipe flow, *J. Fluid Mech.* 608 (2008) 81–112.
doi:10.1017/S0022112008002085.
- [79] G.R. Tabor, M.H. Baba-Ahmadi, Inlet conditions for large eddy simulation: A review, *Comput. Fluids*. 39 (2010) 553–567. doi:10.1016/j.compfluid.2009.10.007.
- [80] S.H. Huang, Q.S. Li, J.R. Wu, A general inflow turbulence generator for large eddy simulation, *J. Wind Eng. Ind. Aerodyn.* 98 (2010) 600–617.
doi:10.1016/j.jweia.2010.06.002.
- [81] X. Wu, Inflow Turbulence Generation Methods, *Annu. Rev. Fluid Mech.* 49 (2017) 23–

49. doi:10.1146/annurev-fluid-010816-060322.
- [82] J.-L. Aider, A. Danet, M. Lesieur, Large-eddy simulation applied to study the influence of upstream conditions on the time-dependant and averaged characteristics of a backward-facing step flow, *J. Turbul.* (2007) N51.
- [83] A.W. Abboud, S.T. Smith, Large eddy simulation of a coaxial jet with a synthetic turbulent inlet, *Int. J. Heat Fluid Flow.* 50 (2014) 240–253.
- [84] K. Liu, R.H. Pletcher, Inflow conditions for the large eddy simulation of turbulent boundary layers: a dynamic recycling procedure, *J. Comput. Phys.* 219 (2006) 1–6.
- [85] M. Nishi, B. Ünsal, F. Durst, G. Biswas, Laminar-to-turbulent transition of pipe flows through puffs and slugs, *J. Fluid Mech.* 614 (2008) 425.
doi:10.1017/S0022112008003315.
- [86] X. Wu, P. Moin, R.J. Adrian, J.R. Baltzer, Osborne Reynolds pipe flow: Direct simulation from laminar through gradual transition to fully developed turbulence, *Proc. Natl. Acad. Sci.* 112 (2015) 7920–7924.
- [87] M. Nishi, Laminar to turbulent transition in pipe flow through puffs and slugs, *Der Technischen Fakultät der Friedrich-Alexander-Universität Erlangen-Nürnberg*, 2009.
- [88] X.I.A. Yang, J. Sadique, R. Mittal, C. Meneveau, Exponential roughness layer and analytical model for turbulent boundary layer flow over rectangular-prism roughness elements, *J. Fluid Mech.* 789 (2016) 127–165. doi:10.1017/jfm.2015.687.
- [89] K. Bhaganagar, L. Chau, Characterizing turbulent flow over 3-D idealized and irregular rough surfaces at low Reynolds number, *Appl. Math. Model.* 39 (2015) 6751–6766.
doi:10.1016/j.apm.2015.02.024.
- [90] S. Vijiapurapu, J. Cui, Performance of turbulence models for flows through rough pipes,

- Appl. Math. Model. 34 (2010) 1458–1466. doi:10.1016/j.apm.2009.08.029.
- [91] C. Kang, K.-S. Yang, Characterization of Turbulent Heat Transfer in Ribbed Pipe Flow, *J. Heat Transfer*. 138 (2016) 041901. doi:10.1115/1.4032150.
- [92] G. Chen, Q. Xiong, P.J. Morris, E.G. Paterson, A. Sergeev, Y. Wang, OpenFOAM for computational fluid dynamics, *Not. AMS*. 61 (2014) 354–363.
- [93] H. Jasak, *Error Analysis and Estimation for the Finite Volume Method with Applications to Fluid Flows*, 1996, (1996).
- [94] J.H. Ferziger, M. Perić, *Computational methods for fluid dynamics*, Springer Berlin, 2002.
- [95] S.W. Van Haren, *Testing DNS capability of OpenFOAM and STAR-CCM*, Master Thesis, University of Delft, 2011.
- [96] D. Vigolo, I.M. Griffiths, S. Radl, H. a. Stone, An experimental and theoretical investigation of particle–wall impacts in a T-junction, *J. Fluid Mech.* 727 (2013) 236–255. doi:10.1017/jfm.2013.200.
- [97] C. Habchi, G. Antar, Direct numerical simulation of electromagnetically forced flows using OpenFOAM, *Comput. Fluids*. 116 (2015) 1–9. doi:http://dx.doi.org/10.1016/j.compfluid.2015.04.011.
- [98] A.I. Iatridis, I.E. Sarris, N.S. Vlachos, Transition of an electromagnetically driven liquid metal flow from laminar to turbulent in a toroidal square duct, *EPL (Europhysics Lett.* 101 (2013) 44005.
- [99] J.R. Brinkerhoff, *Numerical Investigations of Instability and Transition in Attached and Separated Shear Layers*, Carleton University, 2014.
- [100] M.H. Baba-Ahmadi, G. Tabor, Inlet conditions for LES using mapping and feedback control, *Comput. Fluids*. 38 (2009) 1299–1311. doi:10.1016/j.compfluid.2009.02.001.

- [101] G.R. Tabor, M.H. Baba-Ahmadi, E. de Villiers, H.G. Weller, Construction of inlet conditions for LES of a turbulent channel flow, *Proc. Eur. Conf. Comput. Fluid Dyn.* (2004) 1–12.
- [102] C. Chin, J.P. Monty, A. Ooi, Reynolds number effects in DNS of pipe flow and comparison with channels and boundary layers, *Int. J. Heat Fluid Flow.* 45 (2014) 33–40. doi:10.1016/j.ijheatfluidflow.2013.11.007.
- [103] J.G.M. Eggels, F. Unger, M.H. Weiss, J. Westerweel, R.J. Adrian, R. Friedrich, F.T.M. Nieuwstadt, Fully developed turbulent pipe flow: a comparison between direct numerical simulation and experiment, *J. Fluid Mech.* 268 (1994) 175. doi:10.1017/S002211209400131X.
- [104] H.C.H. Ng, J.P. Monty, N. Hutchins, M.S. Chong, I. Marusic, Comparison of turbulent channel and pipe flows with varying Reynolds number, *Exp. Fluids.* 51 (2011) 1261–1281. doi:10.1007/s00348-011-1143-x.
- [105] S. Moghtadernejad, M. Tembely, M. Jadidi, N. Esmail, A. Dolatabadi, Shear driven droplet shedding and coalescence on a superhydrophobic surface, *Phys. Fluids.* 27 (2015) 32106.
- [106] F. Durst, J. Jovanovic, J. Sender, LDA measurements in the near-wall region of a turbulent pipe flow, *J. Fluid Mech.* 295 (1995) 305–335.
- [107] N. Moallemi, Numerical and experimental investigation in the instability and breakup of capillary water jets, University of British Columbia, 2014. https://circle.ubc.ca/bitstream/handle/2429/46991/ubc_2014_spring_moallemi_nima.pdf?sequence=1.
- [108] M. Kadja, D. Touzopoulos, G. Bergeles, Numerical investigation of bifurcation

- phenomena occurring in flows through planar sudden expansions, *Acta Mech.* 153 (2002) 47–61.
- [109] A.G. Panaras, D. Drikakis, High-speed unsteady flows around spiked-blunt bodies, *J. Fluid Mech.* 632 (2009) 69. doi:10.1017/S0022112009006235.
- [110] S. Patankar, *Numerical heat transfer and fluid flow*, CRC press, 1980.
- [111] O. Petit, a I. Bosioc, H. Nilsson, S. Muntean, R.F. Susan-Resiga, A swirl generator case study for OpenFOAM, *IOP Conf. Ser. Earth Environ. Sci.* 12 (2010) 012056. doi:10.1088/1755-1315/12/1/012056.
- [112] S. Megerian, J. Davitian, L.S. de B. Alves, A.R. Karagozian, Transverse-jet shear-layer instabilities. Part 1. Experimental studies, *J. Fluid Mech.* 593 (2007) 93–129.
- [113] R. Sau, K. Mahesh, Optimization of pulsed jets in crossflow, *J. Fluid Mech.* 653 (2010) 365.
- [114] L.L. Yuan, R.L. Street, J.H. Ferziger, Large-eddy simulations of a round jet in crossflow, *J. Fluid Mech.* 379 (1999) 71–104.
- [115] W.J. Devenport, E.P. Sutton, An experimental study of two flows through an axisymmetric sudden expansion, *Exp. Fluids.* 14 (1993) 423–432.
- [116] T. Ma, S. Wang, Interior structural bifurcation and separation of 2D incompressible flows, *J. Math. Phys.* 45 (2004) 1762.
- [117] P.K. Kundu, I.M. Cohen, *Fluid mechanics* 4th ed, (2008).
- [118] J.M.J. den Toonder, F.T.M. Nieuwstadt, Reynolds number effects in a turbulent pipe flow for low to moderate Re, *Phys. Fluids.* 9 (1997) 3398. doi:10.1063/1.869451.
- [119] M. V Zagarola, A.E. Perry, A.J. Smits, Log laws or power laws: the scaling in the overlap region, *Phys. Fluids.* 9 (1997) 2094–2100. doi:10.1063/1.869328.

- [120] J.R. Brinkerhoff, M.I. Yaras, Numerical investigation of the generation and growth of coherent flow structures in a triggered turbulent spot, *J. Fluid Mech.* 759 (2014) 257–294. doi:10.1017/jfm.2014.538.
- [121] M.S. Chong, A.E. Perry, B.J. Cantwell, A general classification of three-dimensional flow fields, *Phys. Fluids A Fluid Dyn.* 2 (1990) 765–777.
- [122] M.D.S. Paul W. Cleary, James E. Hilton, Modelling of industrial particle and multiphase flows, *Powder Technol.* 314 (2017) 232–252. doi:10.1016/J.POWTEC.2016.10.072.
- [123] K. Wang, S. Jiang, X. Ma, Z. Wu, W. Zhang, H. Shao, Study of the destruction of ventilation systems in coal mines due to gas explosions, *Powder Technol.* 286 (2015) 401–411. doi:10.1016/j.powtec.2015.08.020.
- [124] M. Bidabadi, N. Moallemi, A. Shabani, M.A. Abdous, Analysis of size distribution and ignition temperature effects on flame speeds in aluminium dust clouds, *Proc. Inst. Mech. Eng. Part G J. Aerosp. Eng.* 224 (2010). doi:10.1243/09544100JAERO587.
- [125] M. Founti, A. Klipfel, Experimental and computational investigations of nearly dense two-phase sudden expansion flows, *Exp. Therm. Fluid Sci.* 17 (1998) 27–36. doi:10.1016/S0894-1777(97)10046-2.
- [126] M.A. Mergheni, J.-C. Sautet, B.H. Ticha, B.S. Nasrallah, Numerical simulation of sudden-expansion particle-laden flows using the Eulerian lagrangian approach, *Therm. Sci.* 16 (2012) 1005–1012.
- [127] W.A. El-Askary, K.A. Ibrahim, S.M. El-Behery, M.H. Hamed, M.S. Al-Agha, Performance of vertical diffusers carrying Gas-solid flow: experimental and numerical studies, *Powder Technol.* 273 (2015) 19–32. doi:10.1016/j.powtec.2014.12.023.
- [128] F. Song, W. Wang, J. Li, A lattice Boltzmann method for particle-fluid two-phase flow,

- Chem. Eng. Sci. 102 (2013) 442–450. doi:10.1016/j.ces.2013.08.037.
- [129] D.R. Kaushal, K. Sato, T. Toyota, K. Funatsu, Y. Tomita, Effect of particle size distribution on pressure drop and concentration profile in pipeline flow of highly concentrated slurry, *Int. J. Multiph. Flow.* 31 (2005) 809–823.
- [130] R.G. Gillies, C.A. Shook, J. Xu, Modelling heterogeneous slurry flows at high velocities, *Can. J. Chem. Eng.* 82 (2004) 1060–1065.
- [131] J. Schaan, R.J. Sumner, R.G. Gillies, C.A. Shook, The effect of particle shape on pipeline friction for Newtonian slurries of fine particles, *Can. J. Chem. Eng.* 78 (2000) 717–725.
- [132] C.A. Shook, A.S. Bartosik, Particle—wall stresses in vertical slurry flows, *Powder Technol.* 81 (1994) 117–124.
- [133] G.V. Messa, S. Malavasi, Numerical investigation of solid-liquid slurry flow through an upward-facing step, *J. Hydrol. Hydromechanics.* 61 (2013) 126–133g.
- [134] J.R. Fessler, J.K. Eaton, Particle response in a planar sudden expansion flow, *Exp. Therm. Fluid Sci.* 15 (1997) 413–423. doi:10.1016/S0894-1777(97)00010-1.
- [135] K.F. Yu, K.S. Lau, C.K. Chan, Numerical simulation of gas-particle flow in a single-side backward-facing step flow, *J. Comput. Appl. Math.* 163 (2004) 319–331.
doi:10.1016/j.cam.2003.08.077.
- [136] T.B. Anderson, R. Jackson, Fluid mechanical description of fluidized beds. Equations of motion, *Ind. Eng. Chem. Fundam.* 6 (1967) 527–539.
- [137] D. Gidaspow, *Multiphase flow and fluidization: continuum and kinetic theory descriptions*, Academic press, 1994.
- [138] M.J. V. Goldschmidt, R. Beetstra, J.A.M. Kuipers, Hydrodynamic modelling of dense gas-fluidised beds: comparison and validation of 3D discrete particle and continuum models,

- Powder Technol. 142 (2004) 23–47.
- [139] Y. Tsuji, T. Tanaka, S. Yonemura, Cluster patterns in circulating fluidized beds predicted by numerical simulation (discrete particle model versus two-fluid model), Powder Technol. 95 (1998) 254–264.
- [140] R. Benzi, S. Succi, M. Vergassola, The lattice Boltzmann equation: theory and applications, Phys. Rep. 222 (1992) 145–197.
- [141] S.N.P. Vegendla, G.J. Heynderickx, G.B. Marin, Comparison of Eulerian-Lagrangian and Eulerian-Eulerian method for dilute gas-solid flow with side inlet, Comput. Chem. Eng. 35 (2011) 1192–1199. doi:10.1016/j.compchemeng.2010.09.001.
- [142] S. Sivier, E. Loth, J. Baum, R. Löhner, Eulerian-Eulerian and Eulerian-Lagrangian methods in two phase flow, in: M. Napolitano, F. Sabetta (Eds.), Thirteen. Int. Conf. Numer. Methods Fluid Dyn. Proc. Conf. Held Cons. Naz. Delle Ric. Rome, Italy, 6--10 July 1992, Springer Berlin Heidelberg, Berlin, Heidelberg, 1993: pp. 473–477. doi:10.1007/3-540-56394-6_270.
- [143] N.G. Deen, M.V.S. Annaland, M.A. Van der Hoef, J.A.M. Kuipers, Review of discrete particle modeling of fluidized beds, Chem. Eng. Sci. 62 (2007) 28–44.
- [144] B.P.B. Hoomans, J.A.M. Kuipers, W.J. Briels, W.P.M. Van Swaaij, Discrete particle simulation of bubble and slug formation in a two-dimensional gas-fluidised bed: a hard-sphere approach, Chem. Eng. Sci. 51 (1996) 99–118.
- [145] D.M. Snider, P.J. O'Rourke, The multiphase particle-in-cell (MP-PIC) method for dense particle flow, in: Comput. Gas-Solids Flows React. Syst. Theory, Methods Pract. Theory, Methods Pract., IGI Global, 2010: pp. 277–315.
- [146] M.J. Andrews, P.J. O'Rourke, The multiphase particle-in-cell (MP-PIC) method for dense

- particulate flows, *Int. J. Multiph. Flow.* 22 (1996) 379–402. doi:10.1016/0301-9322(95)00072-0.
- [147] D.M. Snider, An incompressible three-dimensional multiphase particle-in-cell model for dense particle flows, *J. Comput. Phys.* 170 (2001) 523–549.
- [148] D.M. Snider, P.J. O’Rourke, M.J. Andrews, Sediment flow in inclined vessels calculated using a multiphase particle-in-cell model for dense particle flows, *Int. J. Multiph. Flow.* 24 (1998) 1359–1382.
- [149] P.J. O’Rourke, D.M. Snider, An improved collision damping time for MP-PIC calculations of dense particle flows with applications to polydisperse sedimenting beds and colliding particle jets, *Chem. Eng. Sci.* 65 (2010) 6014–6028.
doi:10.1016/j.ces.2010.08.032.
- [150] S.E. Harris, D.G. Crighton, Solitons, solitary waves, and voidage disturbances in gas-fluidized beds, *J. Fluid Mech.* 266 (1994) 243–276.
- [151] J.-F. Dietiker, T. Li, R. Garg, M. Shahnam, Cartesian grid simulations of gas–solids flow systems with complex geometry, *Powder Technol.* 235 (2013) 696–705.
doi:10.1016/j.powtec.2012.11.028.
- [152] P.J. O’Rourke, P. (Pinghua) Zhao, D. Snider, A model for collisional exchange in gas/liquid/solid fluidized beds, *Chem. Eng. Sci.* 64 (2009) 1784–1797.
doi:10.1016/j.ces.2008.12.014.
- [153] D.M. Snider, An Incompressible Three-Dimensional Multiphase Particle-in-Cell Model for Dense Particle Flows, *J. Comput. Phys.* 170 (2001) 523–549.
doi:10.1006/jcph.2001.6747.
- [154] G. Williams, *Combustion theory*, Cummings Publ. Co, 1985.

- [155] P.J. O'Rourke, Statistical properties and numerical implementation of a model for droplet dispersion in a turbulent gas, *J. Comput. Phys.* 83 (1989) 345–360.
- [156] A. Putnam, Integratable form of droplet drag coefficient, *Ars J.* 31 (1961) 1467–1468.
- [157] J.F. Richardson, Sedimentation and fluidization part III The sedimentation of uniform fine particles and of two-component mixtures of solids, *Trans Inst. Chem. Eng.* 39 (1961) 348–356.
- [158] F.M. Auzerais, R. Jackson, W.B. Russel, The resolution of shocks and the effects of compressible sediments in transient settling, *J. Fluid Mech.* 195 (1988) 437–462.
- [159] Z. Shang, H. Liu, Simulating Multiphase Flows in Porous Media Using OpenFOAM on Intel Xeon Phi Knights Landing Processors, in: *Proc. Pract. Exp. Adv. Res. Comput. 2017 Sustain. Success Impact - PEARC17*, 2017: pp. 1–7. doi:10.1145/3093338.3093350.
- [160] J.A.L. Zhi Shang, Honggao Liu, High Performance Computing of Multiphase Flows in Porous Media - Using OpenFOAM and the Intel Xeon Phi, Lambert Academic Publishing, 2017. <https://www.lap-publishing.com/catalog/details//store/gb/book/978-3-659-0A80852-4/high-performance-computing-of-multiphase-flows-in-porous-media>.
- [161] M.J. V Goldschmidt, J.M. Link, S. Mellema, J.A.M. Kuipers, Digital image analysis measurements of bed expansion and segregation dynamics in dense gas-fluidised beds, *Powder Technol.* 138 (2003) 135–159.
- [162] T. Li, R. Garg, J. Galvin, S. Pannala, Open-source MFI-X-Dem software for gas-solids flows: Part II—Validation studies, *Powder Technol.* 220 (2012) 138–150.
- [163] R.F. Fedors, R.F. Landel, An empirical method of estimating the void fraction in mixtures of uniform particles of different size, *Powder Technol.* 23 (1979) 225–231.
- [164] A.B. Yu, N. Standish, An analytical—parametric theory of the random packing of

particles, Powder Technol. 55 (1988) 171–186.

Appendix A: Particle-Laden Laminar Flow through a Sudden Expansion

In this section, after describing the numerical approach, the results are structured as follows: first, the symmetric flow structure downstream of the sudden expansion is presented, and the effect of the solid particle phase on the reattachment length and momentum transfer in the recirculation region is described. Next, the effect of solid particles on the onset of flow bifurcation is investigated for a range of Reynolds numbers, expansion ratios, solid volume fractions, and particle diameters. Finally, the influence of flow bifurcation on the bulk transport of solid particles through the sudden expansion is described.

A.1 Particle-laden flow in sudden expansions

In many engineering applications, dilute mixtures of solid particles are also present in the flow, such as coal dust, soot, or sand particles [122–124]. Comparatively fewer studies have focused on the impact of these particles on the flow development through sudden expansions [1,125,126]. Considering the large density differences that may exist between the fluid and solid phases, solid particles may significantly alter the flow development in sudden expansions, leading to significant variations in the overall performance of the flow [127]. Therefore, a detailed study of the impact of dilute solid particles on the separation, recirculation and reattachment mechanisms is needed to support design optimization of devices employing sudden expansions.

When solid particles are present in the flow through the sudden expansion, the solid phase adds complexity to the flow due to non-linear, non-equilibrium phenomena and multi-scale dynamic responses of the solid particles [128]. The complexity intensifies with increasing solid

phase fraction [128]. Although the presence of solid particles typically increases viscous losses [129–131], Shook and Bartosik [132] claimed that viscous losses can be negligibly impacted or even reduced depending on the particle size and mean solid volume fraction. Moreover, solid particles may cause material erosion, damage flow control devices, or affect turbulence dissipation characteristics [133]. Therefore, characterizing the transient solid-fluid dynamics in multiphase sudden expansion flows is essential for design optimization. Fessler and Eaton [134] experimentally investigated the response of a dense solid phase to the turbulent flow after a planar sudden expansion. The particle velocity and concentration distributions were measured for a variety of spherical particle sizes (70 μm diameter copper and 90 and 150 μm diameter glass) at $Re = 17,600$. Their results show relatively few particles are transported into the recirculation regions and a uniform concentration of solid phase occurs downstream of flow reattachment. Yu et al. [135] performed numerical simulations to investigate particle-laden turbulent flow over a backward-facing step. Their study used large eddy simulations (LES) for the Eulerian-based gas phase and a Lagrangian approach for particles that accounted only for the effect of drag and gravitational forces on particle motion. Their numerical predictions were in good agreement with the earlier experimental data obtained by Fessler and Eaton [134]. Founti and Klipfel [125] conducted experimental and computational study to identify the effects of particle motion in a 1% and 5% solid volume fraction flow through a sudden expansion at $Re = 56,000$. Their results show shorter reattachment lengths with 1% volumetric loading of the solid phase, while increasing the solid phase fraction increases the reattachment length back towards the single phase value. At 5% volumetric loading, the reattachment length increased past the single phase due to a reduction of the turbulence kinetic energy of the fluid phase associated with solid-particle collisions [125]. Recently, El-Askary et al. [1] used an Eulerian–Lagrangian approach to investigate the effect of

injection rate, particle diameter, and expansion ratio on the sudden expansion flow development for Reynolds numbers between 10,000 and 200,000. At lower Reynolds numbers, steady laminar flow was observed in the single-phase cases, but the addition of solid phase caused an abrupt unsteadiness in the flow downstream of the expansion.

The above literature indicates that the majority of research has focused on flows at relatively large Reynolds numbers ($Re > 10,000$) and larger solid phase fraction ($>1\%$). Little work has focused on lower Reynolds numbers ($Re < 2,000$) where the laminar flow is very sensitive to disturbances that could be caused by a more dilute particle phase. In particular, the influence of the solid particle phase on the onset of bifurcation in the sudden expansion is not well understood. Therefore, one objective of the present thesis is to employ numerical simulation to investigate the impact of dilute solid particles on the dynamics that lead to bifurcation in laminar sudden expansion flows at low Reynolds numbers.

A.1.1 Numerical methods for solid/fluid multiphase flows

Various computational fluid dynamics (CFD) methods have been suggested to study the multiphase flow behavior, including the two-fluid model (TFM) [136,137], discrete particle model (DPM) [138,139], and the lattice Boltzmann method (LBM) [128,140]. In general, these methods are based on either the Eulerian–Eulerian or Eulerian–Lagrangian families of approaches. In both, the fluid or carrier phase is represented by a continuum [141], with properties computed at constant locations in space [142]. The solid or dispersed phase is then represented by either an Eulerian or Lagrangian description. TFM is an Eulerian-Eulerian approach that solves the solid phase equations as fully interpenetrating continua by computing the collective behavior of a large number of particles rather than the behavior of individual particles. It is widely used in industry-scale simulations due to its lower computational complexity [137].

On the other hand, DPM is an Eulerian- Lagrangian approach where the solid phase is captured based on simulating the transport of individual particles [143]. Hence, particle motion is determined by discrete computations that collectively solve equations of motion for each particle, accounting for fluid-particle and particle-particle forces, to identify the Lagrangian trajectories of particles [144]. While more accurate for individual particles, these approaches suffer from increased computational cost [145].

Multiphase particle-in-cell (MP-PIC) method is a hybrid method that combines the accuracy of the Eulerian-Lagrangian description with the computational efficiency of the Eulerian-Eulerian approach [146]. This is accomplished by grouping Lagrangian particles into discrete “parcels” that are then mapped to and from a computational grid [147]. Lagrangian computations are performed on the parcels to calculate the solid phase. Hence, MP-PIC method is able to perform simulation with computational cost even less than that of conventional TFM simulations by replacing large numbers of particles with fewer parcels [147,148]. Another feature of MP-PIC method is the ability to define the solid phase with realistic particle size distributions and material properties [149]. The MP-PIC method advances earlier stochastic parcel methods by adding a term related to the gradient of an isotropic particle contact pressure in the parcel acceleration equation [150]. The implicit approximations of the parcel buoyant force, parcel drag force, and inter-phase momentum transfer terms are coupled with the contact pressure term, which is also numerically approximated in an implicit fashion. The implicit coupling can improve computational efficiency by minimizing the stability limitations imposed on the computational timestep [149].

Although the MP-PIC method combines advantages of Eulerian and Lagrangian multiphase methods, it also has its own limitations. Firstly, it models only spherical particles. Secondly, the particle size must be small compared to the spacing of the Eulerian grid. Finally, it

suffers from low accuracy at solid volume fractions greater than 5% due to high particle collision frequency. These limitations restrict the application of MP-PIC method, particularly when fine grid resolution is required at higher Reynolds numbers associated with turbulent flow; in such cases, the particle size restriction limits MP-PIC to only dilute suspensions of small particles. The current study models laminar flow laden with small spherical particles with a solid volume fraction less than 5%, which makes the MP-PIC method appropriate.

A.2 Numerical approach

The MP-PIC method is used to couple the particle motion with the fluid dynamics in a two-way coupling by mapping Lagrangian particles to and from a computational grid. In this method, each solid phase is defined as a parcel and may in general contain multiple particles [149,151], but in the current study, only one particle per parcel is considered to increase accuracy.

A.2.1 Computational domain and boundary conditions

The computational domain used in the present study, shown in Figure A-1, consists of sequential two-dimensional channels with heights of d and D mated together to produce a sudden expansion with a step-height of h . The maximum Reynolds number (Re_{max}) is based on the inlet channel height and maximum inlet velocity. The expansion ratio (Er) is defined as the channel height upstream of the sudden expansion to the height downstream. The lengths of the computational domain upstream and downstream of the expansion are $L_i = 10h$ and $L_o = 40h$, respectively. A parabolic inflow boundary is imposed at the inlet boundary for the liquid phase. Solid phase parcels are injected at the inlet with uniform velocity equal to the mean inlet velocity (U_0). Parcels are spatially distributed across the inlet boundary with random distribution. Zero

gauge static pressure and zero streamwise velocity gradient are imposed at the outlet boundary. All walls are represented by no-slip wall boundaries. The outlet boundary is placed far from the expansion to minimize outlet boundary effects on the region of interest. For the $Er = 4.0$ case, two domain lengths ($L_o = 40h$ and $L_o = 60h$) are tested, and insensitivity of the results to either domain length was verified.

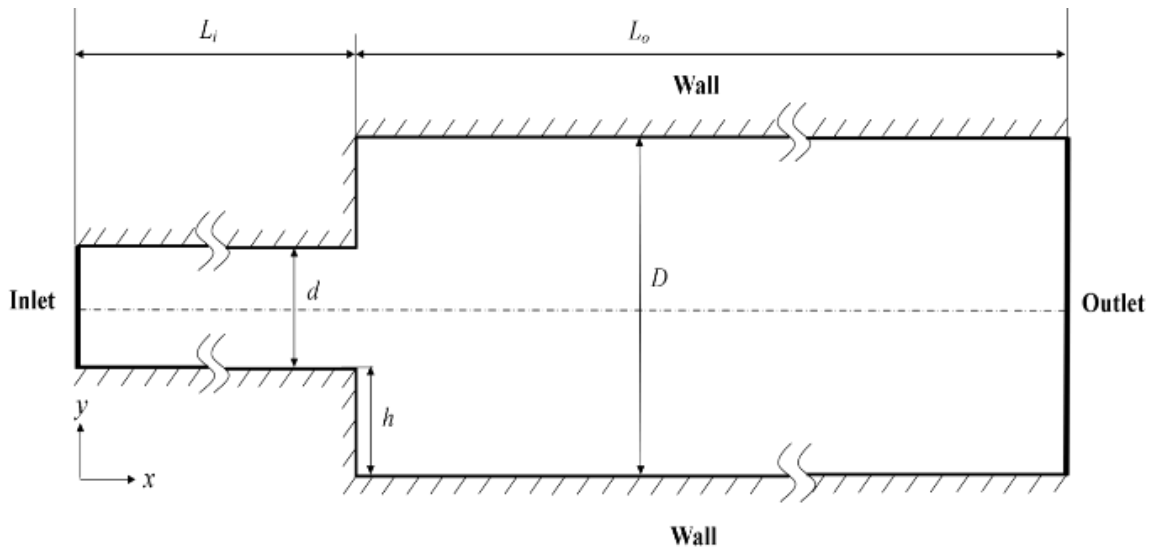


Figure A-1: Schematic of the computational domain

A.2.2 Spatial grid

A structured, non-uniform, orthogonal finite-volume grid is mapped to the computational domain. The total number of grid cells for each expansion ratio in the regions upstream and downstream of the expansion are given in Table A-1. Figure A-2 shows the streamwise and cross-stream grid spacing distributions for the $Er = 4.0$ case. The grid is refined in the region near the no-slip walls and close to the sudden expansion where larger velocity gradients and shear stresses

are expected. As shown in Figure A-2(a), the coarsest grids belong to the inlet and outlet regions, where the streamwise grid spacing in these regions is about twice that of the grid near the sudden expansion (indicated with a dashed line). A similar grid spacing distribution is used for the expansion ratios of 2.0 and 3.0.

A grid independence analysis is performed at four refinement levels for $Re_{max} = 1000$ and $Er = 2.0$ in order to ensure sufficient spatial resolution for all simulations, as reported in chapter 4.

Table A-1: Characteristics of computational grids used

<i>Er</i>	$(N_x, N_y)_i$ <i>Upstream of step</i>	$(N_x, N_y)_o$ <i>Downstream of step</i>	<i>Total cells</i>
2.0	100 × 80	400 × 240	104,000
3.0	100 × 80	800 × 400	328,000
4.0	100 × 80	1800 × 560	1,016,000

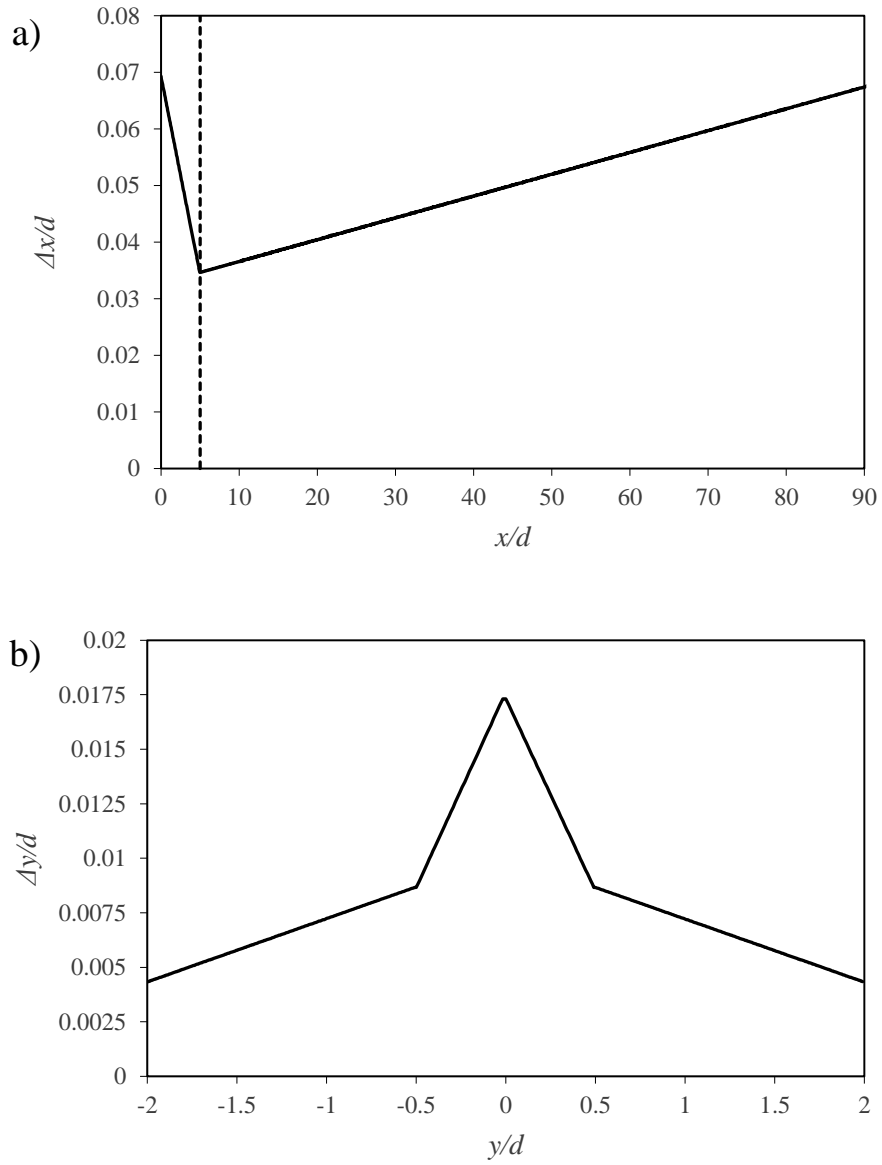


Figure A-2: Distribution of the spatial grid spacing in the (a) streamwise direction at $y = D/2$ and (b) wall-normal direction at $x/h = 20$ for the $Er = 4.0$ case. The dashed line indicates the location of the sudden expansion

A.2.3 Test cases

In the present study, 111 simulations were performed at eight Reynolds numbers between $Re_{max}=200$ and 1000 (increments of 100) and at expansion ratios of $Er = 2.0, 3.0,$ and 4.0 . The range of test cases for each expansion ratio is presented in Table A-2. The range of Reynolds number is wide enough to identify the effect of solid phase fraction (ϕ_s) and particle size on the onset of bifurcation. As the simulations are two-dimensional, an area-based solid phase fraction is used, calculated as,

$$\phi_s = \frac{N_p \pi d_p^2}{4(dL_i + DL_o)} \times 100\% \quad (\text{A.1})$$

where N_p is the total number of particles in the solution at stationary steady state. Depending on the Reynolds number, expansion ratio, and ϕ_s value, the flow may break down into irregular, unsteady fluctuations that mimics transition to turbulence. At lower expansion ratios (e.g. $Er = 2.0$), unsteady break-down occurs at Reynolds numbers above the range in Table A-2, which allows us to systematically quantify the effects of Reynolds number, solid phase fraction, and particle size on the development of bifurcation in the multiphase flow. At higher expansion ratios (e.g. $Er > 3.0$), such unsteady break down occurs at Reynolds within the tested ranges; as the transition to turbulence cannot be accurately captured in the present two-dimensional study, these cases are limited to the qualitative descriptions of the impact of particle phase on bifurcation.

Table A-2: Test cases range for various expansion ratios

<i>Er</i>	<i>Re_{max}</i> range	Volumetric fraction (ϕ_s)	Particle size (d_p/d)	Number of cases
2.0	200 - 1000	0 - 0.03	0 – 0.005	67
3.0	200 - 1000	0 - 0.01	0 and 0.001	22
4.0	200 - 1000	0 - 0.01	0 and 0.001	22

A.2.4 Solution Method

OpenFOAM® discretizes the governing equations by means of the finite volume method [92,105]. The velocity and pressure coupling was solved with the PISO algorithm. Convergence at each timestep was achieved when the root-mean-square residuals of the pressure and momentum equations fell below 5×10^{-8} . Second-order central differencing and second-order Euler backward differencing were used to discretize the spatial and temporal derivatives, respectively. The time-step size in each simulation varied depending on the Reynolds number and grid size in order to keep Courant number below 0.5 [107], with $\Delta t = 10^{-4}$ s being the smallest time-step used. Water at 1 atm and 25°C is the fluid phase. Particle density is considered as 1300 kg/m³. Each simulated test case was initialized with a zero relative static pressure and an initial velocity equal to the mean velocity at the inflow boundary and were then integrated in time for approximately 10 flow through times (defined as L/U_0) to reach a statistically-steady state and then approximately 3 flow through times were collected for analysis. Each simulation was performed in a parallel-processing environment on 36 CPUs using a message-passing interface (MPI) parallelization strategy.

A.2.5 MP-PIC method

The coupled Eulerian-Lagrangian method can be used to describe the collisional exchange in solid-liquid flow of porous media. In multiphase flow, the liquid phase flow can be represented by Navier-Stokes equations using Eulerian approach and the movement of particles can be represented by Lagrangian motion equations. O'Rourke et al. [152] presented the fully coupled Eulerian- Lagrangian governing equations, the MP-PIC (multiphase particle-in-cell) method which was employed in OpenFOAM. The specific equations are described as [153]:

I) *Liquid Phase*

The continuity equation for the liquid phase with no interphase mass transfer is

$$\frac{\partial \theta_f}{\partial t} + \nabla \cdot (\theta_f \mathbf{u}_f) = 0 \quad (\text{A.2})$$

where \mathbf{u}_f and θ_f are the liquid velocity and volume fraction, respectively. The momentum equation for the liquid phase is

$$\frac{\partial (\theta_f \mathbf{u}_f)}{\partial t} + \nabla \cdot (\theta_f \mathbf{u}_f \mathbf{u}_f) = -\frac{1}{\rho_f} \nabla p - \frac{1}{\rho_f} \mathbf{F} + \theta_f \mathbf{g} \quad (\text{A.3})$$

where ρ_f , p , \mathbf{g} are liquid density, liquid pressure, and gravitational acceleration, respectively. \mathbf{F} denotes the rate of momentum exchange per volume between the liquid and particle phases. It should be mentioned that there are some assumptions:

- 1- The liquid phase is incompressible.
- 2- Both liquid and particle phases are isothermal.
- 3- The momentum equation presented for liquid phase neglects viscous molecular diffusion in the liquid but retains the viscous drag between particles and fluid through the interphase drag force, \mathbf{F} .

It should be noted that neglecting the viscous terms has little effect in dense particle flows, and the viscous terms can be easily included in the fluid equation set for cases with lower particle density.

II) *Particulate Phase*

The motion of the particle phase is obtained using the particle probability distribution function $\varphi(\mathbf{x}, \mathbf{u}_p, \rho_p, \Omega_p, t)$, where \mathbf{x} , \mathbf{u}_p , ρ_p , Ω_p represent position, velocity, density, and volume of particle, respectively. As it is assumed that no mass transfer occurs between particles and the liquid, the mass of each particle is constant in time, but particles may have a range of sizes and

densities. The time evolution of φ is achieved by solving a Liouville equation for the particle distribution function [154],

$$\frac{\partial \varphi}{\partial t} + \nabla \cdot (\varphi \mathbf{u}_p) + \nabla_{\mathbf{u}_p} \cdot (\varphi \mathbf{A}) = 0 \quad (\text{A.4})$$

where $\nabla_{\mathbf{u}_p}$ is the divergence operator with respect to particle velocity. The discrete particle acceleration ($\mathbf{A} = \frac{d\mathbf{u}_p}{dt}$) is expressed as [146]:

$$\mathbf{A} = D_p(\mathbf{u}_f - \mathbf{u}_p) - \frac{1}{\rho_p} \nabla p + \mathbf{g} - \frac{1}{\theta_p \rho_p} \nabla \tau \quad (\text{A.5})$$

The terms of Eq. (A.5) represent acceleration due to aerodynamic drag, pressure gradient, gravity, and gradient in the interparticle stress, τ .

The interphase drag model function (D_p) can be expressed using expression of O'Rourke [155]:

$$D_p = C_d \frac{3}{8} \frac{\rho_f}{\rho_p} \frac{|\mathbf{u}_f - \mathbf{u}_p|}{r_p} \quad (\text{A.6})$$

where

$$C_d = \frac{24}{Re_p} \left(\frac{Re_p^{2/3}}{6} \epsilon^{-1.78} + \epsilon^{-2.65} \right) \quad (\text{A.7})$$

$$Re_p = \frac{2\rho_f |\mathbf{u}_f - \mathbf{u}_p| r_p}{\mu_f} \quad (\text{A.8})$$

$$r = \left(\frac{3\Omega_p}{4\pi} \right)^{1/3} \quad (\text{A.9})$$

μ_f is the liquid viscosity and ρ_p is the particle density. In the case of $\epsilon = 1.0$, this drag formulation reduces to the Putnam [156] correlation for solid spheres. The ϵ -dependence of C_d is determined using the experiments of Richardson [157].

The continuum particle stress model is used for collisions between particles. Particles are modeled as a continuum and are estimated by an isotropic interparticle stress where the off-diagonal elements of the stress tensor are neglected. An isotropic solids stress (τ) in the Eq. (3.8) can be used by an expression of the model from Harris and Crighton [150]:

$$\tau = \frac{P_s \theta_p^\beta}{\max[\theta_{cp} - \theta_p, \varepsilon(1 - \theta_p)]}. \quad (\text{A.10})$$

P_s is a constant which has units of pressure. θ_{cp} denotes the particle volume fraction at close packing. Auzerais et al. [158] recommend the constant β in the range of $2 \leq \beta \leq 5$. The original expression by Harris and Crighton was modified to remove the singularity at close pack by adding the ε expression in the denominator which is a small number on the order of 10^{-7} .

The probability function integrated over velocity and mass calculates the probable number of particles per unit volume at x and t in the interval $(\mathbf{u}_p, \mathbf{u}_p + d\mathbf{u}_p)$, $(\rho_p, \rho_p + d\rho_p)$, and $(\Omega_p, \Omega_p + d\Omega_p)$. The particle distribution function defines the particle volume fraction as:

$$\theta_p = \iiint \varphi \Omega_p d\Omega_p d\rho_p d\mathbf{u}_p \quad (\text{A.11})$$

To complete the equations, we require an expression for the interphase momentum transfer function per volume (F) in the Eulerian momentum equation which is defined as:

$$F = \iiint \varphi \Omega_p \rho_p \left[D_p(\mathbf{u}_f - \mathbf{u}_p) - \frac{1}{\rho_p} \nabla p \right] d\Omega_p d\rho_p d\mathbf{u}_p \quad (\text{A.12})$$

By taking the moments of Eq. (3.7), the Eulerian governing equations for the particle phase can be obtained. The particle conservation equations can be obtained by multiplying Eq. (3.7) to by $\rho_p \Omega_p$ and $\rho_p \Omega_p \mathbf{u}_p$ and integrating over particle density, volume, and velocity coordinates. The continuity equation for particle phase is

$$\frac{\partial(\overline{\theta_p \rho_p})}{\partial t} + \nabla \cdot (\overline{\theta_p \rho_p \mathbf{u}_p}) = 0 \quad (\text{A.13})$$

and the momentum equation for particle phase is

$$\begin{aligned} \frac{\partial(\overline{\theta_p \rho_p \mathbf{u}_p})}{\partial t} + \nabla \cdot (\overline{\theta_p \rho_p \mathbf{u}_p \mathbf{u}_p}) = & -\theta_p \nabla p + \nabla \tau_p + \overline{\theta_p \rho_p} \mathbf{g} + \\ & \iiint \varphi \Omega_p \rho_p D_p (\mathbf{u}_f - \mathbf{u}_p) d\Omega_p d\rho_p d\mathbf{u}_p - \nabla \cdot [\iiint \varphi \Omega_p \rho_p (\mathbf{u}_p - \overline{\mathbf{u}_p}) (\mathbf{u}_p - \\ & \overline{\mathbf{u}_p}) d\Omega_p d\rho_p d\mathbf{u}_p] \end{aligned} \quad (\text{A.14})$$

where the mean particle velocity $\overline{\mathbf{u}_p}$ is calculated by

$$\overline{\mathbf{u}_p} = \frac{1}{\overline{\theta_p \rho_p}} \iiint \varphi \Omega_p \rho_p \mathbf{u}_p d\Omega_p d\rho_p d\mathbf{u}_p \quad (\text{A.15})$$

and the average particle density is calculated by

$$\overline{\theta_p \rho_p} = \iiint \varphi \Omega_p \rho_p d\Omega_p d\rho_p d\mathbf{u}_p \quad (\text{A.16})$$

The sum of volume fractions of liquid and particle phases must equal unity, $\theta_p + \theta_f = 1$.

A.3 Validation of the computational approach

Validating the numerical results of particle-laden laminar flow in this specific geometry is hindered by the lack of similar published experiments. Therefore, validation of the numerical algorithm and the spatial and temporal resolutions is performed by comparing results of the single-phase case, chapter 4, to experimental data and numerical predictions available in the literature. As shown in Figure A-3, the shear layer reattachment lengths variation with Reynolds number is in agreement with the data obtained by Kadja et al [108]. For Reynolds numbers less than the critical Reynolds number for bifurcation onset, the upper and lower walls have equal reattachment lengths, while branching occurs at higher Reynolds numbers. In addition, the accuracy of OpenFOAM for direct numerical simulation (DNS) of turbulent flows is also confirmed by the

present authors for turbulent flow in a pipe as shown in chapter 8. The results are in excellent agreement with published experimental and numerical results for the turbulent mean velocity profile, disturbance profiles, and frequency spectra in the turbulent pipe flow.

The MP-PIC method employed in OpenFOAM was validated recently by Shang et al. [159,160] for multiphase flows in a porous reservoir. An experiment of randomly deposited solid particles in a packed bed porous medium by Goldschmidt et al. [161] was used for the validation. Li et al. [162] also used the same experimental data to verify the accuracy of the open-source MFIx-DEM software for gas-solid flows. As shown in Figure A-4, comparison of simulated results [159,162], empirical correlations [163,164], and experimental data [161] reveals that the MP-PIC algorithm in the OpenFOAM solver [159] is able to accurately capture the particle-laden flow.

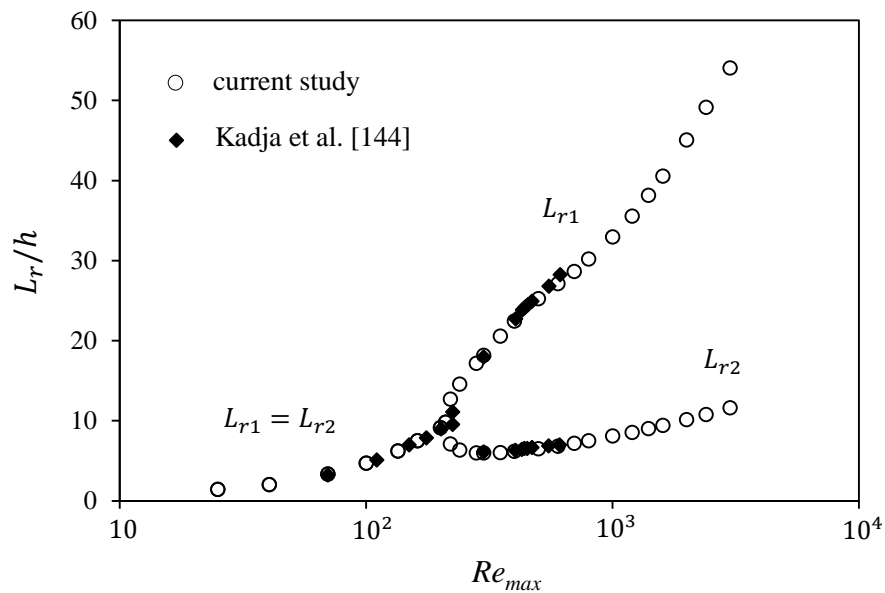


Figure A-3: Comparison of non-dimensional reattachment length (L_r/h) for single-phase flow in a planar sudden expansion at $Er = 2.0$. Subscripts 1 and 2 denote the upper and lower walls, respectively

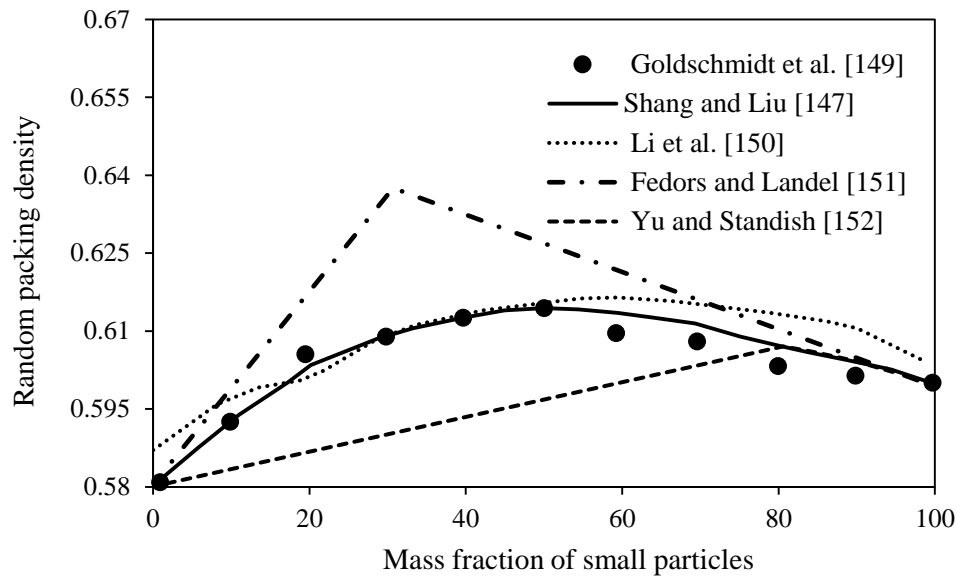
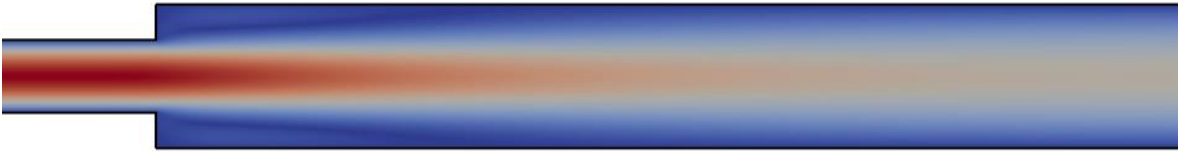


Figure A-4: Comparison of random packing density in packed bed. Modified from Shang and Liu [159]

A.4 Symmetric flow structure

Figure A-5 shows the instantaneous and time-mean velocity magnitude contours for the water phase for cases with $\phi_s = 0.01\%$ and 0.02% at $Re_{max} = 200$ and $Er = 2.0$. As the Reynolds number is less than the critical Reynolds number for bifurcation ($Re_c = 218 \pm 1$ at $Er = 2.0$ according to chapter 4), the mean velocity contours are completely symmetric for all solid fractions studied, although a small asymmetry is observed in the instantaneous contours for the particle-laden cases due to stochastic fluctuations created by the particles in the flow. The mean contours show that these fluctuations induce a reduction in the size of the inviscid core region downstream of the expansion leading to earlier reattachment and attainment of fully developed flow in the downstream channel. These effects are seen even more clearly in plots of the time-mean streamlines, shown in Figure A-6, which shows that the streamlines remain symmetric and the average

a) $|\overline{U}|/U_{max}$ or $|U|/U_{max}$ for $\varphi_s = 0$



b) $|\overline{U}|/U_{max}$ for $\varphi_s = 0.01\%$



c) $|U|/U_{max}$ for $\varphi_s = 0.01\%$



d) $|\overline{U}|/U_{max}$ for $\varphi_s = 0.02\%$



e) $|U|/U_{max}$ for $\varphi_s = 0.02\%$

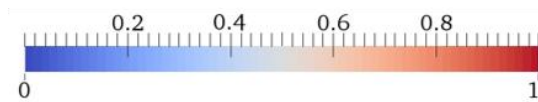


Figure A-5: Contours of velocity magnitude in the water phase at $Re_{max} = 200$ and $Er = 2.0$: (a) mean or instantaneous velocity contour at $\varphi_s = 0$; (b) mean velocity contour for $\varphi_s = 0.01\%$; (c) instantaneous velocity contour for $\varphi_s = 0.01\%$; (d) mean velocity contour for $\varphi_s = 0.02\%$; (e) instantaneous velocity contour for $\varphi_s = 0.02\%$

reattachment lengths are equal on the upper and lower channel walls for all cases. The arrows pointing towards the walls present the time-average locations of flow reattachment. Recirculation regions shrink substantially with the presence of particles; for $\phi_s = 0.01\%$, Figure A-6(b) shows a major decrease in the reattachment length compared to the single-phase case. Figure A-6 (c) shows that further increase in solid phase fraction causes disappearance of the recirculation regions on both the upper and lower walls, leaving only a small separation bubble along the expansion step.

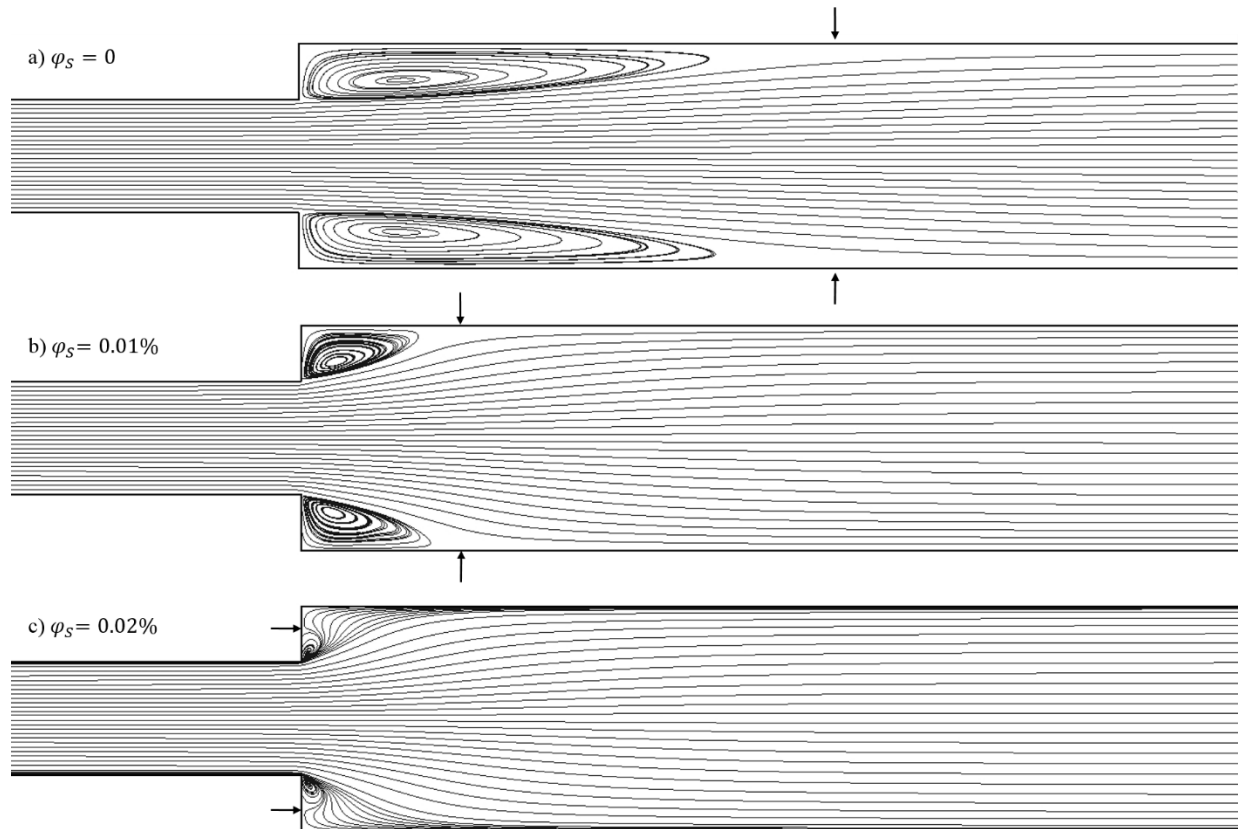


Figure A-6: Time-mean streamline pattern near the sudden expansion for $Re_{max} = 200$, $Er = 2.0$ and $\phi_s = 0$, 0.01% , and 0.02%

The time-averaged streamwise velocity profiles in the water phase immediately downstream of the step are shown in Figure A-7 to identify the effect of particles on cross-stream momentum exchange. Figure A-7(a) and (b) shows that at $x/h = 0$ (i.e. right at the step), the

particle-laden case has a similar velocity profile as the single phase case ($\phi_s = 0$), suggesting the particle phase has a minimal impact on cross-stream momentum exchange upstream of the step. Downstream of the expansion, the velocity profiles indicate substantially different patterns for single phase and particle-laden cases. Reattachment occurs at $x/h = 9.05, 2.36,$ and 0.00 for $\phi_s = 0, 0.01\%,$ and $0.02\%,$ respectively. Figure A-7(c) and (d) show that the flow achieves a nearly-parabolic velocity profile downstream of the expansion for the $\phi_s = 0$ case, while for the particle-laden cases, the profile has much higher velocity magnitude in the near-wall regions and a lower centerline velocity. As the flow travels further downstream of the expansion, the magnitude of the centreline velocity in the $\phi_s = 0$ cases decreases in response to viscous diffusion such that by $x/h = 20,$ a parabolic velocity profile is recovered. In contrast, much less centerline deceleration is noted in the particle-laden flows, as the interaction between particles and their random movement especially toward the walls enhances the cross-stream momentum exchange such that viscous diffusion is no longer dominant. As a result, Figure A-7(c) shows that for $\phi_s = 0.01\%$ and $0.02\%,$ the particles eliminate the reversed-flow region that is present in the $\phi_s = 0$ case and enhance the wall shear stress; computed results at $x/h = 20$ reveal that wall shear stress for $\phi_s = 0.01\%$ is 3.05 times higher than the $\phi_s = 0$ case.

The observations of Figure A-5-Figure A-7 for $Re = 200$ and $Er = 2.0$ are generalized for a range of flow conditions in Figure A-8, which plots the computed average reattachment lengths as a function of the Reynolds number for various expansion ratios and volumetric particle injection fractions (ϕ_{in}), calculated as,

$$\phi_{in} = \frac{N_{in}\pi d_p^2}{4(dU_0)} \times 100\% \quad (\text{A-17})$$

where N_{in} is the number of injected particles per second. As the Reynolds number range covers the region where flow bifurcation has occurred for all expansion ratios, Figure A-8 plots the

reattachment length as the longer of the two recirculation regions. As in Figure A-6, shorter reattachment lengths are observed when solid particles are present. The reattachment length increases with Reynolds number but for multiphase cases, it reaches a threshold value and then becomes almost constant with phase fraction. For higher expansion ratios, the results illustrate a gentler slope of reattachment length as a function of Reynolds number.

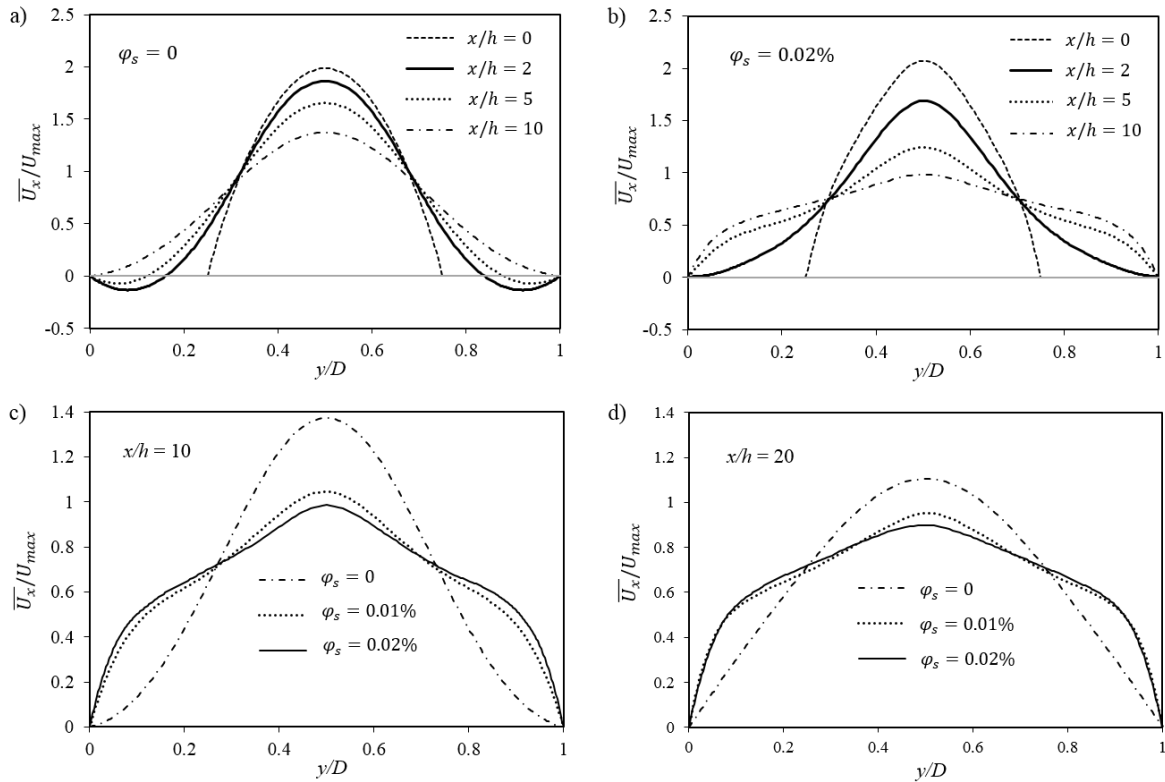


Figure A-7: Comparison of the time-mean velocity profile for $Re_{max} = 200$ and $Er = 2.0$ for various solid phase volume fraction and streamwise locations

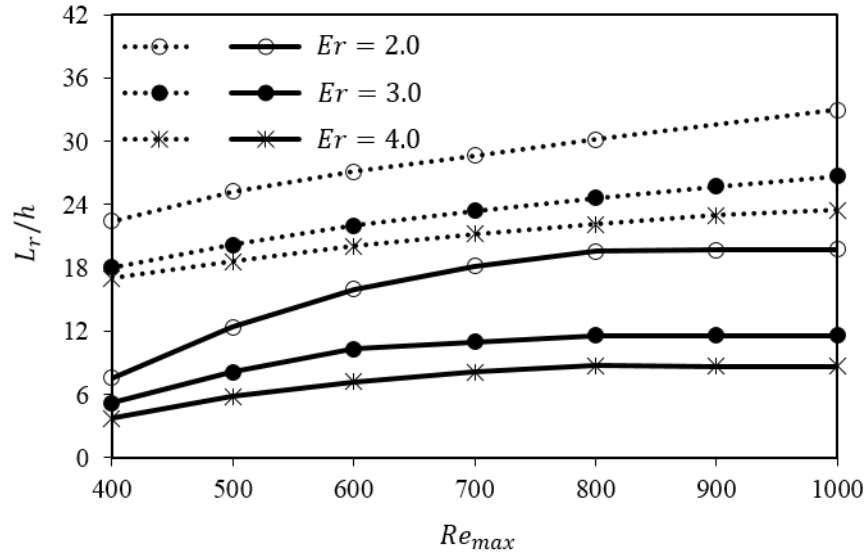


Figure A-8: Average shear layer reattachment length for larger recirculation region for various Reynolds numbers at $Er = 2.0$. Dashed and solid lines represents $\phi_{in} = 0$ and $\phi_{in} = 0.016\%$, respectively

A.5 Effect of solid phase on bifurcation onset

As discussed above, the Reynolds number ranges in Figure A-8 exceed the critical Reynolds number for bifurcation, and thus bifurcation has occurred resulting in asymmetry in the reattached flow. The progression of bifurcation for the $Re_{max} = 400$ and $Er = 2.0$ case is shown in Figure A-9 for the single-phase case through snapshots of the instantaneous flow streamlines at discrete solution times, where time is non-dimensionalized by the time scale $\tau = D^2/(\nu Re_{max})$. Arrows pointing towards and away from the wall indicate time-mean location of flow reattachment and separation, respectively. After $t' = 300$, the flow structure starts to change from symmetric into an asymmetric structure. The bifurcation process completes near $t' = 400$ when the flow reaches its steady state condition and the recirculation regions achieve their terminal lengths ($t' = 0$ represents simulation initiation time).

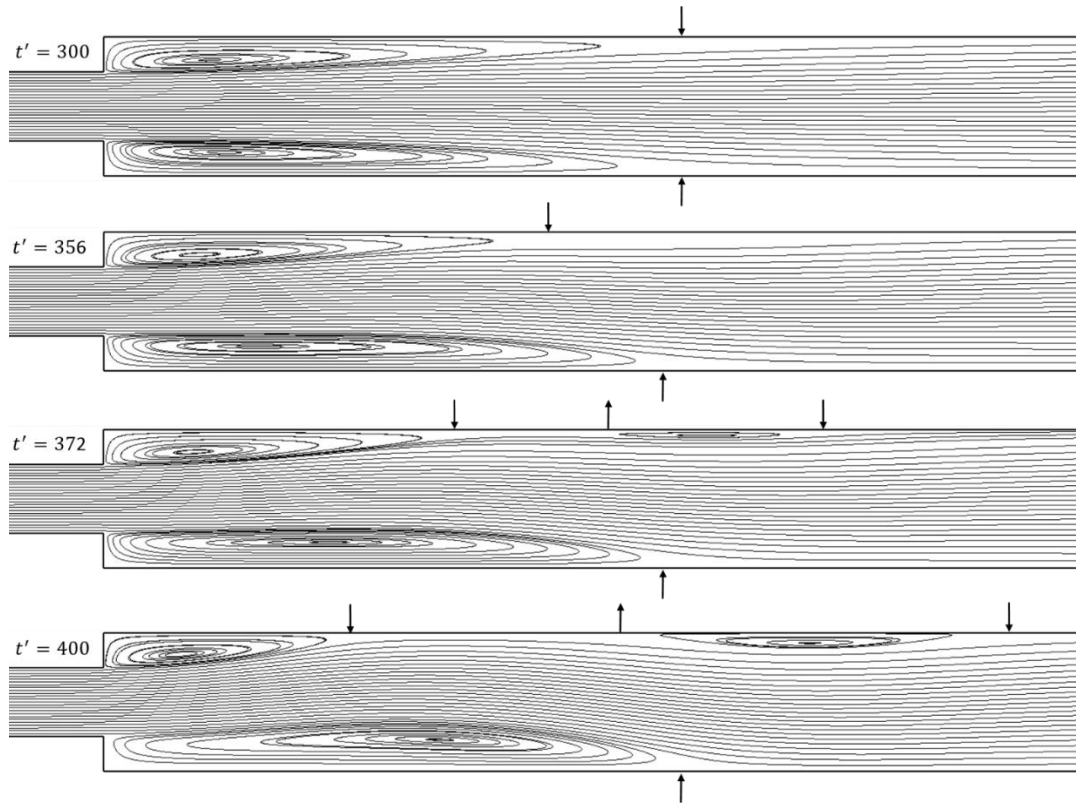


Figure A-9: Temporal evolution of the single phase flow structure at $Re_{max} = 400$ and $Er = 2.0$

In order to address how the presence of solid particles influence bifurcation, qualitative observations of the influence of solid particles on the flow are presented first, followed by quantifying the sensitivity of these effects to the solid phase fraction and particle size. Figure A-10 plots the time-mean reattachment lengths on the upper and lower walls at various Reynolds numbers for $\varphi_{in} = 0$ and $\varphi_{in} = 0.016\%$. Several notable features are visible. First, for the $\varphi_{in} = 0$ case, bifurcation onset occurs distinctly at $Re_{max} = 218$, while for the $\varphi_{in} = 0.016\%$ case, bifurcation is delayed to about $Re_{max} = 400$. Second, bifurcation occurs in the $\varphi_{in} = 0.016\%$ case at a similar reattachment length as in the $\varphi_{in} = 0$ case. This suggests that bifurcation is related not only to the disturbance environment in the symmetric flow field, but also to the shape and receptivity properties of the reversed velocity profile in the vicinity of the reattachment point. This observation

is consistent with earlier observations by in chapter 4, which noted that when the Reynolds number is much larger than the critical Reynolds number, bifurcation initiates as streamwise velocity disturbances localized near the time-averaged reattachment location. It seems the velocity profile near the reattachment point in the particle-laden cases is not receptive to such disturbances until the reattachment length reaches a threshold length. Finally, with further increases in the Reynolds number, the smaller recirculation zone achieves the same reattachment length for both the $\varphi_{in} = 0$ and $\varphi_{in} = 0.016\%$ cases, while the larger recirculation zone experiences an overall reduction in reattachment length consistent with the trends presented in Figure A-8.

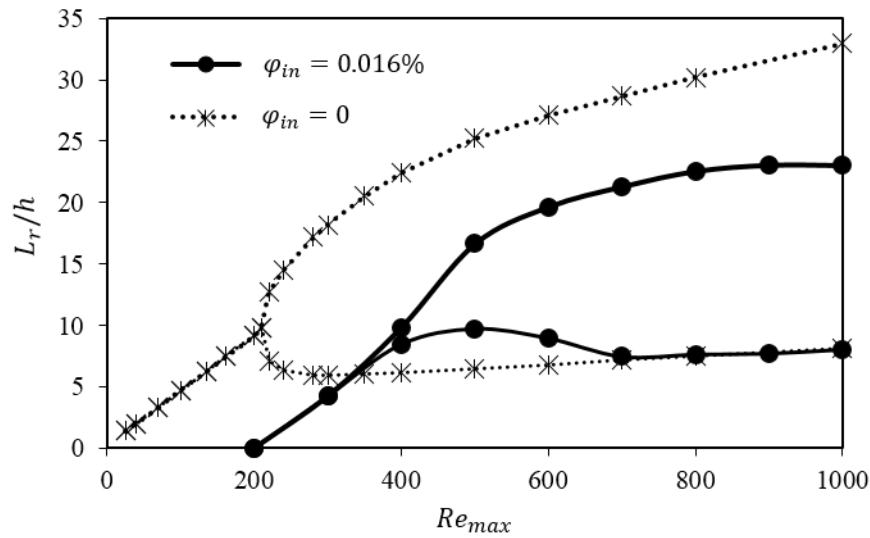


Figure A-10: Average shear layer reattachment lengths for various Reynolds numbers at $Er = 2.0$

At the higher Reynolds numbers studied, bifurcation is a key step towards the global break down of the flow to unsteady fluctuations and eventually turbulence. Although the solid phase delays the onset of bifurcation, it also accelerates the development global unsteadiness in the flow. This is illustrated in Figure A-11 for the $Re = 1000$ case by plotting contours of the instantaneous

and time-mean velocity magnitude for $\varphi_s = 0$ and $\varphi_s = 0.002\%$. For the single-phase case, the time-mean and instantaneous contours are identical, and hence only one is plotted. In the $\varphi_s = 0.002\%$ case, however, not only has the primary recirculation zone shortened, but a global unsteadiness has developed in the flow, which Figure A-11(c) shows is linked to a cascading development of successively smaller-scale recirculation regions. This unsteadiness is generated in the flow by the solid particles even though the particle phase in Figure A-11(c) is very dilute. This confirms that while solid particles delay onset of bifurcation to higher Reynolds numbers relative to the single phase case, they also accelerate the growth of global unsteadiness of the flow.

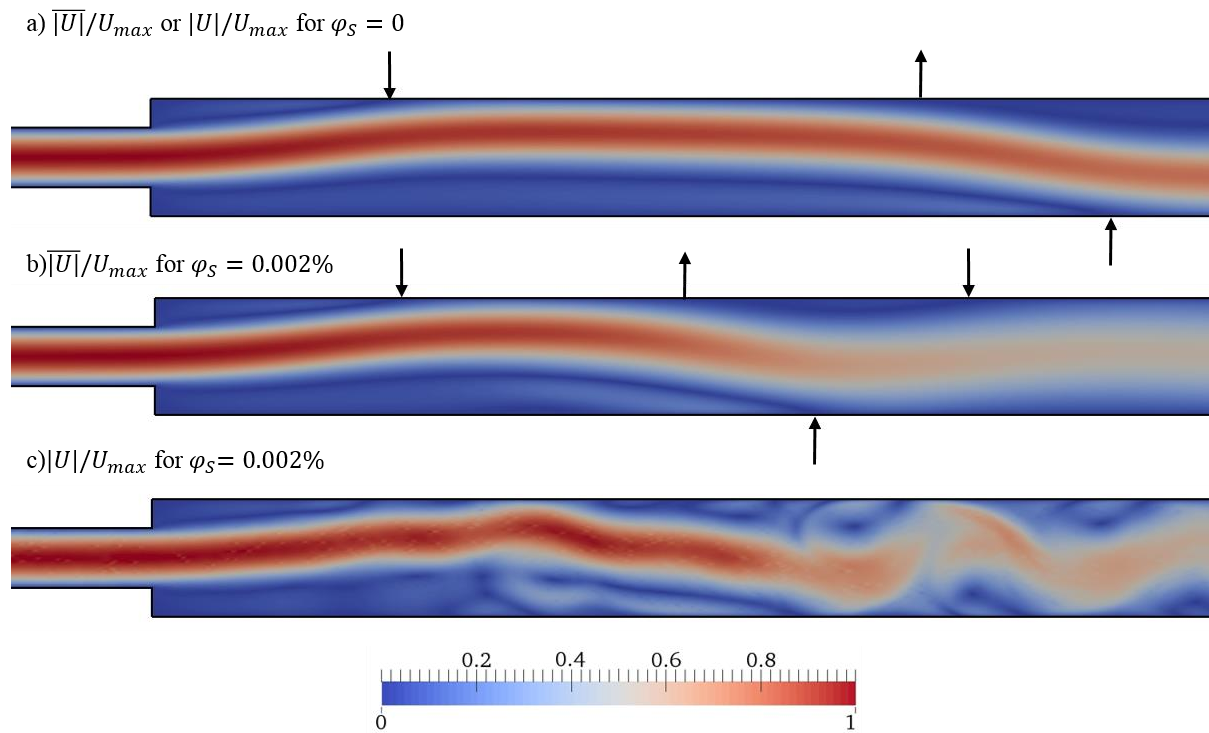


Figure A-11: Contours of velocity magnitude of the water phase for $Re_{max} = 1000$ and $Er = 2.0$: (a) mean or instantaneous velocity contour for $\varphi_s = 0$; (b) mean velocity contour for $\varphi_s = 0.002\%$; (c) instantaneous velocity contour for $\varphi_s = 0.002\%$

Although the results presented in Figure A-9 to Figure A-11 are for a single expansion ratio ($Er = 2.0$), the general conclusions hold for the other expansion ratios studied ($Er = 3.0$ and 4.0). As an illustration, Figure A-12 shows the time-mean streamline pattern for $Er = 3.0$ and $\phi_{in} = 0.016\%$ at various Reynolds numbers. The critical Reynolds number for bifurcation is approximately 80 [36] for the single phase case, but due to the delay caused by the solid phase, symmetric flow is still observed at $Re_{max} = 400$. By $Re = 800$, bifurcation has occurred, and increasing the Reynolds number to $Re_{max} = 1000$ causes growth of secondary recirculation zones inside of the larger primary circulation region (labelled A) and also tertiary recirculation regions beside the smaller primary one (labelled B).

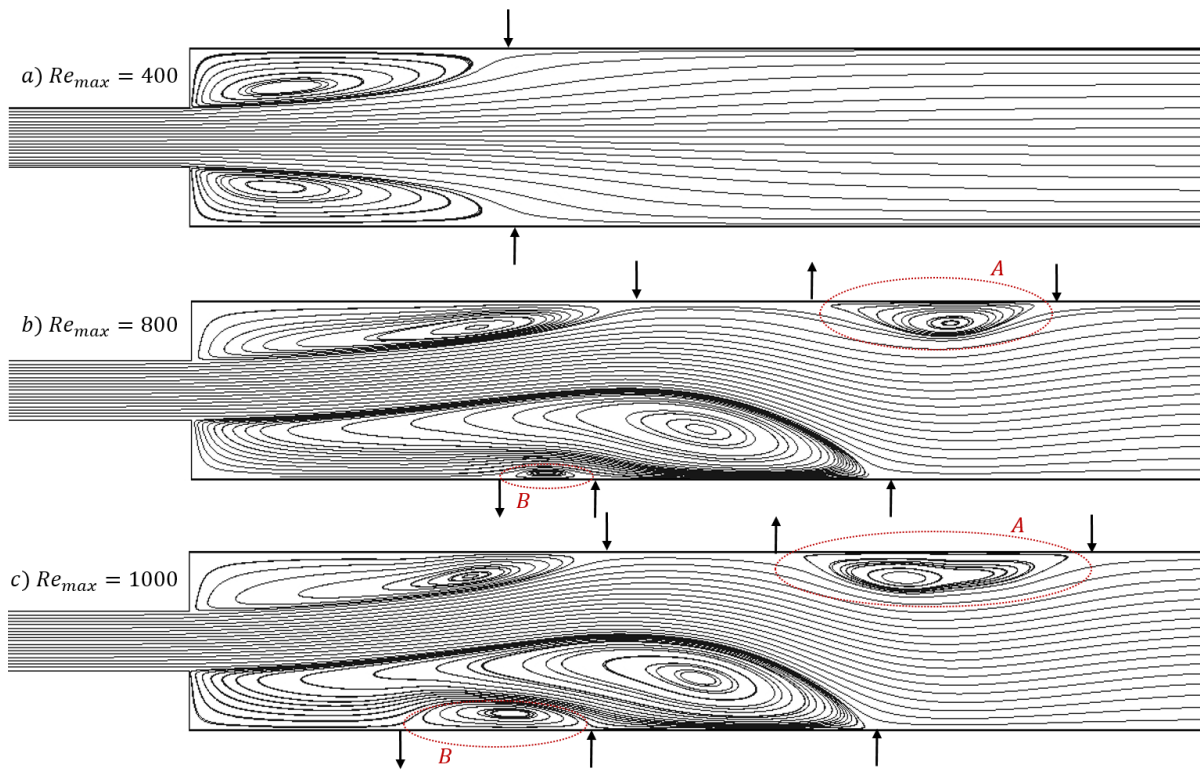


Figure A-12: Time-mean streamline pattern in a sudden expansion for various Reynolds number with volumetric particle injection rate of $\phi_{in} = 0.016\%$ at $Er = 3.0$

Having observed the qualitative effects of solid particles on the flow in the sudden expansion, we now quantify the sensitivity of the above qualitative observations to the solid phase fraction and particle size. This is accomplished in Figure A-13 and Figure A-14 by plotting the reattachment lengths on the upper and lower channel walls at two Reynolds numbers ($Re_{max} = 400$ and 1000) for a range of ϕ_s values and d_p/d values, respectively. As shown in Figure A-13, the maximum difference between the upper and lower reattachment lengths exists for the $\phi_s = 0$ case. As the particle volume fraction increases at a fixed Reynolds number, the asymmetry of the flow decreases as the smaller reattachment location (L_{r1}) moves downstream while the larger reattachment location (L_{r2}) moves upstream until bifurcation disappears at about $\phi_s = 0.04\%$ and 0.012% for $Re_{max} = 400$ and 1000 , respectively. With further increase in the solid phase fraction in the $Re_{max} = 1000$ case, the reattachment length of the symmetric flow decreases due to the growth of secondary recirculation regions inside the primary recirculation regions, ultimately leading to global unsteadiness of the flow, as seen in Figure A-11 and Figure A-12. In the $Re_{max} = 400$ case, increasing ϕ_s causes not only diminished bifurcation but also a near disappearance of the recirculation regions on both walls, as seen in Figure A-6(c).

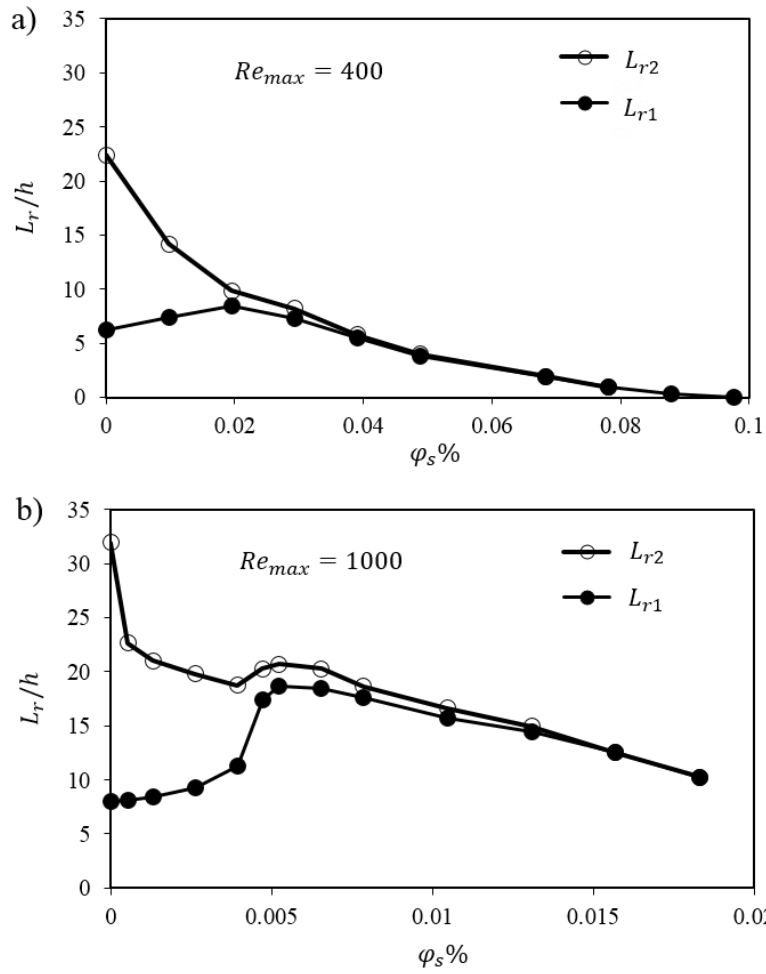


Figure A-13: Average shear layer reattachment lengths at (a) $Re_{max} = 400$ and (b) $Re_{max} = 1000$ for $Er = 2.0$. The particle diameter is fixed at $d_p/d = 0.001$. Subscripts 1 and 2 denote upper and lower walls, respectively

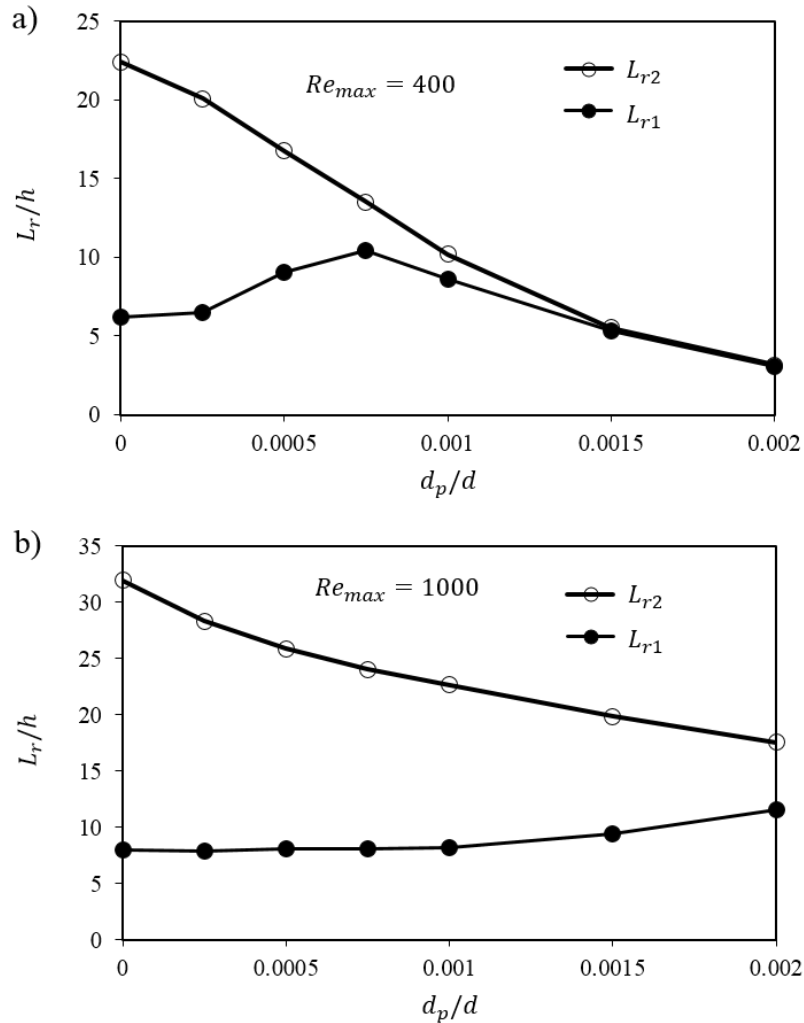


Figure A-14: Average shear layer reattachment lengths at (a) $Re_{max} = 400$ and (b) $Re_{max} = 1000$ for $Er = 2.0$. The solid phase fraction is fixed at $\phi_s = 0.0016\%$. Subscripts 1 and 2 denote upper and lower walls, respectively

The effect of particle size on the upper and lower reattachment lengths, shown in Figure A-14, is consistent with the effect for solid phase fraction. Larger particle sizes tend to decrease the larger reattachment length almost linearly while the smaller reattachment length initially increases to diminish the degree of asymmetry in the flow. Symmetry of the reattachment region is recovered at about $d_p/d = 0.0015$ for $Re_{max} = 400$, while larger particles sizes are required to

recover symmetry at $Re_{max} = 1000$. Further increasing the size of particles is not possible due to MP-PIC limitations on the maximum solid volume per cell. The time-mean streamlines corresponding to various particle sizes are illustrated in Figure A-15. As discussed, the bifurcation disappears with larger particle sizes and the reattachment region then shrinks symmetrically.

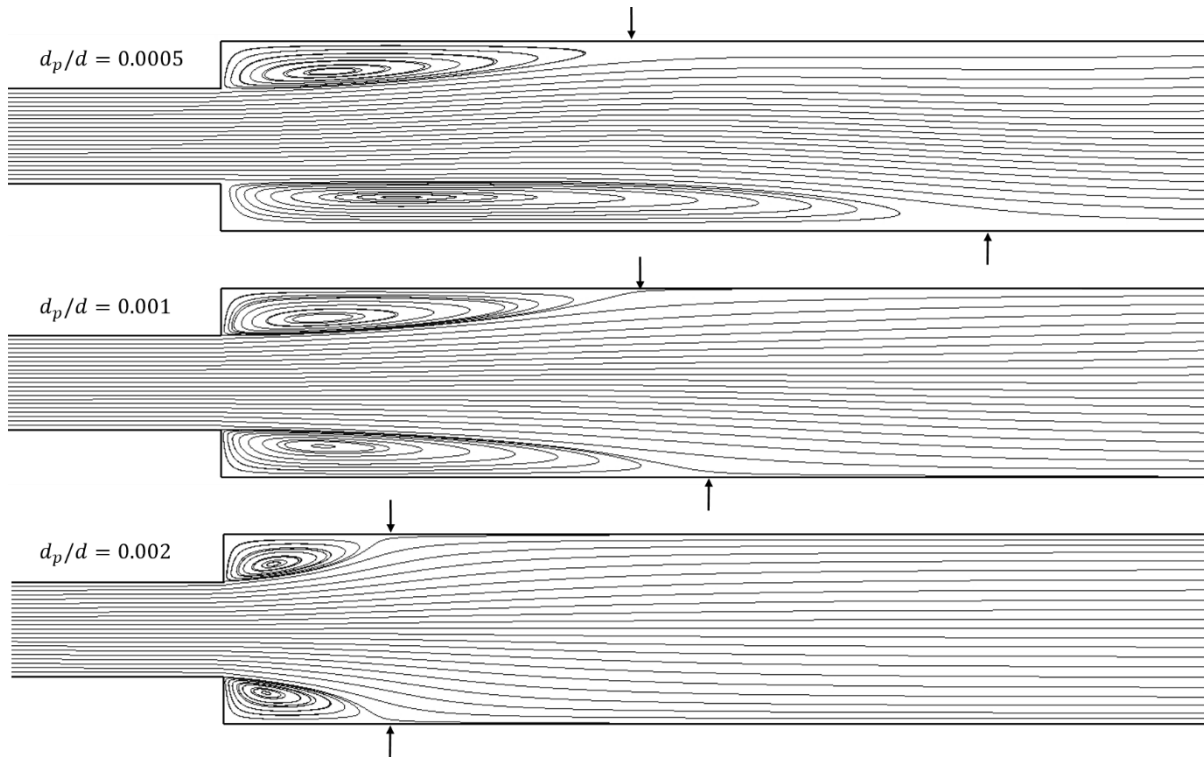


Figure A-15: Time-mean streamline pattern near the expansion for different particle sizes with $Re_{max} = 400$ and $Er = 2.0$

A.6 Transport of suspended particles

The instantaneous position of the suspended particles for cases with $Re_{max} = 400$ and 1000 and $Er = 2.0$ is illustrated in Figure A-16. The volumetric particle injection fraction of these cases is $\varphi_{in} = 0.016$ and the particle size is $d_p/d = 0.001$. The speed of the particles is shown by colouring

them according to their velocity magnitude. Symmetric recirculation regions in the $Re_{max} = 400$ case trap nearly stationary particles. In the $Re_{max} = 1000$ case, bifurcation of the flow is apparent, also trapping particles in the asymmetric recirculation regions.

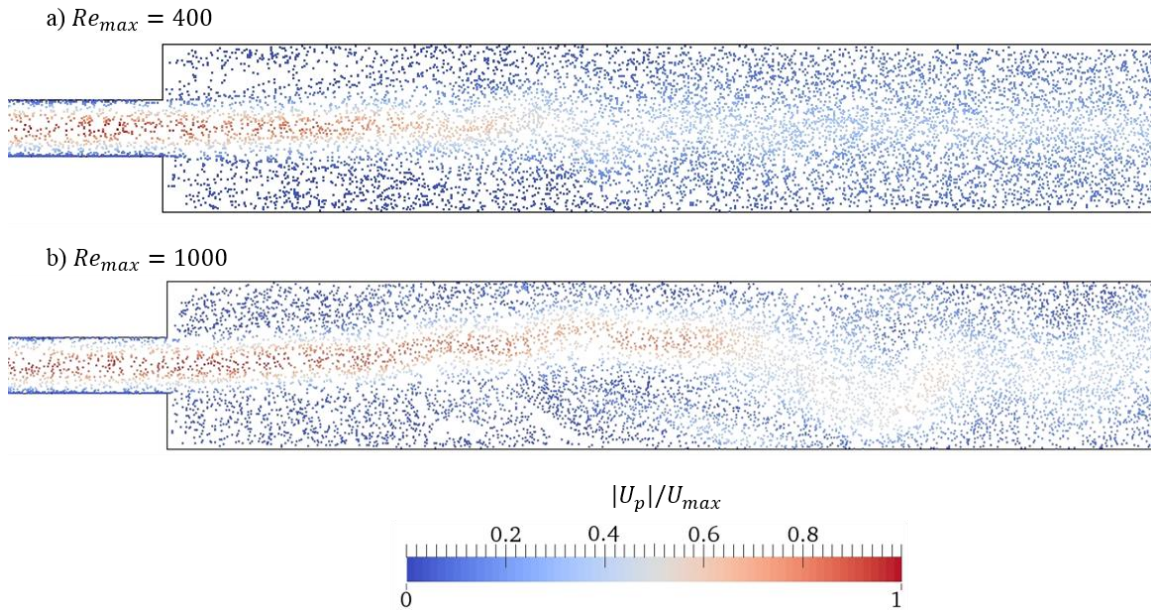


Figure A-16: Zoomed view for instantaneous velocity contour of particles in a sudden expansion with constant volumetric injection rate of particles $\phi_s = 0.0016$: a) $Re_{max} = 400$ and $Er = 3.0$, b) $Re_{max} = 800$ and $Er = 3.0$

The impact of the flow patterns on the residence time of the solid particles is shown in Figure A-17 by colouring the particles according to the period that the particle has existed in the domain (its age), normalized by the age of the oldest particle in the domain. Particles with the highest age occur in the symmetric recirculation regions in the $Re_{max} = 400$ case, whereas much younger particles exist in the $Re_{max} = 1000$ case. Analysis of the unsteady flow shows that wall-normal oscillations of the tip of the high-speed core region at higher Reynolds number causes frequent change in the size of recirculation regions. When the tip of high-speed core shifts in the wall-normal direction, one recirculation region shrinks while the other expands. This oscillation

releases trapped particles from the contracting recirculation zones into the main flow and entrains newer particles from the core flow into the expanding recirculation zones. Bifurcation is therefore an effective method for mixing particles in the laminar sudden expansion flow to achieve relatively uniform particle residence times.

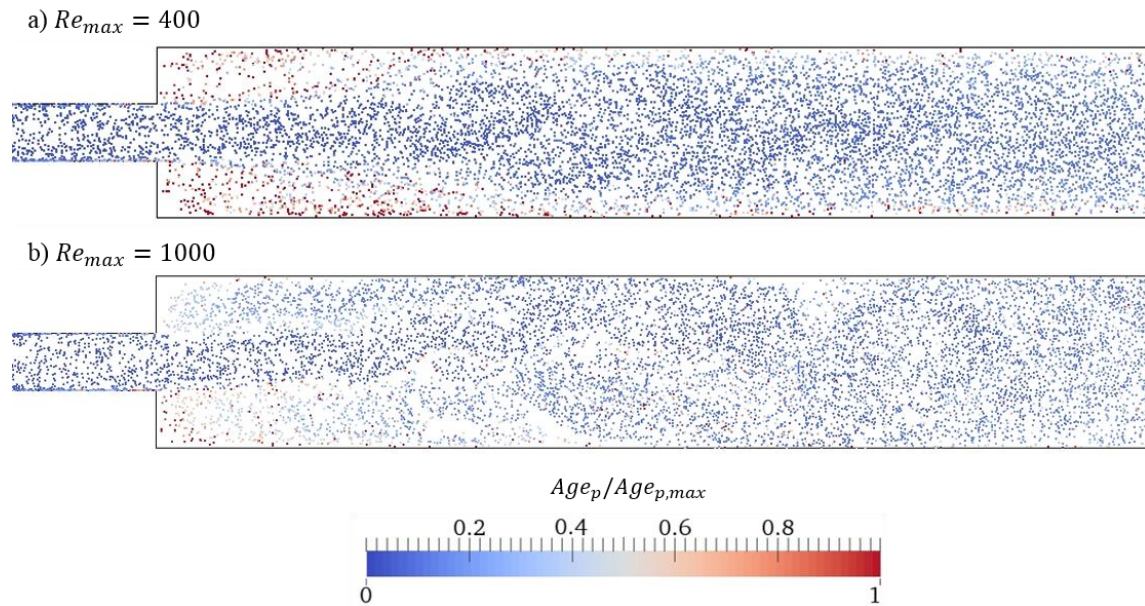


Figure A-17: Zoomed view for age of remained particles in a sudden expansion with constant injection volumetric rate of $\phi_s = 0.0016$: a) $Re_{max} = 400$ and $Er = 3.0$, a) $Re_{max} = 800$ and $Er = 3.0$